

On the Performance and Analysis of Massive MIMO for 5G Wireless Systems

by

Callum Thomas Neil

A thesis
submitted to the Victoria University of Wellington
in fulfilment of the
requirements for the degree of
Doctor of Philosophy
in Engineering.

Victoria University of Wellington
2017

Acknowledgments

The author would like to firstly express his gratitude to his family: Jim, Helen and Fergus Neil, for all their support and encouragement throughout the postgraduate journey.

Callum is grateful to have had the opportunity to undertake postgraduate study, of which Dr. Mansoor Shafi was instrumental. Since Callum's undergraduate studies Mansoor has been a fantastic mentor to Callum, sharing his world class experience and expertise. The contribution of the thesis would not have been as significant without him.

The author thanks Dr. Pawel Dmochowski, Dr. Mansoor Shafi and Prof. Peter Smith for their exceptional supervision. Constructive feedback and creative research ideas from the supervisors were invaluable in the progression of research.

A special acknowledgement is given to Harsh Tataria, a colleague who has provided motivation and encouragement to the author throughout the duration of the Ph.D. Other colleagues who have contributed to the research include Dr. Adrian Garcia-Rodriguez, Dr. Christos Masouros, Dr. Fatih Ustok, Dr. Jawad Mirza and Radek Hes.

Finally Callum would like to thank his friends: Nikau Edwards, Kyle Bellars, Courtney Hill, Caitlin Barclay and Peter Small, for their succour and support.

Callum Thomas Neil, February 2017

Abstract

A novel technical solution, and paradigm shift, envisioned to achieve the significant spectral efficiency enhancements required for Fifth Generation (5G) wireless systems is *massive multiple-input-multiple-output (MIMO)*. Massive MIMO systems scale up the number of transmit (TX) and receive (RX) antennas by at least an order of magnitude relative to conventional multi-user MIMO systems, which have been a key feature in current wireless standards, such as Long Term Evolution. Thus, massive MIMO leverages the spatial dimension by providing significant increases in all the virtues of conventional MIMO systems but on a much larger scale. Namely, data rate, link reliability, energy efficiency, and multiplexing gains can all be increased with massive MIMO systems, while simultaneously reducing inter-user interference through digital processing techniques. Further motivating the surge in research of massive MIMO systems are the additional channel properties which occur when operating with large dimensions. These properties arise as a result of random matrix theory asymptotics and under these conditions random variables become deterministic, simplifying analysis and allowing simple processing techniques to become (near) optimal. These idealistic properties, however, are based on the assumptions of an independent and identically distributed channel matrix with an infinite number of TX antennas.

Physical constraints typically prohibit the deployment of large numbers of TX antennas. It therefore seems natural to determine the number of TX antennas required for large MIMO systems to begin to exhibit these favourable asymptotic properties. Analytically deriving the first and second moments of the composite Wishart channel matrix and numerically defining three convergence metrics, the rate of channel convergence is examined. Limiting matched-filter (MF) and zero-forcing precoding signal-to-interference-plus-noise-ratio (SINR) performances are then analytically derived and rate of convergence shown.

Coordinated distributed MIMO systems can mitigate the detrimental effects of spatial correlation relative to a colocated MIMO system. The instantaneous and limiting MF SINR performance of a distributed massive MIMO system is derived, allowing clear insights into the effects of imperfect channel state

information, spatial correlation, link gains and number of antenna clusters.

The wide bandwidths vacant at millimeter-wave (mmWave) frequency bands are suitable for 5G wireless systems since they occupy regions of uncongested spectrum which enable large contiguous bandwidth carriers. Spatial correlation of an arbitrary antenna array topology is analytically derived for a mmWave channel model. Numerically, the effects of mutual coupling amongst antenna elements is then shown on the effective spatial correlation, eigenvalue structure and user rate of different antenna topologies.

Channel models and measurements across a wide range of candidate bands for 5G wireless systems are then considered, motivated by the different propagation and spatial characteristics between different bands and different channel models within the same band. Key channel modelling and spatial parameter differences are identified and, in turn, their impact on various antenna topologies investigated, in terms of system sum rate, channel eigenvalue structure, effective degrees of freedom and massive MIMO convergence properties.

Acronyms

2D	Two-dimensional
3D	Three-dimensional
3GPP	3rd Generation Partnership Project
4G	Fourth Generation
5G	Fifth Generation
AOA	Angle-of-arrival
AOD	Angle-of-departure
AWGN	Additive white Gaussian noise
BS	Base station
BUPT	Beijing University of Posts and Telecommunications
CDF	Cumulative distribution function
CSI	Channel state information
DOF	Degrees-of-freedom
DPC	Dirty paper coding
DL	Downlink
EDOF	Effective degrees-of-freedom

EMF	Electromotive force
FDD	Frequency-division-duplex
i.i.d.	Independent and identically distributed
LOS	Line-of-sight
LTE	Long Term Evolution
MF	Matched-filter
MIMO	Multiple-input-multiple-output
MMSE	Minimum mean squared error
mmWave	Millimeter-wave
MSE	Mean squared error
MU	Multi-user
NLOS	Non-line-of-sight
PAS	Power azimuth spectrum
PDF	Probability density function
PES	Power elevation spectrum
RF	Radio frequency
RMS	Root mean square
RX	Receiver
RZF	Regularized zero-forcing
SINR	Signal-to-interference-plus-noise-ratio

SLNR	Signal-to-leakage-plus-noise-ratio
SNR	Signal-to-noise-ratio
SVD	Singular value decomposition
TDD	Time-division-duplex
TX	Transmitter
UCA	Uniform cylindrical array
UL	Uplink
ULA	Uniform linear array
URA	Uniform rectangular array
USA	Uniform square array
WPC	White paper collaboration
ZF	Zero-forcing

Notation and Symbols

$ \cdot $	Magnitude of a constant and determinant of a matrix
$\ \cdot\ $	Euclidean norm of a vector
$\ \cdot\ _{\text{F}}$	Frobenius norm of a matrix
$(\cdot)^*$	Conjugate of a complex number
$(\cdot)^{-1}$	Inverse of a constant or matrix
$(\cdot)^{\text{T}}$	Transposition of a vector or matrix
$(\cdot)^{\text{H}}$	Conjugate transposition of a vector or matrix
$\mathbf{0}_{M \times M'}$	$M \times M'$ matrix of zeros
$\mathbf{1}_{M \times M'}$	$M \times M'$ matrix of ones
\mathbf{a}_{RX}	Receiver antenna array response vector
\mathbf{a}_{TX}	Transmitter antenna array response vector
α	Path loss offset constant
B	Bandwidth
β	Path loss exponent
χ_a^2	A chi-squared complex random variable with a degrees-of-freedom
C	Number of clusters

$\mathcal{CN}(\mu, \sigma^2)$	Complex normal distribution with mean μ and variance σ^2
$\text{cov}[\cdot]$	Covariance operator
d	Transmitter to receiver distance, in meters
d_0	Reference distance, in meters
$d_{k,k'}$	Distance between users $k, k' \in 1, \dots, K$, in meters
d_{SC}	Spatial correlation reference distance, in meters
d_λ	Inter-element antenna spacing, in wavelengths
δ	Diagonal dominance
$\det(\cdot)$	Determinant of a matrix
$\text{diag}(\cdot)$	Diagonal matrix generation <i>or</i> diagonal matrix elements
$\exp(\mathbf{x})$	Exponential function of each element of the vector \mathbf{x}
$\text{Exp}(\cdot)$	Exponential distribution
\mathbf{E}	Deviation matrix
$\mathbb{E}[\cdot]$	Expected value
ϵ	Shadow fading standard deviation
ϵ_γ	Cluster shadow fading standard deviation
η	Singular value of a matrix
f	Carrier frequency
$f_X(x)$	Probability density function of x
F	Noise figure

F_{TX}	Transmit antenna array directive gain
$F_X(x)$	Cumulative distribution function of x
\mathbf{g}	Vector with independent elements
G_{TX}	Transmit antenna gain
G_{RX}	Receive antenna gain
G_θ	Vertically polarized antenna gain
γ	Cluster power normalization
Γ	Link gain model decay parameter
h_{RX}	Receiver height in meters
h_{TX}	Transmitter height in meters
\mathbf{H}	Channel matrix
$\bar{\mathbf{H}}$	Mutually coupled channel matrix
$\hat{\mathbf{H}}$	Estimated channel matrix
$\tilde{\mathbf{H}}$	Gaussian error matrix
$\ddot{\mathbf{H}}$	Equivalent channel matrix
$\check{\mathbf{H}}$	Stacked channel matrix to multiple users
\mathbf{H}_{iid}	Channel matrix with i.i.d. entries
\mathbf{H}_{LOS}	Specular channel matrix
$\ddot{\mathbf{H}}_{\text{LOS}}$	Equivalent specular channel matrix
ι	Antenna length

$I_\alpha(\cdot)$	Modified Bessel function of the first kind
\mathbf{I}_M	$M \times M$ identity matrix
\Im	Imaginary component of a complex number
j	Imaginary number
$J_\alpha(\cdot)$	Bessel function of the first kind
K	Number of receivers in a cellular system
K_B	Boltzmann constant
κ	Rician K-factor
$\ddot{\kappa}$	Equivalent Rician K-factor
\varkappa	RZF precoder regularization parameter
L	Number of subpaths per cluster
λ	Wavelength at a carrier frequency
$\mathbf{\Lambda}$	Diagonal matrix of singular values
M	Number of transmit antennas in a cellular system
μ	Mean of a distribution
μ_κ	Rician K-factor mean
N	Number of antenna clusters in a cellular system
N_0	Thermal noise
$\mathcal{N}(\mu, \sigma^2)$	Normal distribution with mean μ and variance σ^2
ν	Ratio of TX antennas to RX antennas

\mathcal{O}	Reads as “order of”
ω	Path loss
p_{LOS}	Probability of LOS propagation
$p_X(x)$	Power angular spectrum of X
P	Link gain
P_{TX}	Transmit power
Poisson (\cdot)	Poisson distribution
ϕ	Azimuth angle
Φ	Distribution of ϕ
φ	LOS azimuth angle
π	Mathematical constant pi
ψ	Azimuth angle
Q	Number of receive antennas per receiver in a cellular system
r	Cell radius
r_t	Delay distribution proportionality factor
\mathbf{r}_{RX}	Receiver spherical unit vector
\mathbf{r}_{TX}	Transmitter spherical unit vector
R	System rate
\mathbf{R}_{RX}	Receiver spatial correlation matrix
$\ddot{\mathbf{R}}_{\text{RX}}$	Equivalent receiver spatial correlation matrix

\mathbf{R}_{TX}	Transmitter spatial correlation matrix
$\ddot{\mathbf{R}}_{\text{RX}}$	Equivalent transmitter spatial correlation matrix
\Re	Real component of a complex number
ρ	Exponential spatial correlation decay parameter
ϱ	Average received cell-edge SNR
\mathbf{s}	Unprecoded vector of data symbols
σ	Standard deviation of a distribution
σ_{κ}	Rician K-factor standard deviation
σ_{ϕ}	Azimuth RMS angular spread
σ_{θ}	Elevation RMS angular spread
$\text{sgn}(\cdot)$	Signum operator
T	Temperature in Kelvin of zero degrees Celsius
\mathbf{T}	Unitary matrix
$\text{tr}(\cdot)$	Trace of a matrix
τ	Precoder/receiver normalization parameter
θ	Elevation angle
Θ	Distribution of θ
ϑ	LOS elevation angle
\mathbf{U}	Unitary matrix
v	Channel power scaling constant

Υ	Link gain and spatial correlation scaling matrix
\mathbf{v}	Noise vector
\mathbf{V}	Normalized “channel” matrix
\mathbf{V}_{iid}	Normalized i.i.d. “channel” matrix
$\text{var}[\cdot]$	Variance operator
\mathbf{W}_{RX}	Receive antennas location matrix
\mathbf{W}_{TX}	Transmit antennas location matrix
X_c	Per-cluster uniform random variable
\mathbf{x}	Precoded data vector
ξ	Imperfect CSI parameter
Ξ	Mutual impedance matrix
$Y_{\phi,c}$	Azimuth central cluster angle random variation
$Y_{\theta,c}$	Elevation central cluster angle random variation
\mathbf{y}	Received signal
Z_A	Antenna impedance
Z_L	Load impedance
Z_M	Mutual impedance
Z_ϕ	Azimuth cluster scaling factor
Z_θ	Elevation cluster scaling factor
\mathbf{Z}	Mutual coupling matrix

ζ	Shadow fading
ζ_γ	Cluster shadow fading

Contents

Acknowledgments	i
Abstract	iii
Acronyms	v
Notation and Symbols	ix
1 Introduction	1
1.1 5G Wireless Communications	1
1.2 Overview and Literature Review	2
1.2.1 Massive MIMO	2
1.2.2 Linear Precoding	4
1.2.3 Spatial Correlation and Mutual Coupling	5
1.2.4 Millimeter-Wave Wireless Communications	6
1.3 Motivation	6
1.3.1 Convergence to Massive MIMO	7
1.3.2 Distributed Antenna Systems	7
1.3.3 Spatial Correlation for Millimeter-Wave Systems	7
1.3.4 Channel Models for 5G Wireless Systems	8
1.4 Contributions	8
1.4.1 Convergence to Massive MIMO	8
1.4.2 Distributed Antenna Systems	9
1.4.3 Spatial Correlation for Millimeter-Wave Systems	10
1.4.4 Channel Models for 5G Wireless Systems	10
1.5 List of Publications	11
1.6 Thesis Outline	12
2 Theoretical Background	13
2.1 MIMO	13
2.1.1 System Model	14
2.1.2 Channel Models	15
2.1.3 Rate and Spectral Efficiency	22

2.2	Linear Precoding	23
2.2.1	MF Precoding	23
2.2.2	ZF Precoding	24
2.2.3	RZF Precoding	24
2.2.4	SLNR Precoding	25
2.3	Spatial Correlation	25
2.3.1	The Exponential Spatial Correlation Model	27
2.4	Mutual Coupling	29
2.5	Massive MIMO	30
2.5.1	Channel Matrix	31
2.5.2	Sum Rate	31
2.5.3	Linear Precoding	32
3	Convergence to Massive MIMO	35
3.1	Introduction	35
3.2	Channel Convergence	37
3.2.1	Rayleigh Fading Channel	38
3.2.2	Rician Fading Channel	42
3.3	SINR Convergence with Linear Precoders	48
3.3.1	Rayleigh Fading Channel	48
3.3.2	Rician Fading Channel	54
3.4	Conclusion	57
4	Distributed Antenna Systems	59
4.1	Introduction	59
4.2	System Description	60
4.3	Instantaneous MF SINR	61
4.3.1	Instantaneous MF SINR Analysis	61
4.3.2	Instantaneous MF SINR Numerical Results	65
4.4	Limiting MF SINR	69
4.4.1	Limiting MF SINR Analysis	69
4.4.2	Limiting MF SINR Numerical Results	80
4.5	Conclusion	82
5	Spatial Correlation for Millimeter-Wave Systems	85
5.1	Introduction	85
5.2	System Model	86
5.2.1	Angular Power Spectra	87
5.3	Spatial Correlation	88
5.3.1	Wide AOD PES	90
5.3.2	Narrow AOD PES	92
5.3.3	Von Mises AOD PES	95

5.3.4	General PES Upper Bound	97
5.4	Convergence to Massive MIMO: Diagonal Dominance	99
5.4.1	Wide AOA PES	101
5.4.2	Narrow AOA PES	101
5.4.3	Von Mises AOA PES	103
5.4.4	General PES Upper Bound	104
5.5	Numerical Mutual Coupling Results	105
5.5.1	Impact of Antenna Separation	105
5.5.2	Eigenvalue Structure	109
5.5.3	User Rate	112
5.6	Conclusion	116
6	Channel Models for 5G Wireless Systems	119
6.1	Introduction	120
6.2	Channel Models	121
6.2.1	Channel Modelling Differences	122
6.3	System Description	123
6.3.1	Simulation Description	123
6.4	System Sum Rate	125
6.4.1	The Impact of Varying Intra-Cluster Angular Spread	125
6.4.2	Cell Wide Sum Rate	132
6.4.3	Impact of User Numbers	133
6.5	Channel Eigenvalue Properties	134
6.5.1	Impact of Inter-Element Antenna Spacings	134
6.5.2	Impact of Propagation Type	139
6.6	Channel Effective Degrees of Freedom	144
6.6.1	Impact of Receiver Antenna Numbers	144
6.6.2	Impact of Number of Users	146
6.7	Channel Convergence to Massive MIMO	147
6.8	Equivalent Rician Fading Channel Model	149
6.8.1	Single Antenna Users, $Q = 1$	152
6.8.2	Double Antenna Users, $Q = 2$	152
6.8.3	Multiple Antenna Users, $Q \geq 3$	152
6.9	Conclusion	153
7	Conclusions and Future Work	157
7.1	Conclusions	157
7.1.1	Convergence to Massive MIMO	158
7.1.2	Distributed Antenna Systems	159
7.1.3	Millimeter-Wave Wireless Communications	159
7.1.4	Channel Models for 5G Wireless Systems	160
7.2	Future Work	161

7.2.1	Eigenvalue Sensitivity	161
7.2.2	Hybrid Beamforming with Sub-Arrays	162
7.2.3	Massive MIMO for TDD or FDD?	162

1

Introduction

This chapter presents an introduction to the thesis. An overview of massive multiple-input-multiple-output (MIMO) technology in the context of Fifth Generation (5G) wireless systems is given before a more detailed breakdown of the key aspects of the thesis, including relevant literature discussion. Motivation of the research is then provided followed by the main contributions, list of publications and thesis outline, respectively.

Massive MIMO technology scales up the number of transmit (TX) and receive (RX) antennas in comparison to conventional multi-user (MU)-MIMO systems by at least an order of magnitude. In ideal situations, massive MIMO offers large improvements in data rates, link reliability, energy efficiency, and multiplexing gains while simultaneously reducing inter-user interference through linear precoding techniques. However, in general, when large numbers of antennas are located in close proximity (in terms of wavelength), the detrimental effects of spatial correlation and mutual coupling amongst antenna elements can significantly reduce performance. However, when operating at millimeter-wave (mmWave) frequencies, the small wavelength allows many more antenna elements to be positioned in a fixed antenna array form factor while preserving the promising performance gains. Hence, massive MIMO and mmWave communication are closely related and both are considered in this thesis.

1.1 5G Wireless Communications

Unprecedented growth and projected exponential increases in the volume of wireless data traffic [1] (5000 fold by the year 2030 [2]) have motivated the

research and development of potential next generation wireless system technologies. These efforts have led to the development of 5G system engineering requirements which are expected to include an aggregate data-rate increase, from Fourth Generation (4G) wireless systems, of three orders of magnitude with peak data rates in the order of tens of Gbps [3–5]. One such novel technical solution, and paradigm shift, envisioned to achieve such significant wireless system enhancements is *massive MIMO* [6–8]. Combined with improvements in area spectral efficiency, from *small cell technology* [9–15], and increased bandwidth, from *mmWave* frequencies [16–21], massive MIMO technology is a promising solution in achieving high data rate ubiquitous coverage. However, many important research challenges need to be resolved before the commercial deployment of massive MIMO is possible.

Several of the issues massive MIMO faces are examined in this thesis, such as

- The near-optimal performance of linear precoding techniques largely rely on users' channels becoming sufficiently decorrelated. Practical aspects such as imperfect channel state information (CSI) and spatial correlation reduce the level of orthogonality, and thus the performance of linear precoding techniques [8, 22].
- As more antennas are added to a fixed antenna array form factor, spatial separation between antenna elements reduces and consequently spatial correlation and mutual coupling between the antenna elements of the array increase [7, 23, 24].
- For evaluating massive MIMO in conjunction with mmWave technology, accurate channel models of the different electromagnetic propagation characteristics at mmWave frequencies need to be established [4, 25, 26]. One distinguishing feature between electromagnetic propagation at mmWave and microwave frequencies is the phenomena of blockages, observed in recent mmWave measurement campaigns [17, 27].

1.2 Overview and Literature Review

An overview and literature review of each of the key topics covered in the thesis is now given.

1.2.1 Massive MIMO

It is well known that, on the downlink (DL), increasing the number of antennas at the base station (BS), i.e., at the TX, can result in large increases in data rate [28–35], link reliability [36], and energy efficiency [8]. In MU systems,

increased TX antenna numbers reduce inter-user interference [7, 37, 38] and increase system diversity through multiplexing gains [39–42]. Massive MIMO, which scales up the number of TX and RX antennas by at least an order of magnitude relative to conventional MU-MIMO systems, leverages the spatial dimension providing significant increases in data rate, link reliability, energy efficiency, and multiplexing gains while reducing inter-user interference. Consequently, the investigation of massive MIMO technology as an emerging technology is well underway [6–8, 43–62].

Further motivating the surge in research activities into massive MIMO systems are the additional channel properties which arise when operating with large numbers of TX antennas. These properties arise as a result of random matrix theory asymptotics [63]. For example, as the number of TX antennas becomes large, users' channels become mutually orthogonal [6, 7, 64]. This is known as *favourable propagation*, and under these conditions simple linear processing techniques, such as matched-filter (MF) and zero-forcing (ZF) precoding, can maximize the sum rate [43, 65–67]. Another virtue of massive MIMO systems is referred to as *channel hardening* [68], where the variance of the Wishart channel matrix decreases proportional to the number of TX antenna numbers, such that the channel entries start to become deterministic [6, 43]. In turn, when random matrices become deterministic and well conditioned, system analysis and precoder design becomes simplified since matrix operations can be computed more easily [7]. For example, the computationally involved matrix inverse required for ZF precoding becomes the identity matrix. These idealistic properties, however, are based on the assumptions of an independent and identically distributed (i.i.d.) channel with an infinite number of TX antennas.

Since the deployment of a very large number of TX antennas may be impractical due to physical constraints, it seems natural to determine the number of TX antennas required for MIMO systems to begin to exhibit these additional benefits. The effects of increasing array size has been the subject of a number of studies, where the singular value spread is most commonly used to quantify the degree of orthogonality between different channels [7, 8, 65, 66, 69]. Favourable propagation is evaluated in [66] by considering the distribution of singular values for two extreme channel scenarios: i.i.d. Rayleigh fading and line-of-sight (LOS) channels. The authors show that both channels offer near favourable propagation for 100 TX antenna elements. Reference [69] also measures the singular value spread of a real massive MIMO channel. Here it is demonstrated that increasing numbers of TX antenna elements both decorrelate and harden users' channels significantly from conventional MIMO systems. In [7], the authors conclude that the asymptotic effects of random matrix theory are observable even for arrays of 10 antennas, although the desirable properties of an “infinite” number of an-

tennas are more prominent at 100 antennas and above. Channel measurements with 128 TX antennas and two single-antenna users were conducted in [56, 65], and it was shown that orthogonality improves for an increasing number of TX antennas, but little improvement beyond a 20 TX antenna element array is seen. Even in the unfavourable channel conditions of closely-spaced users with strong LOS propagation, measured results in [65] indicate that although the singular value spread is significantly larger than in the i.i.d. Rayleigh fading case, a large portion of the i.i.d. Rayleigh fading asymptotic capacity is still achievable in the measured channels.

1.2.2 Linear Precoding

With the large number of antennas expected to be deployed in massive MIMO, the complexity of baseband processing becomes extremely large. Thus, the practical implementation of non-linear digital precoding schemes, such as dirty paper coding (DPC) [70] and vector perturbation [71–73], becomes too difficult. This motivates the study of *linear* precoding [74] techniques for massive MIMO systems, which has received significant recent attention, such as in [7, 43, 45, 51, 53, 54, 56, 66, 69, 75–77].

Early massive MIMO measurements in [56] evaluated the sum rate with ZF precoding and showed that the ZF precoder can achieve 98% of the DPC sum rate, even with a 20 element TX array. A further massive MIMO measurement campaign was carried out by the same authors in [76] which compared the asymptotic ZF precoder performance of 128 element linear and cylindrical antenna arrays to the ideal, i.i.d., channel. The study concluded that the real measured channels achieve most of the performance of the i.i.d. case, even with 10 TX antenna elements. Other measurements in [69] show that ZF can achieve 69% of optimal DPC capacity with a 64 TX antenna element array. The authors in [43] demonstrate that by using linear precoding at the TX, improvements in sum spectral efficiency and energy efficiency of up to two orders of magnitude and three orders of magnitude, respectively, can be achieved by using 100 TX antenna elements. Also lower bounds on sum rate for MF and ZF precoding techniques are derived, including scenarios with channel estimation imperfections [54, 55, 77–79]. The later work in [45] derives instantaneous and asymptotic (with the number of TX antennas) approximations of achievable rates with MF and regularized ZF (RZF) precoding. The authors consider the very general scenario of a multi-cell, distributed antenna cluster system operating in time-division-duplex (TDD) transmission, with unequal link gains, spatial correlation matrices and corrupted CSI from pilot contamination [6].

1.2.3 Spatial Correlation and Mutual Coupling

As more antennas are added to a fixed antenna array form factor, inter-element antenna spacings reduce and consequently spatial correlation [80–84] and mutual coupling [24, 85–89] between antenna elements of the array increases. In massive MIMO systems, the effects of spatial correlation and mutual coupling are more obvious since inter-element spacings are critically reduced and antennas are in close proximity to, and even surrounded by, large numbers of other antenna elements. A number of important metrics of MIMO communication systems, such as the achievable rate and the number of independent data streams (multiplexing gain), have been shown to be highly dependent on the spatial correlation [23, 48, 65, 83, 84, 90–102] and mutual coupling [24, 85–89] characteristics, which are a function of both the transmission channel and the antenna array topology.

Spatially constrained antenna arrays with a very large number of antennas were studied in [83, 103, 104], where scenarios of inter-antenna spacings shorter than half a wavelength were considered, since these arise naturally when a large number of antennas are packed in the fixed physical structures of realistic BSs. Measurements at 2.59 GHz are provided in [99] which compare a horizontal uniform linear array (ULA), a vertical ULA and a uniform rectangular array (URA). The measurement shows that the horizontal ULA is best suited to massive MIMO systems, since the spatial correlation is lower than the other two antenna topologies. [96] considers a (ULA) and uniform square array (USA), concluding that when the spatial correlation structure decays rapidly, against distance, then the USA provides substantial benefits in terms of sum rate over the ULA. [97] analyses the performance of several antenna array topologies (ULA, URA and uniform circular array) in a three-dimensional (3D) channel. The analysis shows that the azimuth angular spread, rather than the elevation angular spread, has a defining impact on the system performance. Furthermore, it is shown that the impacts of the central cluster angles on the system performance is antenna topology dependent.

The impacts of mutual coupling have been shown to be more obvious at smaller inter-element spacings in [7, 24, 85, 87, 89, 105, 105]. Specifically, a fixed length ULA is considered in [89], where simulations demonstrate that mutual coupling adversely impacts both the effective spatial correlation and the received signal-to-noise-ratio (SNR), degrading the average rate. [106] shows that the effective spatial correlation, including mutual coupling, is increased for a ULA with five dipole antenna elements, degrading the number of spatial channels and MIMO system capacity. On the other hand, [24] reports a decrease in spatial correlation of a ULA when mutual coupling is included and thus an increase in its sum rate.

In massive MIMO systems, [104] shows a considerable decrease in the achievable rates due to mutual coupling.

1.2.4 Millimeter-Wave Wireless Communications

The wide bandwidths, available at mmWave frequency bands, are suitable to cope with the demanding data rate specifications of 5G wireless systems because they occupy regions of uncongested spectrum [17–21] that enable large contiguous bandwidth carriers. Consequently, the range of candidate bands being considered for 5G wireless systems has recently been extended to include 6–100 GHz [3]. Coexisting with massive MIMO technology [6, 27, 107] and small cells technology [9–13, 108], mmWave technology is expected to be a key technique in achieving the huge data rates required to meet 5G specifications [1, 4]. The large signal attenuation experienced at mmWave frequencies (due to oxygen absorption [17], object blockages [109, 110], and lack of scattering [98]) can be mitigated by large array gains [111, 112], from massive MIMO, and reduced link distances, from the area densification of small cells. Furthermore, the smaller wavelength at mmWave frequencies allows large numbers of antennas to be packed into limited array form factors [19, 113], and is thus appealing for massive MIMO antenna array design.

A number of papers have focused on characterizing radio wave propagation in the mmWave bands, for example [19, 114–128]. These studies show that the mmWave channel has significantly less multipath richness and a higher probability of LOS propagation, as compared to the microwave bands. Special emphasis has been placed on the development of statistical models based on measurement campaigns performed in urban environments [114, 116–119], which highlight the importance of both antenna directivity and array gains to overcome the increased propagation losses experienced at mmWave bands and also determine the number of antennas required towards this end [98]. Very recently, the 3rd Generation Partnership Project (3GPP) have published an extension of the standardized microwave 3D channel model for Long Term Evolution (LTE) [129], for the frequency spectrum above 6 GHz [130]. The additional modelling components in the new specification include: oxygen absorption (a function of the link distance), wideband transmission extensions, non-stationary user extensions, object blockages and multi-frequency simulation extensions.

1.3 Motivation

Massive MIMO is an emerging technology, which scales up the number of TX and RX antennas by at least an order of magnitude relative to conventional

MU-MIMO systems. This approach leverages the spatial dimension providing significant increases in data rate, link reliability, energy efficiency, and multiplexing gains while reducing inter-user interference. Due to random matrix theory asymptotics, simple linear precoding techniques become near-optimal in a number of channel conditions. Massive MIMO is suited to mmWave bands, since the small wavelength allows the dense packing of antenna elements. Also, the large signal attenuation at mmWave frequencies, due to a lack of scattering, can be overcome by the large array gains of massive MIMO technology.

1.3.1 Convergence to Massive MIMO

Many of the conclusions regarding the realizable performance gains with massive MIMO systems rely on the convergence of the Wishart channel matrix to the identity matrix. It is thus of interest to thoroughly explore the convergence properties of the Wishart channel matrix, and determine the number of TX antennas required for MIMO systems to converge under a number of channel conditions, since physical constraints typically limit the number of TX antenna elements which can be deployed. The limiting values of linear precoding techniques have been shown to be near-optimal in terms of sum rate and therefore the convergence properties of these techniques are also examined in various channel conditions. Hence, in Chapter 3, the convergence properties are analysed for a number of scenarios.

1.3.2 Distributed Antenna Systems

Massive MIMO suffers from spatial correlation more than conventional MIMO systems, since there are large numbers of (closely spaced) antennas in one physical location [80–84]. One design approach to mitigate the adverse effects of spatial correlation is to divide the antennas into multiple antenna clusters, whereby the inter-element antenna distances at each antenna cluster would increase, provided the overall form factors at each array remain the same. Such coordinated distributed systems have the additional advantage of providing greater coverage than a single, co-located, antenna cluster since both the minimum and average distance to a user is reduced and the resultant received SNR is increased [131]. There is therefore a need to analyse the performance of distributed massive MIMO systems. Therefore, the instantaneous and limiting MF SINR is analysed in Chapter 4.

1.3.3 Spatial Correlation for Millimeter-Wave Systems

The antenna array topology and its inherent inter-element antenna spacings have been shown to significantly affect the spatial correlation, mutual cou-

pling and resultant system capacity [23, 48, 65, 83, 84, 90, 96–102]. Furthermore, mmWave communication channels have been shown to suffer from severe spatial correlation due to the limited number of scattering clusters, as well as the narrow inter-cluster and intra-cluster angular spectra, which diminish the multiplexing and diversity gains attainable with large antenna arrays [92, 114, 117–119]. This poses a challenge for mmWave transmission, since the resultant achievable data rates depend on the richness of the multipath channel [23, 91, 132]. However, spatial channel sparsity can be simultaneously leveraged for reducing the number of RF chains required for transmission via hybrid precoding or beamspace strategies [133, 134]. Regardless, accurate models to quantify spatial correlation effects are needed to predict achievable rates and multiplexing gains. Thus, the effects of spatial correlation and mutual coupling on both two-dimensional (2D) and 3D antenna array topologies (i.e., full dimension MIMO [135–139]), including the commonly used ULA, are considered in Chapter 5.

1.3.4 Channel Models for 5G Wireless Systems

5G wireless systems are likely to include mmWave bands to meet the demands for high data rates in combination with existing microwave bands for wide area coverage. Microwave and mmWave frequency bands exhibit enormous variation in channel characteristics. For example, microwave bands provide excellent coverage capabilities but bandwidth is scarce. On the other hand, mmWave bands have an abundance of available spectrum but suffer from high electromagnetic attenuation [20]. There is, therefore, a need to understand the differences in propagation characteristics [140, 141], such as multipath spreads, for the different frequency bands being considered for 5G. Motivated by this, channel models over a wide range of bands are considered and examined. Furthermore, the impacts of these defining parameters on performance metrics such as eigenvalue structure and spectral efficiency are investigated in Chapter 6.

1.4 Contributions

The contributions of this thesis, listed by chapter, are as follows.

1.4.1 Convergence to Massive MIMO

- The rates of convergence of the Wishart channel matrix to favourable propagation and channel hardening, as the number of TX antennas increases with the number of single-antenna users fixed, of Rayleigh and Rician fading channel matrices are analytically derived. Note that the analytical convergence of the Wishart i.i.d. channel matrix, as the number

of TX antenna elements increases with the number of single-antenna users fixed, to favourable propagation and channel hardening in Rayleigh [142] and Rician [143] fading channels has previously been shown in the literature [6]. This analysis is extended here to the more realistic scenario of unequal link gains.

- The convergence properties of the Wishart i.i.d. channel matrix, in Rayleigh and Rician fading channels, is numerically studied by considering three different convergence metrics defined in Section 3.2, for increasing TX antenna numbers, with the ratio of TX antennas to single-antenna users fixed. This characterizes the number of TX antennas required, depending on which convergence property is desired.
- Closed-form limiting expressions, as the number of TX antennas and single-antenna users increase to infinity with a fixed ratio, of the per-user ZF SNR and MF Signal-to-interference-plus-noise-ratio (SINR) are derived for unequal link gains in a Rayleigh fading channel. Note that this has been previously derived for the case where the number of TX antennas increases to infinity with the number of users fixed, which is also included as a preliminary result in Section 3.3.1 for completeness. Also note that closed-form limiting expressions, as the number of TX antennas and single-antenna users increase to infinity with a fixed ratio, of the per-user ZF SNR and MF SINR has previously been derived for equal link gains in [7] for a Rayleigh fading channel. However, it is also included in this chapter to assist in the derivation of the unequal link gain case and for completeness. In turn, the rate of convergence of the average instantaneous per-user ZF SNR and MF SINR is investigated. Since the number of users simultaneously scheduled in a time/frequency resource is typically a key cellular design parameter, these expressions provide insight into the achievable ZF/MF SNR/SINR for a massive MIMO system.
- The performance of the average instantaneous per-user ZF SNR and MF SINR under Rayleigh and Rician fading channels, with and without spatial correlation at the TX, is shown. This illustrates the ZF/MF precoder performance in scenarios of a small and large antenna array aperture.

1.4.2 Distributed Antenna Systems

- Based on a system model which accounts for unequal link gains, imperfect CSI, transmit spatial correlation and an arbitrary number of antenna clusters, a per-user instantaneous MF SINR expression is derived. Numerically, it is then shown that distributing antennas into multiple clusters is hugely beneficial to MF SINR performance in highly spatially correlated

scenarios. Depending on the spatial characteristics of the channel (low or high spatial correlation), this gives practical antenna design recommendations.

- From the previously derived per-user instantaneous MF SINR, a limiting expected per-user MF SINR is derived as the number of antenna elements approaches infinity, whilst maintaining a fixed ratio of the number of transmit antennas to single-antenna users.
- A number of realistic link gain scenarios¹ are used to illustrate the convergence of the instantaneous per-user MF SINR to the limiting expected per-user MF SINR. Numerically, this is shown for spatially correlated and uncorrelated cases.

1.4.3 Spatial Correlation for Millimeter-Wave Systems

- Closed-form expressions for the 3D spatial correlation between any two antenna elements of a Saleh-Valenzuela channel model are derived for wide, narrow and Von Mises [144, 145] power elevation spectrum (PES) as well as an upper bound for the general PES case. These simple expressions give an accurate estimation of the spatial correlation in a number of channel conditions.
- The metric of diagonal dominance is defined to measure the convergence of a user's channel to favourable propagation [43]. Closed-form expressions are then derived for wide, narrow and Von Mises PES, as well as an upper bound. The PES and antenna topology impacts on the rate of convergence to massive MIMO properties are then shown.
- Numerically, the effects of mutual coupling are examined on different antenna array topologies, by analysing the resultant spatial correlation against inter-element spacing, eigenvalue properties and user rates of a mmWave system. It is demonstrated that while mutual coupling reduces spatial correlation for a wide range of inter-element distances and antenna configurations, the variation in SNR becomes the dominant effect and can either increase or decrease user rates depending on inter-element spacing. Practically, the joint characterization of spatial correlation and mutual coupling is beneficial to antenna array design.

1.4.4 Channel Models for 5G Wireless Systems

- The impact of intra-cluster angular spread and user numbers is examined for different antenna topologies on the cell edge, median and peak sum

¹Link gain refers to the inverse of the path loss, which is explicitly defined in Section 2.1.1.

rates of different wireless channel models across microwave and mmWave bands.

- The impacts of inter-element antenna spacings, receiver antenna numbers, propagation type and user numbers are investigated on the eigenvalue structure of various antenna topologies for different channel models across microwave and mmWave bands. Also, the rate of convergence to massive MIMO is explored by considering the eigenvalue ratio. It is shown that the rate of convergence is dependent on the environment, antenna topology and user separation.
- A parameter is defined: effective degrees-of-freedom (EDOF), to measure the total number of data streams the system can support. The effects in terms of different antenna topologies, channel models, user numbers and numbers of receive antennas are then shown on the EDOF.
- An equivalent Rician channel model is developed to approximate the mmWave channel and show agreement via spectral efficiency and ZF SNR. For single stream transmission, only the specular component is needed. For users with two antennas, the composition of a specular and an uncorrelated diffuse component shows good agreement. For more than two antennas per user, insights into the mmWave channel, provided by the Rician approximation, are drawn.

1.5 List of Publications

Published and submitted papers are listed below.

- P. J. Smith, C. T. Neil, M. Shafi, and P. A. Dmochowski, "On the convergence of massive MIMO systems," *IEEE Intl. Conf. Commun.*, pp. 5191-5196, June 2014.
- C. T. Neil, M. Shafi, P. J. Smith, and P. A. Dmochowski, "On the impact of antenna topologies for massive MIMO systems," *IEEE Intl. Conf. Commun.*, pp. 2030-3025, June 2015.
- C. T. Neil, M. Shafi, P. J. Smith, and P. A. Dmochowski, "Deployment issues for massive MIMO systems," *IEEE Intl. Conf. Commun. Workshop*, pp. 1298-1303, June 2015.
- C. T. Neil, A. Garcia-Rodriguez, P. J. Smith, P. A. Dmochowski, C. Masouros, and M. Shafi, "On the performance of spatially correlated large antenna arrays for millimeter-wave frequencies," *submitted to IEEE Trans. Antennas Propag.*, 2016.

- C. T. Neil, M. Shafi, P. J. Smith, P. A. Dmochowski, and J. Zhang, “An evaluation of channel models, frequency bands and antenna topologies for 5G,” *to appear in IEEE Veh. Technol. Conf.*, June 2017.
- C. T. Neil, M. Shafi, P. J. Smith, P. A. Dmochowski, and J. Zhang, “Measurements and models: Massive MIMO for microwave and millimeter-wave frequency bands,” *submitted to IEEE Trans. Antennas Propag.*, 2017.

1.6 Thesis Outline

The remainder of the thesis is organized as follows:

- Chapter 2 provides a theoretical background, including the system model, channel models, and linear precoding techniques used.
- Chapter 3 examines the convergence properties of large scale MIMO systems, with the aim of determining the number of antennas required to realize massive MIMO properties. Rayleigh and Rician fading channels are considered as well as MF and ZF precoding techniques.
- Chapter 4 extends the MF SINR performance and convergence analysis in Chapter 3 to distributed antenna systems. Specifically, the instantaneous and limiting (with the number of TX antennas) performance of the MF precoder is investigated, with the aim of determining and characterizing the impacts of distributing transmit antennas into multiple clusters.
- Chapter 5 considers the Saleh-Valenzuela channel model to model a large antenna array operating at mmWave frequencies. Closed-form expressions for the 3D spatial correlation between any two antenna elements are derived for wide, narrow and Von Mises PES as well as an upper bound for arbitrary PES. Numerically, the effects of mutually coupled antennas are shown on the effective spatial correlation, eigenvalue structure and user rate for different antenna topologies.
- Chapter 6 considers channel models and measurements across a wide range of candidate bands for 5G wireless systems. Light is shed into key channel modelling and spatial parameter differences. In turn, the impact of these parameter differences for various antenna topologies is investigated in terms of system sum rate, channel eigenvalue structure, EDOF and massive MIMO convergence properties.
- Chapter 7 concludes the thesis with key contributions and future research directions.

2

Theoretical Background

This chapter is organized as follows. First, the system model, channel models and rate/spectral efficiency of a MIMO system are discussed. Then MF, ZF, RZF and signal-to-leakage-plus-noise-ratio (SLNR) linear precoding techniques are mathematically motivated and detailed. Spatial correlation and mutual coupling are then defined, followed by some theoretical background for massive MIMO systems.

2.1 MIMO

In this section the system model, channel models and rate/spectral efficiency of a MIMO system are discussed. MIMO systems exploit the spatial domain, such that sufficiently diverse channel vectors can be obtained between each TX antenna to RX antenna pair [28, 29, 146, 147]. The number of independent channels between the TX and RX(s) is known as the *multiplexing gain*, which is equal to the minimum number of TX and RX antennas. Since the capacity of a system scales proportional to the multiplexing gain [148], MIMO systems have been well studied over the past two decades and is now an enabling technology in current wireless system deployments [129, 149].

In this thesis, a quasi-stationary MU-MIMO system is considered, where a total of M TX antennas serves K users, each with Q antennas, on the DL in a single time/frequency resource. It is assumed that $M \geq KQ$ and that half-wavelength vertically polarized isotropic dipole antenna elements are used at both the TX and RX.

2.1.1 System Model

The $Q \times 1$ received signal vector, \mathbf{y} , for an arbitrary user can be described by

$$\begin{bmatrix} y_1 \\ \vdots \\ y_Q \end{bmatrix} = \sqrt{\varrho} \begin{bmatrix} h_{1,1} & \cdots & h_{1,M} \\ \vdots & \ddots & \vdots \\ h_{Q,1} & \cdots & h_{Q,M} \end{bmatrix} \begin{bmatrix} x_1 \\ \vdots \\ x_M \end{bmatrix} + \begin{bmatrix} v_1 \\ \vdots \\ v_Q \end{bmatrix} \quad (2.1)$$

$$\mathbf{y} = \sqrt{\varrho} \mathbf{H} \mathbf{x} + \mathbf{v}, \quad (2.2)$$

where \mathbf{H} is the $Q \times M$ channel matrix, which is dependent on the environment, with different channel models discussed in Section 2.1.2. \mathbf{x} is a $M \times 1$ precoded vector of data symbols, \mathbf{s} , where it is assumed $\mathbb{E}[\|\mathbf{x}^2\|] = 1$, which is dependent on the type of precoder used at the TX. Linear precoders considered in this thesis are discussed in Section 2.2. \mathbf{v} is the $Q \times 1$ i.i.d. additive white Gaussian noise (AWGN) vector with $\mathcal{CN}(0, 1)$ entries. ϱ is the *cell-edge* received SNR at the user (defined and discussed below) which is a function of the path loss. The path loss to a user, at a link distance d , is assumed to follow the close-in free space reference model [150–157], and, in decibels, is given by

$$\omega(d) = \alpha + 10\beta \log_{10}(d) + \zeta, \quad (2.3)$$

where α is the path loss offset constant, β is the path loss exponent and $\zeta \sim \mathcal{N}(0, \epsilon^2)$ denotes the shadow fading, with standard deviation ϵ . The values for α , β and ϵ can be obtained from empirical data, or as an analytical approximation. For example, the path loss offset value (in decibels) is typically calculated analytically via the free-space path loss at a reference distance [158, 159]

$$\alpha = 20 \log_{10} \left(\frac{\lambda}{4\pi d_0} \right), \quad (2.4)$$

where λ is the wavelength of the carrier frequency, f , and d_0 is the reference distance, in meters.

The cell-edge SNR¹, ϱ , is fixed for all users based on 90% area coverage [4]. In decibels, ϱ is thus given by

$$\varrho = 10 \log_{10}(M) + P_{\text{TX}} + G_{\text{TX}} + G_{\text{RX}} - N_0 - \bar{\omega}(0.9r), \quad (2.5)$$

where $10 \log_{10}(M)$ is the TX array gain from M antenna elements, P_{TX} is the TX power, and G_{TX} and G_{RX} are the TX and RX antenna gains, respectively. N_0 denotes the thermal noise, given in decibels by

$$N_0 = F + K_B + T + B, \quad (2.6)$$

where F is the noise figure, K_B is the Boltzmann constant, T is the temperature

¹Depending on the desired outage probability criteria, ϱ is sometimes used to represent the *average* received SNR.

in Kelvin of 0° Celsius and B denotes the bandwidth. In (2.5), $\bar{\omega}(0.9r)$ denotes the fixed cell-edge path loss, at a distance of $d = 0.9r$, where r denotes the cell radius. This is given by

$$\bar{\omega}(0.9r) = \alpha + 10\beta \log_{10}(0.9r) + 1.28\epsilon, \quad (2.7)$$

where a shadow fading margin is also included, with 1.28 corresponding to the 0.9 cumulative distribution function (CDF) z -value of the normalized Gaussian distribution. Throughout the thesis, the cell-edge SNR is fixed to all users based on an area coverage, whereas the path loss, $\omega(d)$, and therefore *link gain*, $P = 1/\omega$, (equal to the inverse path loss) varies between users.

2.1.2 Channel Models

Four different MIMO channel modelling methodologies are now discussed. Namely: Rayleigh fading, Rician fading, the Saleh-Valenzuela model and the standardized channel model developed by the 3GPP. These channel models are assumed to be for a particular frequency at a particular instance in time, and are thus appropriate for modelling the channel of a single time/frequency resource. Since large antenna arrays are of interest throughout the thesis, spatial correlation amongst antenna elements is discussed in Section 2.3.

Rayleigh Fading Channel

A Rayleigh channel is used to model rich scattering environments, such as those at microwave bands and the non-line-of-sight (NLOS)/diffuse component of a Rician fading channel. It is the simplest channel model and allows closed-form analysis in many applications. When modelling spatial correlation at either/both the TX and RX, the *Kronecker model* is used. This means that the linearly independent and linearly dependent (i.e., correlated) components of the composite channel matrix are separable. Note that this is not the case for the Saleh-Valenzuela and 3GPP channel models, introduced in Sections 2.1.2 and 2.1.2, respectively.

The $Q \times M$ spatially correlated Rayleigh fading channel matrix for an arbitrary user can be expressed via the Kronecker model [23, 95, 160–163]

$$\mathbf{H} = \sqrt{P}\mathbf{R}_{\text{RX}}^{1/2}\mathbf{H}_{\text{iid}}\mathbf{R}_{\text{TX}}^{1/2}, \quad (2.8)$$

where \mathbf{H}_{iid} is a $Q \times M$ channel matrix with i.i.d. $\mathcal{CN}(0, 1)$ channel entries, which accounts for small-scale Rayleigh fading, while \mathbf{R}_{TX} and \mathbf{R}_{RX} are the $M \times M$ TX and $Q \times Q$ RX spatial correlation matrices, respectively, discussed in Section 2.3. $P = 1/\omega$ is the link gain from the TX to the RX, where ω is the path loss, given in (2.3).

Rician Fading Channel

Rician fading channels extend the fully diffuse Rayleigh fading channel to allow for the presence of a spatially deterministic specular ray [164–166]. The ratio of deterministic to scattered power is defined as the Rician K-factor, κ , and varying the Rician K-factor allows the modelling channels of diverse properties, e.g., mmWave channels [167].

The $Q \times M$ spatially correlated Rician fading channel matrix for an arbitrary user can be expressed by [161, 168, 169]

$$\mathbf{H} = \sqrt{P} \left(\sqrt{\frac{1}{\kappa + 1}} \mathbf{R}_{\text{RX}}^{1/2} \mathbf{H}_{\text{iid}} \mathbf{R}_{\text{TX}}^{1/2} + \sqrt{\frac{\kappa}{\kappa + 1}} \mathbf{a}_{\text{RX}}(\varphi^{\text{AOA}}, \vartheta^{\text{AOA}}) \mathbf{a}_{\text{TX}}^{\text{H}}(\varphi^{\text{AOD}}, \vartheta^{\text{AOD}}) \right), \quad (2.9)$$

where $\mathbf{a}_{\text{TX}}(\varphi^{\text{AOD}}, \vartheta^{\text{AOD}})$ and $\mathbf{a}_{\text{RX}}(\varphi^{\text{AOA}}, \vartheta^{\text{AOA}})$ denote the rank-1 LOS/specular antenna array response vectors² of the TX and RX [172], respectively, given by

$$\mathbf{a}_{\text{TX}}(\varphi^{\text{AOD}}, \vartheta^{\text{AOD}}) = \exp \left(j \frac{2\pi}{\lambda} \mathbf{W}_{\text{TX}} \mathbf{r}_{\text{TX}}(\varphi^{\text{AOD}}, \vartheta^{\text{AOD}}) \right), \quad (2.10)$$

$$\mathbf{a}_{\text{RX}}(\varphi^{\text{AOA}}, \vartheta^{\text{AOA}}) = \exp \left(j \frac{2\pi}{\lambda} \mathbf{W}_{\text{RX}} \mathbf{r}_{\text{RX}}(\varphi^{\text{AOA}}, \vartheta^{\text{AOA}}) \right), \quad (2.11)$$

where \mathbf{W}_{TX} and \mathbf{W}_{RX} are the $M \times 3$ and $Q \times 3$ location matrices of the TX and RX antenna elements in 3D Cartesian coordinates, respectively. $\mathbf{r}_{\text{TX}}(\varphi^{\text{AOD}}, \vartheta^{\text{AOD}})$ and $\mathbf{r}_{\text{RX}}(\varphi^{\text{AOA}}, \vartheta^{\text{AOA}})$ are the 3×1 LOS spherical unit vectors of the TX and RX, respectively, given by

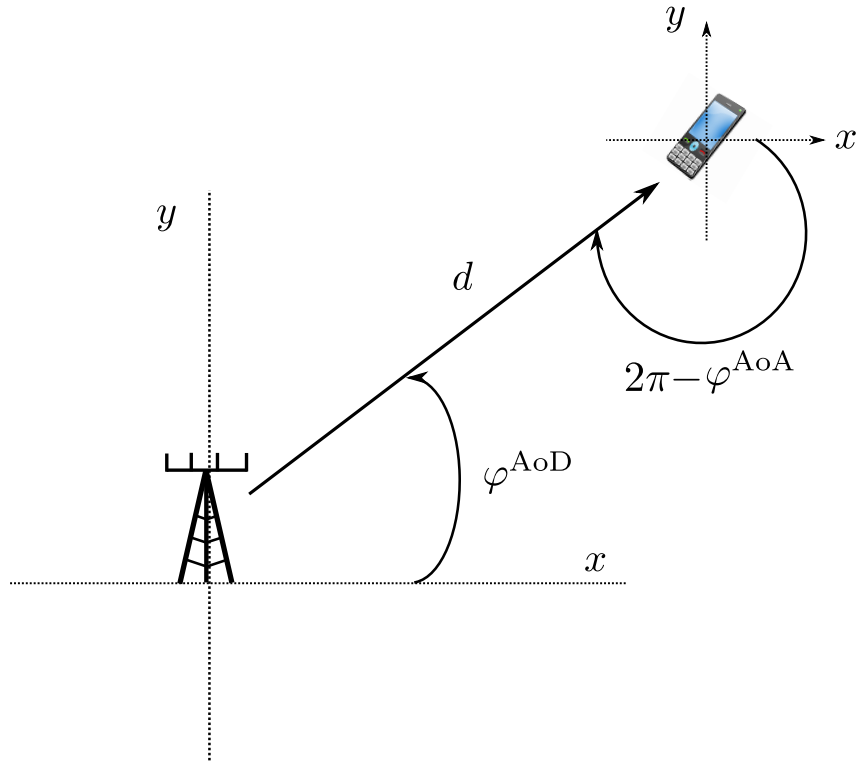
$$\mathbf{r}_{\text{TX}}(\varphi^{\text{AOD}}, \vartheta^{\text{AOD}}) = \begin{bmatrix} \sin(\vartheta^{\text{AOD}}) \cos(\varphi^{\text{AOD}}) \\ \sin(\vartheta^{\text{AOD}}) \sin(\varphi^{\text{AOD}}) \\ \cos(\vartheta^{\text{AOD}}) \end{bmatrix}, \quad (2.12)$$

$$\mathbf{r}_{\text{RX}}(\varphi^{\text{AOA}}, \vartheta^{\text{AOA}}) = \begin{bmatrix} \sin(\vartheta^{\text{AOA}}) \cos(\varphi^{\text{AOA}}) \\ \sin(\vartheta^{\text{AOA}}) \sin(\varphi^{\text{AOA}}) \\ \cos(\vartheta^{\text{AOA}}) \end{bmatrix}. \quad (2.13)$$

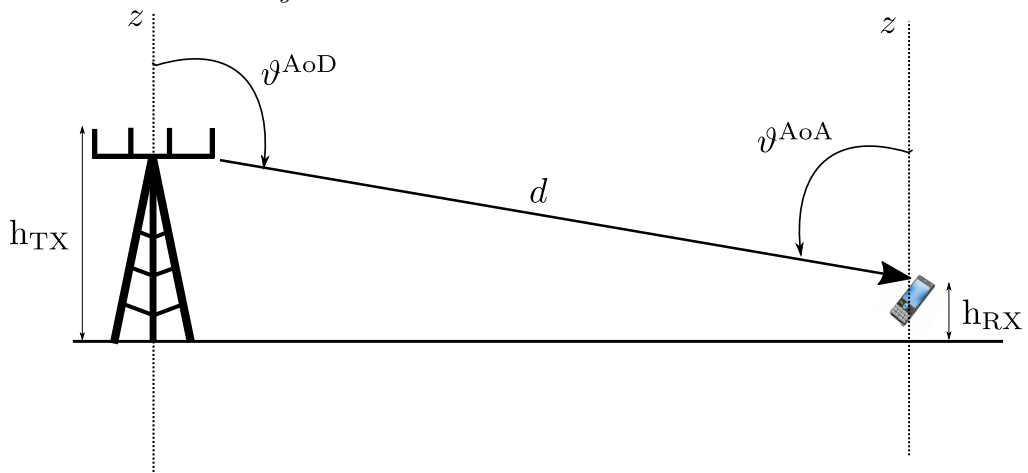
The LOS antenna array response vectors are a function of the LOS azimuth angle-of-arrival (AOA) and angle-of-departure (AOD) (denoted φ^{AOA} and φ^{AOD} , respectively) as well as the elevation AOA and AOD (denoted ϑ^{AOA} and ϑ^{AOD} , respectively), between the TX and RX. These angles are shown in Figure 2.1 with respect to the 3D Cartesian coordinate system, where φ is measured from the x -axis and ϑ is measured from the zenith/ z -axis. The LOS elevation AOD can be calculated to be $\vartheta^{\text{AOD}} = \tan^{-1} \left(\frac{d}{h_{\text{TX}} - h_{\text{RX}}} \right)$, where h_{TX} and h_{RX} are the TX and RX height, respectively. Then $\vartheta^{\text{AOA}} = \pi - \vartheta^{\text{AOD}}$. If the TX

²A far field radiation pattern is assumed [170, 171].

is omnidirectional (i.e., radiating equally in all directions with respect to the azimuth plane) and users are randomly located within a cell, then we also have $\varphi^{\text{AOD}} \sim \mathcal{U}[0, 2\pi)$. Geometrically, one can then calculate φ^{AOA} from φ^{AOD} . However, because a user inherently has a random phase, due to its orientation, with respect to the azimuth plane, it can be assumed that the LOS azimuth AOA is also distributed according to $\varphi^{\text{AOA}} \sim \mathcal{U}[0, 2\pi)$. The LOS AODs are assumed to be independent from the LOS AOAs and the LOS azimuth angles, φ , are assumed to be independent from the LOS elevation angles, ϑ .



(a) LOS azimuth angles, φ^{AOA} and φ^{AOD} , with respect to the x and y axes.



(b) LOS elevation angles, ϑ^{AOA} and ϑ^{AOD} , with respect to the z -axis.

Figure 2.1: LOS azimuth and elevation angles.

Saleh-Valenzuela Channel Model

The Saleh-Valenzuela channel model was proposed in [173] to model indoor radio propagation. The model describes the received signal as several clusters of rays, where each ray has an independent Rayleigh amplitude as well as an independent phase. Physically, the clusters represent scattering objects which reflect the individual rays between the TX and RX. The channel model is appropriate for, and commonly used to model, sparse channels [114, 117–119, 133, 174, 175], such as those at mmWave frequencies, since the received signal can be decomposed into a number of independent spatial clusters of rays and thus multipath components.

The $Q \times M$ DL Saleh-Valenzuela channel matrix for an arbitrary user can be described by

$$\mathbf{H} = \sqrt{P} \sum_{c=1}^C \sqrt{\frac{\gamma_c}{L}} \sum_{l=1}^L h_{\text{iid},c,l} \mathbf{a}_{\text{RX}}(\phi_{c,l}^{\text{AOA}}, \theta_{c,l}^{\text{AOA}}) \mathbf{a}_{\text{TX}}^{\text{H}}(\phi_{c,l}^{\text{AOD}}, \theta_{c,l}^{\text{AOD}}), \quad (2.14)$$

where P is the link gain between the TX and the RX, C is the number of clusters [176], L is the number of rays per cluster, $h_{\text{iid},c,l} \sim \mathcal{CN}(0, 1)$ is the instantaneous channel gain of ray l in cluster c , and γ_c is the normalized power magnitude of cluster c which have been shown to decay exponentially across the clusters [173, 177]. $\mathbf{a}_{\text{TX}}(\phi_{c,l}^{\text{AOD}}, \theta_{c,l}^{\text{AOD}})$ and $\mathbf{a}_{\text{RX}}(\phi_{c,l}^{\text{AOA}}, \theta_{c,l}^{\text{AOA}})$ denote the $M \times 1$ TX and $Q \times 1$ RX antenna array response vectors, respectively, given as

$$\mathbf{a}_{\text{TX}}(\phi_{c,l}^{\text{AOD}}, \theta_{c,l}^{\text{AOD}}) = \exp\left(j \frac{2\pi}{\lambda} \mathbf{W}_{\text{TX}} \mathbf{r}_{\text{TX}}(\phi_{c,l}^{\text{AOD}}, \theta_{c,l}^{\text{AOD}})\right), \quad (2.15)$$

$$\mathbf{a}_{\text{RX}}(\phi_{c,l}^{\text{AOA}}, \theta_{c,l}^{\text{AOA}}) = \exp\left(j \frac{2\pi}{\lambda} \mathbf{W}_{\text{RX}} \mathbf{r}_{\text{RX}}(\phi_{c,l}^{\text{AOA}}, \theta_{c,l}^{\text{AOA}})\right). \quad (2.16)$$

$\mathbf{r}_{\text{TX}}(\phi_{c,l}^{\text{AOD}}, \theta_{c,l}^{\text{AOD}})$ and $\mathbf{r}_{\text{RX}}(\phi_{c,l}^{\text{AOA}}, \theta_{c,l}^{\text{AOA}})$ are the 3×1 NLOS spherical unit vectors of the TX and RX, respectively, given by

$$\begin{aligned} \mathbf{r}_{\text{TX}}(\phi_{c,l}^{\text{AOD}}, \theta_{c,l}^{\text{AOD}}) &= \begin{bmatrix} \sin(\theta_{c,l}^{\text{AOD}}) \cos(\phi_{c,l}^{\text{AOD}}) \\ \sin(\theta_{c,l}^{\text{AOD}}) \sin(\phi_{c,l}^{\text{AOD}}) \\ \cos(\theta_{c,l}^{\text{AOD}}) \end{bmatrix}, \\ \mathbf{r}_{\text{RX}}(\phi_{c,l}^{\text{AOA}}, \theta_{c,l}^{\text{AOA}}) &= \begin{bmatrix} \sin(\theta_{c,l}^{\text{AOA}}) \cos(\phi_{c,l}^{\text{AOA}}) \\ \sin(\theta_{c,l}^{\text{AOA}}) \sin(\phi_{c,l}^{\text{AOA}}) \\ \cos(\theta_{c,l}^{\text{AOA}}) \end{bmatrix}. \end{aligned} \quad (2.17)$$

The NLOS antenna array response vectors are a function of the NLOS azimuth AOAs and AODs (denoted $\phi_{c,l}^{\text{AOA}}$ and $\phi_{c,l}^{\text{AOD}}$, respectively) as well as the NLOS elevation AOAs and AODs (denoted $\theta_{c,l}^{\text{AOA}}$ and $\theta_{c,l}^{\text{AOD}}$, respectively). The azimuth angles, $\phi_{c,l}$, are measured from the x -axis, whereas the elevation angles, $\theta_{c,l}$, are

measured from the zenith/ z -axis, as shown in Figure 2.2. Figure 2.3 shows a multipath channel (only in the azimuth domain) between a ULA of antennas at the TX and a ULA of antennas at the RX. It is assumed that the NLOS AODs are independent of the NLOS AOAs and that the azimuth angles, $\phi_{c,l}$, are independent of elevation angles, $\theta_{c,l}$, for all $c \in 1, \dots, C$ and $l \in 1, \dots, L$.

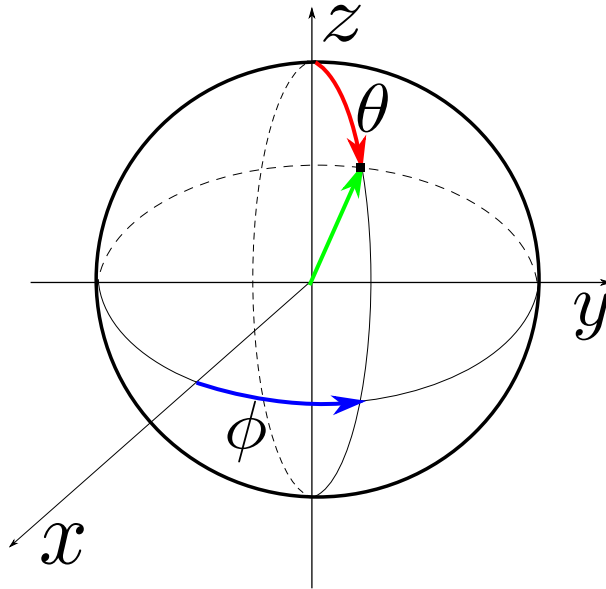


Figure 2.2: NLOS azimuth and elevation angles in 3D Cartesian coordinates.

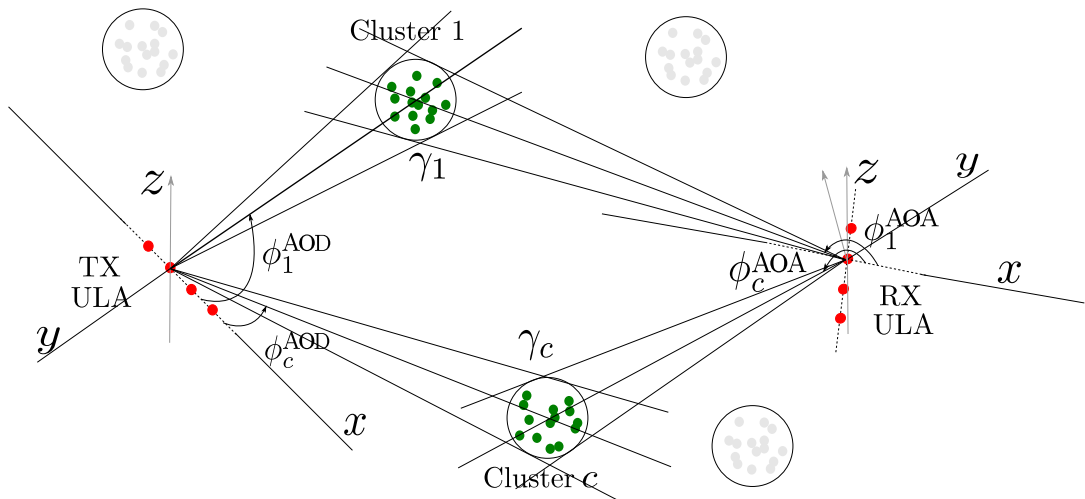


Figure 2.3: Multipath channel (only in the azimuth domain) between a ULA of antennas at the TX and a ULA of antennas at the RX.

In this thesis the AOA power azimuth spectrum (PAS), $p_{\Phi}(\phi_{c,l}^{\text{AOA}})$, and PES, $p_{\Theta}(\theta_{c,l}^{\text{AOA}})$, describe the expected power of *all* the received rays in azimuth and elevation domains, respectively. Likewise, the AOD PAS, $p_{\Phi}(\phi_{c,l}^{\text{AOD}})$, and PES, $p_{\Theta}(\theta_{c,l}^{\text{AOD}})$, describe the expected power of *all* the transmitted rays in azimuth and elevation domains, respectively. The PES is typically much more narrow

than the PAS, and is commonly modelled via the Laplacian, raised cosine and Von Mises distributions [144]. The relationship between the power spectra and the probability density functions (PDFs) of the azimuth and elevation angles are derived from the average received signal power and antenna directivity of a vertically polarized isotropic antenna, while assuming far field radiation [132, 178, 179]. This can be seen by considering the maximized received power of a uniform plane wave in spherical coordinates, given by [132]

$$4\pi = \int_0^{2\pi} \int_0^\pi G_\theta(\phi, \theta) \sin(\theta) d\phi d\theta, \quad (2.18)$$

$$1 = \int_0^{2\pi} \int_0^\pi \sin(\theta) d\phi d\theta, \quad (2.19)$$

where $G_\theta(\phi, \theta)$ is the vertically polarized antenna gain which is equal to $\frac{1}{4\pi}$ for isotropic radiation. Therefore

$$1 = \int_\phi f_\Phi(\phi) d\phi = \int_\phi p_\Phi(\phi) d\phi = \int_0^{2\pi} p_\Phi(\phi) d\phi, \quad (2.20)$$

$$1 = \int_\theta f_\Theta(\theta) d\theta = \int_\theta p_\Theta(\theta) \sin(\theta) d\theta = \int_0^\pi p_\Theta(\theta) \sin(\theta) d\theta, \quad (2.21)$$

where $f_\Phi(\phi)$ and $f_\Theta(\theta)$ denote the PDFs of the azimuth and elevation angles, respectively. This gives the following relationships between the power spectra and the PDFs of the azimuth and elevation angles, respectively, as [129, 132, 171, 180]

$$p_\Phi(\phi) = f_\Phi(\phi), \quad (2.22)$$

$$p_\Theta(\theta) = \frac{f_\Theta(\theta)}{\sin(\theta)}. \quad (2.23)$$

3GPP Channel Model

The 3GPP channel model [129] is standardized for frequencies below 6 GHz and can be used to model urban micro cells and urban macro cells, both for 3D indoor/outdoor scenarios. Due to the complexity in generating the channel model parameters and the fact that it is based on extensive measurement campaigns, carried out by the 3GPP, the channel model is typically only used for detailed simulation purposes.

The NLOS and LOS channel matrix of an arbitrary user can be described as [129, 181, 182]

$$\mathbf{H} = \sqrt{P} \left(\sqrt{\frac{1}{\kappa+1}} \sum_{c=1}^C \sqrt{\frac{\gamma_c}{L}} \sum_{l=1}^L \mathbf{a}_{\text{RX}}(\phi_{c,l}^{\text{AOA}}, \theta_{c,l}^{\text{AOA}}) \mathbf{a}_{\text{TX}}^{\text{H}}(\phi_{c,l}^{\text{AOD}}, \theta_{c,l}^{\text{AOD}}) + \sqrt{\frac{\kappa}{\kappa+1}} \mathbf{a}_{\text{RX}}(\varphi^{\text{AOA}}, \vartheta^{\text{AOA}}) \mathbf{a}_{\text{TX}}^{\text{H}}(\varphi^{\text{AOD}}, \vartheta^{\text{AOD}}) \right), \quad (2.24)$$

where $\mathbf{a}_{\text{RX}}(\phi_{c,l}^{\text{AOA}}, \theta_{c,l}^{\text{AOA}})$, $\mathbf{a}_{\text{TX}}(\phi_{c,l}^{\text{AOD}}, \theta_{c,l}^{\text{AOD}})$, $\mathbf{a}_{\text{RX}}(\varphi^{\text{AOA}}, \vartheta^{\text{AOA}})$ and $\mathbf{a}_{\text{TX}}(\varphi^{\text{AOD}}, \vartheta^{\text{AOD}})$ are defined in (2.16), (2.15), (2.11) and (2.10), respectively. The link gain $P = 1/\omega$ is calculated from (different) NLOS and LOS path loss measurements, when a user in NLOS and LOS channel conditions, respectively. When a user is in NLOS conditions, the Rician K-factor, κ , is zero.

Unlike the parameters for the Rayleigh fading, Rician fading and Saleh-Valenzuela channel models, which are general to any values, the 3GPP channel model parameters have specific measured values and distributions. The generation of key parameter values and distributions are described as follows:

- When the user is in LOS channel conditions, the Rician K-factor is generated via the log-normal distribution, i.e., the Rician K-factor in decibels is distributed as $\mathcal{N}(\mu_\kappa, \sigma_\kappa^2)$, where μ_κ and σ_κ is the measured Rician K-factor mean and standard deviation, respectively, different for urban macro cell and urban micro cell environments.
- The number of clusters, C , and number of paths per cluster, L , is fixed for all users in LOS/NLOS urban macro cell/urban micro cell scenarios.
- The (normalized) cluster powers, γ_c , are generated via

$$\gamma_c = \frac{\gamma'_c}{\sum_{c=1}^C \gamma'_c}, \quad (2.25)$$

with

$$\gamma'_c = \exp(\ln(X_c)(r_t - 1)) 10^{-0.1\zeta_\gamma}, \quad (2.26)$$

where $X_c \sim \mathcal{U}[0, 1)$, r_t is the delay distribution proportionality factor, $\zeta_\gamma \sim \mathcal{N}(0, \epsilon_\gamma^2)$ is the cluster shadow fading in decibels and ϵ_γ is the cluster shadow fading standard deviation.

- The NLOS azimuth angles are generated via

$$\phi_{c,l} = (\bar{X}_c \phi_{0,c} + Y_{\phi,c} + \varphi) + \Delta\phi_{c,l}, \quad (2.27)$$

where φ is defined in Section 2.1.2, \bar{X}_c is equally likely to be ± 1 , $Y_{\phi,c} \sim \mathcal{N}\left(0, \left(\frac{\sigma_\phi}{7}\right)^2\right)$ is the random variation of the central cluster angle, $\phi_{0,c}$, where σ_ϕ is the azimuth root mean square (RMS) angular spread. The PAS is distributed as a wrapped Gaussian, therefore the azimuth central cluster angles, $\phi_{0,c}$, are generated by applying the inverse Gaussian

function

$$\phi_{0,c} = \frac{2 \left(\frac{\sigma_\phi}{1.4}\right) \sqrt{-\ln\left(\frac{\gamma_c}{\max(\gamma_c)}\right)}}{Z_\phi}, \quad (2.28)$$

where ϑ is defined in Section 2.1.2, Z_ϕ is the azimuth cluster scaling factor. $\Delta\phi_{c,l}$ denotes the azimuth intra-cluster path offset, distributed as the wrapped Gaussian $\mathcal{N}(0, C_\phi)$, where C_ϕ is the intra-cluster azimuth spread.

- The NLOS elevation angles are generated via

$$\theta_{c,l} = (\bar{X}_c \theta_{0,c} + Y_{\theta,c} + \vartheta) + \Delta\theta_{c,l}, \quad (2.29)$$

where \bar{X}_c is equally likely to be ± 1 , $Y_{\theta,c} \sim \mathcal{N}\left(0, \left(\frac{\sigma_\theta}{7}\right)^2\right)$ is the random variation of the central cluster angle, $\theta_{0,c}$, where σ_θ is the elevation RMS angular spread. The PES is Laplacian distributed, therefore the elevation central cluster angles, $\theta_{0,c}$, are generated by applying the inverse Laplacian function

$$\theta_{0,c} = -\frac{\sigma_\theta \left(\frac{\gamma_c}{\max(\gamma_c)}\right)}{Z_\theta} \quad (2.30)$$

where Z_θ is the elevation cluster scaling factor. $\Delta\theta_{c,l}$ denotes the elevation intra-cluster path offset, distributed as the wrapped Gaussian $\mathcal{N}(0, C_\theta)$, where C_θ is the intra-cluster elevation spread.

2.1.3 Rate and Spectral Efficiency

Extending the capacity of a single-input-single-output system [183], the rate of an arbitrary user, in bits/s, assuming perfect CSI is available at the TX, for a MIMO system is given by [28, 29, 159, 169]

$$R = B \log_2 \left| \mathbf{I}_Q + \frac{\rho}{M} \mathbf{H} \mathbf{H}^H \right|, \quad (2.31)$$

$$= \sum_{q=1}^{\min(Q,M)} B \log_2 \left(1 + \frac{\rho}{M} \eta_q^2 \right), \quad (2.32)$$

where η_q denotes the q th (ordered) singular value of \mathbf{H} . The spectral efficiency, in bits/s/Hz, is thus obtained by dividing R by the bandwidth. In a MU system, (2.31) is extended to give the *sum rate*, R , as [168]

$$R = B \log_2 \left| \mathbf{I}_{KQ} + \frac{\rho}{M} \check{\mathbf{H}} \check{\mathbf{H}}^H \right| \quad (2.33)$$

where $\check{\mathbf{H}} = [\mathbf{H}_1^T, \dots, \mathbf{H}_K^T]^T$ denotes the stacked $KQ \times M$ channel matrix to all users, with \mathbf{H}_k denoting the $Q \times M$ DL channel to user $k \in 1, \dots, K$.

2.2 Linear Precoding

When multiple users are simultaneously served, precoding of the data at the transmitter can help increase the received SINR/SNR at each user [184]. In this section four common linear precoders used in a multi-user single-antenna are detailed: matched-filter (MF), zero-forcing (ZF), regularized zero-forcing (RZF) and signal-to-leakage-plus-noise ratio (SLNR). Linear precoders are typically sub-optimal, however, they have very low complexity [185] in relation to non-linear precoders, such as DPC [70] and vector perturbation [71–73]. Let \mathbf{H} denote the stacked $K \times M$ DL channel matrix from the BS to all K users, where single-antenna users ($Q = 1$) are assumed in this section for mathematical simplicity and clarity.

2.2.1 MF Precoding

The MF precoder is the most computationally inexpensive precoding technique which aims at maximizing the received power at each user while neglecting the effects of interference to the other co-scheduled users. The $M \times 1$ MF precoded data vector is given by [168]

$$\mathbf{x} = \frac{1}{\sqrt{\tau}} \mathbf{H}^H \mathbf{s}, \quad (2.34)$$

where \mathbf{s} is the $K \times 1$ data symbol vector, with $\mathbb{E}[\|\mathbf{s}\|^2] = 1$, and

$$\tau = \frac{\text{tr}(\mathbf{H}\mathbf{H}^H)}{K}, \quad (2.35)$$

normalizes the average power of the MF precoder. The received signal is thus given by

$$\mathbf{y} = \sqrt{\rho} \mathbf{H}\mathbf{H}^H \frac{\mathbf{s}}{\sqrt{\tau}} + \mathbf{v}, \quad (2.36)$$

giving the instantaneous MF SINR of the k th user as

$$\text{SINR}_k^{\text{MF}} = \frac{\frac{\rho}{K\tau} |\mathbf{h}_k \mathbf{h}_k^H|^2}{1 + \frac{\rho}{K\tau} \sum_{\substack{k'=1 \\ k' \neq k}}^K |\mathbf{h}_k \mathbf{h}_{k'}^H|^2}, \quad (2.37)$$

where v_k denotes the k th entry of \mathbf{v} , where $\mathbb{E}[|v_k|^2] = 1$, and \mathbf{h}_k denotes the k th column of \mathbf{H} , i.e., the $1 \times M$ DL channel from the TX to user k .

2.2.2 ZF Precoding

The ZF precoding technique forces all intra-cell interference to zero by using coherent superposition of wave-fronts to send null vectors to all co-scheduled users. The ZF precoder is more computationally expensive than the MF precoder as it requires a matrix inverse of $\mathbf{H}\mathbf{H}^H$. The $M \times 1$ ZF precoder transmitted symbol vector, \mathbf{x} , is given by

$$\mathbf{x} = \frac{1}{\sqrt{\tau}} \mathbf{H}^H (\mathbf{H}\mathbf{H}^H)^{-1} \mathbf{s}, \quad (2.38)$$

where the average power in \mathbf{x} is normalized via

$$\tau = \frac{\text{tr} \left((\mathbf{H}\mathbf{H}^H)^{-1} \right)}{K}. \quad (2.39)$$

The $K \times 1$ received signal is thus given by

$$\mathbf{y} = \sqrt{\frac{\varrho}{\tau}} \mathbf{s} + \mathbf{v}, \quad (2.40)$$

giving the instantaneous ZF SNR as

$$\text{SNR}^{\text{ZF}} = \frac{\varrho}{\text{tr} \left((\mathbf{H}\mathbf{H}^H)^{-1} \right)}, \quad (2.41)$$

where the noise power is normalized to 1. Note that the matrix inverse in (2.38), (2.39) and (2.41) requires $M \geq KQ$, which is assumed throughout this thesis.

2.2.3 RZF Precoding

Since the ZF normalization parameter, τ , in (2.39), can become large when the matrix inverse is computed, due to small singular values in the channel, the ZF precoder performs poorly at low SNR. The RZF precoding technique, however, introduces a regularization parameter, \varkappa , to the ZF precoder to help improve the ZF precoding performance at low SNR by aiming to minimize the mean squared error (MSE) of the transmitted and received symbol vector. The $M \times 1$ RZF precoder transmitted symbol vector, \mathbf{x} , is thus given by

$$\mathbf{x} = \frac{1}{\sqrt{\tau}} \mathbf{H}^H (\mathbf{H}\mathbf{H}^H + \varkappa \mathbf{I}_M)^{-1} \mathbf{s}, \quad (2.42)$$

where the average power in \mathbf{x} is normalized via

$$\tau = \frac{\text{tr} \left((\mathbf{H}\mathbf{H}^H + \varkappa \mathbf{I}_M)^{-1} \right)}{K}. \quad (2.43)$$

The regularization parameter, \varkappa , can thus be seen to control the amount of inter-user interference. For example, when $\varkappa = 0$, (2.42) is equal to the ZF

transmitted symbol vector in (2.38) and inter-user interference is zero. On the other hand, for non-zero \varkappa there is some inter-user interference, however, \varkappa can be chosen to improve the condition number of the channel matrix, \mathbf{H} , such that the matrix inverse in (2.42) and (2.43) behaves well. This leads to many variants, such as the SLNR precoder discussed below. However, in the case of the RZF precoder, \varkappa is chosen to minimize the MSE.

From (2.42), the $K \times 1$ received signal for the RZF precoder is given by

$$\mathbf{y} = \sqrt{\frac{\rho}{\tau}} \mathbf{H} \mathbf{H}^H (\mathbf{H} \mathbf{H}^H + \varkappa \mathbf{I}_M)^{-1} \mathbf{s}. \quad (2.44)$$

2.2.4 SLNR Precoding

The SLNR precoder has the same general form as the RZF precoder, however rather than minimizing the MSE of the transmitted and received symbol vectors, as is the case for the RZF precoder, the SLNR precoder aims to maximize the signal-to-leakage-plus-noise-ratio [186, 187]. The $M \times 1$ SLNR precoder transmitted symbol vector to user $k \in 1, \dots, K$, \mathbf{x}_k , is given by

$$\mathbf{x}_k = \left(\hat{\mathbf{H}}_k^H \hat{\mathbf{H}}_k + \varkappa \mathbf{I}_M \right)^{-1} \mathbf{H}_k^H s_k, \quad (2.45)$$

where s_k is the k th entry of \mathbf{s} , \mathbf{H}_k is the $1 \times M$ DL channel matrix to user k , $\hat{\mathbf{H}}_k = [\mathbf{H}_1^T, \dots, \mathbf{H}_{k-1}^T, \mathbf{H}_{k+1}^T, \dots, \mathbf{H}_K^T]^T$ is the concatenated channel matrix of all users except user k . The transmitted symbol vector is normalized such that $\mathbb{E} [\|\mathbf{x}_k\|^2] = 1$. The received signal for user k is then given by

$$y_k = \sqrt{\frac{1}{\tau}} \mathbf{H}_k \left(\hat{\mathbf{H}}_k^H \hat{\mathbf{H}}_k + \varkappa \mathbf{I}_M \right)^{-1} \mathbf{H}_k^H s_k + v_k. \quad (2.46)$$

where τ is the normalization parameter, given by

$$\tau = \frac{\|\mathbf{H}\|_F^2}{K}, \quad (2.47)$$

where $\|\mathbf{H}\|_F = \sqrt{\text{tr}(\mathbf{H}^H \mathbf{H})}$ is the Frobenius norm of \mathbf{H} .

2.3 Spatial Correlation

In this section spatial correlation is discussed. Spatial correlation describes the linear dependence of two or more signals in space. Without loss of generality, the following notation and discussion relates to spatial correlation at the TX.

The spatial correlation coefficient, $R_{m,m'}$, between two TX antennas, $m, m' \in$

$1, \dots, M$, channels is defined as [188]

$$R_{m,m'} = \frac{\text{cov}[\mathbf{h}_m, \mathbf{h}_{m'}]}{\sqrt{\text{var}[\mathbf{h}_m]\text{var}[\mathbf{h}_{m'}]}}, \quad (2.48)$$

where $|R_{m,m'}| \leq 1$, with equality when the two TX antenna elements channels are linearly dependent, known as *fully correlated*. On the other hand, when $R_{m,m'} = 0$, the two TX antenna elements channels *uncorrelated*. Various channel characteristics can influence the level of spatial correlation. For example, in a NLOS channel, increasing the number of clusters, C , (in (2.14)) and/or increasing the width of the angular spectra is likely to reduce the level of spatial correlation in the channel. This is because two colocated antenna elements are more likely to transmit/receive signals which have undergone sufficiently independent scattering. On the other hand, in the unique case of a single specular (LOS) ray, two colocated antenna elements will be fully correlated since there is no diversity in the channel.

Spatial correlation can also be affected by varying the layout/topology of antenna array such that channels between adjacent antenna elements are sufficiently correlated or decorrelated. For example, *in general*, spatial correlation can be reduced by increasing the inter-element spacing between antennas. The effects of antenna topologies on spatial correlation are analysed in Chapter 5 for a number of different channel propagation characteristics. Three such antenna topologies considered are:

1. A ULA placed on the x, y -plane.
2. A URA with one dimension parallel to the z -axis and another dimension placed on the x, y -plane.
3. A uniform cylindrical array (UCA) where a number of x, y -plane circles of antennas are stacked parallel to the z -axis.

The ULA, URA and UCA antenna topologies are shown in Figures 2.4, 2.5 and 2.6, respectively. For both the URA and UCA, we assume that the number of antennas parallel to the x, y -plane are the same as the number of antennas parallel to the z -axis. The antenna array response vectors for each topology are given in (2.15) and (2.16), where the TX and RX antenna location matrices, \mathbf{W}_{TX} and \mathbf{W}_{RX} , respectively, are topology specific.

Typically the resultant expression in computing (2.48) is too complex to perform any meaningful statistical analysis, and therefore a number of simplified spatial correlation models have been proposed. A common and simple spatial correlation model, which is used throughout the thesis, is known as the *exponential spatial correlation model* [189], and is described below.

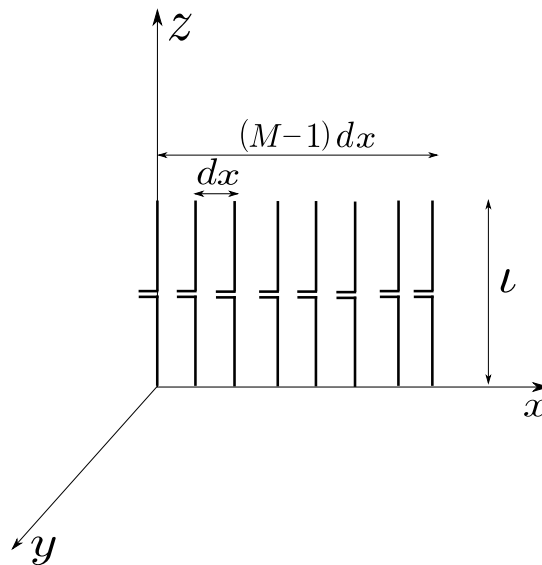


Figure 2.4: ULA antenna topology on the x -axis with M dipole antennas, of length l , with an inter-element spacing of dx .

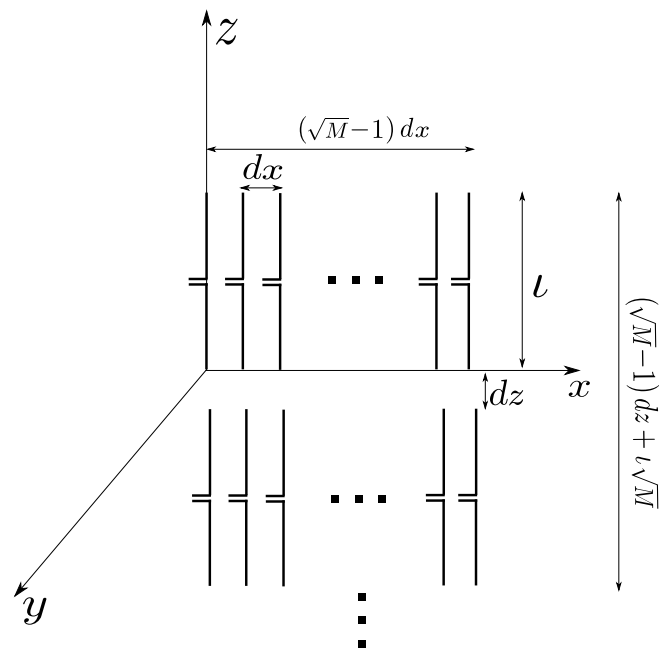


Figure 2.5: URA antenna topology on the x, z -plane consisting of \sqrt{M} dipoles on the x -axis, with inter-element spacing of dx , and \sqrt{M} dipoles on the z -axis, with inter-element spacing of dz . Each dipole antenna element is of length l .

2.3.1 The Exponential Spatial Correlation Model

The most simplistic spatial correlation model is known as the exponential spatial correlation model [189]. The model was proposed by fitting an exponential curve to the non-monotonically decaying peaks of the true spatial correlation. It is a crude approximation to the true spatial correlation and can be described with a single parameter, thus making it desirable from an analytical perspective.

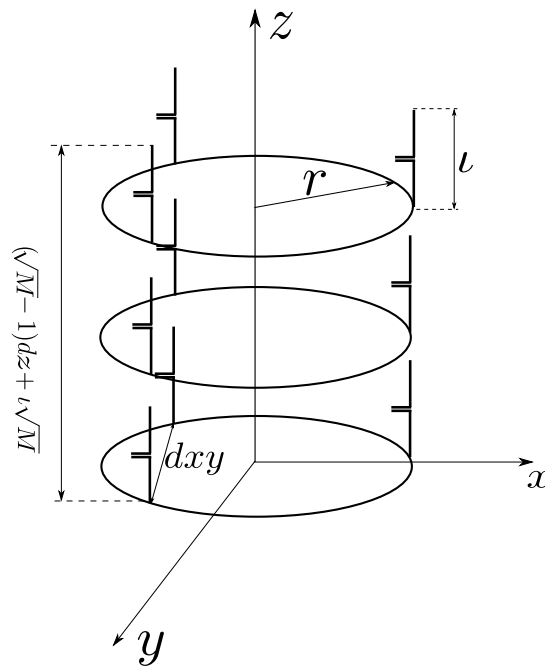


Figure 2.6: UCA antenna topology with \sqrt{M} x, y -plane circles of dipole antennas separated on the z -axis by dz . Each x, y -plane circle of antennas has radius r and inter-element spacing $dx y$. Each dipole antenna element is of length l .

The TX spatial correlation matrix, \mathbf{R}_{TX} , using the exponential spatial correlation model, can be described by

$$\mathbf{R}_{\text{TX}} = \begin{bmatrix} 1 & \rho & \cdots & \rho^{M-1} \\ (\rho)^* & 1 & \cdots & \rho^{M-2} \\ \vdots & \vdots & \ddots & \vdots \\ (\rho^{M-1})^* & (\rho^{M-2})^* & \cdots & 1 \end{bmatrix}, \quad (2.49)$$

where ρ is the exponential spatial correlation decay parameter, with $|\rho| \leq 1$. Large $|\rho|$ indicates high spatial correlation, and vice-versa.

Example: In Figure 2.7, an exponential spatial correlation model is shown approximating the true spatial correlation. Here, the true spatial correlation is obtained by computing the spatial correlation of a ULA, positioned on the x -axis, with $\theta = \frac{\pi}{2}$ and ϕ uniformly distributed on $[\frac{\pi}{2} - \frac{\pi}{9}, \frac{\pi}{2} + \frac{\pi}{9}]$, i.e., from (2.15)³

$$R_{m,m'} = \frac{9}{2\pi} \int_{\frac{\pi}{2} - \frac{\pi}{9}}^{\frac{\pi}{2} + \frac{\pi}{9}} \exp(j2\pi d_\lambda \cos(\phi)) d\phi. \quad (2.50)$$

For more details of these types of spatial correlation calculations, see Section 5. The exponential approximation in Figure 2.7 was found by fitting the best

³The central azimuth angle, $\frac{\pi}{2}$, and the offsets, $\pm\frac{\pi}{9}$, are arbitrary chosen for example purposes.

exponential decay to the peaks of $|\mathbf{R}_{m,m'}|$.

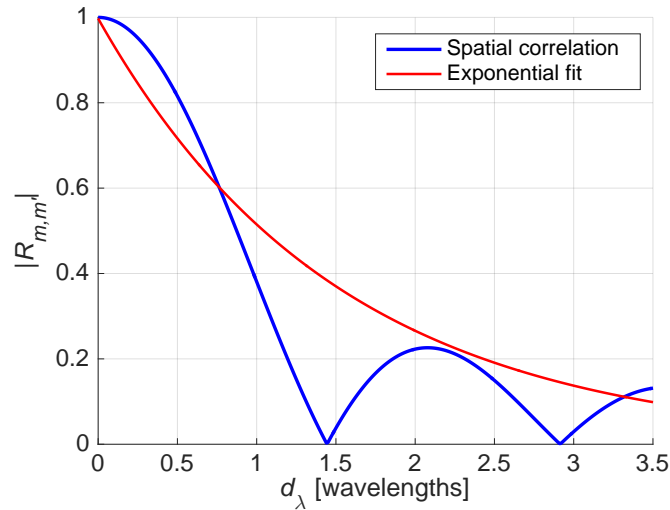


Figure 2.7: Absolute value of the spatial correlation between two TX antenna elements $m, m' \in 1, \dots, M$ as a function of inter-element spacing, d_λ , and a fitted exponential spatial correlation model.

2.4 Mutual Coupling

In this thesis, mutual coupling between antennas is modelled between (ideal) dipole antenna elements. In general, mutual coupling between two antenna elements can be interpreted as the voltage produced at the terminal of one antenna element as a result of a current being induced on a the other antenna element [87, 171]. Mutual coupling has been shown to influence the resultant spatial correlation and system performance, especially for close inter-element antenna spacings [24, 87, 171, 190–196], and it is therefore considered in Chapter 5.

The global mutual coupling matrix can be expressed as [83, 85]

$$\mathbf{Z} = (Z_A + Z_L) (\mathbf{\Xi} + Z_L \mathbf{I}_M)^{-1}, \quad (2.51)$$

where Z_A is the antenna impedance, Z_L is the load or termination impedance and $\mathbf{\Xi}$ is the mutual impedance matrix given by [171]

$$\mathbf{\Xi} = \begin{bmatrix} Z_A & Z_M^{1,2} & \dots & Z_M^{1,M-1} & Z_M^{1,M} \\ Z_M^{2,1} & Z_A & \dots & Z_M^{2,M-1} & Z_M^{2,M} \\ \vdots & \vdots & \vdots & \vdots & \vdots \\ Z_M^{M,1} & Z_M^{M,2} & \dots & Z_M^{M,M-1} & Z_A \end{bmatrix}, \quad (2.52)$$

if mutual coupling is modelled at the TX. $Z_M^{m,m'}$ denotes the mutual impedance

between antenna elements $m, m' \in 1, \dots, M$, which is dependent on the antenna inter-element spacings as well as the relative antenna configuration/orientation. The mutual impedances are obtained by employing the electromotive force (EMF) method due to its numerical convenience [89, 171], rather than the integral equation-moment method, which requires a lengthy formulation [171]. It should be noted that the mutual coupling matrix, \mathbf{Z} , is only dependent of the inter-element spacings and relative antenna configuration/orientation. Therefore, mutual coupling is independent on the propagation environment, whereas spatial correlation, discussed in Section 2.3, is heavily dependent on both the inter-element spacings and the channel matrix [23, 91, 132]. The mutually coupled channel matrix of an arbitrary user, $\bar{\mathbf{H}}$, is given by the Kronecker model [106]

$$\bar{\mathbf{H}} = \mathbf{Z}_{\text{RX}} \mathbf{H} \mathbf{Z}_{\text{TX}}, \quad (2.53)$$

where \mathbf{Z}_{RX} and \mathbf{Z}_{TX} denote the $Q \times Q$ RX and $M \times M$ TX mutual coupling matrices, respectively, as given in (2.51). As an example, for a Rayleigh fading channel with spatial correlation and mutual coupling, the channel matrix will then become

$$\mathbf{H} = \sqrt{P} \mathbf{Z}_{\text{RX}} \mathbf{R}_{\text{RX}}^{1/2} \mathbf{H}_{\text{iid}} \mathbf{R}_{\text{TX}}^{1/2} \mathbf{Z}_{\text{TX}}. \quad (2.54)$$

Likewise, the user rate is then

$$R = B \log_2 \left| \mathbf{I}_Q + \frac{P\varrho}{M} \mathbf{Z}_{\text{RX}} \mathbf{R}_{\text{RX}}^{1/2} \mathbf{H}_{\text{iid}} \mathbf{R}_{\text{TX}}^{1/2} \mathbf{Z}_{\text{TX}} \left(\mathbf{Z}_{\text{RX}} \mathbf{R}_{\text{RX}}^{1/2} \mathbf{H}_{\text{iid}} \mathbf{R}_{\text{TX}}^{1/2} \mathbf{Z}_{\text{TX}} \right)^{\text{H}} \right|. \quad (2.55)$$

2.5 Massive MIMO

This section introduces some relevant theoretical background on massive MIMO. Naturally, all previously presented theoretical background, on MIMO, also applies to massive MIMO, however, this section aims to address the *additional* properties and issues which arise for massive MIMO, i.e., a MIMO system with a very large number of TX antennas. These properties and issues do not apply for conventional MIMO systems.

The seminal work by T. L. Marzetta in 2010 [6] and others [7, 8, 45] considered a MIMO system with an infinite number of TX antennas, concluding that massive MIMO systems are a promising direction for future wireless systems. In particular, it was shown that, in the limit of an infinite number of TX antennas, the effects of fast fading and uncorrelated noise average out, and the only remaining impairment results from corrupted CSI though the re-use of pilot signals in multi-cell scenarios⁴. In TDD systems this corresponds to the BSs

⁴This limitation of massive MIMO was later disproven in [197, 198] under certain circum-

uplink channel estimate, through channel reciprocity, being corrupted by users in adjacent cells using the same pilot sequence. In frequency-division-duplex (FDD) systems, this corresponds to the BS transmitting duplicates of the (limited) number of pilot sequences, as the number of DL pilot sequences required scales with the number of TX antennas.

The effects of increasing numbers of TX antennas on the channel matrix, sum rate, linear precoding techniques, spatial correlation and mutual coupling are discussed below where single antenna users are assumed for mathematical simplicity and clarity.

2.5.1 Channel Matrix

Here, the effects of an infinite number of TX antennas on $\frac{\mathbf{H}\mathbf{H}^H}{M}$ is shown. Assuming a power scaled i.i.d. $K \times M$ channel matrix, $\mathbf{H} = [\mathbf{H}_1, \dots, \mathbf{H}_K]^T$, where \mathbf{H}_k is the $1 \times M$ DL channel matrix from the TX to user $k \in 1, \dots, K$, then as the number of TX antennas, M , tends to infinity, for fixed K , $\frac{\mathbf{H}\mathbf{H}^H}{M}$ approaches a diagonal matrix, i.e.,

$$\lim_{M \rightarrow \infty} \left(\frac{\mathbf{H}\mathbf{H}^H}{M} \right) = \lim_{M \rightarrow \infty} \left(\mathbf{P}^{1/2} \frac{\mathbf{H}_{\text{iid}}\mathbf{H}_{\text{iid}}^H}{M} \mathbf{P}^{1/2} \right) = \mathbf{P}, \quad (2.56)$$

since each of the K users', $1 \times M$, i.i.d. channels becomes orthogonal [6, 199]. Here, $\mathbf{P} = \text{diag}(P_1, \dots, P_K)$ is a $K \times K$ diagonal matrix consisting of the link gains to each user. Note that in this section, for the case of exposition, uncorrelated channels are assumed, so that $\mathbf{H} = \mathbf{P}^{1/2}\mathbf{H}_{\text{iid}}$. This is known as favourable propagation [43], and under these conditions, the channel singular values become equal, i.e., $\eta_1 = \eta_2 = \dots = \eta_{\min(M,K)}$.

2.5.2 Sum Rate

The effects of an infinite number of TX antennas on the sum rate is now shown. Since $\frac{\mathbf{H}_{\text{iid}}\mathbf{H}_{\text{iid}}^H}{M}$ converges to the identity matrix, \mathbf{I}_K , as $M \rightarrow \infty$ [6, 199], the multiplexing gain is maximized and thus the sum rate achieves capacity (optimal sum rate). This can be seen by considering the limit of (2.33), as $M \rightarrow \infty$,

$$\lim_{M \rightarrow \infty} (R) = \lim_{M \rightarrow \infty} \left(B \log_2 \left| \mathbf{I}_K + \frac{\varrho}{M} \mathbf{H}\mathbf{H}^H \right| \right) \quad (2.57)$$

$$= B \log_2 |\mathbf{I}_K + \varrho \mathbf{P}|, \quad (2.58)$$

which for equal link gains amongst users ($\mathbf{P} = P\mathbf{I}_K$), is

$$\lim_{M \rightarrow \infty} (R) = B \log_2 |\mathbf{I}_K + \varrho P \mathbf{I}_K| \quad (2.59)$$

$$= KB \log_2 (1 + \varrho P). \quad (2.60)$$

The sum rate is seen to scale with the number of users, K . Note that in the case of multiple antenna users, the sum rate increased proportionately to the number of receive antennas at the user, Q . However, the effects of pilot contamination in both TDD and FDD systems reduce the sum rate by the same amount. Therefore (2.58) and (2.60) remains the same for $Q > 1$.

2.5.3 Linear Precoding

In this subsection, a background on linear precoding for massive MIMO is given for the simple case where the channel is uncorrelated, i.e., $\mathbf{H} = \mathbf{H}_{\text{iid}}$.

Another key observation that arises when $M \rightarrow \infty$ is that linear precoders have been shown to perform near to the optimal [7, 73, 168] for i.i.d. channels and a finite number of transmit antennas, M , since the processing effectively renders the users' channels *asymptotically* orthogonal, i.e., $\frac{\mathbf{H}_{\text{iid}}\mathbf{H}_{\text{iid}}^H}{M} \approx \mathbf{I}_K$. Thus MF and ZF precoding techniques become equivalent, i.e., as M becomes very large with fixed K , the transmitted symbol vector for the MF precoder can be approximated by

$$\mathbf{x} = \frac{1}{\sqrt{\tau}} \mathbf{H}_{\text{iid}}^H \mathbf{s} \quad (2.61)$$

$$= \sqrt{\frac{K}{\text{tr}(\mathbf{H}_{\text{iid}}\mathbf{H}_{\text{iid}}^H)}} \mathbf{H}_{\text{iid}}^H \mathbf{s} \quad (2.62)$$

$$= \sqrt{\frac{K}{M \text{tr}\left(\frac{\mathbf{H}_{\text{iid}}\mathbf{H}_{\text{iid}}^H}{M}\right)}} \mathbf{H}_{\text{iid}}^H \mathbf{s} \quad (2.63)$$

$$\approx \sqrt{\frac{K}{M \text{tr}(\mathbf{I}_K)}} \mathbf{H}_{\text{iid}}^H \mathbf{s} \quad (2.64)$$

$$= \frac{1}{\sqrt{M}} \mathbf{H}_{\text{iid}}^H \mathbf{s}. \quad (2.65)$$

Likewise, as M becomes very large with fixed K , the transmitted symbol vector for the ZF precoder is given by

$$\mathbf{x} = \frac{1}{\sqrt{\tau}} \mathbf{H}_{\text{iid}}^H (\mathbf{H}_{\text{iid}}\mathbf{H}_{\text{iid}}^H)^{-1} \mathbf{s} \quad (2.66)$$

$$= \sqrt{\frac{K}{\text{tr}\left((\mathbf{H}_{\text{iid}}\mathbf{H}_{\text{iid}}^H)^{-1}\right)}} \mathbf{H}_{\text{iid}}^H (\mathbf{H}_{\text{iid}}\mathbf{H}_{\text{iid}}^H)^{-1} \mathbf{s} \quad (2.67)$$

$$= \sqrt{\frac{K}{\frac{1}{M} \text{tr}\left(\left(\frac{\mathbf{H}_{\text{iid}}\mathbf{H}_{\text{iid}}^H}{M}\right)^{-1}\right)}} \frac{1}{M} \mathbf{H}_{\text{iid}}^H \left(\frac{\mathbf{H}_{\text{iid}}\mathbf{H}_{\text{iid}}^H}{M}\right)^{-1} \mathbf{s} \quad (2.68)$$

$$\approx \sqrt{\frac{K}{\frac{1}{M} \text{tr}\left((\mathbf{I}_K)^{-1}\right)}} \frac{1}{M} \mathbf{H}_{\text{iid}}^H (\mathbf{I}_K)^{-1} \mathbf{s} \quad (2.69)$$

$$= \frac{1}{\sqrt{M}} \mathbf{H}_{\text{iid}}^H \mathbf{s}. \quad (2.70)$$

Hence ZF precoding and MF precoding become equivalent as $M \rightarrow \infty$. From (2.65) and (2.70) the received SINR of user k then becomes

$$\text{SINR}_k = \frac{\frac{\rho}{K} |\mathbf{H}_{\text{iid},k} \mathbf{x}|^2}{1 + \frac{\rho}{K} \sum_{\substack{k'=1 \\ k' \neq k}}^K |\mathbf{H}_{\text{iid},k'} \mathbf{x}|^2} \quad (2.71)$$

$$= \frac{\frac{\sqrt{M}\rho}{K} \left| \frac{\mathbf{H}_{\text{iid},k} \mathbf{H}_{\text{iid},k}^H}{M} s_k \right|^2}{1 + \frac{\sqrt{M}\rho}{K} \sum_{\substack{k'=1 \\ k' \neq k}}^K \left| \frac{\mathbf{H}_{\text{iid},k'} \mathbf{H}_{\text{iid},k'}^H}{M} s_k \right|^2} \quad (2.72)$$

$$= \frac{\frac{\sqrt{M}\rho}{K} \left| \frac{\mathbf{H}_{\text{iid},k} \mathbf{H}_{\text{iid},k}^H}{M} s_k \right|^2}{1 + \frac{\sqrt{M}\rho}{K} \sum_{\substack{k'=1 \\ k' \neq k}}^K \left| \frac{\mathbf{H}_{\text{iid},k'} \mathbf{H}_{\text{iid},k'}^H}{M} s_k \right|^2} \quad (2.73)$$

$$\approx \frac{\sqrt{M}\rho}{K} |s_k|^2, \quad (2.74)$$

since $\frac{\mathbf{H}_{\text{iid},k'} \mathbf{H}_{\text{iid},k}^H}{M} \approx 0$ and $\frac{\mathbf{H}_{\text{iid},k} \mathbf{H}_{\text{iid},k}^H}{M} \approx 1$ for very large M . Thus, the transmitted symbol is recovered, with strength proportional to the received SNR, ρ , and the square root of the number of TX antennas, M .

3

Convergence to Massive MIMO

In this chapter, the convergence properties of large scale MIMO systems are examined with the aim of determining the number of antennas required to realize massive MIMO properties. Characteristics of both Rayleigh and Rician fading channel matrices are considered, and their asymptotic behaviour is studied. Under a Rayleigh fading channel, limiting per-user ZF SNR and MF SINR are derived for scenarios of equal and unequal link gains, as the number of TX and RX antennas (with fixed ratio) increases without bound. Numerically, the effects of spatial correlation are shown for both Rayleigh and Rician fading channels, as well as the impact of increasing LOS strength on the rate of convergence of the Rician fading channel. It is seen that the rate of convergence of the per-user ZF SINR, to its limiting value, is quicker than that of the MF precoder due to its additional inter-user interference component. Furthermore, increased LOS strength, in a Rician fading channel, increases the rate of convergence to favourable propagation and channel hardening, while reducing and increasing the performance of ZF and MF precoders, respectively.

3.1 Introduction

Motivating the surge of research activities into massive MIMO systems are the additional channel properties which arise when operating with large numbers of TX antennas. These properties arise as a result of random matrix theory asymptotics [63]. For example, as the number of TX antennas becomes large, users' channels become mutually orthogonal [64]. This is known as *favourable propagation*, and under these conditions simple linear processing techniques, such as MF and ZF precoding, can maximize the sum rate [43, 65–67]. Another virtue

of massive MIMO systems is referred to as *channel hardening* [68], where the variance of the elements of $\mathbf{V}_{\text{iid}} = \frac{\mathbf{H}_{\text{iid}}\mathbf{H}_{\text{iid}}^{\text{H}}}{M}$ decreases proportional to the number of TX antenna numbers, M , such that the entries of \mathbf{V}_{iid} start to become deterministic [6, 43]. In turn, when random matrix elements become deterministic and well conditioned, system analysis and precoder design becomes simplified since matrix operations can be computed more easily [7]. For example, the computationally intensive matrix inverse required for ZF precoding becomes simply the inverse of an identity matrix. These idealistic properties, however, are based on the assumptions of an i.i.d. channel with an infinite number of TX antennas. In summary, favourable propagation and channel hardening can be defined as when \mathbf{V}_{iid} becomes diagonal and deterministic, respectively, as the number of transmit antennas, $M \rightarrow \infty$.

Since the deployment of a very large number of antennas may be impractical due to physical constraints, it seems natural to determine the number of antennas required for MIMO systems to begin to exhibit these additional benefits. This is the focus of the chapter and the contributions are summarized below:

1. The rates of convergence of $\mathbf{V} = \frac{\mathbf{H}\mathbf{H}^{\text{H}}}{M}$ to favourable propagation and channel hardening, as $M \rightarrow \infty$ with $K \leq M$ fixed, of Rayleigh and Rician fading channel matrices are analytically derived. Note that the analytical convergence of \mathbf{V}_{iid} to favourable propagation and channel hardening in Rayleigh [142] and Rician [143] fading channels is well known. This analysis is extended to the scenario of unequal link gains.¹
2. The convergence properties of \mathbf{V}_{iid} , in Rayleigh and Rician fading channels, is numerically studied by considering three different convergence metrics defined in Section 3.2, for $M \rightarrow \infty$ with both $K \leq M$ fixed and $\nu = \frac{M}{K}$ fixed. Practically, the convergence metrics aid the design of a system since the number of antennas required to guarantee the magnitude of a particular convergence metric is shown.
3. Closed-form limiting expressions, as $M, K \rightarrow \infty$ with fixed $\nu = \frac{M}{K}$, of the per-user ZF SNR and MF SINR are derived² for unequal link gains³ in a Rayleigh fading channel. In turn, the rate of convergence of the average instantaneous per-user ZF SNR and MF SINR is investigated.

¹In the Rayleigh fading case a particular users channel is given by $\mathbf{H} = \sqrt{P}\mathbf{H}_{\text{iid}}$, whereas the users channel is given by $\mathbf{H} = \sqrt{P} \left(\sqrt{\frac{1}{\kappa+1}}\mathbf{H}_{\text{iid}} + \sqrt{\frac{\kappa}{\kappa+1}}\mathbf{a}_{\text{RX}}(\varphi^{\text{AOA}}, \vartheta^{\text{AOA}})\mathbf{a}_{\text{TX}}^{\text{H}}(\varphi^{\text{AOD}}, \vartheta^{\text{AOD}}) \right)$ in the Rician fading scenario.

²This has been previously derived for the case where $M \rightarrow \infty$ with $K \leq M$ fixed [6], but is also included as a preliminary result in Section 3.3.1 for completeness.

³Closed-form limiting expressions, as $M, K \rightarrow \infty$ with fixed $\nu = \frac{M}{K}$, of the per-user ZF SNR and MF SINR has previously been derived for equal link gains in [7] for a Rayleigh fading channel. However, it is also included in this chapter to assist in the derivation of the unequal link gain case and for completeness.

4. The performance of the average instantaneous per-user ZF SNR and MF SINR under Rayleigh and Rician fading channels, with and without spatial correlation at the TX, is shown.

Note that single-antenna users are considered such that the rate of convergence of \mathbf{V} (*channel convergence* in Section 3.2) can be compared to the rate of convergence of the average per-user MF SINR (*linear precoding convergence* in Section 3.3), which only operates with single stream transmission [57].

3.2 Channel Convergence

The convergence of \mathbf{V} to \mathbf{I}_K is examined in Sections 3.2.1 and 3.2.2 for Rayleigh and Rician fading channels, respectively. For both types of channels, the rate of convergence of \mathbf{V} to favourable propagation and channel hardening properties are mathematically analysed for the case where $M \rightarrow \infty$ with $K \leq M$ fixed. The first and second moments of \mathbf{V} are used as a measure of favourable propagation, while the second moment is also used to measure channel hardening.

For both Rayleigh and Rician fading channels, three different convergence metrics are defined as follows. Let the $K \times M$ matrix $\mathbf{H}_{\text{iid}} = [\mathbf{h}_{\text{iid},1}^T, \dots, \mathbf{h}_{\text{iid},K}^T]^T$ denote the concatenation of the K users' $1 \times M$ channel vectors, where $\mathbf{h}_{\text{iid},k}$ is the k th users DL i.i.d. channel vector. The convergence of \mathbf{V}_{iid} to \mathbf{I}_K can be evaluated by examining a number of well known properties of \mathbf{V}_{iid} and a deviation matrix $\mathbf{E} = \mathbf{V}_{\text{iid}} - \mathbf{I}_K$. The following metrics are considered: *mean absolute deviation*, *eigenvalue ratio* and *diagonal dominance*, respectively defined as

$$\text{Mean absolute deviation} = \frac{1}{K^2} \sum_{k=1}^K \sum_{k'=1}^K |E_{k,k'}|, \quad (3.1)$$

$$\text{Eigenvalue ratio} = \frac{\eta_{\max}^2}{\eta_{\min}^2}, \quad (3.2)$$

$$\text{Diagonal Dominance} = \frac{\sum_{k=1}^K V_{\text{iid},k,k}}{\sum_{k=1}^K \sum_{\substack{k'=1 \\ k' \neq k}}^K |V_{\text{iid},k,k'}|}, \quad (3.3)$$

where η_{\max} and η_{\min} denote the maximum and minimum singular values of \mathbf{V}_{iid} , respectively, $E_{k,k'}$ denotes the (k, k') th entry of \mathbf{E} , and $V_{\text{iid},k,k'}$ denotes the (k, k') th entry of \mathbf{V}_{iid} . Two types of convergence scenarios are considered:

1. $M \rightarrow \infty$ with $K \leq M$ fixed, denoted by $\lim_{M \rightarrow \infty} (\cdot)$,
2. $K, M \rightarrow \infty$ with $\nu = \frac{K}{M}$ fixed, denoted by $\lim_{K, M \rightarrow \infty} (\cdot)$,

where $M \geq K$ in both cases.

3.2.1 Rayleigh Fading Channel

In this subsection, the Rayleigh fading channel given in (2.8) is considered for an uncorrelated TX antenna array, i.e., the composite $K \times M$ DL channel matrix to K users is given by

$$\mathbf{H} = \mathbf{P}^{1/2} \mathbf{H}_{\text{iid}}. \quad (3.4)$$

Rayleigh Fading Channel Analysis

The convergence of a Rayleigh fading channel to favourable propagation and channel hardening is now shown. The diagonal and off-diagonal elements of \mathbf{V} are examined independently.

Theorem 3.1. *Let $V_{k,k}$ denote the (k, k) th entry of \mathbf{V} , for $k \in 1, \dots, K$, and X_k denote a χ_M^2 random variable with M complex degrees-of-freedom (DOF), then*

$$V_{k,k} = \frac{P_k X_k}{M}. \quad (3.5)$$

Proof.

$$V_{k,k} = \left(\frac{\mathbf{H}\mathbf{H}^H}{M} \right)_{k,k} \quad (3.6)$$

$$= \left(\frac{\mathbf{P}^{1/2} \mathbf{H}_{\text{iid}} \mathbf{H}_{\text{iid}}^H \mathbf{P}^{1/2}}{M} \right)_{k,k} \quad (3.7)$$

$$= \frac{\sqrt{P_k} \mathbf{h}_{\text{iid},k} \mathbf{h}_{\text{iid},k}^H \sqrt{P_k}}{M} \quad (3.8)$$

$$= \frac{P_k \sum_{m=1}^M |H_{\text{iid},k,m}|^2}{M} \quad (3.9)$$

$$= \frac{P_k X_k}{M}, \quad (3.10)$$

where $H_{\text{iid},k,m}$ denotes the (k, m) th element of \mathbf{H}_{iid} . ■

Corollary 3.1. *Since $\mathbb{E}[X_k] = M$ and $\text{var} \left[\frac{X_k}{M} \right] = \frac{1}{M}$ [200],*

$$\mathbb{E}[V_{k,k}] = \mathbb{E} \left[\frac{P_k X_k}{M} \right] = P_k, \quad (3.11)$$

$$\text{var}[V_{k,k}] = \text{var} \left[\frac{P_k X_k}{M} \right] = \frac{P_k^2}{M}. \quad (3.12)$$

Thus $\lim_{M \rightarrow \infty} (\text{var}[V_{k,k}]) = 0$, i.e., the diagonal elements of \mathbf{V} converge to their expected value, P_k , with the variance decreasing proportional to the number of TX antennas, M .

Theorem 3.2. Let $Y_{k,k'} = \sum_{m=1}^M H_{\text{iid},k,m} H_{\text{iid},k',m}^{\text{H}}$, then for $k, k' \in 1, \dots, K$, $k' \neq k$,

$$V_{k,k'} = \frac{\sqrt{P_k P_{k'}} Y_{k,k'}}{M}. \quad (3.13)$$

Proof.

$$V_{k,k'} = \left(\frac{\mathbf{H}\mathbf{H}^{\text{H}}}{M} \right)_{k,k'} \quad (3.14)$$

$$= \left(\frac{\mathbf{P}^{1/2} \mathbf{H}_{\text{iid}} \mathbf{H}_{\text{iid}}^{\text{H}} \mathbf{P}^{1/2}}{M} \right)_{k,k'} \quad (3.15)$$

$$= \frac{\sqrt{P_k} \mathbf{h}_{\text{iid},k} \mathbf{h}_{\text{iid},k'}^{\text{H}} \sqrt{P_{k'}}}{M} \quad (3.16)$$

$$= \frac{\sqrt{P_k P_{k'}} \sum_{m=1}^M H_{\text{iid},k,m} H_{\text{iid},k',m}^{\text{H}}}{M} \quad (3.17)$$

$$= \frac{\sqrt{P_k P_{k'}} Y_{k,k'}}{M}. \quad (3.18)$$

■

Corollary 3.2. Since $\mathbb{E}[Y_{k,k'}] = 0$ and

$$\text{var} \left[\frac{Y_{k,k'}}{M} \right] = \text{var} \left[\frac{\sum_{m=1}^M H_{\text{iid},k,m} H_{\text{iid},k',m}^{\text{H}}}{M} \right] \quad (3.19)$$

$$= \frac{\text{var} \left[\sum_{m=1}^M H_{\text{iid},k,m} H_{\text{iid},k',m}^{\text{H}} \right]}{M^2} \quad (3.20)$$

$$= \frac{\sum_{m=1}^M \text{var} \left[H_{\text{iid},k,m} H_{\text{iid},k',m}^{\text{H}} \right]}{M^2} \quad (3.21)$$

$$= \frac{\sum_{m=1}^M \mathbb{E} \left[|H_{\text{iid},k,m}|^2 |H_{\text{iid},k',m}^{\text{H}}|^2 \right]}{M^2} \quad (3.22)$$

$$= \frac{1}{M}, \quad (3.23)$$

then for $k \neq k'$,

$$\mathbb{E} [V_{k,k'}] = \mathbb{E} \left[\frac{\sqrt{P_k P_{k'}} Y_{k,k'}}{M} \right] = 0, \quad (3.24)$$

$$\text{var} [V_{k,k'}] = \text{var} \left[\frac{\sqrt{P_k P_{k'}} Y_{k,k'}}{M} \right] = \frac{P_k P_{k'}}{M}. \quad (3.25)$$

Thus $\lim_{M \rightarrow \infty} (\text{var} [V_{k,k'}]) = 0$, i.e., the off-diagonal elements of \mathbf{V} converge to their

expected value, 0, with the variance decreasing proportional to the number of TX antennas.

Corollary 3.3. *Using the known convergence of \mathbf{V}_{iid} to \mathbf{I}_K as $M \rightarrow \infty$ [142], for finite K ,*

$$\lim_{M \rightarrow \infty} (\mathbf{V}) = \lim_{M \rightarrow \infty} \left(\frac{\mathbf{H}\mathbf{H}^H}{M} \right) = \lim_{M \rightarrow \infty} \left(\frac{\mathbf{P}^{1/2} \mathbf{H}_{\text{iid}} \mathbf{H}_{\text{iid}}^H \mathbf{P}^{1/2}}{M} \right) = \mathbf{P}, \quad (3.26)$$

Essentially, the speed of convergence of \mathbf{V} to channel hardening is controlled by the convergence of \mathbf{V}_{iid} to \mathbf{I}_K with the P_k and $\sqrt{P_k P_{k'}}$ values scaling the variances of the diagonal and off-diagonal elements of \mathbf{V} , respectively.

Rayleigh Fading Channel Numerical Results

The convergence of \mathbf{V}_{iid} to \mathbf{I}_K is now numerically examined for the three convergence metrics defined in (3.1)-(3.3). Each convergence metric is evaluated and averaged over 1000 channel realizations.

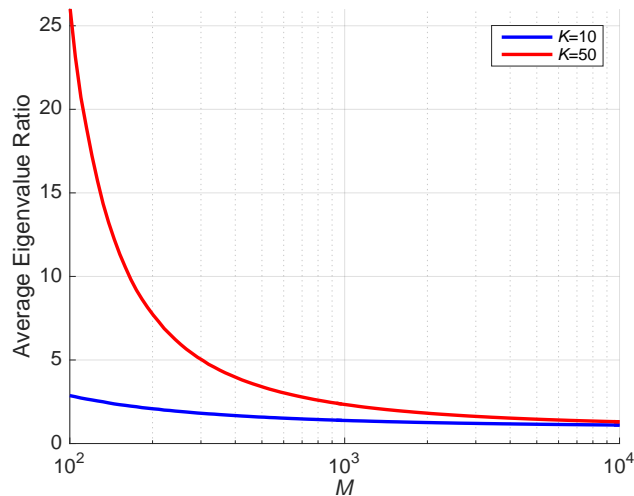


Figure 3.1: Average eigenvalue ratio as a function of the number of TX antennas, M , for an i.i.d. channel with the number of users, K , fixed.

Figure 3.1 shows the eigenvalue ratio of \mathbf{V}_{iid} as a function of M for the convergence scenario where K is fixed at 10 and 50. It can be seen that for both values of K , the eigenvalue ratio will only converge to 1 when M is of the order of 10^4 . Even for values of M as large as 100, the eigenvalue ratio for $K = 50$ is more than 8 times larger than the corresponding value for $K = 10$.

However, when Figure 3.2 is considered, showing the mean absolute deviation of \mathbf{V}_{iid} from the identity matrix, \mathbf{I}_K , it is noted that this difference quickly approaches zero. For example, in Figure 3.1, for $M = 500$ and $K = 50$ the

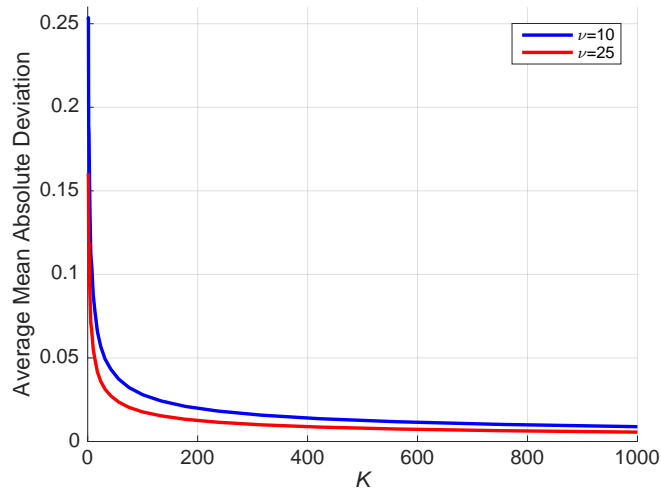


Figure 3.2: Average mean absolute deviation as a function of the number of users, K , for an i.i.d. channel with $\nu = \frac{M}{K}$ fixed.

eigenvalue ratio is about 4, yet in Figure 3.2, when $K = 50$, and the corresponding $M = 500$, the mean absolute deviation is less than 0.05.

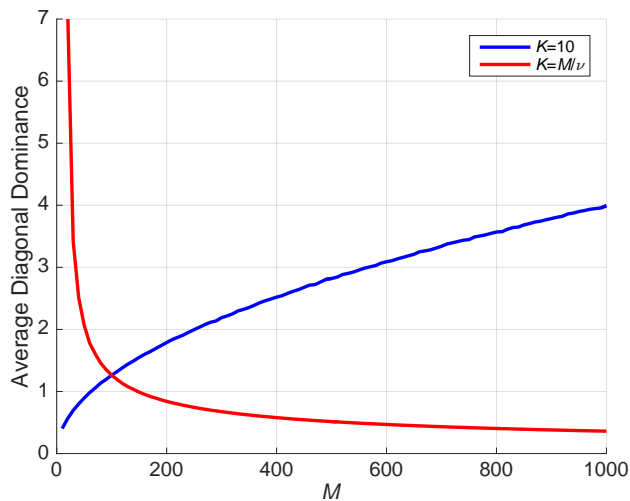


Figure 3.3: Average diagonal dominance as a function of the number of TX antennas, M , for an i.i.d. channel with K both fixed, at 10, and variable, where $K = \frac{M}{\nu}$, $\nu = 10$.

In Figure 3.3, it is observed that \mathbf{V}_{iid} becomes increasingly diagonally dominant for fixed K as $M \rightarrow \infty$ since \mathbf{V}_{iid} has a fixed dimension ($K \times K$) and the sum of the diagonal elements grows faster than the fixed number of off-diagonals. In contrast as both M and K grow large, \mathbf{V}_{iid} becomes less diagonally dominant. This follows as the number of off-diagonal elements increases as K^2 and the total contribution of the off-diagonals becomes dominant. It can be shown that

the diagonal dominance measure grows proportionally to \sqrt{M} for fixed K and decays proportionally to $\frac{1}{\sqrt{M}}$ as both M and K increase.

It is concluded that the number of antennas required for \mathbf{V}_{iid} to be close to \mathbf{I}_K (Figure 3.2) is far less than the number required for an eigenvalue ratio of 1 (Figure 3.1), because the eigenvalues are sensitive to the large number of (small) off-diagonal elements in \mathbf{V}_{iid} . This is supported by the result in Figure 3.3, which shows that the convergence of the off-diagonal elements of \mathbf{V}_{iid} to zero is slow.

3.2.2 Rician Fading Channel

After examining the convergence of the Rayleigh fading channel, the convergence of the Rician fading channel, given in (2.9), is now considered.

Rician Fading Channel Analysis

As was the case for the Rayleigh fading channel, the first two moments of \mathbf{V} are used as a measure of favourable propagation, while the second moment is also used to measure channel hardening. All analysis is performed for the convergence scenario where $M \rightarrow \infty$ with $K \leq M$ fixed.

Theorem 3.3. *Let $\kappa_k, \mathbf{R}_{\text{TX}}, \varphi_k^{\text{AOD}}$ and ϑ_k^{AOD} denote the Rician K -factor, TX spatial correlation matrix, LOS azimuth AOD and LOS elevation AOD of user k , respectively $\forall k$. Let $a_{\text{TX},m}(\varphi_k^{\text{AOD}}, \vartheta_k^{\text{AOD}})$ denote the m th element of $\mathbf{a}_{\text{TX}}(\varphi_k^{\text{AOD}}, \vartheta_k^{\text{AOD}}) \forall m, k$, then the first moment of \mathbf{V} for $k, k' \in 1, \dots, K$ is given by*

$$\begin{aligned} \mathbb{E}[V_{k,k'}] &= \sqrt{\frac{P_k P_{k'}}{(\kappa_k + 1)(\kappa_{k'} + 1)}} \mathbb{E} \left[\frac{\mathbf{h}_{\text{iid},k} \mathbf{R}_{\text{TX}} \mathbf{h}_{\text{iid},k'}^{\text{H}}}{M} \right] \\ &+ \sqrt{\frac{P_k P_{k'} \kappa_k \kappa_{k'}}{(\kappa_k + 1)(\kappa_{k'} + 1)}} \frac{1}{M} \sum_{m=1}^M a_{\text{TX},m}^{\text{H}}(\varphi_k^{\text{AOD}}, \vartheta_k^{\text{AOD}}) a_{\text{TX},m}(\varphi_{k'}^{\text{AOD}}, \vartheta_{k'}^{\text{AOD}}). \end{aligned} \quad (3.27)$$

Proof. Let \mathbf{h}_k denote the $1 \times M$ DL channel to user $k \in 1, \dots, K$,

$$\begin{aligned} \mathbb{E}[V_{k,k'}] &= \mathbb{E} \left[\left(\frac{\mathbf{H} \mathbf{H}^{\text{H}}}{M} \right)_{k,k'} \right] = \mathbb{E} \left[\frac{\mathbf{h}_k \mathbf{h}_{k'}^{\text{H}}}{M} \right] \quad (3.28) \\ &= \mathbb{E} \left[\frac{\sqrt{P_k P_{k'}}}{M} \left(\sqrt{\frac{1}{\kappa_k + 1}} \mathbf{h}_{\text{iid},k} \mathbf{R}_{\text{TX}}^{1/2} + \sqrt{\frac{\kappa_k}{\kappa_k + 1}} \mathbf{a}_{\text{TX}}^{\text{H}}(\varphi_k^{\text{AOD}}, \vartheta_k^{\text{AOD}}) \right) \right. \\ &\quad \left. \times \left(\sqrt{\frac{1}{\kappa_{k'} + 1}} \mathbf{R}_{\text{TX}}^{1/2} \mathbf{h}_{\text{iid},k'}^{\text{H}} + \sqrt{\frac{\kappa_{k'}}{\kappa_{k'} + 1}} \mathbf{a}_{\text{TX}}(\varphi_{k'}^{\text{AOD}}, \vartheta_{k'}^{\text{AOD}}) \right) \right] \quad (3.29) \\ &= \mathbb{E} \left[\sqrt{\frac{P_k P_{k'}}{(\kappa_k + 1)(\kappa_{k'} + 1)}} \frac{\mathbf{h}_{\text{iid},k} \mathbf{R}_{\text{TX}} \mathbf{h}_{\text{iid},k'}^{\text{H}}}{M} \right] \\ &\quad + \mathbb{E} \left[\sqrt{\frac{P_k P_{k'} \kappa_k \kappa_{k'}}{(\kappa_k + 1)(\kappa_{k'} + 1)}} \frac{\mathbf{h}_{\text{iid},k} \mathbf{R}_{\text{TX}}^{1/2} \mathbf{a}_{\text{TX}}(\varphi_{k'}^{\text{AOD}}, \vartheta_{k'}^{\text{AOD}})}{M} \right] \end{aligned}$$

$$\begin{aligned}
& + \mathbb{E} \left[\sqrt{\frac{P_k P_{k'} \kappa_k}{(\kappa_k + 1)(\kappa_{k'} + 1)}} \frac{\mathbf{a}_{\text{TX}}^{\text{H}}(\varphi_k^{\text{AOD}}, \vartheta_k^{\text{AOD}}) \mathbf{R}_{\text{TX}}^{1/2} \mathbf{h}_{\text{iid},k'}^{\text{H}}}{M} \right] \\
& + \mathbb{E} \left[\sqrt{\frac{P_k P_{k'} \kappa_k \kappa_{k'}}{(\kappa_k + 1)(\kappa_{k'} + 1)}} \frac{\mathbf{a}_{\text{TX}}^{\text{H}}(\varphi_k^{\text{AOD}}, \vartheta_k^{\text{AOD}}) \mathbf{a}_{\text{TX}}(\varphi_{k'}^{\text{AOD}}, \vartheta_{k'}^{\text{AOD}})}{M} \right] \quad (3.30) \\
& = \sqrt{\frac{P_k P_{k'}}{(\kappa_k + 1)(\kappa_{k'} + 1)}} \mathbb{E} \left[\frac{\mathbf{h}_{\text{iid},k} \mathbf{R}_{\text{TX}} \mathbf{h}_{\text{iid},k'}^{\text{H}}}{M} \right] \\
& + \sqrt{\frac{P_k P_{k'} \kappa_k \kappa_{k'}}{(\kappa_k + 1)(\kappa_{k'} + 1)}} \frac{1}{M} \sum_{m=1}^M a_{\text{TX},m}^{\text{H}}(\varphi_k^{\text{AOD}}, \vartheta_k^{\text{AOD}}) a_{\text{TX},m}(\varphi_{k'}^{\text{AOD}}, \vartheta_{k'}^{\text{AOD}}), \quad (3.31)
\end{aligned}$$

where the Rician channel, \mathbf{H} , is given in (2.9) and the two middle expectations in (3.30) are zero since $\mathbb{E}[\mathbf{h}_{\text{iid},k}] = 0 \forall k$. ■

Corollary 3.4. *The expected value of the diagonal elements of \mathbf{V} is*

$$\mathbb{E}[V_{k,k}] = P_k. \quad (3.32)$$

Proof. From (3.27),

$$\mathbb{E}[V_{k,k}] = \frac{P_k}{\kappa_k + 1} \frac{\text{tr}(\mathbf{R}_{\text{TX}})}{M} + \frac{P_k \kappa_k}{\kappa_k + 1} \frac{1}{M} \sum_{m=1}^M |a_{\text{TX},m}^{\text{H}}(\varphi_k^{\text{AOD}}, \vartheta_k^{\text{AOD}})|^2 \quad (3.33)$$

$$= \frac{P_k}{\kappa_k + 1} + \frac{P_k \kappa_k}{\kappa_k + 1} = \frac{P_k(1 + \kappa_k)}{\kappa_k + 1} = P_k, \quad (3.34)$$

since $\text{tr}(\mathbf{R}_{\text{TX}}) = M$ and each element of an antenna array response vector has unit magnitude. ■

Corollary 3.5. *The expected value of the off-diagonal elements of \mathbf{V} is*

$$\mathbb{E}[V_{k,k'}] = \sqrt{\frac{P_k P_{k'} \kappa_k \kappa_{k'}}{(\kappa_k + 1)(\kappa_{k'} + 1)}} \frac{\mathbf{a}_{\text{TX}}^{\text{H}}(\varphi_k^{\text{AOD}}, \vartheta_k^{\text{AOD}}) \mathbf{a}_{\text{TX}}(\varphi_{k'}^{\text{AOD}}, \vartheta_{k'}^{\text{AOD}})}{M}. \quad (3.35)$$

Proof. Using the fact that $\mathbb{E} \left[\text{tr} \left(\frac{\mathbf{h}_{\text{iid},k} \mathbf{R}_{\text{TX}} \mathbf{h}_{\text{iid},k'}^{\text{H}}}{M} \right) \right] = 0$, for $k' \neq k$, in (3.27) gives the desired result. ■

The expected value of the off-diagonals of \mathbf{V} are only a function of the LOS component of the Rician channel and are thus deterministic. $\mathbb{E}[V_{k,k'}]$ becomes zero in the case where either user has a fully scattered channel ($\kappa_k = 0$ or $\kappa_{k'} = 0$). Also, the amplitude $\mathbb{E}[V_{k,k'}]$ increases proportional to both the Rician K-factor and the LOS spatial correlation (i.e., the similarity between the k th and k' th LOS antenna array response vectors).

Corollary 3.6. *The expected absolute value of the off-diagonal elements of \mathbf{V} is*

bounded by

$$|\mathbb{E}[V_{k,k'}]| < \sqrt{P_k P_{k'}} \frac{|\mathbf{a}_{\text{TX}}^{\text{H}}(\varphi_k^{\text{AOD}}, \vartheta_k^{\text{AOD}}) \mathbf{a}_{\text{TX}}(\varphi_{k'}^{\text{AOD}}, \vartheta_{k'}^{\text{AOD}})|}{M}. \quad (3.36)$$

Proof. Using the fact that $\left| \sqrt{\frac{\kappa_k \kappa_{k'}}{(\kappa_k + 1)(\kappa_{k'} + 1)}} \right| < 1$ gives the desired result. \blacksquare

Since the LOS antenna array response vectors are not usually the same, their product will tend to be small and the division by M causes convergence to zero. Only for specially selected angles will this term not tend to zero⁴, i.e., when the angles between the users are almost identical giving $M \approx |\mathbf{a}_{\text{TX}}^{\text{H}}(\varphi_k^{\text{AOD}}, \vartheta_k^{\text{AOD}}) \times \mathbf{a}_{\text{TX}}(\varphi_{k'}^{\text{AOD}}, \vartheta_{k'}^{\text{AOD}})|$.

Theorem 3.4. *The variance of the elements of \mathbf{V} is given by*

$$\begin{aligned} \text{var}[V_{k,k'}] &= \frac{P_k P_{k'}}{(\kappa_k + 1)(\kappa_{k'} + 1)} \frac{\text{tr}(\mathbf{R}_{\text{TX}}^2)}{M^2} \\ &+ \frac{P_k P_{k'} \kappa_{k'}}{(\kappa_k + 1)(\kappa_{k'} + 1)} \frac{\mathbf{a}_{\text{TX}}^{\text{H}}(\varphi_{k'}^{\text{AOD}}, \vartheta_{k'}^{\text{AOD}}) \mathbf{R}_{\text{TX}} \mathbf{a}_{\text{TX}}(\varphi_{k'}^{\text{AOD}}, \vartheta_{k'}^{\text{AOD}})}{M^2} \\ &+ \frac{P_k P_{k'} \kappa_k}{(\kappa_k + 1)(\kappa_{k'} + 1)} \frac{\mathbf{a}_{\text{TX}}^{\text{H}}(\varphi_k^{\text{AOD}}, \vartheta_k^{\text{AOD}}) \mathbf{R}_{\text{TX}} \mathbf{a}_{\text{TX}}(\varphi_k^{\text{AOD}}, \vartheta_k^{\text{AOD}})}{M^2}. \end{aligned} \quad (3.37)$$

Proof. Writing the variance in terms of expectations, gives

$$\text{var}[V_{k,k'}] = \text{var}\left[\left(\frac{\mathbf{H}\mathbf{H}^{\text{H}}}{M}\right)_{k,k'}\right] = \mathbb{E}\left[\left|\frac{\mathbf{h}_k \mathbf{h}_{k'}^{\text{H}}}{M}\right|^2\right] - \left|\mathbb{E}\left[\frac{\mathbf{h}_k \mathbf{h}_{k'}^{\text{H}}}{M}\right]\right|^2. \quad (3.38)$$

Then computing the first term in (3.38),

$$\begin{aligned} \mathbb{E}\left[\left|\frac{\mathbf{h}_k \mathbf{h}_{k'}^{\text{H}}}{M}\right|^2\right] &= \mathbb{E}\left[\left(\frac{\mathbf{h}_k \mathbf{h}_{k'}^{\text{H}}}{M}\right) \left(\frac{\mathbf{h}_k \mathbf{h}_{k'}^{\text{H}}}{M}\right)^{\text{H}}\right] \\ &= \frac{P_k P_{k'}}{(\kappa_k + 1)(\kappa_{k'} + 1)} \mathbb{E}\left[\frac{\mathbf{h}_{\text{iid},k} \mathbf{R}_{\text{TX}} \mathbf{h}_{\text{iid},k'}^{\text{H}} \mathbf{h}_{\text{iid},k'} \mathbf{R}_{\text{TX}} \mathbf{h}_{\text{iid},k}^{\text{H}}}{M^2}\right] \\ &+ \frac{P_k P_{k'} \kappa_{k'}}{(\kappa_k + 1)(\kappa_{k'} + 1)} \mathbb{E}\left[\frac{\mathbf{h}_{\text{iid},k} \mathbf{R}_{\text{TX}}^{1/2} \mathbf{a}_{\text{TX}}(\varphi_{k'}^{\text{AOD}}, \vartheta_{k'}^{\text{AOD}}) \mathbf{a}_{\text{TX}}^{\text{H}}(\varphi_{k'}^{\text{AOD}}, \vartheta_{k'}^{\text{AOD}}) \mathbf{R}_{\text{TX}}^{1/2} \mathbf{h}_{\text{iid},k}^{\text{H}}}{M^2}\right] \\ &+ \frac{P_k P_{k'} \kappa_k}{(\kappa_k + 1)(\kappa_{k'} + 1)} \mathbb{E}\left[\frac{\mathbf{a}_{\text{TX}}^{\text{H}}(\varphi_k^{\text{AOD}}, \vartheta_k^{\text{AOD}}) \mathbf{R}_{\text{TX}}^{1/2} \mathbf{h}_{\text{iid},k'}^{\text{H}} \mathbf{h}_{\text{iid},k'} \mathbf{R}_{\text{TX}}^{1/2} \mathbf{a}_{\text{TX}}(\varphi_k^{\text{AOD}}, \vartheta_k^{\text{AOD}})}{M^2}\right] \\ &+ \frac{P_k P_{k'} \kappa_k \kappa_{k'}}{(\kappa_k + 1)(\kappa_{k'} + 1)} \mathbb{E}\left[\frac{|\mathbf{a}_{\text{TX}}^{\text{H}}(\varphi_k^{\text{AOD}}, \vartheta_k^{\text{AOD}}) \mathbf{a}_{\text{TX}}(\varphi_{k'}^{\text{AOD}}, \vartheta_{k'}^{\text{AOD}})|^2}{M^2}\right] \end{aligned} \quad (3.40)$$

⁴Note that this is only true when $M \rightarrow \infty$ leads to large antenna array form factors, i.e., not for space constrained antenna arrays [84].

$$\begin{aligned}
&= \frac{P_k P_{k'}}{(\kappa_k + 1)(\kappa_{k'} + 1)} \frac{\text{tr}(\mathbf{R}_{\text{TX}}^2)}{M^2} \\
&\quad + \frac{P_k P_{k'} \kappa_{k'}}{(\kappa_k + 1)(\kappa_{k'} + 1)} \frac{\mathbf{a}_{\text{TX}}^H(\varphi_{k'}^{\text{AOD}}, \vartheta_{k'}^{\text{AOD}}) \mathbf{R}_{\text{TX}} \mathbf{a}_{\text{TX}}(\varphi_{k'}^{\text{AOD}}, \vartheta_{k'}^{\text{AOD}})}{M^2} \\
&\quad + \frac{P_k P_{k'} \kappa_k}{(\kappa_k + 1)(\kappa_{k'} + 1)} \frac{\mathbf{a}_{\text{TX}}^H(\varphi_k^{\text{AOD}}, \vartheta_k^{\text{AOD}}) \mathbf{R}_{\text{TX}} \mathbf{a}_{\text{TX}}(\varphi_k^{\text{AOD}}, \vartheta_k^{\text{AOD}})}{M^2} \\
&\quad + \frac{P_k P_{k'} \kappa_k \kappa_{k'}}{(\kappa_k + 1)(\kappa_{k'} + 1)} \frac{|\mathbf{a}_{\text{TX}}(\varphi_k^{\text{AOD}}, \vartheta_k^{\text{AOD}}) \mathbf{a}_{\text{TX}}^H(\varphi_{k'}^{\text{AOD}}, \vartheta_{k'}^{\text{AOD}})|^2}{M^2}, \quad (3.41)
\end{aligned}$$

where twelve of the sixteen terms in the expansion of (3.39) are zero, since $\mathbb{E}[\mathbf{h}_{\text{id},k}] = 0 \forall k$ (from (2.9)). Substituting (3.41) and (3.35) in (3.38), gives the desired result. \blacksquare

Under certain circumstances (which occur with probability zero), the variance in (3.37) can remain non-zero as $M \rightarrow \infty$. For example, if all correlations are unity, i.e., $\mathbf{R}_{\text{TX}} = \mathbf{1}_{M \times M}$ and $\frac{\text{tr}(\mathbf{R}_{\text{TX}}^2)}{M^2} = 1$. Also if $\mathbf{a}_{\text{TX}}(\varphi_k^{\text{AOD}}, \vartheta_k^{\text{AOD}}) = \mathbf{1}_{M \times 1} \forall k$ and $\mathbf{R}_{\text{TX}} = \mathbf{1}_{M \times M}$ then $\frac{\mathbf{a}_{\text{TX}}^H(\varphi_k^{\text{AOD}}, \vartheta_k^{\text{AOD}}) \mathbf{R}_{\text{TX}} \mathbf{a}_{\text{TX}}(\varphi_k^{\text{AOD}}, \vartheta_k^{\text{AOD}})}{M^2} = 1$. However, whenever the correlations decay to zero with separation, as M increases, it can be shown that $\lim_{M \rightarrow \infty} (\text{var}[V_{k,k'}]) = 0$. Again, this depends on an unlimited antenna array form factor [84].

Rician Fading Channel Numerical Results

In this subsection, the effects of increased LOS strength, in a Rician fading channel, are shown on the rate of convergence of \mathbf{V}_{id} to \mathbf{I}_K for the three convergence metrics defined in (3.1)-(3.3). Each convergence metric is evaluated and averaged over 1000 channel realizations. In each case, a Rician K-factor of zero is shown to represent the fully diffuse/NLOS channel case, whereas Rician K-factors of $\kappa = 1$ and $\kappa = 9$ represent 50% and 90% specular/LOS strength, respectively. The LOS antenna array response vectors in (2.8) are generated for a half-wavelength spaced ULA with negligible LOS elevation angle, i.e., $\vartheta_k^{\text{AOD}} = \frac{\pi}{2} \forall k$, and uniformly located users in a circular cell, i.e., $\varphi_k^{\text{AOD}} \sim \mathcal{U}[0, 2\pi) \forall k$. Note that unlike the results presented in [84], the antenna array form factor is not constrained in space and therefore the inter-element antenna spacing, $d_\lambda = 0.5$, does not change with increasing numbers of transmit antennas, M .

In Figure 3.4 the eigenvalue ratio is shown as a function of the number of transmit antennas, M , where $K = 10$ and $K = 50$. It is seen that for a larger Rician K-factor, κ , the rate of convergence of the eigenvalue ratio to 1 becomes slower, as $M \rightarrow \infty$. For example, at a system size of $M = 10^4$ and $K = 50$, an increase in the Rician K-factor from $\kappa = 0$ to $\kappa = 9$ results in an increase in the eigenvalue ratio of approximately 3.5 times. Likewise, the difference in eigenvalue ratio between $K = 10$ and $K = 50$ drastically increases with κ . It is

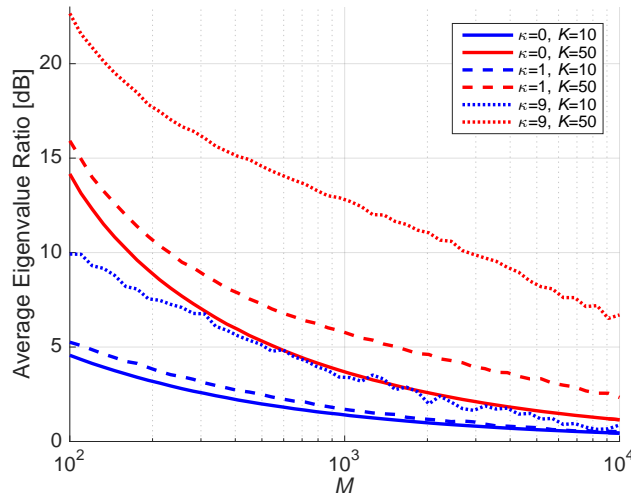


Figure 3.4: Average eigenvalue ratio as a function of the number of TX antennas, M , and Rician K-factor, κ , for an uncorrelated Rician fading channel, with the number of users, K , fixed and an inter-element antenna spacing of $d_\lambda = 0.5$ wavelengths.

also seen that for large κ , the variability of the eigenvalue ratio is increased such that the numerical curves in Figure 3.4 no longer decay smoothly for $\kappa = 9$. This can be explained by considering the variance of \mathbf{V} , given in (3.37), for the uncorrelated, equal link gain scenario ($P_k = 1 \forall k$), i.e.,

$$\text{var} [\mathbf{V}_{\text{iid},k,k'}] = \frac{1}{M^2 (\kappa_k + 1) (\kappa_{k'} + 1)} [M + \kappa_k \mathbf{a}_{\text{TX}}^{\text{H}} (\varphi_{k'}^{\text{AOD}}, \vartheta_{k'}^{\text{AOD}}) \mathbf{a}_{\text{TX}} (\varphi_k^{\text{AOD}}, \vartheta_k^{\text{AOD}}) + \kappa_{k'} \mathbf{a}_{\text{TX}}^{\text{H}} (\varphi_k^{\text{AOD}}, \vartheta_k^{\text{AOD}}) \mathbf{a}_{\text{TX}} (\varphi_{k'}^{\text{AOD}}, \vartheta_{k'}^{\text{AOD}})]. \quad (3.42)$$

Increases in κ_k or $\kappa_{k'}$ are then seen to increase the weighting of the variance on the LOS antenna array response vectors for fixed M . Since there is also large variability in the LOS antenna array response vectors between drops ($\varphi_k^{\text{AOD}} \sim \mathcal{U}[0, 2\pi] \forall k$), it follows that there becomes an unstable behaviour in the variance of \mathbf{V}_{iid} and thus the eigenvalue ratio, which tends to extremely sensitive to channel variation [201].

In Figure 3.5 the mean absolute deviation of \mathbf{V}_{iid} from the identity matrix, \mathbf{I}_K , is shown for a Rician fading channel. Contrary to the eigenvalue ratio (shown in Figure 3.4), a larger Rician K-factor κ is seen to increase the rate of converge of \mathbf{V}_{iid} to \mathbf{I}_K in terms of its mean absolute deviation. By considering the variance of the diagonal and off-diagonal elements of \mathbf{V}_{iid} , given by $\text{var} [\mathbf{V}_{\text{iid},k,k}] = \frac{2\kappa_k + 1}{M(\kappa_k + 1)^2}$ and (3.42), respectively (from (3.37)), it can be seen that the rate of convergence of $\text{var} [\mathbf{V}_{\text{iid}}]$ to 0, as $M \rightarrow \infty$, is increased for larger Rician K-factors. Intuitively this is consistent, since the specular component of the Rician channel is deterministic and therefore any increases in κ will result in the channel

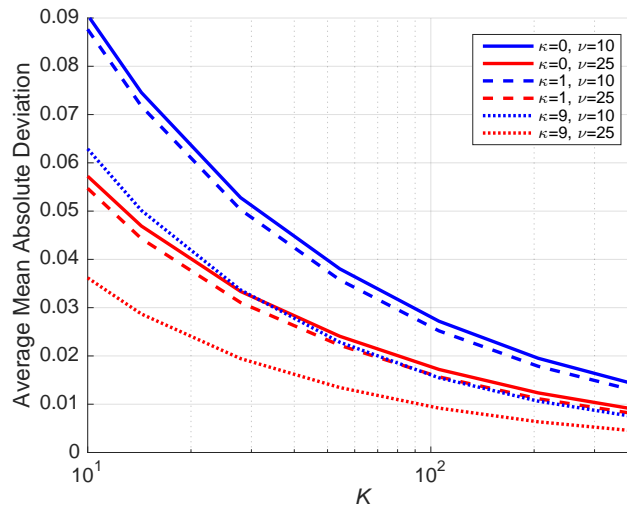


Figure 3.5: Average mean absolute deviation as a function of the number of users, K , and Rician K-factor, κ , for an uncorrelated Rician fading channel, with the ratio $\nu = \frac{M}{K}$ fixed and an inter-element antenna spacing of $d_\lambda = 0.5$ wavelengths.

matrix \mathbf{V}_{iid} becoming more deterministic and therefore hardened.

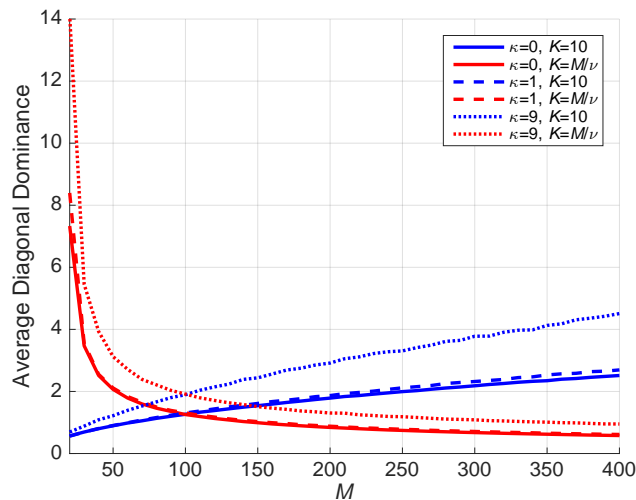


Figure 3.6: Average diagonal dominance as a function of TX antennas, M , and Rician K-factor, κ , for an uncorrelated Rician fading channel with K both fixed, at 10, and variable, where $K = \frac{M}{\nu}$, $\nu = 10$, and an inter-element antenna spacing of $d_\lambda = 0.5$ wavelengths.

In Figure 3.6, it is observed that the diagonal dominance of \mathbf{V}_{iid} increases for fixed K and decreases for $K = \frac{M}{10}$. The reader is referred to Section 3.2.1 for a discussion regarding this phenomena. As the Rician K-factor, κ , is increased, \mathbf{V}_{iid} becomes more diagonally dominant. This is because the diagonal elements $\mathbf{V}_{\text{iid},k,k}$ are converging to their limiting value ($= 1$) much quicker for large κ

(where $\text{var} [\mathbf{V}_{\text{iid},k,k}] = \frac{2\kappa_k+1}{M(\kappa_k+1)^2} = \frac{\kappa_k+\frac{1}{2}}{2M(\kappa_k+1)^2} \approx \frac{1}{2M(\kappa_k+1)}$ for large κ_k). As with the mean absolute deviation, the effective Rician fading channel has a larger proportion of deterministic channel values with larger κ , i.e., smaller numbers of random components, and therefore it becomes more diagonally dominant.

From Figures 3.4, 3.5, and 3.6, it is concluded that a larger Rician K-factor results in a quicker rate of convergence of the mean absolute deviation and diagonal dominance to its limiting value. However, the eigenvalue ratio convergence behaves differently since eigenvalues are extremely sensitive to variations in the channel [201], which are increased for larger κ values, since the LOS antenna array response vectors become more important and lead to a statistical structure in the channel which affects the eigenvalues.

Table 3.1 summarizes the magnitude of the three convergence metrics for different TX antenna numbers, M , and Rician K-factors, κ , for fixed numbers of users, $K = 10$.

Table 3.1: Magnitudes of convergence metrics

	Eigenvalue ratio		Mean absolute deviation [dB]		Diagonal dominance	
	$M = 100$	$M = 1000$	$M = 100$	$M = 1000$	$M = 100$	$M = 1000$
$\kappa = 0$	2.9	1.4	-10.6	-15.6	1.3	4.0
$\kappa = 1$	3.4	1.5	-10.7	-15.9	1.3	4.4
$\kappa = 9$	10.1	2.3	-12.2	-18.1	1.9	7.7

3.3 SINR Convergence with Linear Precoders

Due to their simplicity and optimality in massive MIMO systems [56], MF and ZF precoding techniques are now examined for i.i.d. and spatially correlated TX antenna arrays for Rayleigh and Rician fading channels. As in [7], the convergence scenario where $\nu = \frac{M}{K}$ is fixed with $K, M \rightarrow \infty$ is considered⁵.

3.3.1 Rayleigh Fading Channel

Here, limiting expressions for the ZF SNR and MF SINR for the unequal link gain scenarios are derived. First, a summary of the equal link gain results [7] is included, as these are needed for the unequal link gain scenario derivations. For the equal link gains case, the channel matrix becomes $\mathbf{H} = \mathbf{H}_{\text{iid}}$.

Lemma 3.1. (ZF SNR, Equal Link Gains) For $\mathbf{H} = \mathbf{H}_{\text{iid}}$, from (2.41),

⁵It has previously been shown in Section 2.5.3 that for K fixed and $M \rightarrow \infty$ that MF and ZF precoding performance is equivalent.

the limiting per-user ZF SNR as $M, K \rightarrow \infty$ with fixed $\nu = \frac{M}{K}$ is given by [7],

$$\lim_{K, M \rightarrow \infty} (\text{SNR}^{\text{ZF}}) = \varrho(\nu - 1). \quad (3.43)$$

Proof. Using the fact that for fixed $\nu = \frac{M}{K}$, $\lim_{K, M \rightarrow \infty} \left(\text{tr} \left((\mathbf{H}_{\text{iid}} \mathbf{H}_{\text{iid}}^{\text{H}})^{-1} \right) \right) = \frac{1}{(\nu-1)}$ [202] gives the desired result. ■

Theorem 3.5. (ZF SNR, Unequal Link Gains) For $\mathbf{H} = \mathbf{P}^{1/2} \mathbf{H}_{\text{iid}}$, from (2.41), the limiting per-user ZF SNR as $M, K \rightarrow \infty$ with fixed $\nu = \frac{M}{K}$ is given by,

$$\lim_{K, M \rightarrow \infty} (\text{SNR}^{\text{ZF}}) = \frac{\varrho(\nu - 1)}{\overline{\left(\frac{1}{P}\right)}}, \quad (3.44)$$

where $\overline{\left(\frac{1}{P}\right)}$ is the limiting value of $\overline{\left(\frac{1}{P}\right)} = \frac{1}{K} \sum_{k=1}^K \frac{1}{P_k}$, assuming it exists.

Proof. Considering the denominator of (2.41) and using known properties of the inverse Wishart matrix [203]

$$\mathbb{E} \left[(\mathbf{H} \mathbf{H}^{\text{H}})^{-1} \right] = \mathbb{E} \left[\left(\mathbf{P}^{1/2} \mathbf{H}_{\text{iid}} \mathbf{H}_{\text{iid}}^{\text{H}} \mathbf{P}^{1/2} \right)^{-1} \right] \quad (3.45)$$

$$= \frac{\mathbf{P}^{-1}}{M - K}, \quad (3.46)$$

and therefore

$$\mathbb{E} \left[\text{tr} \left((\mathbf{H} \mathbf{H}^{\text{H}})^{-1} \right) \right] = \mathbb{E} \left[\text{tr} \left(\left(\mathbf{P}^{1/2} \mathbf{H}_{\text{iid}} \mathbf{H}_{\text{iid}}^{\text{H}} \mathbf{P}^{1/2} \right)^{-1} \right) \right] \quad (3.47)$$

$$= \frac{\sum_{k=1}^K \frac{1}{P_k}}{M - K} \quad (3.48)$$

$$= \frac{\overline{\left(\frac{1}{P}\right)}}{\nu - 1}. \quad (3.49)$$

Assuming that $\overline{\left(\frac{1}{P}\right)}$ converges to a limit, $\overline{\left(\frac{1}{P}\right)}$, as $M, K \rightarrow \infty$ then it follows that, as the variance vanishes [188],

$$\lim_{K, M \rightarrow \infty} \left(\text{tr} \left((\mathbf{H} \mathbf{H}^{\text{H}})^{-1} \right) \right) = \lim_{K, M \rightarrow \infty} \left(\text{tr} \left(\left(\mathbf{P}^{1/2} \mathbf{H}_{\text{iid}} \mathbf{H}_{\text{iid}}^{\text{H}} \mathbf{P}^{1/2} \right)^{-1} \right) \right) \quad (3.50)$$

$$= \overline{\left(\frac{1}{P}\right)}, \quad (3.51)$$

which completes the proof. ■

Lemma 3.2. (MF SINR, Equal Link Gains) For $\mathbf{H} = \mathbf{H}_{\text{iid}}$, from (2.37),

the limiting per-user MF SINR as $M, K \rightarrow \infty$ with fixed $\nu = \frac{M}{K}$ is given by [7],

$$\lim_{K, M \rightarrow \infty} (\text{SINR}_k^{\text{MF}}) = \frac{\varrho\nu}{\varrho + 1}. \quad (3.52)$$

Proof. From (2.37), the instantaneous MF SINR for the k th user can be written as

$$\text{SINR}_k^{\text{MF}} = \frac{\frac{\varrho M^2}{K\tau} \left| \frac{\mathbf{h}_{\text{iid},k} \mathbf{h}_{\text{iid},k}^{\text{H}}}{M} \right|^2}{1 + \frac{\varrho(K-1)M}{K\tau} \frac{1}{(K-1)M} \sum_{\substack{k'=1 \\ k' \neq k}}^K \left| \mathbf{h}_{\text{iid},k} \mathbf{h}_{\text{iid},k'}^{\text{H}} \right|^2}, \quad (3.53)$$

then the limiting value can be given as

$$\begin{aligned} & \lim_{K, M \rightarrow \infty} (\text{SINR}_k^{\text{MF}}) \\ &= \frac{\lim_{K, M \rightarrow \infty} \left(\frac{\varrho M}{K} \right) \lim_{K, M \rightarrow \infty} \left(\frac{M}{\tau} \right) \lim_{K, M \rightarrow \infty} \left(\left| \frac{\mathbf{h}_{\text{iid},k} \mathbf{h}_{\text{iid},k}^{\text{H}}}{M} \right|^2 \right)}{1 + \lim_{K, M \rightarrow \infty} \left(\frac{\varrho(K-1)}{K} \right) \lim_{K, M \rightarrow \infty} \left(\frac{M}{\tau} \right) \lim_{K, M \rightarrow \infty} \left(\frac{1}{(K-1)M} \sum_{\substack{k'=1 \\ k' \neq k}}^K \left| \mathbf{h}_{\text{iid},k} \mathbf{h}_{\text{iid},k'}^{\text{H}} \right|^2 \right)}. \end{aligned} \quad (3.54)$$

The convergence of the three limits in (3.54) are now independently considered, as $K, M \rightarrow \infty$ with fixed $\nu = \frac{M}{K}$. First,

$$\lim_{K, M \rightarrow \infty} \left(\frac{\tau}{M} \right) = \lim_{K, M \rightarrow \infty} \left(\frac{1}{K} \left(\text{tr} \left(\frac{\mathbf{H}_{\text{iid}} \mathbf{H}_{\text{iid}}^{\text{H}}}{M} \right) \right) \right) \quad (3.55)$$

$$= \frac{1}{K} \text{tr}(\mathbf{I}_K) \quad (3.56)$$

$$= 1, \quad (3.57)$$

since $\frac{\tau}{M}$ converges to the mean as the variance vanishes. Also,

$$\begin{aligned} & \lim_{K, M \rightarrow \infty} \left(\frac{1}{(K-1)M} \sum_{\substack{k'=1 \\ k' \neq k}}^K \left| \mathbf{h}_{\text{iid},k} \mathbf{h}_{\text{iid},k'}^{\text{H}} \right|^2 \right) \\ &= \lim_{K, M \rightarrow \infty} \left(\frac{\sum_{\substack{k'=1 \\ k' \neq k}}^K \text{tr} \left(\mathbf{h}_{\text{iid},k} \mathbf{h}_{\text{iid},k'}^{\text{H}} \mathbf{h}_{\text{iid},k'} \mathbf{h}_{\text{iid},k}^{\text{H}} \right)}{(K-1)M} \right) \end{aligned} \quad (3.58)$$

$$= \lim_{K, M \rightarrow \infty} \left(\sum_{\substack{k'=1 \\ k' \neq k}}^K \frac{\text{tr} \left(\mathbf{h}_{\text{iid}, k'}^H \mathbf{h}_{\text{iid}, k'} \mathbf{h}_{\text{iid}, k}^H \mathbf{h}_{\text{iid}, k} \right)}{(K-1)M} \right) \quad (3.59)$$

$$= 1, \quad (3.60)$$

as $\mathbb{E} [\mathbf{h}_k^H \mathbf{h}_k] = \mathbf{I}_M \forall k$ and the variance of the summation vanishes. Then, using the known convergence of $\frac{\mathbf{h}_{\text{iid}, k} \mathbf{h}_{\text{iid}, k}^H}{M}$ to $\mathbf{I} \forall k$ as $M \rightarrow \infty$ [142], and further substituting (3.57) and (3.60) in (3.54), the limit of (3.53) is obtained. ■

Theorem 3.6. (MF SINR, Unequal Link Gains) For $\mathbf{H} = \mathbf{P}^{1/2} \mathbf{H}_{\text{iid}}$, from (2.37), the limiting per-user MF SINR as $M, K \rightarrow \infty$ with fixed $\nu = \frac{M}{K}$ is given by

$$\lim_{K, M \rightarrow \infty} (\text{SINR}_k^{\text{MF}}) = \frac{\varrho \nu P_k^2}{\vec{P} + \varrho P_k \vec{P}}, \quad (3.61)$$

where \vec{P} is the limiting value of $\frac{1}{K} \sum_{k=1}^K P_k$, as $K \rightarrow \infty$, assuming it exists.

Proof. From (2.37), the instantaneous SINR of the k th user can be written as

$$\text{SINR}_k^{\text{MF}} = \frac{\frac{\varrho}{K\tau} P_k^2 \left| \mathbf{h}_{\text{iid}, k} \mathbf{h}_{\text{iid}, k}^H \right|^2}{1 + \frac{\varrho P_k}{K\tau} \sum_{\substack{k'=1 \\ k' \neq k}}^K P_{k'} \left| \mathbf{h}_{\text{iid}, k} \mathbf{h}_{\text{iid}, k'}^H \right|^2} \quad (3.62)$$

$$= \frac{\frac{\varrho \frac{M}{K} P_k^2}{\frac{\tau}{M}} \left| \frac{\mathbf{h}_{\text{iid}, k} \mathbf{h}_{\text{iid}, k}^H}{M} \right|^2}{1 + \frac{\varrho}{P_k} \frac{\tau}{M} \left(\frac{1}{K} \sum_{\substack{k'=1 \\ k' \neq k}}^K P_{k'} \right) \frac{\sum_{\substack{k'=1 \\ k' \neq k}}^K P_{k'} \left| \mathbf{h}_{\text{iid}, k} \mathbf{h}_{\text{iid}, k'}^H \right|^2}{M \sum_{\substack{k'=1 \\ k' \neq k}}^K P_{k'}}}. \quad (3.63)$$

The limiting MF SINR for user k can then be written as

$$\begin{aligned} & \lim_{K, M \rightarrow \infty} (\text{SINR}_k^{\text{MF}}) \\ &= \frac{\lim_{K, M \rightarrow \infty} \left(\frac{\varrho \frac{M}{K} P_k^2}{\frac{\tau}{M}} \right) \lim_{K, M \rightarrow \infty} \left(\left| \frac{\mathbf{h}_{\text{iid}, k} \mathbf{h}_{\text{iid}, k}^H}{M} \right|^2 \right)}{1 + \frac{\varrho}{P_k} \lim_{K, M \rightarrow \infty} \left(\frac{\tau}{M} \right) \lim_{K, M \rightarrow \infty} \left(\frac{1}{K} \sum_{\substack{k'=1 \\ k' \neq k}}^K P_{k'} \right) \frac{\lim_{K, M \rightarrow \infty} \left(\frac{1}{MK} \sum_{\substack{k'=1 \\ k' \neq k}}^K P_{k'} \left| \mathbf{h}_{\text{iid}, k} \mathbf{h}_{\text{iid}, k'}^H \right|^2 \right)}{\lim_{K, M \rightarrow \infty} \left(\frac{1}{K} \sum_{\substack{k'=1 \\ k' \neq k}}^K P_{k'} \right)}}. \end{aligned} \quad (3.64)$$

The convergence of the limits in (3.64) are now independently considered, as $K, M \rightarrow \infty$ with fixed $\nu = \frac{M}{K}$. First,

$$\lim_{K, M \rightarrow \infty} \left(\frac{\tau}{M} \right) = \lim_{K, M \rightarrow \infty} \left(\frac{1}{K} \left(\text{tr} \left(\frac{\mathbf{H}\mathbf{H}^H}{M} \right) \right) \right) \quad (3.65)$$

$$= \lim_{K, M \rightarrow \infty} \left(\frac{1}{K} \left(\text{tr} \left(\frac{\mathbf{P}^{1/2} \mathbf{H}_{\text{iid}} \mathbf{H}_{\text{iid}}^H \mathbf{P}^{1/2}}{M} \right) \right) \right) \quad (3.66)$$

$$= \lim_{K, M \rightarrow \infty} \left(\frac{1}{K} \left(\text{tr}(\mathbf{P}) \right) \right) \quad (3.67)$$

$$= \lim_{K, M \rightarrow \infty} \left(\frac{1}{K} \sum_{k=1}^K P_k \right) \quad (3.68)$$

$$= \vec{P}, \quad (3.69)$$

assuming that the limit \vec{P} exists, which follows since $\lim_{K, M \rightarrow \infty} \left(\frac{\tau}{M} \right) = \mathbb{E} \left[\frac{\tau}{M} \right]$ as the variance vanishes. Note that if the limit \vec{P} exists then

$$\lim_{K, M \rightarrow \infty} \left(\frac{1}{K} \sum_{\substack{k'=1 \\ k' \neq k}}^K P_{k'} \right) = \vec{P}. \quad (3.70)$$

Also, from Section (3.60) and (3.69),

$$\lim_{K, M \rightarrow \infty} \left(\frac{1}{MK} \sum_{\substack{k'=1 \\ k' \neq k}}^K P_{k'} |\mathbf{h}_{\text{iid},k} \mathbf{h}_{\text{iid},k'}^H|^2 \right) = \vec{P}. \quad (3.71)$$

In the numerator of (3.64), as shown before, $\lim_{M \rightarrow \infty} \left(\frac{\mathbf{h}_{\text{iid},k} \mathbf{h}_{\text{iid},k}^H}{M} \right) = 1$ and therefore combining (3.69), (3.70) and (3.71) with (3.64), the limiting SINR of (3.63) can be obtained. \blacksquare

Link Gain Models

Cases with equal and unequal link gains are considered. The equal link gain case models a single-user MIMO system where one user has K co-located antennas. This is used as a reference case. While not considered by other authors, the unequal link gain case models K distributed users, where each user has a different link gain due to path-loss, shadow fading, etc. However, since the log-normal random variable does not converge easily for moderately sized K , due to the large variation in values which it generates, $\frac{1}{K} \sum_{k=1}^K P_k$ will not easily converge to \vec{P} using the classic link gain model (given in (2.3)). A new link gain model is therefore proposed, described below, to illustrate convergence. This proposed link gain model samples K evenly spaced users link gains from

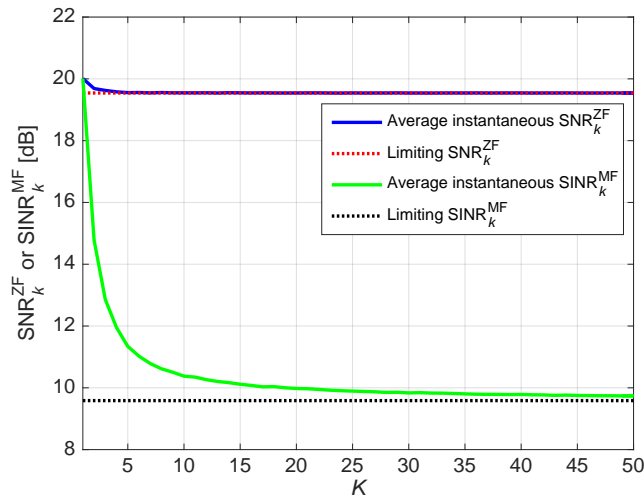
a restricted interval of a smoothly decaying function.

P_k values are selected from the limiting function $P(x) = A\Gamma^x$, where Γ is arbitrarily set such that $0 < \Gamma < 1$, $A = P_{\max}$, and $0 < x < x_0$, such that $x_0 = \frac{\log(P_{\min}/P_{\max})}{\log(\Gamma)}$. This allows us to control the range of the link gains in the interval $[P_{\min}, P_{\max}] = [A\Gamma^{x_0}, A]$ and also to control the rate of decay of the link gains by Γ . Given the parameters $P_{\min}, P_{\max}, \Gamma$ and the number of users, K , the P_k values are given by $P_k = P\left(\frac{x_0}{2K}(2k-1)\right)$ which gives the K values of P_1, P_2, \dots, P_K as the values of $P(x)$ using K values of x evenly spread over $[0, x_0]$.

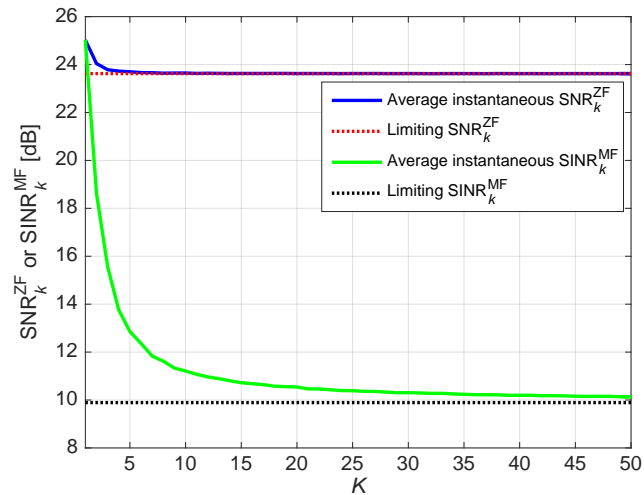
Numerical Results

Spatially Uncorrelated Channel: Figures 3.7a and 3.7b show the convergence properties of the ZF and MF precoders for equal and unequal link gains, respectively. The average per-user instantaneous SNR for a ZF precoder in both cases of equal and unequal link gains converges to the limit quickly. For example, in Figures 3.7a and 3.7b, when $K = 10$ and $M = 100$ the mean value of the per-user SNR already approaches the asymptotic limit for infinite antennas. It can be observed in both figures that the limiting per-user MF SINR is smaller than the limiting per-user ZF SNR; the MF precoder SINR is effectively reduced by a factor of $\varrho + 1$ when ν is large (looking at (3.43) and (3.52)). This difference is obvious in Figures 3.7a and 3.7b even for $\nu = 10$. The average per-user instantaneous MF SINR takes a longer time to converge to its limiting value because of the additional random variables in the numerator and denominator of (3.53). The unequal link gain case for the MF precoder has additional terms in (3.62) which manifest itself in a small increase of the per-user SINR as compared to the equal link gains case. The per-user MF SINR is also smaller relative to the per-user ZF SNR due to the inter-user interference terms in the denominator of (3.53) and (3.62); the boost in the SINR in the numerator due to the co-phasing terms $|\mathbf{h}_k \mathbf{h}_k^H|^2$ is not enough to compensate for the inter-user interference given by $\sum_{\substack{k'=1 \\ k' \neq k}}^K |\mathbf{h}_k \mathbf{h}_{k'}^H|^2$.

Spatially Correlated Channel: Here the exponential spatial correlation model is employed, described in Section 2.3.1, to numerically evaluate the effects of spatial correlation on the average instantaneous and limiting performance of the per-user ZF SNR and MF SINR. Numerically, the effects of two types of spatial correlation are shown: a large inter-element spatial correlation, where $\rho = 0.9$, and a low inter-element spatial correlation, where $\rho = 0.5$. It is seen that spatial correlation introduces a large penalty in the average per-user instantaneous SNR and SINR for both ZF and MF precoders (equal and unequal



(a) Equal link gains.



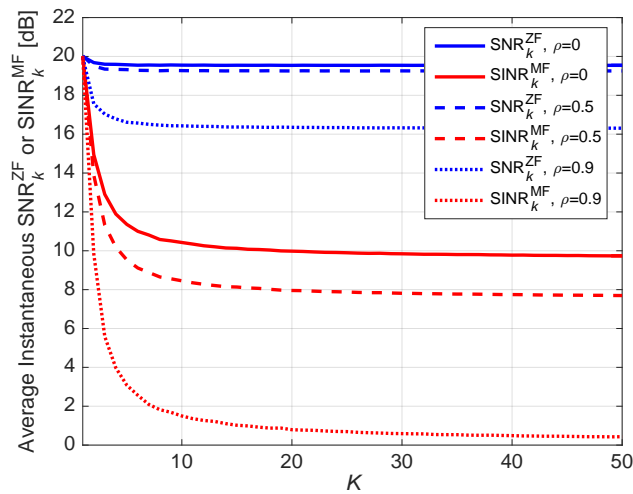
(b) Unequal link gains.

Figure 3.7: Average instantaneous and limiting per-user ZF SNR and MF SINR, as a function of the number of single-antenna users, K , where $\nu = 10$, $\varrho = 10$ dB.

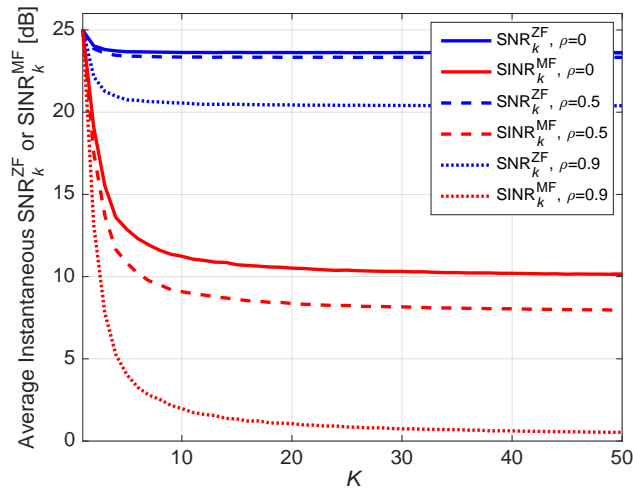
link gains), when compared to the corresponding spatially uncorrelated case. The ZF SNR and MF SINR for the lower value of correlation ($\rho = 0.5$) should be similar to the i.i.d. channel for the two precoders - and this is indeed the case.

3.3.2 Rician Fading Channel

In this subsection, MF SINR and ZF SNR precoding performances are numerically evaluated in a Rician fading channel. As was the case for the numerical results exploring the convergence of \mathbf{V}_{iid} to \mathbf{I}_K in Section 3.2.2, a space-



(a) Equal link gains.

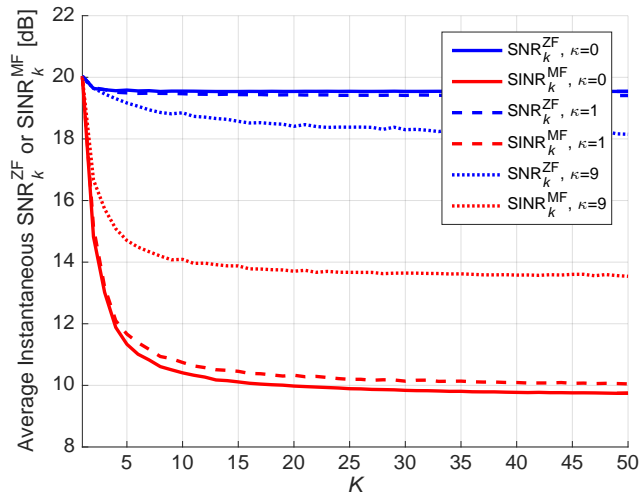


(b) Unequal link gains.

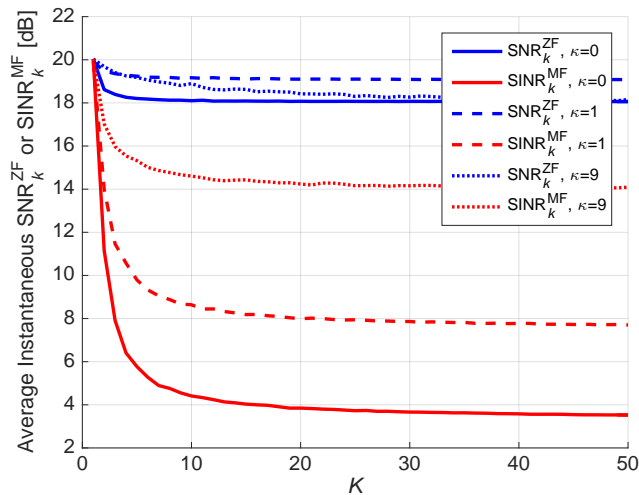
Figure 3.8: Spatially correlated average instantaneous per-user ZF SNR and MF SINR, as a function of the number of single-antenna users, K , where $\nu = 10$, $\varrho = 10$ dB.

unconstrained ULA is assumed with a $d_\lambda = \frac{1}{2}$ wavelength inter-element spacing and negligible LOS elevation angle, i.e., $\vartheta_k^{\text{AOD}} = \frac{\pi}{2} \forall k$. Users are randomly located in a circular cell, i.e., $\varphi_k^{\text{AOD}} \sim \mathcal{U}[0, 2\pi) \forall k$.

In Figures 3.9a and 3.9b the average instantaneous per-user ZF SNR and MF SINR performance for spatially uncorrelated and correlated environments is shown, respectively, as a function of the number of single-antenna users, K . As in the Rayleigh fading case, spatial correlation is modelled via the exponential model, given in (2.49). When no spatial correlation is modelled (Figure 3.9a), the SNR performance the ZF precoder is reduced with increasing κ since the increased ratio of deterministic channel components in the composite channel



(a) Uncorrelated channel.

(b) Spatially correlated channel with $\rho = 0.8$.Figure 3.9: Average instantaneous per-user ZF SNR and MF SINR, as a function of the number of single-antenna users, K , where $\nu = 10$, $\varrho = 10$ dB.

are effectively reducing its spatial diversity.

On the other hand, the MF precoder performance increases with κ , as was seen in [67, 204], because the MF interference power, $\sum_{\substack{k'=1 \\ k' \neq k}}^K |\mathbf{h}_k \mathbf{h}_{k'}^H|^2$,

κ is increased. This fact can be shown by considering the MF interference power in the two extreme cases: a fully NLOS channel, $\kappa = 0$, and a fully LOS channel, $\kappa = \infty$, in Figure 3.10. The MF interference power for the fully LOS channel is seen to have an enormous variability, relative to the fully NLOS channel MF interference power. However, in a large proportion of channel instances, the MF interference power is lower in the fully LOS channel than the fully NLOS

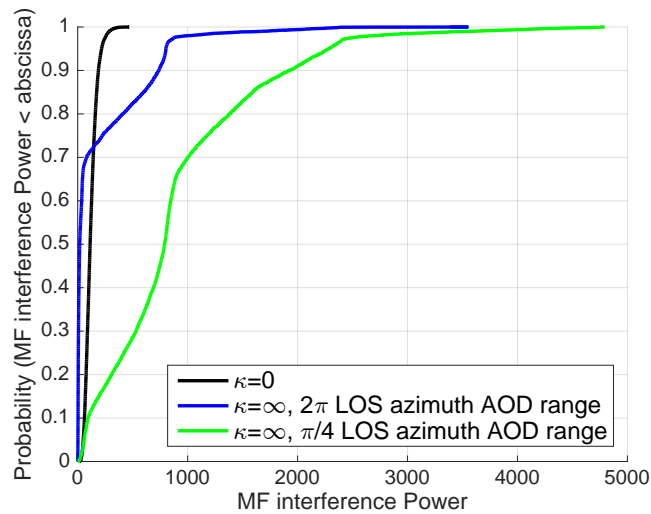


Figure 3.10: MF interference power for fully scattered, $\kappa = 0$, and fully LOS, $\kappa = \infty$, channels with $K = 4$ and $\nu = 10$. LOS azimuth angle ranges of $\varphi^{\text{AOD}} \sim \mathcal{U}[0, 2\pi)$ and $\varphi^{\text{AOD}} \sim \mathcal{U}[0, \frac{\pi}{4})$ are shown.

channel, thus causing the MF SINR to increase with κ . This is because the large range of LOS azimuth AODs ($\varphi \sim \mathcal{U}[0, 2\pi)$) are resulting in near-orthogonal LOS antenna array response vectors. A smaller range of LOS azimuth AODs scenario ($\varphi \sim \mathcal{U}[0, \frac{\pi}{4})$) is also included in Figure 3.10, showing that the MF interference power is extremely sensitive to the location of the users, and thus the diversity of the LOS antenna array response vectors.

In the spatially correlated Rician fading channel scenario (Figure 3.9b), both the ZF SNR and MF SINR performance increases with larger κ since the (large) spatial correlation is reducing the diversity and rank of the NLOS channel. Compared with the uncorrelated case (Figure 3.9a), the spatial correlation is significantly reducing the MF precoding performance. For example, an average instantaneous per-user MF SINR is reduced by approximately 6 dB at $K = 50$ with a fully NLOS channel.

3.4 Conclusion

In this chapter, the number of antennas required for a system to achieve massive MIMO properties have been analysed for Rayleigh and Rician fading channels. For the Rayleigh fading channel, it is seen that the convergence to favourable propagation and channel hardening are controlled by the convergence of an i.i.d. channel to the identity matrix. Numerically, it was seen that a larger Rician K-factor results in a quicker rate of convergence of the mean absolute deviation and diagonal dominance limiting value. However, the eigenvalue ratio convergence behaved differently since the eigenvalues are extremely sensitive to

variations in the channel, which are increased for larger κ , since the LOS antenna array response vectors create a statistical structure in the channel affecting the eigenvectors.

ZF SNR and MF SINR closed-form instantaneous and limiting expressions for scenarios of equal and unequal user link gains in a Rayleigh fading channel have been derived, as $K, M \rightarrow \infty$ with fixed ν . Interestingly, the per-user SNR/SINR for both ZF and MF precoders are less sensitive to M . In particular the per-user SNR for a ZF precoder converges quickly even for small values of M even though the SNR expression requires the computation of the inverse of a matrix. In a Rician fading channel, ZF SNR performance decreases with κ , due to reduced channel diversity, whereas the MF SINR performance increases with κ because the MF interference power is reduced.

4

Distributed Antenna Systems

In this chapter, the MF SINR performance and convergence analysis presented in Chapter 3 is extended to distributed antenna systems. Specifically, the instantaneous and limiting (in the number of TX antennas) performance of a MF precoder is investigated, with the aim of determining and characterizing the impacts of distributing transmit antennas into multiple clusters. The system model considered incorporates the effects of transmit spatial correlation, unequal link gains and imperfect CSI. Instantaneous and limiting expected MF SINR expressions of an arbitrary user are derived. From these expressions, clear insights into the effects of link gains, spatial correlation and CSI imperfections are drawn. Numerically, it is shown that distributing antennas into multiple clusters increases both the per-user instantaneous received SNR and average per-user instantaneous MF SINR, relative to a co-located antenna system, with significant increases in spatially correlated scenarios. Spatial correlation and CSI imperfections are shown to decrease instantaneous and limiting MF SINR performance, but do not influence the rate of convergence of the MF SINR to its limiting expression, as the number of TX antennas increases indefinitely.

4.1 Introduction

As more antennas are added to a fixed antenna array form factor, inter-element antenna spacings reduce and consequently spatial correlation between antenna elements of the array increases [80–84] degrading system performance [23, 91]. In large-scale MIMO systems, the adverse effects of spatial correlation are more obvious since antennas are in close proximity to large numbers of other antenna elements. One design approach to mitigate the adverse effects of spatial cor-

relation is to divide the antennas into multiple *antenna clusters*, whereby the inter-element antenna distances at each antenna cluster would increase, provided the overall form factors remain the same. Such coordinated distributed systems have the additional advantage of providing greater coverage than a single, co-located, antenna cluster since both the minimum and average distance to a user is reduced and the resultant received SNR is increased [131, 205, 206]. Thus, applied to large-scale MIMO, distributed systems have been the subject of a number of recent studies, such as [80, 205, 207–219].

The primary aim of this chapter is to analyse the performance of distributed MF precoding for large-scale antenna arrays¹. Specifically, the effects of the number of antenna clusters on the average instantaneous and *limiting* (which is different from [80, 207–217]) expected per-user MF SINR is of interest. The contributions of this chapter can be summarized as follows:

- Accounting for unequal link gains, imperfect CSI, transmit spatial correlation and an arbitrary number of antenna clusters, a per-user instantaneous MF SINR expression is derived. Numerically, it is then shown that distributing antennas into multiple clusters is greatly beneficial to MF SINR performance in highly spatially correlated scenarios.
- From the previously derived per-user instantaneous MF SINR, a limiting expected per-user MF SINR is derived as the number of antenna elements approaches infinity, whilst maintaining a fixed ratio of the number of transmit antennas to single-antenna users.
- A number of realistic link gain scenarios are used to illustrate the convergence of the instantaneous per-user MF SINR to the limiting expected per-user MF SINR. Numerically, this is shown for spatially correlated and uncorrelated cases.

4.2 System Description

The Rayleigh fading channel model in (2.8) is extended to a distributed antenna system where the M TX antennas, divided equally among N antenna clusters, serve K single-antenna users, on the DL. Coordination between multiple antenna clusters is assumed [217, 222, 223]. The $K \times M$ channel matrix, \mathbf{H} , is then

$$\mathbf{H} = \begin{bmatrix} \sqrt{P_{1,1}}\mathbf{H}_{\text{iid},1,1}\mathbf{R}_{\text{TX}}^{1/2} & \cdots & \sqrt{P_{1,N}}\mathbf{H}_{\text{iid},1,N}\mathbf{R}_{\text{TX}}^{1/2} \\ \vdots & \ddots & \vdots \\ \sqrt{P_{K,1}}\mathbf{H}_{\text{iid},K,1}\mathbf{R}_{\text{TX}}^{1/2} & \cdots & \sqrt{P_{K,N}}\mathbf{H}_{\text{iid},K,N}\mathbf{R}_{\text{TX}}^{1/2} \end{bmatrix}, \quad (4.1)$$

¹Since exact limiting analysis of ZF precoding in distributed systems is difficult [220], only MF precoding is examined. For limiting approximations of ZF precoding, see [221].

where $P_{k,n}$ and $\mathbf{H}_{\text{iid},k,n}$ denote the link gain and $K \times \frac{M}{N}$ i.i.d. channel matrix, respectively, between user $k \in 1, \dots, K$ and antenna cluster $n \in 1, \dots, N$. \mathbf{R}_{TX} denotes the $\frac{M}{N} \times \frac{M}{N}$ spatial correlation matrix at each antenna cluster, assumed to be equal for all antenna clusters.

Imperfect CSI is modelled using the simple statistical model given by [224, 225],

$$\hat{\mathbf{H}} = \xi \mathbf{H} + \sqrt{1 - \xi^2} \tilde{\mathbf{H}}, \quad (4.2)$$

where $\hat{\mathbf{H}}$ denotes the estimated channel matrix, $\tilde{\mathbf{H}}$ is the Gaussian error matrix, independent and statistically identical to \mathbf{H} , and $0 \leq \xi \leq 1$ controls the accuracy of the CSI.

In this chapter, both instantaneous and limiting MF SINR performance is of interest. Numerical results include multi-user simulations, where the instantaneous and limiting MF SINR is averaged over the users, K . For clarity, each of the terms used in this chapter are defined as follows:

- $\text{SINR}_k^{\text{MF}}$ denotes the instantaneous per-user MF SINR,
- $\frac{1}{K} \sum_{k=1}^K \text{SINR}_k^{\text{MF}}$ denotes the average instantaneous per-user MF SINR,
- $\lim_{K \rightarrow \infty} \mathbb{E} [\text{SINR}_k^{\text{MF}}]$ denotes the limiting expected per-user MF SINR,
- $\frac{1}{K} \sum_{k=1}^K \lim_{K \rightarrow \infty} \mathbb{E} [\text{SINR}_k^{\text{MF}}]$ denotes the average limiting expected per-user MF SINR.

4.3 Instantaneous MF SINR

In this section, the instantaneous per-user MF SINR is derived for the channel model in (4.1), with CSI imperfections modelled by (4.2). Numerically, the instantaneous per-user MF SINR is then examined for a number of system scenarios.

4.3.1 Instantaneous MF SINR Analysis

Combining (4.2) with (2.34) and (2.35), the MF-precoded transmitted signal, \mathbf{x} , and average power normalization, τ , with CSI inaccuracy, are respectively given by

$$\mathbf{x} = \frac{1}{\sqrt{\tau}} \hat{\mathbf{H}}^H \mathbf{s}, \quad (4.3)$$

and

$$\tau = \frac{\text{tr}(\widehat{\mathbf{H}}\widehat{\mathbf{H}}^H)}{K}. \quad (4.4)$$

Substituting (4.3) in (2.2), the combined received signal for all users is thus given by

$$\mathbf{y} = \sqrt{\frac{\rho}{\tau}} \mathbf{H}\widehat{\mathbf{H}}^H \mathbf{s} + \mathbf{v}, \quad (4.5)$$

with user $k \in 1, \dots, K$ receiving

$$y_k = \sqrt{\frac{\rho}{\tau}} \mathbf{h}_k \widehat{\mathbf{H}}^H \mathbf{s} + v_k. \quad (4.6)$$

Lemma 4.1. *Let $\widetilde{\mathbf{h}}_k$ and \mathbf{h}_k denote the k th user's Gaussian error vector and channel vector, respectively, i.e., the k th row of $\widetilde{\mathbf{H}}$ and \mathbf{H} , respectively. Then*

$$\mathbb{E} \left[\widetilde{\mathbf{h}}_k^H \widetilde{\mathbf{h}}_k \right] = \begin{bmatrix} P_{k,1} \mathbf{R}_{\text{TX}} & & \\ & \ddots & \\ & & P_{k,N} \mathbf{R}_{\text{TX}} \end{bmatrix} = \mathbf{\Upsilon}_k, \quad (4.7)$$

where $\mathbf{\Upsilon}_k$ is the $M \times M$ block diagonal matrix which contains both the link gain coefficients and spatial correlation effects for user k .

Proof. Since, in (4.2), $\widetilde{\mathbf{H}}$ is statistically identical to \mathbf{H} ,

$$\mathbb{E} \left[\widetilde{\mathbf{h}}_k^H \widetilde{\mathbf{h}}_k \right] = \mathbb{E} \left[\mathbf{h}_k^H \mathbf{h}_k \right] \quad (4.8)$$

$$= \mathbb{E} \left[\begin{bmatrix} \sqrt{P_{k,1}} \mathbf{R}_{\text{TX}}^{1/2} \mathbf{H}_{k,1}^H \\ \vdots \\ \sqrt{P_{k,N}} \mathbf{R}_{\text{TX}}^{1/2} \mathbf{H}_{k,N}^H \end{bmatrix} \begin{bmatrix} \sqrt{P_{k,1}} \mathbf{H}_{k,1} \mathbf{R}_{\text{TX}}^{1/2}, \dots, \sqrt{P_{k,N}} \mathbf{H}_{k,N} \mathbf{R}_{\text{TX}}^{1/2} \end{bmatrix} \right] \quad (4.9)$$

$$= \begin{bmatrix} P_{k,1} \mathbf{R}_{\text{TX}} & & \\ & \ddots & \\ & & P_{k,N} \mathbf{R}_{\text{TX}} \end{bmatrix} = \mathbf{\Upsilon}_k. \quad (4.10)$$

Note that \mathbf{h}_k can be expressed as $\mathbf{h}_k = \mathbf{g}_k \mathbf{\Upsilon}_k^{1/2}$, where $\mathbf{g}_k \in \mathbb{C}^{1 \times M}$ contains independent $\mathcal{CN}(0,1)$ elements. ■

Proposition 4.1. *The expected value of the signal power of the k th user's received signal in (4.6) is given by*

$$\mathbb{E} \left[\left| \sqrt{\frac{\rho}{\tau}} \mathbf{h}_k \widehat{\mathbf{h}}_k^H s_k \right|^2 \right] \approx \frac{\rho}{K \mathbb{E}[\tau]} \left(\xi^2 \mathbb{E} \left[\left| \widehat{\mathbf{h}}_k \widehat{\mathbf{h}}_k^H \right|^2 \right] + (1 - \xi^2) \mathbb{E} \left[\widehat{\mathbf{h}}_k \mathbf{\Upsilon}_k \widehat{\mathbf{h}}_k^H \right] \right). \quad (4.11)$$

Proof.

$$\mathbb{E} \left[\left| \sqrt{\frac{\varrho}{\tau}} \mathbf{h}_k \widehat{\mathbf{h}}_k^H s_k \right|^2 \right] \approx \frac{\varrho \mathbb{E} [s_k^2]}{\mathbb{E} [\tau]} \mathbb{E} \left[\left| (\xi \widehat{\mathbf{h}}_k + \sqrt{1 - \xi^2} \widetilde{\mathbf{h}}_k) \widehat{\mathbf{h}}_k^H \right|^2 \right] \quad (4.12)$$

$$= \frac{\varrho}{K \mathbb{E} [\tau]} \left(\xi^2 \mathbb{E} \left[\left| \widehat{\mathbf{h}}_k \widehat{\mathbf{h}}_k^H \right|^2 \right] + (1 - \xi^2) \mathbb{E} \left[\widetilde{\mathbf{h}}_k \widehat{\mathbf{h}}_k^H \widehat{\mathbf{h}}_k \widetilde{\mathbf{h}}_k^H \right] \right) \quad (4.13)$$

$$= \frac{\varrho}{K \mathbb{E} [\tau]} \left(\xi^2 \mathbb{E} \left[\left| \widehat{\mathbf{h}}_k \widehat{\mathbf{h}}_k^H \right|^2 \right] + (1 - \xi^2) \mathbb{E} \left[\text{tr} \left(\widehat{\mathbf{h}}_k \widetilde{\mathbf{h}}_k^H \widetilde{\mathbf{h}}_k \widehat{\mathbf{h}}_k^H \right) \right] \right) \quad (4.14)$$

$$= \frac{\varrho}{K \mathbb{E} [\tau]} \left(\xi^2 \mathbb{E} \left[\left| \widehat{\mathbf{h}}_k \widehat{\mathbf{h}}_k^H \right|^2 \right] + (1 - \xi^2) \mathbb{E} \left[\widehat{\mathbf{h}}_k \boldsymbol{\Upsilon}_k \widehat{\mathbf{h}}_k^H \right] \right), \quad (4.15)$$

where $\mathbb{E} [s_k^2] = \frac{1}{K}$ and the Laplacian approximation $\mathbb{E} \left[\frac{1}{\tau} \right] \approx \frac{1}{\mathbb{E} [\tau]}$, which is very accurate for large systems [208, 226–228] is used in (4.12). (4.15) is obtained from Lemma 4.1. \blacksquare

Proposition 4.2. *The expected value of the interference and noise power of the k th user's received signal in (4.6) can be shown to be*

$$\mathbb{E} \left[\left| \sqrt{\frac{\varrho}{\tau}} \sum_{\substack{k'=1 \\ k' \neq k}}^K \mathbf{h}_k \widehat{\mathbf{h}}_{k'}^H s_{k'} + v_k \right|^2 \right] \approx \frac{\varrho}{K \mathbb{E} [\tau]} \sum_{\substack{k'=1 \\ k' \neq k}}^K \left(\xi^2 \mathbb{E} \left[\left| \widehat{\mathbf{h}}_k \widehat{\mathbf{h}}_{k'}^H \right|^2 \right] + (1 - \xi^2) \mathbb{E} \left[\widehat{\mathbf{h}}_k \boldsymbol{\Upsilon}_k \widehat{\mathbf{h}}_{k'}^H \right] \right) + 1, \quad (4.16)$$

where the noise power is normalized to unity, i.e., $\mathbb{E} [v_k^2] = 1$.

Proof. Using the Laplacian approximation, as in Proposition 4.1.

$$\mathbb{E} \left[\left| \sqrt{\frac{\varrho}{\tau}} \sum_{\substack{k'=1 \\ k' \neq k}}^K \mathbf{h}_k \widehat{\mathbf{h}}_{k'}^H s_{k'} + v_k \right|^2 \right] \approx \frac{\varrho}{\mathbb{E} [\tau]} \mathbb{E} \left[\left(\sum_{\substack{k'=1 \\ k' \neq k}}^K \mathbf{h}_k \widehat{\mathbf{h}}_{k'}^H s_{k'} \right) \left(\sum_{\substack{k''=1 \\ k'' \neq k}}^K \widehat{\mathbf{h}}_{k''} \mathbf{h}_k^H s_{k''} \right) \right] + \mathbb{E} [v_k^2] \quad (4.17)$$

$$= \frac{\varrho}{K \mathbb{E} [\tau]} \sum_{\substack{k'=1 \\ k' \neq k}}^K \mathbb{E} \left[\left| \mathbf{h}_k \widehat{\mathbf{h}}_{k'}^H \right|^2 \right] + 1 \quad (4.18)$$

$$= \frac{\varrho}{K \mathbb{E} [\tau]} \sum_{\substack{k'=1 \\ k' \neq k}}^K \mathbb{E} \left[\left| (\xi \widehat{\mathbf{h}}_k + \sqrt{1 - \xi^2} \widetilde{\mathbf{h}}_k) \widehat{\mathbf{h}}_{k'}^H \right|^2 \right] + 1 \quad (4.19)$$

$$= \frac{\rho}{K\mathbb{E}[\tau]} \sum_{\substack{k'=1 \\ k' \neq k}}^K \left(\xi^2 \mathbb{E} \left[\left| \widehat{\mathbf{h}}_k \widehat{\mathbf{h}}_{k'}^H \right|^2 \right] + (1 - \xi^2) \mathbb{E} \left[\widehat{\mathbf{h}}_{k'} \widetilde{\mathbf{h}}_k^H \widetilde{\mathbf{h}}_k \widehat{\mathbf{h}}_{k'}^H \right] \right) + 1 \quad (4.20)$$

$$= \frac{\rho}{K\mathbb{E}[\tau]} \sum_{\substack{k'=1 \\ k' \neq k}}^K \left(\xi^2 \mathbb{E} \left[\left| \widehat{\mathbf{h}}_k \widehat{\mathbf{h}}_{k'}^H \right|^2 \right] + (1 - \xi^2) \mathbb{E} \left[\widehat{\mathbf{h}}_{k'} \boldsymbol{\Upsilon}_k \widehat{\mathbf{h}}_{k'}^H \right] \right) + 1, \quad (4.21)$$

where (4.21) is obtained from Lemma 4.1. ■

Combining (4.11) and (4.16), the expected MF SINR for the k th user is given by the Laplacian approximation

$$\mathbb{E} [\text{SINR}_k^{\text{MF}}] \approx \frac{\frac{\rho}{K\mathbb{E}[\tau]} \left(\xi^2 \mathbb{E} \left[\left| \widehat{\mathbf{h}}_k \widehat{\mathbf{h}}_k^H \right|^2 \right] + (1 - \xi^2) \mathbb{E} \left[\widehat{\mathbf{h}}_k \boldsymbol{\Upsilon}_k \widehat{\mathbf{h}}_k^H \right] \right)}{\frac{\rho}{K\mathbb{E}[\tau]} \sum_{\substack{k'=1 \\ k' \neq k}}^K \left(\xi^2 \mathbb{E} \left[\left| \widehat{\mathbf{h}}_k \widehat{\mathbf{h}}_{k'}^H \right|^2 \right] + (1 - \xi^2) \mathbb{E} \left[\widehat{\mathbf{h}}_{k'} \boldsymbol{\Upsilon}_k \widehat{\mathbf{h}}_{k'}^H \right] \right) + 1}. \quad (4.22)$$

Similarly, the instantaneous MF SINR performance, for a particular channel realization, is given by

$$\text{SINR}_k^{\text{MF}} = \frac{\frac{\rho}{K\tau} \left(\xi^2 \left| \widehat{\mathbf{h}}_k \widehat{\mathbf{h}}_k^H \right|^2 + (1 - \xi^2) \widehat{\mathbf{h}}_k \boldsymbol{\Upsilon}_k \widehat{\mathbf{h}}_k^H \right)}{\frac{\rho}{K\tau} \sum_{\substack{k'=1 \\ k' \neq k}}^K \left(\xi^2 \left| \widehat{\mathbf{h}}_k \widehat{\mathbf{h}}_{k'}^H \right|^2 + (1 - \xi^2) \widehat{\mathbf{h}}_{k'} \boldsymbol{\Upsilon}_k \widehat{\mathbf{h}}_{k'}^H \right) + 1}. \quad (4.23)$$

For perfect CSI, $\xi = 1$, (4.23) becomes

$$\text{SINR}_k^{\text{MF}} = \frac{\frac{\rho}{K\tau} \left| \widehat{\mathbf{h}}_k \widehat{\mathbf{h}}_k^H \right|^2}{\frac{\rho}{K\tau} \sum_{\substack{k'=1 \\ k' \neq k}}^K \left| \widehat{\mathbf{h}}_k \widehat{\mathbf{h}}_{k'}^H \right|^2 + 1} \quad (4.24)$$

$$= \frac{\frac{\rho}{K\tau} \left| \mathbf{h}_k \mathbf{h}_k^H \right|^2}{\frac{\rho}{K\tau} \sum_{\substack{k'=1 \\ k' \neq k}}^K \left| \mathbf{h}_k \mathbf{h}_{k'}^H \right|^2 + 1}. \quad (4.25)$$

Similarly for no CSI, $\xi = 0$, the MF SINR for the k th user is

$$\text{SINR}_k^{\text{MF}} = \frac{\frac{\rho}{K\tau} \widehat{\mathbf{h}}_k \boldsymbol{\Upsilon}_k \widehat{\mathbf{h}}_k^H}{\frac{\rho}{K\tau} \sum_{\substack{k'=1 \\ k' \neq k}}^K \widehat{\mathbf{h}}_{k'} \boldsymbol{\Upsilon}_k \widehat{\mathbf{h}}_{k'}^H + 1} \quad (4.26)$$

$$= \frac{\frac{\rho}{K\tau} \widetilde{\mathbf{h}}_k \boldsymbol{\Upsilon}_k \widetilde{\mathbf{h}}_k^H}{\frac{\rho}{K\tau} \sum_{\substack{k'=1 \\ k' \neq k}}^K \widetilde{\mathbf{h}}_{k'} \boldsymbol{\Upsilon}_k \widetilde{\mathbf{h}}_{k'}^H + 1}. \quad (4.27)$$

4.3.2 Instantaneous MF SINR Numerical Results

In this subsection, the performance of instantaneous MF SINR, given in (4.23), is numerically evaluated for a number of system scenarios. Path loss parameters used in all instantaneous simulations are taken from the standardized urban macro cell NLOS microwave measurements by 3GPP [129], and are given in Table 4.1. When $N = 1$, the single antenna cluster is positioned in the centre of the coverage region. However when $N \geq 2$, the antenna clusters are positioned equidistant on the edge of the coverage region. In each case, there is an exclusion radius around each antenna cluster of 30 m.

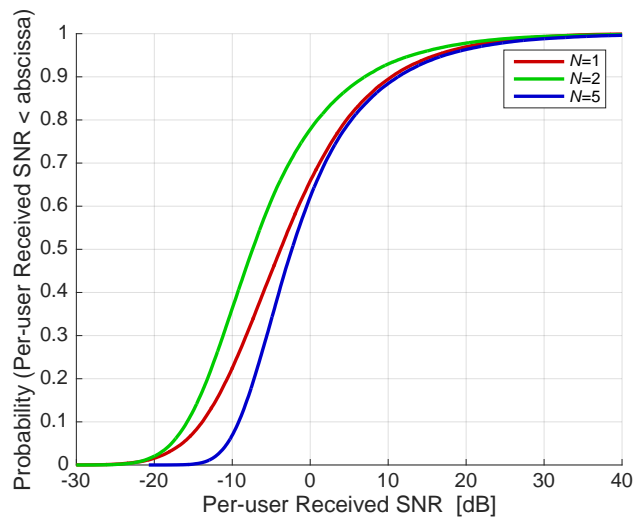
Note that MF SINR performance is highly dependent on the per-user received SNR which is, in turn, dependent on the TX(s) to user distances. Therefore, the effects of distributed antenna systems on the per-user received SNR is first investigated, as to not misrepresent how distributed antenna systems affect the MF SINR.

Table 4.1: Path loss parameters

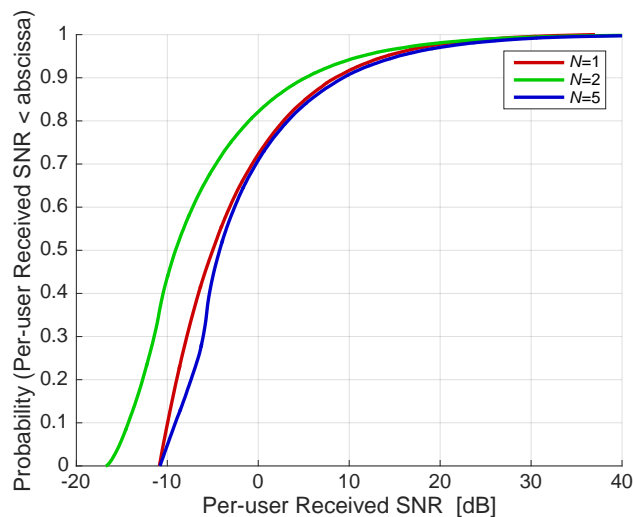
Parameter	Numerical Value
Path loss offset constant, α	13.5 dB
Path loss exponent, β	3.92
Shadow fading standard deviation, ϵ	6 dB
BS to user distance, d	$30 < d \leq 500$ m

Using the path loss parameters in Table 4.1, a per-user received SNR CDF is shown in Figure 4.1 as a function of the number of antenna clusters, N , for a median per-user received SNR, SNR_k , of -5 dB² for cases of including and excluding (log-normal) shadow fading. For $N > 1$, the per-user received SNR, SNR_k , is averaged over the antenna clusters, i.e., $\text{SNR}_k = \frac{1}{N} \sum_{n=1}^N \frac{P_{k,n}}{\sigma^2}$. The per-user received SNR CDF is smallest for $N = 2$ antenna clusters, as there are large parts of the cell where the link gains from both antenna clusters to the user are weak, e.g., near the cell-edge half way between the two antenna clusters. The per-user received SNR is the largest for $N = 5$, as an arbitrary user is likely to be relatively close to at least one antenna cluster. Since the path loss increases with distance quickly, at a rate of $d^\beta = d^{3.92}$, it follows that the more antenna clusters there are, the smaller the minimum distance between a user and an antenna cluster there is, resulting in a larger SNR_k . Furthermore, the larger the path loss exponent, β , is, the more advantageous it is to have a larger number of antenna clusters, N , and vice-versa. For large N , the low SNR region of the

²The median received SNR, SNR_k , is computed for the single antenna cluster case, i.e., $10^{-5/10} = \frac{P_{k,1}}{\sigma^2} \forall k$, where σ^2 is the receiver noise power, assumed equal for all users. The required TX power to guarantee the median SNR of -5 dB is then used at *all* antenna clusters, independent of N .



(a) Shadow fading included.



(b) Shadow fading excluded.

Figure 4.1: Per-user received SNR CDF as a function of the number of antenna clusters, N , for a median received SNR of -5 dB.

CDF occurs when the user is located in the centre of the cell region. However, this is relatively unlikely since users are located in the circular coverage region based on an area coverage [4]. For all N , the high SNR region of the CDF indicates when a user is very close to one antenna cluster.

It should be noted that when shadow fading is included, the difference between $N = 5$ and $N = 1$ SNR _{k} scenarios is more pronounced. This is because the shadow fading provides an enormous variation in link gains which dominates the CDFs. As the shadow fading standard deviation, ϵ , increases, the low SNR and high SNR regions of the CDF become elongated. Also, for $N \neq 1$, the median per-user received SNR will increase with larger N , since with more antenna clusters, at least one of the log-normal shadow fades is likely to be strong.

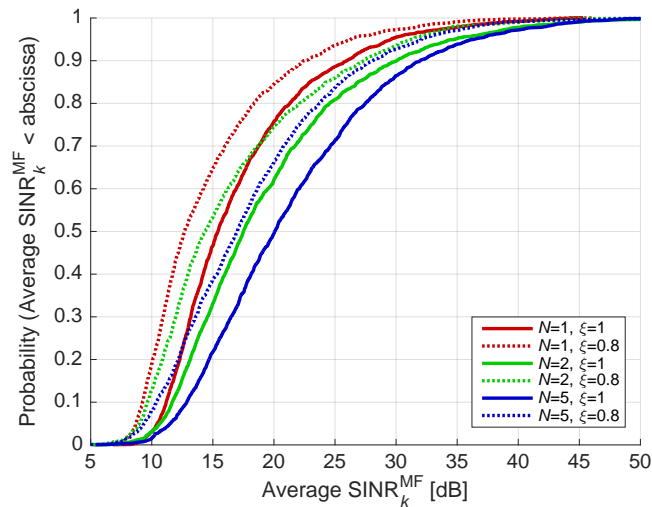


Figure 4.2: Uncorrelated average instantaneous per-user MF SINR CDF as a function of the number of antenna clusters, N , and CSI accuracy parameter, ξ , where $M = 100$ and $\nu = 10$.

In Figure 4.2, the uncorrelated average instantaneous per-user MF SINR CDF, (4.23), is shown as a function of the number of antenna clusters, N , and CSI accuracy parameter, ξ , where $M = 100$ and $\nu = 10$. In all cases of N , the average instantaneous per-user MF SINR is reduced by approximately 3 dB when ξ is reduced from one to 0.8, i.e., reducing the CSI accuracy parameter by 0.2 effectively halves the MF SINR performance. Also, the average instantaneous per-user MF SINR is shown to scale almost linearly with N . For example, considering the perfect CSI cases, the median CDF values for $N = 1, 2$ and 5 are approximately 15.5, 17.5 and 20.5 dB, respectively. This large increase with N is largely due to better cell coverage (seen in Figure 4.1).

In Figure 4.3, the spatially correlated average instantaneous per-user MF SINR CDF is shown as a function of the number of antenna clusters³, N , and CSI accuracy parameter, ξ , where $M = 100$ and $\nu = 10$. The exponential spatial correlation model, described in Section 2.3.1, is assumed, with two scenarios shown: a fixed array form factor per antenna cluster⁴ (therefore $\rho = 0.9^N$) and a fixed spatial correlation parameter⁵ per antenna cluster, where $\rho = 0.9$. Results for these two scenarios are shown in Figures 4.3a and 4.3b. In Figure 4.3a there is a large decrease in the average instantaneous per-user MF SINR for

³It is assumed that the distance between antenna clusters is much larger than the antenna array form factors, and therefore spatial correlation between antenna clusters is zero.

⁴Assuming both the exponential spatial correlation model and fixed array form factor, every antenna multiple of N , i.e., nN for $n \in \mathbb{Z}^+$, is placed at another antenna cluster location. Therefore, the exponential spatial correlation parameter, with an increase in virtual inter-element antenna distance, is reduced from ρ to ρ^N .

⁵Practically, this is equivalent to a fixed minimum inter-element spacing between antenna elements, independent on N .

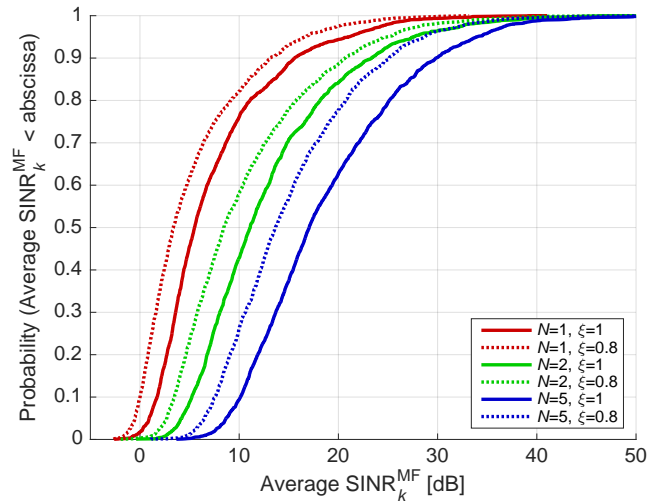
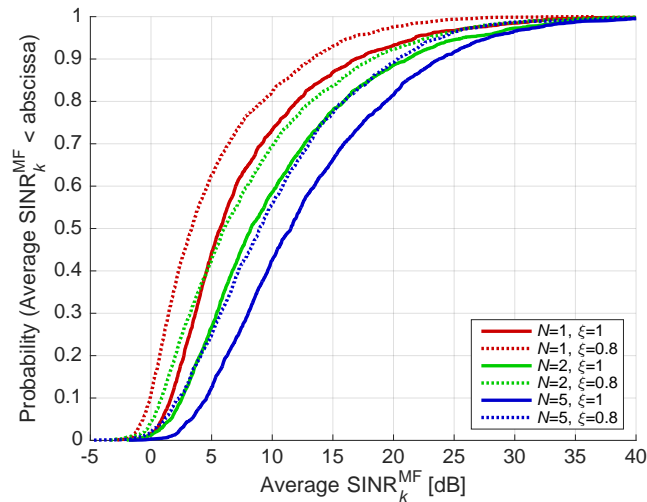
(a) Fixed array form factor, $\rho = 0.9^N$.(b) Fixed spatial correlation parameter, $\rho = 0.9$.

Figure 4.3: Spatially correlated average instantaneous per-user MF SINR CDF as a function of the number of antenna clusters, N , and CSI accuracy parameter, ξ , where $M = 100$ and $\nu = 10$.

the co-located antenna cluster case, relative to the $N = 5$ case, since the spatial correlation between adjacent antenna elements is significantly larger ($\rho = 0.9$ versus $\rho = 0.9^5 \approx 0.59$, respectively). Thus, maintaining a fixed array form factor for each antenna cluster is extremely beneficial for MF SINR performance in spatially correlated channels.

Even in the case of a fixed exponential spatial correlation parameter per antenna cluster (Figure 4.3b), it is observed that there *larger* difference in the performance between $N = 1$ and $N = 5$ relative to the uncorrelated scenario (Figure 4.2). For example, the gap in median SINR increases from approximately 4.7 dB to 5.8 dB. This is because the number of spatially correlated pairs of an-

tennas are being reduced from $M(M - 1)$, when $N = 1$, to $M(\frac{M}{5} - 1)$, when $N = 5$. The aggregate effects of the large number of spatially correlated pairs of antennas, in the colocated case, are reducing the MF SINR performance.

4.4 Limiting MF SINR

In this section, the limiting expected per-user MF SINR is considered for the convergence scenario where $K, M \rightarrow \infty$ with a fixed ratio of $\nu = \frac{M}{K}$. Note that although finite N is considered, the analysis can be extended to the case where $N \rightarrow \infty$. The limits also hold for the instantaneous per-user MF SINR, given in (4.23), but this derivation is a little more complex, relying on non-standard central limit theorems [229]. Hence, for ease of exposition, the limits are derived for the expected per-user MF SINR. Note that MF SINR limiting expressions for fixed $\frac{M}{K}$ are derived in [45] for a more general distributed system, with unequal spatial correlation matrices at each antenna cluster. However, due to the overly complex nature of the derived limiting expressions in [45], little insight can be drawn. In this section, the derived limiting per-user MF SINR provides a clear understanding of how the various system parameters influences the performance.

4.4.1 Limiting MF SINR Analysis

Since the asymptotic behaviour is of interest, (4.22) can be written as

$$\begin{aligned} & \lim_{K \rightarrow \infty} \mathbb{E} [\text{SINR}_k^{\text{MF}}] \\ & \approx \frac{\frac{\rho\nu}{\lim_{K \rightarrow \infty} \mathbb{E}[\frac{\tau}{M}]} \left(\xi^2 \lim_{K \rightarrow \infty} \mathbb{E} \left[\left| \frac{\hat{\mathbf{h}}_k \hat{\mathbf{h}}_k^{\text{H}}}{M} \right|^2 \right] + \frac{1-\xi^2}{M} \lim_{K \rightarrow \infty} \mathbb{E} \left[\frac{\hat{\mathbf{h}}_k \boldsymbol{\Upsilon}_k \hat{\mathbf{h}}_k^{\text{H}}}{M} \right] \right)}{\frac{\rho\nu}{\lim_{K \rightarrow \infty} \mathbb{E}[\frac{\tau}{M}]} \lim_{K \rightarrow \infty} \sum_{\substack{k'=1 \\ k' \neq k}}^K \left(\xi^2 \mathbb{E} \left[\left| \frac{\hat{\mathbf{h}}_k \hat{\mathbf{h}}_{k'}^{\text{H}}}{M} \right|^2 \right] + (1 - \xi^2) \mathbb{E} \left[\frac{\hat{\mathbf{h}}_{k'} \boldsymbol{\Upsilon}_k \hat{\mathbf{h}}_{k'}^{\text{H}}}{M^2} \right] \right) + 1}, \end{aligned} \quad (4.28)$$

assuming that the limit exists. The limiting expressions, as $M \rightarrow \infty$ with fixed ν , of the expectations given in (4.28) are now evaluated.

Lemma 4.2. *Using an eigen-decomposition of \mathbf{R}_{TX} ,*

$$\boldsymbol{\Upsilon}_k = \boldsymbol{\psi} \mathbf{Q}_k \boldsymbol{\psi}^{\text{H}}, \quad (4.29)$$

where \mathbf{Q}_k is a $M \times M$ diagonal matrix containing the eigenvalues of $\boldsymbol{\Upsilon}_k$ and $\boldsymbol{\psi}$ is a $M \times M$ unitary matrix.

Proof.

$$\mathbf{\Upsilon}_k = \begin{bmatrix} P_{k,1} \mathbf{R}_{\text{TX}} & & \\ & \ddots & \\ & & P_{k,N} \mathbf{R}_{\text{TX}} \end{bmatrix} = \begin{bmatrix} P_{k,1} \mathbf{U} \mathbf{\Lambda} \mathbf{U}^H & & \\ & \ddots & \\ & & P_{k,N} \mathbf{U} \mathbf{\Lambda} \mathbf{U}^H \end{bmatrix} \quad (4.30)$$

$$= \begin{bmatrix} \mathbf{U} & & \\ & \ddots & \\ & & \mathbf{U} \end{bmatrix} \begin{bmatrix} P_{k,1} \mathbf{\Lambda} & & \\ & \ddots & \\ & & P_{k,N} \mathbf{\Lambda} \end{bmatrix} \begin{bmatrix} \mathbf{U}^H & & \\ & \ddots & \\ & & \mathbf{U}^H \end{bmatrix} \quad (4.31)$$

$$= \boldsymbol{\psi} \mathbf{Q}_k \boldsymbol{\psi}^H, \quad (4.32)$$

where $\mathbf{\Lambda}$ is the $\frac{M}{N} \times \frac{M}{N}$ diagonal matrix of eigenvalues of \mathbf{R}_{TX} and \mathbf{U} is a $\frac{M}{N} \times \frac{M}{N}$ unitary matrix. Note that $\boldsymbol{\psi}$ is fixed for all $\mathbf{\Upsilon}_k$, as it only depends on \mathbf{R}_{TX} , which is assumed to be the same at each antenna cluster. ■

Lemma 4.3. For $\mathbf{g}_k \in \mathbb{C}^{1 \times M}$ with independent $\mathcal{CN}(0, 1)$ elements, and, for an arbitrary $\mathbf{\Upsilon}_k$,

$$\lim_{K \rightarrow \infty} \mathbb{E} \left[\frac{\mathbf{g}_k \mathbf{\Upsilon}_k \mathbf{g}_k^H}{M} \right] = \overline{P}_k, \quad (4.33)$$

where $\overline{P}_k = \frac{1}{N} \sum_{n=1}^N P_{k,n}$.

Proof.

$$\lim_{K \rightarrow \infty} \mathbb{E} \left[\frac{\mathbf{g}_k \mathbf{\Upsilon}_k \mathbf{g}_k^H}{M} \right] = \lim_{K \rightarrow \infty} \frac{1}{M} \mathbb{E} [\mathbf{g}_k \boldsymbol{\psi} \mathbf{Q}_k \boldsymbol{\psi}^H \mathbf{g}_k^H] \quad (4.34)$$

$$= \lim_{K \rightarrow \infty} \frac{1}{M} \mathbb{E} [\tilde{\mathbf{g}}_k \mathbf{Q}_k \tilde{\mathbf{g}}_k^H] \quad (4.35)$$

$$= \lim_{K \rightarrow \infty} \frac{1}{M} \sum_{m=1}^M \mathbb{E} [Q_{k,m,m} |\tilde{g}_{k,m}|^2] \quad (4.36)$$

$$= \lim_{K \rightarrow \infty} \frac{1}{M} \text{tr}(\mathbf{Q}_k) \quad (4.37)$$

$$= \lim_{K \rightarrow \infty} \frac{1}{M} \sum_{n=1}^N P_{k,n} \text{tr}(\mathbf{\Lambda}) \quad (4.38)$$

$$= \lim_{K \rightarrow \infty} \frac{1}{M} \sum_{n=1}^N P_{k,n} \frac{M}{N} \quad (4.39)$$

$$= \overline{P}_k, \quad (4.40)$$

where $\tilde{\mathbf{g}}_k = \mathbf{g}_k \boldsymbol{\psi} \in \mathbb{C}^{1 \times M}$ has i.i.d. $\mathcal{CN}(0, 1)$ elements, $Q_{k,m,m}$ is the m th diagonal element of \mathbf{Q}_k , and $\tilde{g}_{k,m}$ is the m th element of $\tilde{\mathbf{g}}_k$. Note that (4.37) holds since $\mathbb{E} [|\tilde{g}_{k,m}|^2] = 1$. ■

Note that $\frac{\mathbf{g}_k \mathbf{\Upsilon}_k \mathbf{g}_k^H}{M} \rightarrow \overline{P}_k$ as $K \rightarrow \infty$ by the weak version of the law of large numbers, so that expectation is not required in (4.33). To see this result, consider

(4.36) without the expectation:

$$\lim_{K \rightarrow \infty} \frac{\mathbf{g}_k \boldsymbol{\Upsilon}_k \mathbf{g}_k^H}{M} = \lim_{K \rightarrow \infty} \frac{1}{M} \sum_{m=1}^M Q_{k,m,m} |\tilde{g}_{k,m}|^2. \quad (4.41)$$

The $|\tilde{g}_{k,m}|^2$ terms are i.i.d. exponentials with unit mean. Hence, the average in (4.41) is the average of M non-identical, but independent, random variables. From [230], this average converges to the mean as long as the variance vanishes. Hence the limit of $\frac{\mathbf{g}_k \boldsymbol{\Upsilon}_k \mathbf{g}_k^H}{M}$ is the same as the limit of $\mathbb{E} \left[\frac{\mathbf{g}_k \boldsymbol{\Upsilon}_k \mathbf{g}_k^H}{M} \right]$ and is given by \overline{P}_k . This is useful later in Proposition 4.3.

Theorem 4.1. For $k \in 1, \dots, K$,

$$\lim_{K \rightarrow \infty} \mathbb{E} \left[\frac{\widehat{\mathbf{h}}_k \widehat{\mathbf{h}}_k^H}{M} \right] = \overline{P}_k. \quad (4.42)$$

Proof. Since $\widehat{\mathbf{h}}_k$ has the same statistics as \mathbf{h}_k , from Lemma 4.1, $\widehat{\mathbf{h}}_k$ can be written as $\widehat{\mathbf{h}}_k = \mathbf{g}_k \boldsymbol{\Upsilon}_k^{1/2}$, where the elements of \mathbf{g}_k are i.i.d. $\mathcal{CN}(0, 1)$. Hence, $\mathbb{E} \left[\frac{\widehat{\mathbf{h}}_k \widehat{\mathbf{h}}_k^H}{M} \right] = \frac{1}{M} \mathbb{E} \left[\mathbf{g}_k \boldsymbol{\Upsilon}_k^{1/2} \boldsymbol{\Upsilon}_k^{1/2} \mathbf{g}_k^H \right] = \frac{1}{M} \mathbb{E} \left[\mathbf{g}_k \boldsymbol{\Upsilon}_k \mathbf{g}_k^H \right]$. Then, using Lemma 4.3, the desired result is obtained. ■

Theorem 4.2. For $k \in 1, \dots, K$,

$$\lim_{K \rightarrow \infty} \mathbb{E} \left[\frac{\widehat{\mathbf{h}}_k \boldsymbol{\Upsilon}_k \widehat{\mathbf{h}}_k^H}{M} \right] = \overline{P}_k^2 \overline{\Lambda^2}, \quad (4.43)$$

where $\overline{P}_k^2 = \frac{1}{N} \sum_{n=1}^N P_{k,n}^2$ and $\overline{\Lambda^2}$ is the limiting value of $\frac{N}{M} \sum_{m=1}^{M/N} \Lambda_{m,m}^2$, where $\Lambda_{m,m}$ denotes the m th diagonal entry of $\boldsymbol{\Lambda}$.

Proof. Since $\widehat{\mathbf{h}}_k$ has the same statistics as \mathbf{h}_k , from Lemma 4.1, $\widehat{\mathbf{h}}_k = \mathbf{g}_k \boldsymbol{\Upsilon}_k^{1/2}$, where the elements of \mathbf{g}_k are i.i.d. $\mathcal{CN}(0, 1)$. Hence,

$$\lim_{K \rightarrow \infty} \mathbb{E} \left[\frac{\widehat{\mathbf{h}}_k \boldsymbol{\Upsilon}_k \widehat{\mathbf{h}}_k^H}{M} \right] = \lim_{K \rightarrow \infty} \frac{1}{M} \mathbb{E} \left[\mathbf{g}_k \boldsymbol{\Upsilon}_k^{1/2} \boldsymbol{\Upsilon}_k \boldsymbol{\Upsilon}_k^{1/2} \mathbf{g}_k^H \right] \quad (4.44)$$

$$= \lim_{K \rightarrow \infty} \frac{1}{M} \mathbb{E} \left[\mathbf{g}_k \boldsymbol{\Upsilon}_k^2 \mathbf{g}_k^H \right] \quad (4.45)$$

$$= \lim_{K \rightarrow \infty} \frac{1}{M} \mathbb{E} \left[\mathbf{g}_k \boldsymbol{\psi} \mathbf{Q}_k^2 \boldsymbol{\psi}^H \mathbf{g}_k^H \right] \quad (4.46)$$

$$= \lim_{K \rightarrow \infty} \frac{1}{M} \mathbb{E} \left[\tilde{\mathbf{g}}_k \mathbf{Q}_k^2 \tilde{\mathbf{g}}_k^H \right] \quad (4.47)$$

$$= \lim_{K \rightarrow \infty} \frac{1}{M} \sum_{m=1}^M \mathbb{E} \left[Q_{k,m,m}^2 |\tilde{g}_{k,m}|^2 \right] \quad (4.48)$$

$$= \lim_{K \rightarrow \infty} \frac{1}{M} \text{tr} \left(\mathbf{Q}_k^2 \right) \quad (4.49)$$

$$= \lim_{K \rightarrow \infty} \frac{1}{M} \sum_{n=1}^N P_{k,n}^2 \text{tr}(\Lambda^2) \quad (4.50)$$

$$= \lim_{K \rightarrow \infty} \left(\frac{1}{N} \sum_{n=1}^N P_{k,n}^2 \right) \lim_{K \rightarrow \infty} \left(\frac{N}{M} \sum_{m=1}^{M/N} \Lambda_{m,m}^2 \right) \quad (4.51)$$

$$= \overline{P_k^2} \overline{\Lambda^2}. \quad (4.52)$$

■

Theorem 4.3. *Let the MF precoder normalization constant τ be defined as in (4.4), then*

$$\lim_{K \rightarrow \infty} \mathbb{E} \left[\frac{\tau}{M} \right] = \overline{P}, \quad (4.53)$$

where \overline{P} is the limiting average of the $P_{k,n}$ values over k and n .

Proof.

$$\lim_{K \rightarrow \infty} \mathbb{E} \left[\frac{\tau}{M} \right] = \lim_{K \rightarrow \infty} \frac{1}{M} \mathbb{E} \left[\frac{\text{tr}(\widehat{\mathbf{H}}\widehat{\mathbf{H}}^H)}{K} \right] \quad (4.54)$$

$$= \lim_{K \rightarrow \infty} \frac{1}{K} \sum_{k=1}^K \mathbb{E} \left[\frac{1}{M} \widehat{\mathbf{h}}_k \widehat{\mathbf{h}}_k^H \right] \quad (4.55)$$

$$= \lim_{K \rightarrow \infty} \frac{1}{K} \sum_{k=1}^K \mathbb{E} \left[\frac{1}{M} \widehat{\mathbf{g}}_k \boldsymbol{\Upsilon}_k \widehat{\mathbf{g}}_k^H \right] \quad (4.56)$$

$$= \lim_{K \rightarrow \infty} \frac{1}{KN} \sum_{k=1}^K \sum_{n=1}^N P_{k,n} \quad (4.57)$$

$$= \overline{P}, \quad (4.58)$$

where (4.57) is obtained from (4.34)-(4.39). ■

Proposition 4.3. *The limiting signal power of the k th user, from the numerator of (4.28), as $K \rightarrow \infty$ is given by*

$$\frac{\varrho\nu}{\lim_{K \rightarrow \infty} \mathbb{E} \left[\frac{\tau}{M} \right]} \left(\xi^2 \lim_{K \rightarrow \infty} \mathbb{E} \left[\left| \frac{\widehat{\mathbf{h}}_k \widehat{\mathbf{h}}_k^H}{M} \right|^2 \right] + \frac{1 - \xi^2}{M} \lim_{K \rightarrow \infty} \mathbb{E} \left[\frac{\widehat{\mathbf{h}}_k \boldsymbol{\Upsilon}_k \widehat{\mathbf{h}}_k^H}{M} \right] \right) = \frac{\varrho\nu \xi^2 \overline{P_k}^2}{\overline{P}}. \quad (4.59)$$

Proof. Substituting the results from Theorems 4.1, 4.2 and 4.3 into the numerator of (4.28) gives

$$\frac{\varrho\nu}{\lim_{K \rightarrow \infty} \mathbb{E} \left[\frac{\tau}{M} \right]} \left(\xi^2 \lim_{K \rightarrow \infty} \mathbb{E} \left[\left| \frac{\widehat{\mathbf{h}}_k \widehat{\mathbf{h}}_k^H}{M} \right|^2 \right] + \frac{1 - \xi^2}{M} \lim_{K \rightarrow \infty} \mathbb{E} \left[\frac{\widehat{\mathbf{h}}_k \boldsymbol{\Upsilon}_k \widehat{\mathbf{h}}_k^H}{M} \right] \right)$$

$$= \lim_{K \rightarrow \infty} \frac{\varrho\nu}{\overline{P}} \left(\xi^2 \overline{P}_k^2 + \frac{(1-\xi^2)}{M} \overline{P}_k^2 \overline{\Lambda^2} \right) \quad (4.60)$$

$$= \frac{\varrho\nu \xi^2 \overline{P}_k^2}{\overline{P}}, \quad (4.61)$$

where (4.61) is obtained since the limit in (4.52) is finite and $\frac{1-\xi^2}{M} \rightarrow 0$ as $K \rightarrow \infty$. \blacksquare

Also, note that $\lim_{K \rightarrow \infty} \frac{\widehat{\mathbf{h}}_k \widehat{\mathbf{h}}_k^H}{M} = \overline{P}_k$, so that $\lim_{K \rightarrow \infty} \left| \frac{\widehat{\mathbf{h}}_k \widehat{\mathbf{h}}_k^H}{M} \right|^2 = \overline{P}_k^2$ which explains the first term in (4.60).

Theorem 4.4. For $k, k' \in 1, \dots, K$,

$$\lim_{K \rightarrow \infty} \sum_{\substack{k'=1 \\ k' \neq k}}^K \mathbb{E} \left[\left| \frac{\widehat{\mathbf{h}}_k \widehat{\mathbf{h}}_{k'}^H}{M} \right|^2 \right] = \frac{\overline{\Lambda^2} \overline{P_{k,k'}}}{\nu}, \quad (4.62)$$

where $\overline{P_{k,k'}}$ is the limiting average cross product of the k th user's link gains with all other users' link gains.

Proof. Using $\widehat{\mathbf{h}}_k = \mathbf{g}_k \mathbf{\Upsilon}_k^{1/2} \forall k$, $\mathbf{\Upsilon}_k = \boldsymbol{\psi} \mathbf{Q}_k \boldsymbol{\psi}^H \forall k$ and $\widetilde{\mathbf{g}}_k = \mathbf{g}_k \boldsymbol{\psi} \forall k$, for $k, k' \in 1, \dots, K$

$$\lim_{K \rightarrow \infty} \sum_{\substack{k'=1 \\ k' \neq k}}^K \mathbb{E} \left[\left| \frac{\widehat{\mathbf{h}}_k \widehat{\mathbf{h}}_{k'}^H}{M} \right|^2 \right] = \lim_{K \rightarrow \infty} \frac{1}{M^2} \sum_{\substack{k'=1 \\ k' \neq k}}^K \mathbb{E} \left[\left| \mathbf{g}_k \mathbf{\Upsilon}_k^{1/2} \mathbf{\Upsilon}_{k'}^{1/2} \mathbf{g}_{k'}^H \right|^2 \right] \quad (4.63)$$

$$= \lim_{K \rightarrow \infty} \frac{1}{M^2} \sum_{\substack{k'=1 \\ k' \neq k}}^K \mathbb{E} \left[\left| \widetilde{\mathbf{g}}_k \mathbf{Q}_k^{1/2} \mathbf{Q}_{k'}^{1/2} \widetilde{\mathbf{g}}_{k'}^H \right|^2 \right] \quad (4.64)$$

$$= \lim_{K \rightarrow \infty} \frac{1}{M^2} \sum_{\substack{k'=1 \\ k' \neq k}}^K \mathbb{E} \left[\widetilde{\mathbf{g}}_k \mathbf{Q}_k^{1/2} \mathbf{Q}_{k'}^{1/2} \widetilde{\mathbf{g}}_{k'}^H \widetilde{\mathbf{g}}_{k'} \mathbf{Q}_{k'}^{1/2} \mathbf{Q}_k^{1/2} \widetilde{\mathbf{g}}_k^H \right] \quad (4.65)$$

$$= \lim_{K \rightarrow \infty} \frac{1}{M^2} \sum_{\substack{k'=1 \\ k' \neq k}}^K \mathbb{E} \left[\widetilde{\mathbf{g}}_k \mathbf{Q}_k \mathbf{Q}_{k'} \widetilde{\mathbf{g}}_{k'}^H \right] \quad (4.66)$$

$$= \lim_{K \rightarrow \infty} \frac{1}{M^2} \sum_{\substack{k'=1 \\ k' \neq k}}^K \text{tr} (\mathbf{Q}_k \mathbf{Q}_{k'}) \quad (4.67)$$

$$= \lim_{K \rightarrow \infty} \frac{1}{M^2} \sum_{\substack{k'=1 \\ k' \neq k}}^K \sum_{n=1}^N P_{k,n} P_{k',n} \text{tr} (\Lambda^2) \quad (4.68)$$

$$= \lim_{K \rightarrow \infty} \frac{K-1}{\nu K} \frac{\text{tr} (\Lambda^2) N}{M} \sum_{\substack{k'=1 \\ k' \neq k}}^K \sum_{n=1}^N \frac{P_{k,n} P_{k',n}}{N(K-1)} \quad (4.69)$$

$$= \frac{\overline{\Lambda^2 P_{k,k'}}}{\nu}. \quad (4.70)$$

■

Theorem 4.5. For $k, k' \in 1, \dots, K$,

$$\lim_{K \rightarrow \infty} \sum_{\substack{k'=1 \\ k' \neq k}}^K \mathbb{E} \left[\frac{\widehat{\mathbf{h}}_{k'}' \mathbf{\Upsilon}_k \widehat{\mathbf{h}}_{k'}^H}{M^2} \right] = \frac{\overline{\Lambda^2 P_{k,k'}}}{\nu}. \quad (4.71)$$

Proof. Using $\widehat{\mathbf{h}}_k = \mathbf{g}_k \mathbf{\Upsilon}_k^{1/2} \forall k$, $\mathbf{\Upsilon}_k = \boldsymbol{\psi} \mathbf{Q}_k \boldsymbol{\psi}^H \forall k$ and $\widetilde{\mathbf{g}}_k = \mathbf{g}_k \boldsymbol{\psi} \forall k$, for $k, k' \in 1, \dots, K$

$$\lim_{K \rightarrow \infty} \sum_{\substack{k'=1 \\ k' \neq k}}^K \mathbb{E} \left[\frac{\widehat{\mathbf{h}}_{k'}' \mathbf{\Upsilon}_k \widehat{\mathbf{h}}_{k'}^H}{M^2} \right] = \lim_{K \rightarrow \infty} \frac{K-1}{\nu K} \sum_{\substack{k'=1 \\ k' \neq k}}^K \frac{\mathbb{E} [\widetilde{\mathbf{g}}_{k'}' \mathbf{Q}_k \mathbf{Q}_{k'}' \widetilde{\mathbf{g}}_{k'}^H]}{M(K-1)} \quad (4.72)$$

$$= \lim_{K \rightarrow \infty} \frac{K-1}{\nu K} \sum_{\substack{k'=1 \\ k' \neq k}}^K \frac{\text{tr}(\mathbf{Q}_k \mathbf{Q}_{k'})}{M(K-1)} \quad (4.73)$$

$$= \lim_{K \rightarrow \infty} \frac{K-1}{\nu K} \text{tr}(\Lambda^2) \sum_{\substack{k'=1 \\ k' \neq k}}^K \sum_{n=1}^N \frac{P_{k,n} P_{k',n}}{M(K-1)} \quad (4.74)$$

$$= \lim_{K \rightarrow \infty} \frac{K-1}{\nu K} \frac{\text{tr}(\Lambda^2) N}{M} \sum_{\substack{k'=1 \\ k' \neq k}}^K \sum_{n=1}^N \frac{P_{k,n} P_{k',n}}{N(K-1)} \quad (4.75)$$

$$= \frac{\overline{\Lambda^2 P_{k,k'}}}{\nu}. \quad (4.76)$$

■

Proposition 4.4. The limiting interference and noise power of the k th user, from the denominator of (4.28), as $K \rightarrow \infty$ is given by

$$\begin{aligned} & \frac{\varrho \nu}{\lim_{K \rightarrow \infty} \mathbb{E} \left[\frac{\tau}{M} \right]} \lim_{K \rightarrow \infty} \sum_{\substack{k'=1 \\ k' \neq k}}^K \left(\xi^2 \mathbb{E} \left[\left| \frac{\widehat{\mathbf{h}}_k \widehat{\mathbf{h}}_{k'}^H}{M} \right|^2 \right] + (1 - \xi^2) \mathbb{E} \left[\frac{\widehat{\mathbf{h}}_{k'}' \mathbf{\Upsilon}_k \widehat{\mathbf{h}}_{k'}^H}{M^2} \right] \right) + 1 \\ & = \frac{\varrho \overline{\Lambda^2 P_{k,k'}}}{\overline{P}} + 1. \end{aligned} \quad (4.77)$$

Proof. Substituting the results from Theorems 4.3, 4.4 and 4.5 into the denominator of (4.28) gives

$$\frac{\varrho \nu}{\lim_{K \rightarrow \infty} \mathbb{E} \left[\frac{\tau}{M} \right]} \lim_{K \rightarrow \infty} \sum_{\substack{k'=1 \\ k' \neq k}}^K \left(\xi^2 \mathbb{E} \left[\left| \frac{\widehat{\mathbf{h}}_k \widehat{\mathbf{h}}_{k'}^H}{M} \right|^2 \right] + (1 - \xi^2) \mathbb{E} \left[\frac{\widehat{\mathbf{h}}_{k'}' \mathbf{\Upsilon}_k \widehat{\mathbf{h}}_{k'}^H}{M^2} \right] \right) + 1$$

$$= \frac{\varrho\nu}{\bar{P}} \left(\xi^2 \frac{\overline{\Lambda^2 P_{k,k'}}}{\nu} + (1 - \xi^2) \frac{\overline{\Lambda^2 P_{k,k'}}}{\nu} \right) + 1 \quad (4.78)$$

$$= \frac{\overline{\varrho\Lambda^2 P_{k,k'}}}{\bar{P}} + 1. \quad (4.79)$$

■

Thus, combining (4.59) and (4.79), the limiting expected MF SINR for the k th user, in (4.22), is given by

$$\lim_{K \rightarrow \infty} \mathbb{E} [\text{SINR}_k^{\text{MF}}] = \frac{\frac{\varrho\nu\xi^2\overline{P_k^2}}{\bar{P}}}{\frac{\overline{\varrho\Lambda^2 P_{k,k'}}}{\bar{P}} + 1} = \frac{\varrho\nu\xi^2\overline{P_k^2}}{\overline{\varrho P_{k,k'}} \overline{\Lambda^2} + \bar{P}}. \quad (4.80)$$

From (4.80), the effects of each component on the per-user MF SINR limit can be examined.

- The average received SNR, ϱ , boosts the signal power but also the interference power leading to a ceiling on the per-user MF SINR limit, as $\lim_{K \rightarrow \infty} \mathbb{E} [\text{SINR}_k^{\text{MF}}] \rightarrow \frac{\nu\xi^2\overline{P_k^2}}{\overline{P_{k,k'}} \overline{\Lambda^2}}$ as $\varrho \rightarrow \infty$.
- The ratio, ν , increases the SINR due to increased diversity.
- The CSI factor, ξ , decreases the signal power but the extra interference created by imperfect CSI disappears in the limit due to averaging.
- $\overline{\Lambda^2}$ reduces the SINR and implies that spatial correlation reduces SINR. To see this, consider the extreme cases of an i.i.d. channel ($\mathbf{R}_{\text{TX}} = \Lambda = \Lambda^2 = \mathbf{I}_{M/N}$) and a fully spatially correlated channel, where $\mathbf{R}_{\text{TX}} = \mathbf{1}_{M/N}$, $\Lambda = \text{diag}(\frac{M}{N}, 0, \dots, 0)$ and $\Lambda^2 = \text{diag}((\frac{M}{N})^2, 0, \dots, 0)$. These scenarios give $\overline{\Lambda^2} = 1$ and $\overline{\Lambda^2} = \frac{M}{N}$, respectively. Clearly, the $\overline{\Lambda^2}$ term increases with spatial correlation and reduces the per-user MF SINR limit.
- \bar{P} reduces performance as it is a measure of the total power of the received signals which includes the aggregate interference.
- $\overline{P_{k,k'}}$ reduces performance as it is an inverse measure of orthogonality. If the desired user $k \in 1, \dots, K$ has strong links on the antennas in a set of antenna clusters $\mathcal{A} \subset \{1, 2, \dots, N\}$ and all the interferers have weak link gains in \mathcal{A} then the ‘‘cross product’’ term $\overline{P_{k,k'}}$ is weak. Here, the channels are close to orthogonal (on average) and performance is enhanced.

Finally, several special cases of (4.80) are considered.

Corollary 4.1. *For perfect CSI, $\xi = 1$, the limiting expected per-user MF SINR given by*

$$\lim_{K \rightarrow \infty} \mathbb{E} [\text{SINR}_k^{\text{MF}}] = \frac{\varrho \nu \overline{P}_k^{-2}}{\varrho \overline{P}_{k,k'} \overline{\Lambda^2 + \overline{P}}}. \quad (4.81)$$

Corollary 4.2. *For uncorrelated TX antenna arrays, $\mathbf{R}_{\text{TX}} = \mathbf{I}_{M/N}$, the limiting expected per-user MF SINR given by*

$$\lim_{K \rightarrow \infty} \mathbb{E} [\text{SINR}_k^{\text{MF}}] = \frac{\varrho \nu \xi^2 \overline{P}_k^{-2}}{\varrho \overline{P}_{k,k'} + \overline{P}}. \quad (4.82)$$

Corollary 4.3. *For equal link gains amongst users and antenna clusters, $P_{k,n} = P \forall k, n$, the limiting expected per-user MF SINR given by*

$$\lim_{K \rightarrow \infty} \mathbb{E} [\text{SINR}_k^{\text{MF}}] = \frac{\varrho \nu \xi^2 P}{\varrho P \overline{\Lambda^2 + 1}}. \quad (4.83)$$

Corollary 4.4. *For uncorrelated TX antenna arrays, $\mathbf{R}_{\text{TX}} = \mathbf{I}_{M/N}$, and equal link gains amongst users and antenna clusters, $P_{k,n} = P \forall k, n$, the limiting expected per-user MF SINR given by*

$$\lim_{K \rightarrow \infty} \mathbb{E} [\text{SINR}_k^{\text{MF}}] = \frac{\varrho \nu \xi^2 P}{\varrho P + 1}. \quad (4.84)$$

Corollary 4.5. *For perfect CSI, $\xi = 1$, uncorrelated TX antenna arrays, $\mathbf{R}_{\text{TX}} = \mathbf{I}_{M/N}$, and equal link gains amongst users and antenna clusters, $P_{k,n} = P \forall k, n$, the limiting expected per-user MF SINR given by*

$$\lim_{K \rightarrow \infty} \mathbb{E} [\text{SINR}_k^{\text{MF}}] = \frac{\varrho \nu P}{\varrho P + 1}. \quad (4.85)$$

Note that (4.85) agrees with the result derived in (3.52), when $P = 1$, and (4.84) agrees with results in [7], when $P = 1$.

In (4.80), a limiting expected per-user value is presented which can be evaluated for a particular link gain model. Link gain scenarios are now proposed, extending the co-located link gain model presented in Section 3.3.1, to evaluate the (distributed) limiting results. As an example, the limiting per-user MF SINR, in (4.80), is analytically evaluated for the scenario of a single antenna cluster ($N = 1$).

Link Gain Model

As discussed in Section 3.3.1 for the co-located antenna system, the classic link gain model (given in (2.3)), will obscure the limiting effects since the log-normal

random variable does not easily converge. Thus, the link gains between each antenna cluster and each user are assumed to be drawn from a limiting link gain profile defined by $P(x)$ for $0 \leq x \leq 1$. For any finite number of users, K , the link gains are defined by $P((2k-1)/2K)$ for $k = 1, \dots, K$. See Figure 4.4 for illustration.

Since it is awkward to construct reasonable scenarios for more than two antenna clusters, due to the proliferation of potential profiles, convergence of instantaneous to limiting SINR results are shown for $N = 1$ and $N = 2$ cases. For the first antenna cluster (when $N = 2$) $P(x) = P_{\max} \left(\frac{P_{\min}}{P_{\max}} \right)^x$, where P_{\min} and P_{\max} are the minimum and maximum link gains, respectively. This simple model also appears in [47, 231] as a way of characterizing differing user link gains with a simple exponential profile and only two parameters. For simplicity, it is assumed that the second cluster has the same link gain profile as the first antenna cluster. However, it is unrealistic to assume that the same users have the same link gains at both antenna clusters. Hence, three scenarios for the second antenna cluster are considered:

1. The second antenna cluster link gains are identical to that of the link gains at the first antenna cluster.
2. The second antenna cluster link gains are the reversed link gains from the first antenna cluster. This scenario is motivated by the likelihood that a user with a strong link gain from the first antenna cluster will have a weak gain from the second antenna cluster.
3. The second antenna cluster link gains are strongest when the users are receiving moderate strength link gains from the first antenna cluster. While the second antenna cluster link gains are weakest when the users are receiving either strong or weak strength link gains from the first antenna cluster. This is an intermediate scenario, between link gain scenarios 1 and 2.

An example of the three link gain scenarios for the second antenna cluster are shown in Figure 4.4.

This approach gives a limiting link gain profile as $K \rightarrow \infty$ and allows us to investigate convergence. However, it is tightly constrained by the choice of $P(x)$ and the link gain scenarios listed above.

Limiting Expected Per-user MF SINR Analytical Example: Co-located Antenna System

As an analytical example, the limiting expected per-user MF SINR is considered using the link gain model proposed in Section 4.4.1 for $N = 1$, i.e., $P(x) =$

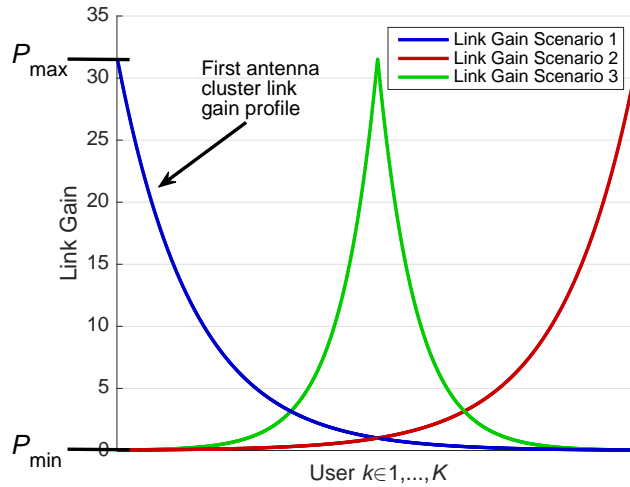


Figure 4.4: Link gain scenarios of the second antenna cluster when $N = 2$.

$P_{\max} \left(\frac{P_{\min}}{P_{\max}} \right)^x$. Thus, evaluating the three link gain terms in (4.80),

$$\bar{P}_k = \frac{1}{N} \sum_{n=1}^N P_{k,n} = P_{k,1}, \quad (4.86)$$

and

$$\bar{P} = \lim_{K \rightarrow \infty} \frac{1}{NK} \sum_{n=1}^N \sum_{k=1}^K P_{k,n} \quad (4.87)$$

$$= \lim_{K \rightarrow \infty} \frac{1}{K} \sum_{k=1}^K P_{k,1} \quad (4.88)$$

$$= \int_0^1 P(x) dx \quad (4.89)$$

$$= P_{\max} \int_0^1 \left(\frac{P_{\min}}{P_{\max}} \right)^x dx \quad (4.90)$$

$$= P_{\max} \int_0^1 \exp \left(x \ln \left(\frac{P_{\min}}{P_{\max}} \right) \right) dx \quad (4.91)$$

$$= \frac{P_{\max}}{\ln \left(\frac{P_{\min}}{P_{\max}} \right)} \left(\exp \left(\ln \left(\frac{P_{\min}}{P_{\max}} \right) \right) - 1 \right) \quad (4.92)$$

$$= \frac{P_{\max} \left(\frac{P_{\min}}{P_{\max}} - 1 \right)}{\ln \left(\frac{P_{\min}}{P_{\max}} \right)} \quad (4.93)$$

$$= \frac{P_{\max} - P_{\min}}{\ln(P_{\max}) - \ln(P_{\min})}. \quad (4.94)$$

Also,

$$\overline{P_{k,k'}} = \lim_{K \rightarrow \infty} \frac{1}{NK} \sum_{n=1}^N \sum_{\substack{k'=1 \\ k' \neq k}}^K P_{k,n} P_{k',n} \quad (4.95)$$

$$= \lim_{K \rightarrow \infty} \frac{1}{K} \sum_{\substack{k'=1 \\ k' \neq k}}^K P_{k,1} P_{k',1} \quad (4.96)$$

$$= P_{k,1} \overline{P} \quad (4.97)$$

$$= P_{k,1} \frac{P_{\max} - P_{\min}}{\ln(P_{\max}) - \ln(P_{\min})}. \quad (4.98)$$

Evaluating the mean of the limiting MF SINR across all users,

$$\lim_{K \rightarrow \infty} \left(\frac{1}{K} \sum_{k=1}^K \mathbb{E} [\text{SINR}_k^{\text{MF}}] \right) = \lim_{K \rightarrow \infty} \left(\frac{1}{K} \sum_{k=1}^K \frac{\varrho \nu \xi^2 \overline{P}_k^2}{\varrho \overline{P}_{k,k'} \overline{\Lambda}^2 + \overline{P}} \right) \quad (4.99)$$

$$= \frac{\varrho \nu \xi^2}{\left(\frac{P_{\max} - P_{\min}}{\ln(P_{\max}) - \ln(P_{\min})} \right)} \lim_{K \rightarrow \infty} \left(\frac{1}{K} \sum_{k=1}^K \frac{P_{k,1}^2}{\varrho P_{k,1} \overline{\Lambda}^2 + 1} \right) \quad (4.100)$$

$$= \frac{P_{\max}^2 \varrho \nu \xi^2}{\left(\frac{P_{\max} - P_{\min}}{\ln(P_{\max}) - \ln(P_{\min})} \right)} \int_0^1 \frac{\left(\frac{P_{\min}}{P_{\max}} \right)^{2x}}{\varrho P_{\max} \left(\frac{P_{\min}}{P_{\max}} \right)^x \overline{\Lambda}^2 + 1} dx. \quad (4.101)$$

Letting $u = \left(\frac{P_{\min}}{P_{\max}} \right)^x \rightarrow \ln(u) = x \ln \left(\frac{P_{\min}}{P_{\max}} \right) \rightarrow x = \frac{\ln(u)}{\ln \left(\frac{P_{\min}}{P_{\max}} \right)} \rightarrow \frac{dx}{du} = \frac{1}{u \ln \left(\frac{P_{\min}}{P_{\max}} \right)}$,

$$\begin{aligned} & \lim_{K \rightarrow \infty} \left(\frac{1}{K} \sum_{k=1}^K \mathbb{E} [\text{SINR}_k^{\text{MF}}] \right) \\ &= \frac{P_{\max}^2 \varrho \nu \xi^2}{\left(\frac{P_{\max} - P_{\min}}{\ln(P_{\max}) - \ln(P_{\min})} \right)} \int_1^{\frac{P_{\min}}{P_{\max}}} \frac{u^2}{\varrho P_{\max} \overline{\Lambda}^2 u + 1} \frac{1}{u \ln \left(\frac{P_{\min}}{P_{\max}} \right)} du \end{aligned} \quad (4.102)$$

$$= \frac{P_{\max}^2 \varrho \nu \xi^2}{\left(\frac{P_{\max} - P_{\min}}{\ln(P_{\max}) - \ln(P_{\min})} \right) \ln \left(\frac{P_{\min}}{P_{\max}} \right)} \int_1^{\frac{P_{\min}}{P_{\max}}} \frac{u}{\varrho P_{\max} \overline{\Lambda}^2 u + 1} du \quad (4.103)$$

$$= \frac{P_{\max}^2 \varrho \nu \xi^2}{P_{\min} - P_{\max}} \int_1^{\frac{P_{\min}}{P_{\max}}} \frac{u + \frac{1}{\varrho P_{\max} \overline{\Lambda}^2} - \frac{1}{\varrho P_{\max} \overline{\Lambda}^2}}{\varrho P_{\max} \overline{\Lambda}^2 u + 1} du \quad (4.104)$$

$$= \frac{P_{\max}^2 \varrho \nu \xi^2}{P_{\min} - P_{\max}} \int_1^{\frac{P_{\min}}{P_{\max}}} \left(\frac{1}{\varrho P_{\max} \overline{\Lambda}^2} - \frac{1}{\varrho P_{\max} \overline{\Lambda}^2 u + 1} \right) du \quad (4.105)$$

$$= \frac{P_{\max}^2 \varrho \nu \xi^2}{P_{\min} - P_{\max}} \left(\left[\frac{u}{\varrho P_{\max} \overline{\Lambda}^2} \right]_{u=1}^{\frac{P_{\min}}{P_{\max}}} - \left[\frac{\ln \left(\varrho P_{\max} \overline{\Lambda}^2 u + 1 \right)}{\left(\varrho P_{\max} \overline{\Lambda}^2 \right)^2} \right]_{u=1}^{\frac{P_{\min}}{P_{\max}}} \right) \quad (4.106)$$

$$= \frac{P_{\max}^2 \varrho \nu \xi^2}{P_{\min} - P_{\max}} \left(\frac{\frac{P_{\min}}{P_{\max}} - 1}{\varrho P_{\max} \overline{\Lambda}^2} - \frac{\ln(\varrho P_{\min} \overline{\Lambda}^2 + 1) - \ln(\varrho P_{\max} \overline{\Lambda}^2 + 1)}{(\varrho P_{\max} \overline{\Lambda}^2)^2} \right). \quad (4.107)$$

Hence, for any limiting link gain model, the exact limit in (4.80) can be evaluated.

4.4.2 Limiting MF SINR Numerical Results

In this subsection, the rate of convergence of instantaneous per-user MF SINR to its corresponding expected limiting value is shown. Due to the constraints on the choice of link gains, convergence is shown only for scenarios of $N = 1$ and $N = 2$, as discussed in Section 4.4.1. For both values of N , P_{\max} and P_{\min} are chosen to be 15 and -15 dB, respectively, as these two values are approximately equal to the respective peak and cell edge received SNRs, as shown in Figure 4.1, for a -5 dB median received SNR.

In Figure 4.5 the average instantaneous and limiting expected per-user MF SINR is shown for a single antenna cluster. It can be seen that CSI imperfections, ξ , decrease both average instantaneous and average limiting expected per-user MF SINR, as was shown in Section 4.3.2 for instantaneous CDF performance. This is due to the linear relationship between CSI imperfections and limiting expected per-user MF SINR, seen in (4.80). Also, as the number of single-antenna users increases, the average instantaneous per-user MF SINR approaches its corresponding average limiting expected value but is still yet to *fully* converge for $K = 50$ (and $M = 500$ transmit antenna elements). This was also seen in Figure 3.7b, from Chapter 3, in the co-located antenna system case. The corresponding uncorrelated, perfect CSI case, with $N = 1$, is shown in Figure 4.5a. Both figures show the average instantaneous per-user MF SINR within 0.5 dB of the corresponding expected limiting value for $K = 50$, with different limiting values resulting from the different limiting link gain models considered in each chapter. Furthermore, spatial correlation is seen to reduce each limiting expected MF SINR value by approximately 9 dB, independent of the CSI accuracy, ξ . This is verified by observing the expected limiting per-user MF SINR, in (4.80), where for any presence of spatial correlation, $\overline{\Lambda}^2 > 1$, the denominator reduces.

In Figure 4.6 the average instantaneous and average limiting expected per-user MF SINR is shown for $N = 2$ antenna clusters. Comparing Figures 4.5 and 4.6, it is observed that the additional antenna cluster has almost no effect on both the rate of convergence and the uncorrelated limiting expected per-user MF SINR, with minor differences coming from the choice of link gain scenario. This is due to the fact that $\overline{P}_{k,k'}$ in (4.80) tends to be small compared to \overline{P} . This observation is different from the instantaneous MF SINR numerical results, shown in Section

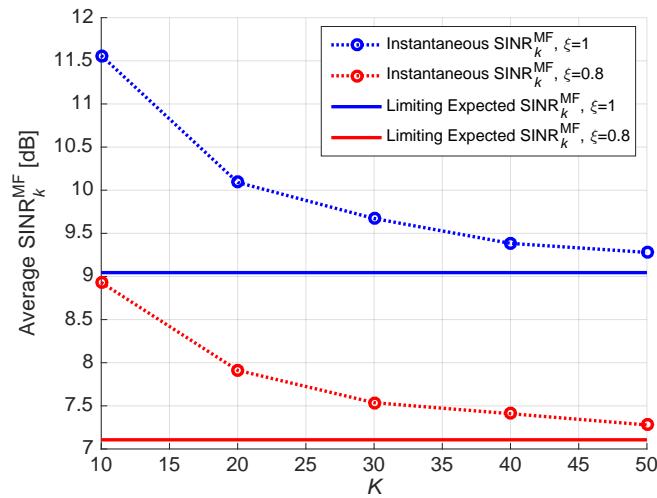
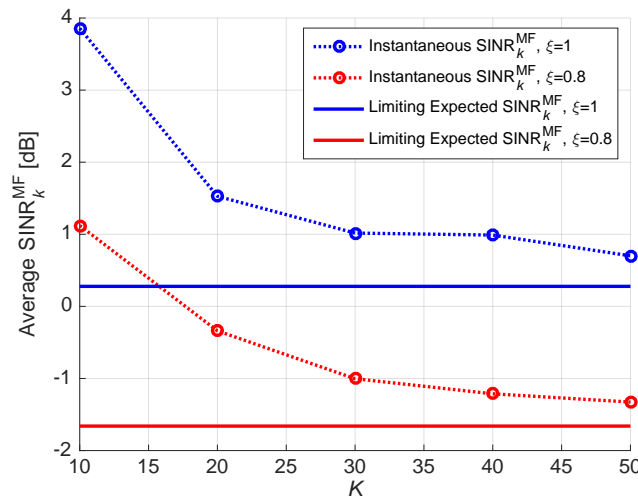
(a) Uncorrelated channel, $\mathbf{R}_{\text{TX}} = \mathbf{I}_M$.(b) Spatially correlated channel with $\rho = 0.9$.

Figure 4.5: Average instantaneous and average limiting expected per-user MF SINR for $N = 1$ antenna cluster, as a function of the number of single-antenna users, K , and CSI accuracy parameter, ξ , with $\nu = 10$.

4.3.2, since the link gains are restricted to follow the limiting model, rather than being distance, and therefore antenna cluster location, dependent. Also, for all three link gain scenarios considered for the second antenna cluster, in Figure 4.6, there are small differences in the MF SINR performance at smaller system sizes and have nearly an identical MF SINR performance for large systems. This is consistent with the fact that for large numbers of antennas, the aggregate interference is a dominant factor for MF precoding. In spatially correlated scenarios, the limiting expected per-user MF SINR is larger for $N = 2$ since, assuming fixed array form factors, ρ is reduced from 0.9 to 0.81.

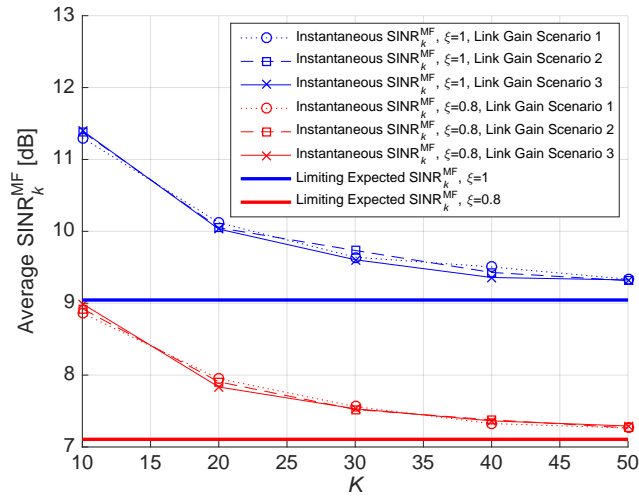
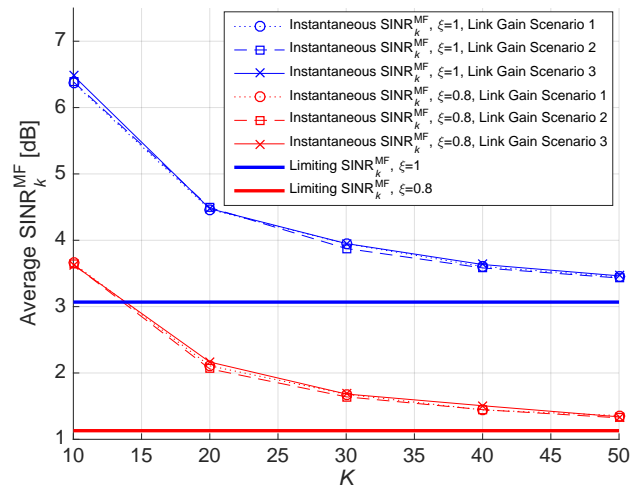
(a) Uncorrelated channel, $\mathbf{R}_{\text{TX}} = \mathbf{I}_{M/2}$.(b) Spatially correlated channel with $\rho = 0.9^2 = 0.81$.

Figure 4.6: Average instantaneous and average limiting expected per-user MF SINR for $N = 2$ antenna clusters, as a function of the number of single-antenna users, K , CSI accuracy parameter, ξ , and link gain scenario, with $\nu = 10$.

4.5 Conclusion

In this chapter, a per-user instantaneous MF SINR expression is derived based on a system model which accounts for unequal link gains, imperfect CSI, transmit spatial correlation and an arbitrary number of antenna clusters. Numerically, it is shown that distributing antennas into multiple clusters benefits the per-user received SNR since users are more likely to be receiving a strong signal from an antenna cluster and, as a result, the average per-user instantaneous MF SINR is increased. In spatially correlated scenarios, distributing antenna

elements increases the MF SINR performance further, relative to the co-located antenna system case, since inter-element antenna spacings increase and the spatial correlation effects are reduced.

Limiting expected per-user MF SINR is then derived as the number of antenna elements approaches infinity, whilst maintaining a fixed ratio of the number of transmit antennas to single-antenna users. The convergence of the per-user instantaneous MF SINR to the limiting expected per-user MF SINR is then shown for scenarios of one and two antenna clusters. Results show that the rate of convergence is not affected by spatial correlation or CSI imperfections, but the convergence of limiting link gain parameters, which is influenced by the link gain model considered. CSI imperfections cause a considerable decrease in all instantaneous and limiting MF SINR results.

5

Spatial Correlation for Millimeter-Wave Systems

Chapters 3 and 4 considered Rayleigh and Rician fading channel models. In this chapter a Saleh-Valenzuela channel model is considered to model a large antenna array operating at mmWave frequencies. Based on the Saleh-Valenzuela channel model, closed-form expressions for the 3D spatial correlation between any two antenna elements are derived for wide, narrow and Von Mises power elevation spectra (PES) as well as an upper bound for arbitrary PES. We show the effects of the PES on the convergence to massive MIMO properties by defining and deriving a diagonal dominance metric. Numerically, the effects of mutually coupled antennas are shown on the effective spatial correlation, eigenvalue structure and user rate for different antenna topologies. We conclude that although mutual coupling can significantly reduce spatial correlation for side-by-side dipole antennas, the change in antenna effective gain, and therefore SNR, from mutual coupling becomes a dominating effect and ultimately determines the antenna array performance of a mmWave system.

5.1 Introduction

To provide insights into the practical design of antenna arrays for mmWave systems, closed-form expressions characterizing the 3D spatial correlation of a Saleh-Valenzuela channel model [173] are derived. The Saleh-Valenzuela channel model is appropriate for, and commonly used to model, sparse channels [114, 117–119, 133, 174, 175, 232], such as mmWave channels, since the received signal can be decomposed into a number of independent spatial clus-

ters of rays. Furthermore, the analysis is valid for the standardized microwave NLOS channel model developed by the 3GPP [129]. This allows us to analyse the differences in the channel and system performance when different array topologies, such as ULAs, URAs and UCAs, are employed. In particular, metrics conventionally employed for the analysis of systems with a large number of co-located antennas are considered, such as diagonal dominance, which is analytically characterized, and user rate. Additionally, the system eigenvalue properties are explored for a variety of antenna structures with the aim of determining their influence on the array spatial multiplexing gain [233]. Overall, the results derived in this chapter allow us to characterize the impact of employing different array topologies in mmWave systems.

The contributions of this chapter are summarized:

1. Closed-form expressions for the 3D spatial correlation between any two antenna elements of a Saleh-Valenzuela channel model are derived for wide, narrow and Von Mises [144,145] PES as well as an upper bound for the general PES case.
2. The metric diagonal dominance is defined to measure the convergence of a user's channel to favourable propagation [43]¹. Closed-form expressions are then derived for wide, narrow and Von Mises PES, as well as an upper bound. The PES and antenna topology impacts on the rate of convergence to massive MIMO properties are then shown.
3. Numerically, the effects of mutual coupling are examined on different antenna array topologies, by analysing the resultant spatial correlation against inter-element spacing, eigenvalue properties and user rates of a mmWave system. It is demonstrated that while mutual coupling reduces spatial correlation for a wide range of inter-element distances and antenna configurations, the variation in SNR becomes the dominant effect and can either increase or decrease user rates depending on inter-element spacing.

5.2 System Model

A single-cell DL system with an M antenna element BS and users with Q antennas is considered. The $Q \times M$ DL Saleh-Valenzuela channel matrix for an arbitrary user is given (2.14), and described in Section 2.1.2.

¹Diagonal dominance has previously been defined for a single-antenna users UL channel in Chapter 3. In this chapter, diagonal dominance is defined for a DL channel where the user can have an arbitrary number of receive antenna elements.

5.2.1 Angular Power Spectra

It is common to define the angular variation in clustered channels via a power azimuth spectra (PAS) and PES for the central cluster angles and another, different, PAS/PES for the subpaths within a cluster. In this work, it is more convenient to define the global PAS and PES of all subpaths as $p_{\Phi}(\phi) = f_{\Phi}(\phi)$ and $p_{\Theta}(\theta) = \frac{f_{\Theta}(\theta)}{\sin(\theta)}$, respectively. Here, $f_{\Phi}(\phi)$ and $f_{\Theta}(\theta)$ denote the PDFs of the azimuth and elevation angles of an arbitrary subpath. We assume that the TX is omnidirectional with respect to the azimuth domain, as in mmWave measurement campaigns [114, 117–119, 150, 234, 235]. Because the azimuth central cluster angle-of-departures (AODs) are $\mathcal{U}[0, 2\pi)$, it also follows that $p_{\Phi}(\phi_{c,l}^{\text{AOD}}) \sim \mathcal{U}[0, 2\pi) \forall c, l$ since the addition of a random offset to a $\mathcal{U}[0, 2\pi)$ remains uniform over $[0, 2\pi)$ variable. Similarly, we assume the central cluster AOAs are $\mathcal{U}[0, 2\pi)$ in azimuth and hence $p_{\Phi}(\phi_{c,l}^{\text{AOA}}) \sim \mathcal{U}[0, 2\pi) \forall c, l$. On the other hand, we cannot make such simple assumptions concerning the global AOD and AOA PES since they depend on a number of factors, such as user location and downtilt angle of the antenna array. Three different cases for the PES are therefore given, as well as an upper bound on the spatial correlation for any PES. The three different PES scenarios include two opposing cases: wide and narrow PES, as well as the commonly used Von Mises distributed PES [144, 145] with arbitrary location and concentration parameters. Here, the three PES cases and the spatial correlation upper bound are detailed:

1. *Wide PES*: The PES has a wide, uniform distribution, i.e., $p_{\Theta}(\theta_{c,l})$ is constant over $[0, \pi) \forall c, l$. This is the case for antennas which are isotropic at the TX and an isotropic channel at the RX. For example, an antenna array serving users in an urban canyon.
2. *Narrow PES*: The PES has a narrow, uniform distribution, i.e., $p_{\Theta}(\theta_{c,l})$ is constant over $\theta_0 - \Delta\theta_{c,l}$ and $\theta_0 + \Delta\theta_{c,l} \forall c, l$, where $\Delta\theta_{c,l}$ is a small elevation intra-cluster subpath offset of subpath l of cluster c with respect to the central cluster angle, θ_0 ². This is the case for directive antennas and channels of sparse elevation spectrum.
3. *Von Mises PES*: The PES is distributed according to the Von Mises distribution [144, 145], i.e., $p_{\Theta}(\theta_{c,l}) \sim \frac{\exp(\tilde{\kappa} \cos(\theta_{c,l} - \mu))}{2\pi I_0(\tilde{\kappa})}$, with mean μ and variance $1 - \frac{I_1(\tilde{\kappa})}{I_0(\tilde{\kappa})}$, where $\tilde{\kappa}$ is the concentration parameter and $I_0(\cdot)$ denotes the zeroth order modified Bessel function. The Von Mises is commonly used to model power spectra as it approximates the Gaussian well [236].
4. *Upper bound*: A spatial correlation upper bound, for any PES, which is

²For the narrow PES case, all clusters have the same elevation central cluster angle, θ_0 . However, the subpaths in each cluster are random.

valid as long as there is some non-zero distance between antennas on the x, y -plane, i.e., $dxy_{m,m'} > 0 \forall m, m'$ at the TX.

5.3 Spatial Correlation

In this section, closed-form expressions for the spatial correlation of the Saleh-Valenzuela channel given in (2.14) are derived for wide, narrow and Von Mises PES. A spatial correlation upper bound for an arbitrary PES is also given. The derived expressions can be used to model the spatial correlation at either the TX or RX. Without loss of generality, the notation, results and conclusions in this section are considered for spatial correlation at the TX, i.e., $\mathbf{R} = \mathbf{R}_{\text{TX}}$.

Lemma 5.1. *Suppose $dx_{m,m'} = dx_m - dx_{m'}$, $dy_{m,m'} = dy_m - dy_{m'}$, $dz_{m,m'} = dz_m - dz_{m'}$ and $dxy_{m,m'} = \sqrt{dx_{m,m'}^2 + dy_{m,m'}^2}$ denotes the distances in wavelengths between antenna element $m, m' \in 1, \dots, M$ relative to the x -axis, y -axis, z -axis, and x, y -plane, respectively, then the spatial correlation between TX antenna elements m and m' , with $p_{\Phi}(\phi_{c,l}^{\text{AOD}}) \sim \mathcal{U}[0, 2\pi) \forall c, l$ and a general $p_{\Theta}(\theta_{c,l}^{\text{AOD}})$, is given as*

$$R_{m,m'} = \frac{1}{CL} \sum_{c=1}^C \sum_{l=1}^L \int_{\theta_{c,l}^{\text{AOD}}} \exp(j2\pi dz_{m,m'} \cos(\theta_{c,l}^{\text{AOD}})) \times J_0(2\pi dxy_{m,m'} \sin(\theta_{c,l}^{\text{AOD}})) p_{\Theta}(\theta_{c,l}^{\text{AOD}}) \sin(\theta_{c,l}^{\text{AOD}}) d\theta_{c,l}^{\text{AOD}}. \quad (5.1)$$

Proof. Let \mathbf{h}_m be the m th column of \mathbf{H} , then using the definition in (2.48),

$$R_{m,m'} = \frac{\text{cov}[\mathbf{h}_m, \mathbf{h}_{m'}]}{\sqrt{\text{var}[\mathbf{h}_m] \text{var}[\mathbf{h}_{m'}]}} = \frac{\mathbb{E}[(\mathbf{h}_m^H - \mathbb{E}[\mathbf{h}_m^H])(\mathbf{h}_{m'} - \mathbb{E}[\mathbf{h}_{m'}])]}{\sqrt{\mathbb{E}[\|\mathbf{h}_m^H - \mathbb{E}[\mathbf{h}_m^H]\|^2] \mathbb{E}[\|\mathbf{h}_{m'} - \mathbb{E}[\mathbf{h}_{m'}]\|^2]}} \quad (5.2)$$

$$= \frac{\mathbb{E}[\mathbf{h}_m^H \mathbf{h}_{m'}]}{\sqrt{\mathbb{E}[\|\mathbf{h}_m^H\|^2] \mathbb{E}[\|\mathbf{h}_{m'}\|^2]}}, \quad (5.3)$$

as all channels have zero mean, i.e., from (2.14), $\mathbb{E}[\mathbf{h}_m] = 0 \forall m$. Denoting $a_{\text{TX},m}(\phi_{c,l}^{\text{AOD}}, \theta_{c,l}^{\text{AOD}})$ as the m th entry of $\mathbf{a}_{\text{TX}}(\phi_{c,l}^{\text{AOD}}, \theta_{c,l}^{\text{AOD}})$, the denominator of (5.3) can be computed as

$$\mathbb{E}[\|\mathbf{h}_m^H\|^2] = \mathbb{E} \left[\left(\frac{1}{\sqrt{L}} \sum_{c=1}^C \sum_{l=1}^L h_{\text{iid},c,l} \mathbf{a}_{\text{RX}}(\phi_{c,l}^{\text{AOA}}, \theta_{c,l}^{\text{AOA}}) a_{\text{TX},m}^*(\phi_{c,l}^{\text{AOD}}, \theta_{c,l}^{\text{AOD}}) \right)^H \times \left(\frac{1}{\sqrt{L}} \sum_{c=1}^C \sum_{l=1}^L h_{\text{iid},c,l} \mathbf{a}_{\text{RX}}(\phi_{c,l}^{\text{AOA}}, \theta_{c,l}^{\text{AOA}}) a_{\text{TX},m}(\phi_{c,l}^{\text{AOD}}, \theta_{c,l}^{\text{AOD}}) \right) \right] \quad (5.4)$$

$$= \frac{1}{L} \sum_{c=1}^C \sum_{l=1}^L \mathbb{E} [|h_{\text{iid},c,l}|^2] \mathbb{E} [\| \mathbf{a}_{\text{RX}}^{\text{H}} (\phi_{c,l}^{\text{AOA}}, \theta_{c,l}^{\text{AOA}}) \|^2] \times \mathbb{E} [|a_{\text{TX},m} (\phi_{c,l}^{\text{AOD}}, \theta_{c,l}^{\text{AOD}})|^2] \quad (5.5)$$

$$= \frac{1}{L} \sum_{c=1}^C \sum_{l=1}^L \mathbb{E} [\gamma_c] \left(\sum_{q=1}^Q \mathbb{E} [|a_{\text{RX},q}^{\text{H}} (\phi_{c,l}^{\text{AOA}}, \theta_{c,l}^{\text{AOA}})|^2] \right) \times \mathbb{E} [|a_{\text{TX},m} (\phi_{c,l}^{\text{AOD}}, \theta_{c,l}^{\text{AOD}})|^2] \quad (5.6)$$

$$= Q = \mathbb{E} [\| \mathbf{h}_{m'} \|^2], \quad (5.7)$$

since $\mathbb{E} [\gamma_c] = 1/C$ and each entry of $\mathbf{a}_{\text{RX}} (\phi_{c,l}^{\text{AOA}}, \theta_{c,l}^{\text{AOA}})$ and $\mathbf{a}_{\text{TX}} (\phi_{c,l}^{\text{AOD}}, \theta_{c,l}^{\text{AOD}})$ has unit norm. Likewise, the numerator of (5.3) can be calculated as

$$\mathbb{E} [\mathbf{h}_m^{\text{H}} \mathbf{h}_{m'}] = \frac{1}{L} \sum_{c=1}^C \sum_{l=1}^L \mathbb{E} [\| \mathbf{a}_{\text{RX}} (\phi_{c,l}^{\text{AOA}}, \theta_{c,l}^{\text{AOA}})^{\text{H}} \|^2] \mathbb{E} [|h_{\text{iid},c,l}|^2] \times \mathbb{E} [a_{\text{TX},m} (\phi_{c,l}^{\text{AOD}}, \theta_{c,l}^{\text{AOD}}) a_{\text{TX},m'}^* (\phi_{c,l}^{\text{AOD}}, \theta_{c,l}^{\text{AOD}})] \quad (5.8)$$

$$= \frac{Q}{CL} \sum_{c=1}^C \sum_{l=1}^L \mathbb{E} [a_{\text{TX},m} (\phi_{c,l}^{\text{AOD}}, \theta_{c,l}^{\text{AOD}}) a_{\text{TX},m'}^* (\phi_{c,l}^{\text{AOD}}, \theta_{c,l}^{\text{AOD}})]. \quad (5.9)$$

Combining (5.7) and (5.9), the spatial correlation in (5.3) can be written as

$$R_{m,m'} = \frac{1}{CL} \sum_{c=1}^C \sum_{l=1}^L \mathbb{E} [a_{\text{TX},m} (\phi_{c,l}^{\text{AOD}}, \theta_{c,l}^{\text{AOD}}) a_{\text{TX},m'}^* (\phi_{c,l}^{\text{AOD}}, \theta_{c,l}^{\text{AOD}})] \quad (5.10)$$

$$= \frac{1}{CL} \sum_{c=1}^C \sum_{l=1}^L \int_{\theta_{c,l}^{\text{AOD}}} \int_{\phi_{c,l}^{\text{AOD}}} \exp \left(j \frac{2\pi}{\lambda} (\mathbf{W}_{\text{TX},m} - \mathbf{W}_{\text{TX},m'}) \mathbf{r}_{\text{TX}} (\phi_{c,l}^{\text{AOD}}, \theta_{c,l}^{\text{AOD}}) \right) \times f_{\Phi} (\phi_{c,l}^{\text{AOD}}) f_{\Theta} (\theta_{c,l}^{\text{AOD}}) d\phi_{c,l}^{\text{AOD}} d\theta_{c,l}^{\text{AOD}} \quad (5.11)$$

$$= \frac{1}{CL} \sum_{c=1}^C \sum_{l=1}^L \int_{\theta_{c,l}^{\text{AOD}}} \int_{\phi_{c,l}^{\text{AOD}}} \exp (j 2\pi [dx_{m,m'} \sin (\theta_{c,l}^{\text{AOD}}) \cos (\phi_{c,l}^{\text{AOD}}) + dy_{m,m'} \sin (\theta_{c,l}^{\text{AOD}}) \sin (\phi_{c,l}^{\text{AOD}}) + dz_{m,m'} \cos (\theta_{c,l}^{\text{AOD}})]) \times p_{\Phi} (\phi_{c,l}^{\text{AOD}}) p_{\Theta} (\theta_{c,l}^{\text{AOD}}) \sin (\theta_{c,l}^{\text{AOD}}) d\phi_{c,l}^{\text{AOD}} d\theta_{c,l}^{\text{AOD}} \quad (5.12)$$

$$= \frac{1}{CL} \sum_{c=1}^C \sum_{l=1}^L \int_{\theta_{c,l}^{\text{AOD}}} \exp (j 2\pi dz_{m,m'} \cos (\theta_{c,l}^{\text{AOD}})) \left(\int_{\phi_{c,l}^{\text{AOD}}} \exp (j 2\pi \sin (\theta_{c,l}^{\text{AOD}}) \times [dx_{m,m'} \cos (\phi_{c,l}^{\text{AOD}}) + dy_{m,m'} \sin (\phi_{c,l}^{\text{AOD}})]) p_{\Phi} (\phi_{c,l}^{\text{AOD}}) d\phi_{c,l}^{\text{AOD}} \right) \times p_{\Theta} (\theta_{c,l}^{\text{AOD}}) \sin (\theta_{c,l}^{\text{AOD}}) d\theta_{c,l}^{\text{AOD}}, \quad (5.13)$$

where $\mathbf{W}_{\text{TX},m}$ denotes the m th row of \mathbf{W}_{TX} . Evaluating the integral in (5.13) with respect to $\phi_{c,l}^{\text{AOD}}$,

$$\int_{\phi_{c,l}^{\text{AOD}}} \exp (j 2\pi \sin (\theta_{c,l}^{\text{AOD}}) [dx_{m,m'} \cos (\phi_{c,l}^{\text{AOD}}) + dy_{m,m'} \sin (\phi_{c,l}^{\text{AOD}})]) p (\phi_{c,l}^{\text{AOD}}) d\phi_{c,l}^{\text{AOD}}$$

$$= \frac{1}{2\pi} \int_0^{2\pi} \exp \left(j2\pi \sin(\theta_{c,l}^{\text{AOD}}) \sqrt{dx_{m,m'}^2 + dy_{m,m'}^2} \cos(\phi_{c,l}^{\text{AOD}} + \tilde{\phi}) \right) d\phi_{c,l}^{\text{AOD}} \quad (5.14)$$

$$= \frac{1}{2\pi} \int_0^{2\pi} \exp(j2\pi \sin(\theta_{c,l}^{\text{AOD}}) dxy_{m,m'} \cos(\phi_{c,l}^{\text{AOD}})) d\phi_{c,l}^{\text{AOD}} \quad (5.15)$$

$$= J_0(2\pi \sin(\theta_{c,l}^{\text{AOD}}) dxy_{m,m'}), \quad (5.16)$$

where the phase offset in (5.14), $\tilde{\phi} = \text{atan2}(dx_{m,m'}, dy_{m,m'}) + \frac{\pi}{2}$, has no effect because the integration is taken over a whole period, and the integral in (5.15) is evaluated in [237] pp. 491. Substituting (5.16) in (5.13) gives the desired result. ■

5.3.1 Wide AOD PES

In this subsection, the spatial correlation expression in (5.1) is evaluated for a wide AOD PES. Numerically, the effect of inter-element antenna spacing is then shown on the magnitude of the derived wide AOD PES spatial correlation expression.

Theorem 5.1. *Suppose $\text{sinc}(x) = \frac{\sin(\pi x)}{\pi x}$ denotes the normalized sinc function and $dxyz_{m,m'} = \sqrt{dxy_{m,m'}^2 + dz_{m,m'}^2}$ is the distance in wavelengths between antenna elements m and m' in 3D Cartesian coordinates, then for $p_{\Theta}(\theta_{c,l}^{\text{AOD}})$ constant over $[0, \pi) \forall c, l$, the spatial correlation between two TX antenna elements $m, m' \in 1, \dots, M$, is*

$$R_{m,m'} = \frac{1}{CL} \sum_{c=1}^C \sum_{l=1}^L \text{sinc}(2dxyz_{m,m'}) = \text{sinc}(2dxyz_{m,m'}), \quad (5.17)$$

Proof. For any two antenna elements $m, m' \in 1, \dots, M$,

$$R_{m,m'} = A \int_0^{\pi} \exp(j2\pi dz_{m,m'} \cos(\theta_{c,l}^{\text{AOD}})) J_0(2\pi dxy_{m,m'} \sin(\theta_{c,l}^{\text{AOD}})) \times p_{\Theta}(\theta_{c,l}^{\text{AOD}}) \sin(\theta_{c,l}^{\text{AOD}}) d\theta_{c,l}^{\text{AOD}}, \quad (5.18)$$

where A is the scaling constant to make sure the elevation PDF integrates to one. A is calculated as

$$1 = A \int_{\theta_{c,l}^{\text{AOD}}} p_{\Theta}(\theta_{c,l}^{\text{AOD}}) \sin(\theta_{c,l}^{\text{AOD}}) d\theta_{c,l}^{\text{AOD}} = A \int_0^{\pi} \sin(\theta_{c,l}^{\text{AOD}}) d\theta_{c,l}^{\text{AOD}} = 2A. \quad (5.19)$$

Therefore $A = \frac{1}{2}$. Substituting $u = -\cos(\theta_{c,l}^{\text{AOD}})$, from (5.18) we have

$$R_{m,m'} = \frac{1}{2} \int_{-1}^1 \exp(-j2\pi dz_{n,n'} u) J_0(2\pi dxy_{n,n'} \sqrt{1-u^2}) \frac{\sin(\theta_{c,l}^{\text{AOD}})}{\sin(\theta_{c,l}^{\text{AOD}})} du \quad (5.20)$$

$$= \frac{1}{2} \int_{-1}^1 \exp(-j2\pi dz_{n,n'}u) I_0(j2\pi dxy_{n,n'}\sqrt{1-u^2}) du \quad (5.21)$$

$$= \frac{\sinh\left(\sqrt{(j2\pi dz_{n,n'})^2 + (j2\pi dxy_{n,n'})^2}\right)}{\sqrt{(j2\pi dz_{n,n'})^2 + (j2\pi dxy_{n,n'})^2}} \quad (5.22)$$

$$= \frac{\sinh\left(j2\pi\sqrt{dz_{n,n'}^2 + dxy_{n,n'}^2}\right)}{j2\pi\sqrt{dz_{n,n'}^2 + dxy_{n,n'}^2}} \quad (5.23)$$

$$= \frac{-j \sin(-2\pi dxyz_{n,n'})}{j2\pi dxyz_{n,n'}} \quad (5.24)$$

$$= \text{sinc}(2dxyz_{n,n'}), \quad (5.25)$$

where the evaluated integral, in (5.21), is given in [237] pp. 698. ■

From (5.17), we observe that:

- Increasing the distance between any two TX antennas by the same amount in any direction decorrelates the two antennas equally (non-monotonically).
- The nulls of $|R_{m,m'}|$ (or zero crossings of $R_{m,m'}$) occur when $dxyz_{m,m'} = \frac{n}{2}$ for $n \in \mathbb{Z}^+$, i.e., an antenna array can experience zero spatial correlation if adjacent antennas are placed at a half wavelength apart. Although this can be achieved easily with a ULA, it cannot be achieved with the URA and UCA topologies, as antenna elements spacings are not always a multiple of a half-wavelength.

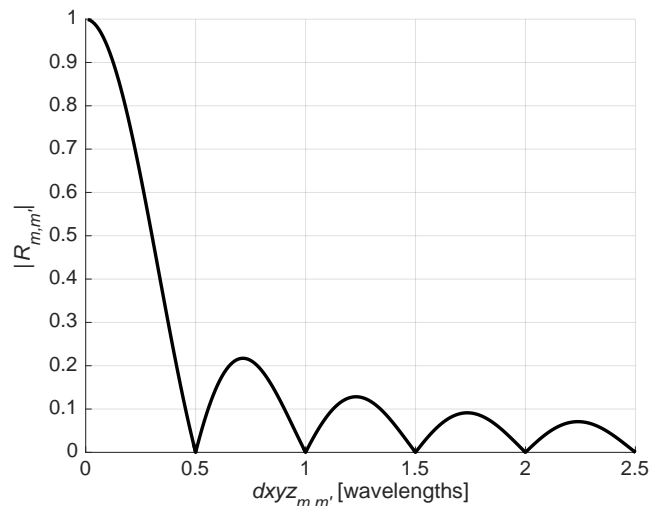


Figure 5.1: Wide AOD PES spatial correlation magnitude, $|R_{m,m'}|$, between two TX antennas, m and m' , as a function of 3D inter-element spacing, $dxyz_{m,m'}$.

In Figure 5.1 the wide AOD PES spatial correlation magnitude, $|R_{m,m'}|$, between two TX antennas, $m, m' \in 1, \dots, M$, is shown as a function of their 3D

inter-element spacing, $dxyz_{m,m'}$. It can be seen that the height of the spatial correlation peaks decays as $dxyz_{m,m'}$ increases.

5.3.2 Narrow AOD PES

In this subsection, the spatial correlation expression in (5.1) is evaluated for a narrow AOD PES. Numerically, the effect of inter-element antenna spacing is then shown on the magnitude of the derived narrow AOD PES spatial correlation expression.

Theorem 5.2. For $p_{\Theta}(\theta_{c,l}^{\text{AOD}})$ constant over $[\theta_0^{\text{AOD}} - \Delta\theta_{c,l}^{\text{AOD}}, \theta_0^{\text{AOD}} + \Delta\theta_{c,l}^{\text{AOD}}]$ $\forall c, l$, where $\Delta\theta_{c,l}^{\text{AOD}}$ is small, the spatial correlation between two TX antenna elements $m, m' \in 1, \dots, M$, can be approximated as

$$R_{m,m'} \approx \exp(j2\pi dz_{m,m'} \cos(\theta_0^{\text{AOD}})) J_0(2\pi dxy_{m,m'} \sin(\theta_0^{\text{AOD}})). \quad (5.26)$$

Proof. The integral in (5.1) can be approximated by its range multiplied by the central value. To ensure the elevation PDF integrates to 1,

$$\begin{aligned} 1 &= A \int_{\theta_{c,l}^{\text{AOD}}} p_{\Theta}(\theta_{c,l}^{\text{AOD}}) \sin(\theta_{c,l}^{\text{AOD}}) d\theta_{c,l}^{\text{AOD}} \\ &= A \int_{\theta_0^{\text{AOD}} - \Delta\theta_{c,l}^{\text{AOD}}}^{\theta_0^{\text{AOD}} + \Delta\theta_{c,l}^{\text{AOD}}} \sin(\theta_{c,l}^{\text{AOD}}) d\theta_{c,l}^{\text{AOD}} \approx 2A\Delta\theta_{c,l}^{\text{AOD}} \sin(\theta_0^{\text{AOD}}). \end{aligned} \quad (5.27)$$

Therefore $A \approx \frac{1}{(2\Delta\theta_{c,l}^{\text{AOD}} \sin(\theta_0^{\text{AOD}}))}$. From (5.1),

$$\begin{aligned} R_{m,m'} &\approx \frac{1}{CL} \sum_{c=1}^C \sum_{l=1}^L \frac{1}{2\Delta\theta_{c,l}^{\text{AOD}} \sin(\theta_0^{\text{AOD}})} \int_{\theta_0^{\text{AOD}} - \Delta\theta_{c,l}^{\text{AOD}}}^{\theta_0^{\text{AOD}} + \Delta\theta_{c,l}^{\text{AOD}}} \sin(\theta_{c,l}^{\text{AOD}}) \\ &\quad \times \exp(j2\pi dz_{m,m'} \cos(\theta_{c,l}^{\text{AOD}})) J_0(2\pi dxy_{m,m'} \sin(\theta_{c,l}^{\text{AOD}})) d\theta_{c,l}^{\text{AOD}} \end{aligned} \quad (5.28)$$

$$= \frac{1}{CL} \sum_{c=1}^C \sum_{l=1}^L \exp(j2\pi dz_{m,m'} \cos(\theta_0^{\text{AOD}})) J_0(2\pi dxy_{m,m'} \sin(\theta_0^{\text{AOD}})) \quad (5.29)$$

$$= \exp(j2\pi dz_{m,m'} \cos(\theta_0^{\text{AOD}})) J_0(2\pi dxy_{m,m'} \sin(\theta_0^{\text{AOD}})). \quad (5.30)$$

■

Here, insights into the narrow AOD PES spatial correlation (at the TX), given in (5.26), are drawn:

- The expression in (5.26) is independent of the intra-cluster elevation AOD offsets, $\Delta\theta_{c,l}^{\text{AOD}}$, and therefore the intra-cluster elevation AOD spreads, because the multiple rays of each cluster are approximated by the constant elevation central cluster AOD, θ_0^{AOD} . For the same reason, $R_{m,m'}$ is independent of the number of subpaths, L .

- $R_{m,m'}$ is independent of azimuth angles because the AOD PAS is uniform over its entire range.
- $R_{m,m'}$ decreases non-monotonically with $dxy_{m,m'}$, as increased x, y -plane spacing tends to reduce $|R_{m,m'}|$ since it affects the modulus of (5.26) via the Bessel function.
- For a fixed $dxy_{m,m'}$, the modulus, $J_0(2\pi dxy_{m,m'} \sin(\theta_0^{\text{AOD}}))$, is reduced when $\sin(\theta_0^{\text{AOD}})$ is maximized. This occurs when $\theta_0^{\text{AOD}} = \frac{\pi}{2}$, i.e., when the central AOD is broadside to the TX antenna array with respect to the z -axis. At this elevation AOD, the phase shift disappears and the resultant spatial correlation becomes $R_{m,m'} = J_0(2\pi dxy_{m,m'})$, i.e., only a function of the x, y -plane inter-element spacings.
- When the central AOD is end-fire to the TX antenna array with respect to the z -axis, the resultant spatial correlation becomes $R_{m,m'} = \exp(j2\pi dz_{m,m'})$, i.e., only a function of the z -axis inter-element spacings. Note that here the spatial correlation has a magnitude of one. This is a mathematical peculiarity and is due to the fact that in this scenario there is just a phase shift in the elevation domain between m and m' .
- This scenario can be generalized to a narrow angular spread within clusters of fixed but different central cluster AODs, i.e., the combined PES of *all* clusters may not be narrow, however the PES of subpaths within a single cluster is narrow. In this case, (5.26) becomes

$$R_{m,m'} = \frac{1}{C} \sum_{c=1}^C \exp(j2\pi dz_{m,m'} \cos(\theta_{0,c}^{\text{AOD}})) J_0(2\pi dxy_{m,m'} \sin(\theta_{0,c}^{\text{AOD}})). \quad (5.31)$$

In this scenario, the phase shift, $\exp(j2\pi dz_{m,m'} \cos(\theta_0^{\text{AOD}}))$, is able to decrease $|R_{m,m'}|$ non-monotonically. A larger z -axis spacing increases the phase oscillations and hence the C components are more likely to be out of phase and cancel, reducing $|R_{m,m'}|$ by a different mechanism than $dxy_{m,m'}$.

To date, all 3D spatial channel model measurement campaigns express the elevation AOD central cluster angles as some small random variation around the LOS angle to the user, ϑ^{AOD} [118, 119, 129]³. To examine the accuracy of (5.26) to the true spatial correlation for increasing intra-cluster subpath offsets, $\Delta\theta_{c,l}^{\text{AOD}}$, we assume $\theta_0^{\text{AOD}} = \vartheta^{\text{AOD}}$ following [114]. Therefore,

$$R_{m,m'} = \exp(j2\pi dz_{m,m'} \cos(\vartheta^{\text{AOD}})) J_0(2\pi dxy_{m,m'} \sin(\vartheta^{\text{AOD}})). \quad (5.32)$$

³Any downtilting of the TX antenna array would affect the relative LOS angle, ϑ^{AOD} . However, we assume no mechanical downtilting of any antenna arrays.

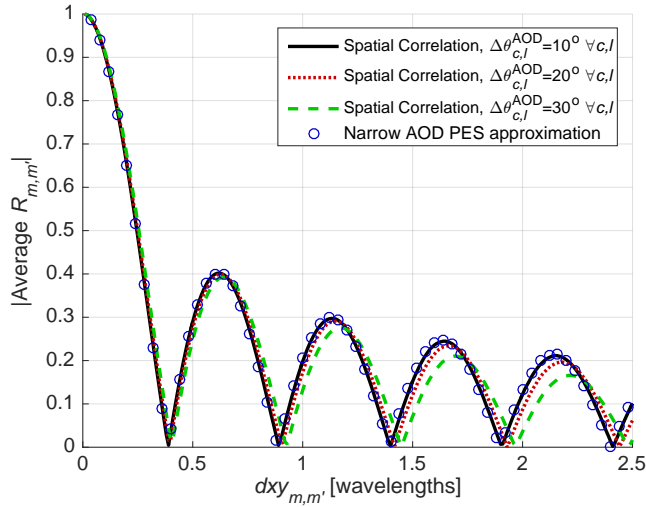


Figure 5.2: Magnitude of the average spatial correlation between two TX antennas, m and m' , for narrow AOD PES as a function of their x, y -plane inter-element spacing, $dxy_{m,m'}$, and elevation AOD ray offsets, $\Delta\theta_{c,l}^{\text{AOD}}$. $dz_{m,m'} = 0$.

In Figure 5.2 we show good agreement between the magnitude of the average spatial correlation between two TX antennas, $m, m' \in 1, \dots, M$, for narrow AOD PES as a function of their x, y -plane inter-element spacing, $dxy_{m,m'}$, and elevation AOD subpath offsets, $\Delta\theta_{c,l}^{\text{AOD}}$. The spatial correlation is averaged over 10^4 LOS angles⁴, ϑ^{AOD} . It can be seen that as the elevation AOD subpath offsets, $\Delta\theta_{c,l}^{\text{AOD}}$, are increased, the narrow AOD PES becomes a less accurate approximation to the spatial correlation. This is intuitive since we are approximating the spatial correlation in (5.1) by a single elevation AOD. However, the simple narrow AOD PES results are surprisingly accurate even up to $\Delta\theta_{c,l}^{\text{AOD}} = 30^\circ \forall c, l$. We also see that the peaks of the spatial correlation are slightly reduced in magnitude as the elevation AOD subpath offsets, $\Delta\theta_{c,l}^{\text{AOD}}$, are increased. This is a result of greater angular diversity in the system and the extreme case is the wide AOD PES, shown in Figure 5.1. Furthermore, we observe that the nulls of the spatial correlation magnitude occur for smaller distances as $\Delta\theta_{c,l}^{\text{AOD}}$ is reduced. This is because the LOS elevation angle to the user, ϑ^{AOD} , is nearly always relatively close to 90° (due to user location) as $\Delta\theta_{c,l}^{\text{AOD}}$ becomes smaller, therefore increasing the Bessel function argument, i.e., $\sin(\theta_{c,l}^{\text{AOD}}) = \sin(\theta_0^{\text{AOD}} + \Delta\theta_{c,l}^{\text{AOD}}) = \sin(\vartheta^{\text{AOD}} + \Delta\theta_{c,l}^{\text{AOD}}) \approx \sin(\vartheta^{\text{AOD}}) \approx 1 \forall c, l$, for small $\Delta\theta_{c,l}^{\text{AOD}}$. On the other hand, as $\Delta\theta_{c,l}^{\text{AOD}}$ increases, there becomes a higher likelihood that the magnitude of $\sin(\theta_{c,l}^{\text{AOD}})$ is reduced for a particular ray. The extreme case, where the first null occurs at a distance of $dxy_{m,m'} = 0.5$, is equivalent to the wide AOD PES shown in Figure 5.1.

⁴The user is located between $30 \leq d \leq 200\text{m}$ based on area coverage, with a TX height of $h_{\text{TX}} = 17\text{m}$ and a RX height of $h_{\text{RX}} = 2\text{m}$ [114].

5.3.3 Von Mises AOD PES

In this subsection, the spatial correlation expression in (5.1) is evaluated for a Von Mises AOD PES. Numerically, the effect of inter-element antenna spacing is then shown on the magnitude of the derived Von Mises AOD PES spatial correlation expression.

Theorem 5.3. For $p_{\Theta}(\theta_{c,l}^{\text{AOD}}) \sim \frac{\exp(\tilde{\kappa} \cos(\theta_{c,l}^{\text{AOD}} - \mu))}{2\pi I_0(\tilde{\kappa})}$, the spatial correlation between two TX antenna elements $m, m' \in 1, \dots, M$, can be approximated by

$$R_{m,m'} \approx \frac{\text{sinc}\left(2\sqrt{dxy_{m,m'}^2 + \left(dz_{m,m'} - j\frac{\tilde{\kappa} \cos(\mu)}{2\pi}\right)^2}\right)}{\text{sinc}\left(j\frac{\tilde{\kappa} \cos(\mu)}{\pi}\right)}. \quad (5.33)$$

Proof. For any two antenna elements $m, m' \in 1, \dots, M$, the spatial correlation in (5.1) can be approximated as

$$R_{m,m'} = \frac{A}{2\pi I_0(\tilde{\kappa})} \int_0^\pi \exp(j2\pi dz_{n,n'} \cos(\theta_{c,l}^{\text{AOD}})) J_0(2\pi dxy_{n,n'} \sin(\theta_{c,l}^{\text{AOD}})) \times \sin(\theta_{c,l}^{\text{AOD}}) \exp(\tilde{\kappa} \cos(\theta_{c,l}^{\text{AOD}} - \mu)) d\theta_{c,l}^{\text{AOD}} \quad (5.34)$$

$$\approx \frac{A \exp(\tilde{\kappa} \sin(\mu))}{2\pi I_0(\tilde{\kappa})} \int_0^\pi \exp(j2\pi dz_{n,n'} \cos(\theta_{c,l}^{\text{AOD}})) J_0(2\pi dxy_{n,n'} \sin(\theta_{c,l}^{\text{AOD}})) \times \sin(\theta_{c,l}^{\text{AOD}}) \exp(\tilde{\kappa} \cos(\mu) \cos(\theta_{c,l}^{\text{AOD}})) d\theta_{c,l}^{\text{AOD}}, \quad (5.35)$$

where A is the scaling constant to ensure the elevation PDF integrates to unity and $\tilde{\kappa} \sin(\mu) \sin(\theta_{c,l}^{\text{AOD}}) \approx \tilde{\kappa} \sin(\mu)$, since $\theta_{c,l}^{\text{AOD}} \approx \frac{\pi}{2}$. To calculate A ,

$$1 = A \int_{\theta_{c,l}^{\text{AOD}}} p_{\Theta}(\theta_{c,l}^{\text{AOD}}) \sin(\theta_{c,l}^{\text{AOD}}) d\theta_{c,l}^{\text{AOD}} = \frac{A \exp(\tilde{\kappa} \sin(\mu))}{2\pi I_0(\tilde{\kappa})} \int_0^\pi \sin(\theta_{c,l}^{\text{AOD}}) \exp(\tilde{\kappa} \cos(\mu) \cos(\theta_{c,l}^{\text{AOD}})) d\theta_{c,l}^{\text{AOD}} \quad (5.36)$$

$$= \frac{A \exp(\tilde{\kappa} \sin(\mu))}{2\pi I_0(\tilde{\kappa})} \int_{-1}^1 \exp(-\tilde{\kappa} \cos(\mu) u) du \quad (5.37)$$

$$= \frac{A \exp(\tilde{\kappa} \sin(\mu))}{2\pi \tilde{\kappa} \cos(\mu) I_0(\tilde{\kappa})} [\exp(\tilde{\kappa} \cos(\mu)) - \exp(-\tilde{\kappa} \cos(\mu))] \quad (5.38)$$

$$= \frac{A \exp(\tilde{\kappa} \sin(\mu)) \sinh(\tilde{\kappa} \cos(\mu))}{\pi \tilde{\kappa} \cos(\mu) I_0(\tilde{\kappa})}, \quad (5.39)$$

where $u = -\cos(\theta_{c,l}^{\text{AOD}})$ is substituted in (5.37). Therefore

$$A = \frac{\pi \tilde{\kappa} \cos(\mu) I_0(\tilde{\kappa})}{\exp(\tilde{\kappa} \sin(\mu)) \sinh(\tilde{\kappa} \cos(\mu))}. \quad (5.40)$$

Denoting $D = 2\pi dxy_{m,m'}$, $E = \frac{\tilde{\kappa} \cos(\mu)}{j}$, $G = 2\pi dz_{n,n'}$ and substituting $x =$

– $\cos(\theta_{c,l}^{\text{AOD}})$ the integral in (5.35) can be evaluated as

$$\int_{-1}^1 J_0\left(D\sqrt{1-x^2}\right) [\cos(Gx) + j \sin(Gx)] [\cos(Ex) + j \sin(Ex)] dx \quad (5.41)$$

$$\begin{aligned} &= \int_{-1}^1 J_0\left(D\sqrt{1-x^2}\right) \cos((G+E)x) dx + j \int_{-1}^1 J_0\left(D\sqrt{1-x^2}\right) \sin((G+E)x) dx \\ &= \frac{2 \sin\left(\sqrt{D^2 + (G+E)^2}\right)}{\sqrt{D^2 + (G+E)^2}}, \end{aligned} \quad (5.42)$$

where the second term in (5.41) integrates to zero. The desired result is obtained by substituting (5.42) and the normalization constant, A , into (5.35). ■

From (5.33) it can be seen that:

- Increasing the inter-element spacing on the either the x, y -plane or z -axis decreases the spatial correlation non-monotonically.
- If $dxy_{m,m'} = 0$,

$$R_{m,m'} = \frac{\text{sinc}\left(2dz_{m,m'} - j\frac{\tilde{\kappa}\cos(\mu)}{\pi}\right)}{\text{sinc}\left(j\frac{\tilde{\kappa}\cos(\mu)}{\pi}\right)}. \quad (5.43)$$

Apart from when $dz_{m,m'} = 0$, $R_{m,m'}$ can never be zero since $2dz_{m,m'} \neq \frac{j\tilde{\kappa}\cos(\mu)}{\pi} \forall dz_{m,m'}$.

- If $dz_{m,m'} = 0$,

$$R_{m,m'} = \frac{\text{sinc}\left(2\sqrt{dxy_{m,m'}^2 - \left(\frac{\tilde{\kappa}\cos(\mu)}{2\pi}\right)^2}\right)}{\text{sinc}\left(j\frac{\tilde{\kappa}\cos(\mu)}{\pi}\right)}, \quad (5.44)$$

and the nulls of $|R_{m,m'}|$ occur when $dxy_{m,m'} = \sqrt{\frac{n}{4} + \left(\frac{\tilde{\kappa}\cos(\mu)}{2\pi}\right)^2}$ for $n \in \mathbb{Z}^+$. For example, at $\mu = \frac{\pi}{2}$ and $\mu = \frac{\pi}{3}$, the first null of $|R_{m,m'}|$ occurs at $dxy_{m,m'} = \frac{1}{2}$ and $dxy_{m,m'} = \sqrt{\frac{1}{4} + \left(\frac{\tilde{\kappa}}{2\pi}\right)^2}$ wavelengths, respectively.

- For $\mu = \frac{\pi}{2}$, $R_{m,m'}$ becomes equal to the wide AOD PES spatial correlation in (5.17).
- As μ approaches 0 or π , $R_{m,m'}$ increases.
- As the concentration parameter $\tilde{\kappa} \rightarrow 0$, the distribution of $\theta_{c,l}^{\text{AOD}}$ becomes uniform over $[0, \pi) \forall c, l$ and $R_{m,m'}$ becomes equal to the wide AOD PES spatial correlation in (5.17).

- As the concentration parameter $\tilde{\kappa} \rightarrow \infty$, the AOD PES becomes infinitesimally small and thus $R_{m,m'} \approx 1$.

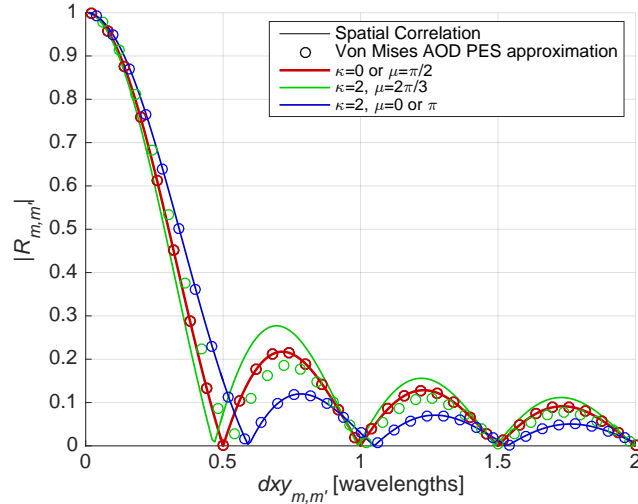


Figure 5.3: Spatial correlation magnitude between two TX antennas, m and m' , for a Von Mises AOD PES as a function of their x, y -plane inter-element spacing, $dxy_{m,m'}$.

In Figure 5.3 the accuracy of the average spatial correlation between two TX antennas, $m, m' \in 1, \dots, M$, is shown for a Von Mises AOD PES approximation as a function of their x, y -plane inter-element spacing, $dxy_{m,m'}$. It can be seen that the approximation is exact for $\kappa = 0$, $\mu = \frac{\pi}{2}$, $\mu = 0$ and $\mu = \pi$. For $\kappa = 2$ and $\mu = \frac{2\pi}{3}$, the approximation is reasonably good for small spacings and large spacings.

5.3.4 General PES Upper Bound

In this subsection, an upper bound on the spatial correlation expression in (5.1) is derived for any AOD PES.

Theorem 5.4. *For an arbitrary PES, (5.1) is bounded by*

$$R_{m,m'} \leq \frac{1}{CL} \sum_{c=1}^C \sum_{l=1}^L \frac{1}{\pi \sqrt{dxy_{m,m'}}} \mathbb{E} \left[\frac{1}{\sqrt{\sin(\theta_{c,l}^{\text{AOD}})}} \right], \quad (5.45)$$

Proof. For two antenna elements $m, m' \in 1, \dots, M$, (5.1) can be written as

$$R_{m,m'} = \frac{1}{CL} \sum_{c=1}^C \sum_{l=1}^L \mathbb{E} [\exp(j2\pi dz_{m,m'} \cos(\theta_{c,l}^{\text{AOD}})) J_0(2\pi dxy_{m,m'} \sin(\theta_{c,l}^{\text{AOD}}))]]$$

$$\leq \frac{1}{CL} \sum_{c=1}^C \sum_{l=1}^L \mathbb{E} [|J_0(2\pi dxy_{m,m'} \sin(\theta_{c,l}^{\text{AOD}}))|] \quad (5.46)$$

$$\approx \frac{1}{CL} \sum_{c=1}^C \sum_{l=1}^L \mathbb{E} \left[\left| \sqrt{\frac{2 \cos\left(2\pi dxy_{m,m'} \sin\left(\theta_{c,l}^{\text{AOD}}\right) - \frac{\pi}{4}\right)}{2\pi^2 dxy_{m,m'} \sin\left(\theta_{c,l}^{\text{AOD}}\right)}} \right| \right] \quad (5.47)$$

$$\leq \frac{1}{CL} \sum_{c=1}^C \sum_{l=1}^L \frac{1}{\pi \sqrt{dxy_{m,m'}}} \mathbb{E} \left[\frac{1}{\left| \sqrt{\sin\left(\theta_{c,l}^{\text{AOD}}\right)} \right|} \right] \quad (5.48)$$

$$= \frac{1}{CL} \sum_{c=1}^C \sum_{l=1}^L \frac{1}{\pi \sqrt{dxy_{m,m'}}} \mathbb{E} \left[\frac{1}{\sqrt{\sin\left(\theta_{c,l}^{\text{AOD}}\right)}} \right], \quad (5.49)$$

where (5.47) uses the approximation $J_0(x) \approx \sqrt{\frac{2}{\pi x}} \cos\left(x - \frac{\pi}{4}\right)$ [238], which is a good approximation for $x \geq 1$, i.e., for $dxy_{m,m'} \geq \frac{1}{2\pi \sin(\theta_{c,l}^{\text{AOD}})}$. The spatial correlation upper bound in (5.48) comes because $|\cos(\cdot)| \leq 1$ and (5.49) is obtained because $\left| \sqrt{\sin(\theta_{c,l}^{\text{AOD}})} \right| = \sqrt{\sin(\theta_{c,l}^{\text{AOD}})}$ for $\theta_{c,l}^{\text{AOD}} \in [0, \pi] \forall c, l$. ■

From (5.45), it can be seen that:

- The $R_{m,m'}$ upper bound is reduced for larger $dxy_{m,m'}$.
- For deterministic elevation AODs, the spatial correlation upper bound becomes

$$R_{m,m'} \leq \frac{1}{CL} \sum_{c=1}^C \sum_{l=1}^L \frac{1}{\pi \sqrt{dxy_{m,m'} \sin\left(\theta_{c,l}^{\text{AOD}}\right)}} \quad (5.50)$$

$$= \frac{1}{CL} \sum_{c=1}^C \sum_{l=1}^L \frac{1}{\pi \sqrt{dxy_{m,m'} \sin\left(\theta_{0,c}^{\text{AOD}} + \Delta\theta_{c,l}^{\text{AOD}}\right)}}, \quad (5.51)$$

and elevation AOD spreads affect the upper bound of $R_{m,m'}$ differently depending on the central cluster angles, $\theta_{0,c}^{\text{AOD}}$.

- For $\theta_{0,c}^{\text{AOD}}$ away from $\frac{\pi}{2}$, i.e., towards the end-fire of the TX antenna array with respect to the z -axis:
 - * Large AOD spreads increase the probability of $\Delta\theta_{c,l}^{\text{AOD}}$ being large and thus the probability of $\theta_{c,l}^{\text{AOD}}$ being close to $\frac{\pi}{2}$, reducing the $R_{m,m'}$ upper bound.
 - * Small AOD spreads increase the probability of $\Delta\theta_{c,l}^{\text{AOD}}$ being small and thus the probability of $\theta_{c,l}^{\text{AOD}}$ being close to either 0 or π , increasing the $R_{m,m'}$ upper bound.

- For $\theta_{0,c}^{\text{AOD}}$ close to $\frac{\pi}{2}$, i.e., towards the broadside of the TX antenna array with respect to the z -axis:
 - * Large AOD spreads increase the probability of $\Delta\theta_{c,l}^{\text{AOD}}$ being large and thus the probability of $\theta_{c,l}^{\text{AOD}}$ being close to 0 or π , increasing the $R_{m,m'}$ upper bound.
 - * Small AOD spreads increase the probability of $\Delta\theta_{c,l}^{\text{AOD}}$ being small and thus the probability of $\theta_{c,l}^{\text{AOD}}$ being close to $\frac{\pi}{2}$, decreasing the $R_{m,m'}$ upper bound.
- Similarly, PES which are more concentrated (e.g., Laplacian [144, 180]) reduce the $R_{m,m'}$ upper bound when the central cluster angle, $\theta_{0,c}^{\text{AOD}}$, is closer to the broadside of the TX antenna array and vice-versa.

5.4 Convergence to Massive MIMO: Diagonal Dominance

In this section, the rate of convergence of a user's channel to favourable massive MIMO propagation [43] is explored for the different antenna topologies, as the number of RX antennas, Q , becomes large. The convergence of a user's channel is measured by defining the *diagonal dominance*⁵, δ , as⁶

$$\delta = \frac{\frac{1}{Q(Q-1)} \sum_{q=1}^Q \sum_{\substack{q'=1 \\ q' \neq q}}^Q \left| \mathbb{E} [\mathbf{h}_q \mathbf{h}_{q'}^H] \right|}{\frac{1}{Q} \sum_{q=1}^Q \mathbb{E} [\mathbf{h}_q \mathbf{h}_q^H]}, \quad (5.52)$$

where \mathbf{h}_q denotes the q th row of \mathbf{H} . Note that δ will converge to zero when channels between antenna elements, of the user, become orthogonal, i.e., the diagonal elements become large relative to the off-diagonals in the summations. Note here that the diagonal dominance is a function of the user antenna array and therefore (5.52) is dependent on the number of user antennas, Q , and AOAs, rather the number of BS antennas, M , and AODs⁷.

⁵Diagonal dominance has previously been defined for a composite, concatenated, channel of K single-antenna user's in Chapter 3. In this chapter, diagonal dominance is defined for a users channel, where the user can have an arbitrary number of receive antenna elements.

⁶In Chapter 3, three different convergence metrics were considered (mean absolute deviation, eigenvalue ratio and diagonal dominance) since the primary aim of the chapter was to investigate massive MIMO channel convergence. Only diagonal dominance is considered in this chapter, however, as the focus is on analytically deriving the effects of antenna topology and inter-element spacing on a number of different performance metrics, including channel convergence.

⁷Since a DL channel is considered, the diagonal dominance is defined for a particular user. However, all the analysis holds in the case of an UL channel, where the diagonal dominance

Lemma 5.2. *Given the Saleh-Valenzuela channel model in (2.14) and an AOA PAS of $\mathbf{p}_\Phi(\phi_{c,l}^{\text{AOA}}) \sim \mathcal{U}[0, 2\pi) \forall c, l$, as discussed in Section 5.2.1, the diagonal dominance can be written as*

$$\delta = \frac{1}{Q(Q-1)} \sum_{q=1}^Q \sum_{\substack{q'=1 \\ q' \neq q}}^Q \frac{1}{CL} \times \left| \sum_{c=1}^C \sum_{l=1}^L \mathbb{E} \left[\exp(j2\pi dz_{q,q'} \cos(\theta_{c,l}^{\text{AOA}})) J_0(2\pi dxy_{q,q'} \sin(\theta_{c,l}^{\text{AOA}})) \right] \right|, \quad (5.53)$$

Proof. Let \mathbf{h}_q denotes the q th row of \mathbf{H} , then

$$\mathbb{E} [\mathbf{h}_q \mathbf{h}_q^H] = \mathbb{E} \left[\left(\frac{1}{\sqrt{L}} \sum_{c=1}^C \sum_{l=1}^L h_{\text{iid},c,l} a_{\text{RX},q}(\phi_{c,l}^{\text{AOA}}, \theta_{c,l}^{\text{AOA}}) \mathbf{a}_{\text{TX}}^H(\phi_{c,l}^{\text{AOD}}, \theta_{c,l}^{\text{AOD}}) \right) \times \left(\frac{1}{\sqrt{L}} \sum_{c=1}^C \sum_{l=1}^L h_{\text{iid},c,l} a_{\text{RX},q'}(\phi_{c,l}^{\text{AOA}}, \theta_{c,l}^{\text{AOA}}) \mathbf{a}_{\text{TX}}^H(\phi_{c,l}^{\text{AOD}}, \theta_{c,l}^{\text{AOD}}) \right)^H \right] \quad (5.54)$$

$$= \frac{1}{L} \sum_{c=1}^C \sum_{l=1}^L \mathbb{E} [|h_{\text{iid},c,l}|^2] \mathbb{E} [\| \mathbf{a}_{\text{TX}}^H(\phi_{c,l}^{\text{AOD}}, \theta_{c,l}^{\text{AOD}}) \|^2] \times \mathbb{E} [a_{\text{RX},q}(\phi_{c,l}^{\text{AOA}}, \theta_{c,l}^{\text{AOA}}) a_{\text{RX},q'}^*(\phi_{c,l}^{\text{AOA}}, \theta_{c,l}^{\text{AOA}})] \quad (5.55)$$

$$= \frac{M}{CL} \sum_{c=1}^C \sum_{l=1}^L \mathbb{E} [a_{\text{RX},q}(\phi_{c,l}^{\text{AOA}}, \theta_{c,l}^{\text{AOA}}) a_{\text{RX},q'}^*(\phi_{c,l}^{\text{AOA}}, \theta_{c,l}^{\text{AOA}})] \quad (5.56)$$

$$= \frac{M}{CL} \sum_{c=1}^C \sum_{l=1}^L \int_{\theta_{c,l}^{\text{AOA}}} \int_{\phi_{c,l}^{\text{AOA}}} \exp \left(j \frac{2\pi}{\lambda} (\mathbf{W}_{\text{RX},q} - \mathbf{W}_{\text{RX},q'}) \mathbf{r}_{\text{RX}}(\phi_{c,l}^{\text{AOA}}, \theta_{c,l}^{\text{AOA}}) \right) \times \sin(\theta_{c,l}^{\text{AOA}}) p_\Phi(\phi_{c,l}^{\text{AOA}}) p_\Theta(\theta_{c,l}^{\text{AOA}}) d\phi_{c,l}^{\text{AOA}} d\theta_{c,l}^{\text{AOA}} \quad (5.57)$$

$$= \frac{M}{CL} \sum_{c=1}^C \sum_{l=1}^L \int_{\theta_{c,l}^{\text{AOA}}} \left(\int_0^{2\pi} \exp(j2\pi \sin(\theta_{c,l}^{\text{AOA}}) \times [dx_{q,q'} \cos(\phi_{c,l}^{\text{AOA}}) + dy_{q,q'} \sin(\phi_{c,l}^{\text{AOA}})]) p_\Phi(\phi_{c,l}^{\text{AOA}}) d\phi_{c,l}^{\text{AOA}} \right) \times \exp(j2\pi dz_{q,q'} \cos(\theta_{c,l}^{\text{AOA}})) \sin(\theta_{c,l}^{\text{AOA}}) p_\Theta(\theta_{c,l}^{\text{AOA}}) d\theta_{c,l}^{\text{AOA}} \quad (5.58)$$

$$= \frac{M}{CL} \sum_{c=1}^C \sum_{l=1}^L \int_{\theta_{c,l}^{\text{AOA}}} \exp(j2\pi dz_{q,q'} \cos(\theta_{c,l}^{\text{AOA}})) J_0(2\pi dxy_{q,q'} \sin(\theta_{c,l}^{\text{AOA}})) \times \sin(\theta_{c,l}^{\text{AOA}}) p_\Theta(\theta_{c,l}^{\text{AOA}}) d\theta_{c,l}^{\text{AOA}} \quad (5.59)$$

$$= \frac{M}{CL} \sum_{c=1}^C \sum_{l=1}^L \mathbb{E} [\exp(j2\pi dz_{q,q'} \cos(\theta_{c,l}^{\text{AOA}})) J_0(2\pi dxy_{q,q'} \sin(\theta_{c,l}^{\text{AOA}}))], \quad (5.60)$$

where steps from (5.58) to (5.59) are analogous to (5.14) to (5.16) with $\mathbf{p}_\Phi(\phi_{c,l}^{\text{AOA}}) \sim \mathcal{U}[0, 2\pi) \forall c, l$. Substituting (5.60) in (5.52), where $\mathbb{E} [\mathbf{h}_q \mathbf{h}_q^H] = M$, gives the

would be defined for a particular BS antenna array.

desired result. ■

5.4.1 Wide AOA PES

In this subsection, the diagonal dominance expression in (5.53) is evaluated for a wide AOA PES. Numerically, the effect of increasing receive antenna elements, antenna topology and inter-element antenna spacing are then shown on the convergence of the derived wide AOA PES diagonal dominance expression.

Corollary 5.1. *Suppose $dxyz_{q,q'}$ denotes the distance in wavelengths between antenna elements q and q' in 3D Cartesian coordinates, then analogous to the steps of the wide AOD PES spatial correlation, given in (5.18)-(5.25), evaluating the diagonal dominance in (5.53) for a wide AOA PES, i.e., $p_{\Theta}(\theta_{c,l}^{\text{AOA}})$ constant over $[0, \pi) \forall c, l$, δ gives*

$$\delta = \frac{1}{Q(Q-1)} \sum_{q=1}^Q \sum_{\substack{q'=1 \\ q' \neq q}}^Q |\text{sinc}(2dxyz_{q,q'})|. \quad (5.61)$$

From (5.61), it can be observed that:

- Increasing the distance between two antennas by the same amount in any direction decreases δ equally (non-monotonically).
- Assuming uniform spacings in any direction, δ will be zero when $dxyz_{q,q'} = \frac{n}{2}$ for $n \in \mathbb{Z}^+$. This can be achieved easily with a ULA, however it cannot be achieved with the URA and UCA topologies, as antenna elements spacings are not always a multiple of a 1/2 wavelength.

In Figure 5.4, the diagonal dominance of a user's channel, δ , is shown for wide AOA PES, as a function of the number of receive antenna elements, Q , antenna topology and antenna inter-element spacing. d_{λ} denotes the antenna inter-element spacing in wavelengths. It can be seen that an increase in inter-element spacing from $d_{\lambda} = 0.125$ to 1.25 wavelengths results in nearly an order of magnitude decrease in δ . The ULA has a lower value of δ as it has fewer adjacent antenna elements, compared with the URA and UCA. Also, as Q increases, the value of δ of the URA and UCA converge to be similar to each other. As was the case for an i.i.d. Rayleigh fading channel in Chapter 3, the diagonal dominance asymptotically converges to a limiting value with increasing antenna numbers.

5.4.2 Narrow AOA PES

In this subsection, the diagonal dominance expression in (5.53) is evaluated for a narrow AOA PES. Numerically, the effect of increasing receive antenna elements, antenna topology and inter-element antenna spacing are then shown on

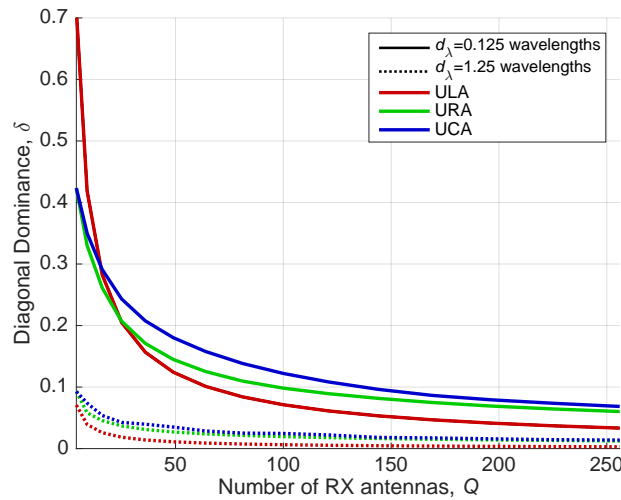


Figure 5.4: Diagonal dominance of a user's channel, δ , for a wide AOA PES, as a function of the number of receive antenna elements, Q , antenna topology and antenna inter-element spacing.

the convergence of the derived narrow AOA PES diagonal dominance expression.

Corollary 5.2. *Since $|\exp(jx)| = 1$, analogous to steps (5.27)-(5.30), the diagonal dominance of a user's channel, with a narrow AOA PES, can be approximated as*

$$\delta = \frac{1}{Q(Q-1)} \sum_{q=1}^Q \sum_{\substack{q'=1 \\ q' \neq q}}^Q \left| \exp(j2\pi dz_{q,q'} \cos(\theta_0^{\text{AOA}})) J_0(2\pi dxy_{q,q'} \sin(\theta_0^{\text{AOA}})) \right| \quad (5.62)$$

$$= \frac{1}{Q(Q-1)} \sum_{q=1}^Q \sum_{\substack{q'=1 \\ q' \neq q}}^Q \left| J_0(2\pi dxy_{q,q'} \sin(\theta_0^{\text{AOA}})) \right|. \quad (5.63)$$

Some insights from (5.63) can be drawn:

- δ is independent of $dz_{q,q'}$.
- As discussed for the narrow AOD PES spatial correlation in Section 5.3.2, δ is independent of the angular spreads, the number of subpaths, L , and azimuth angles. δ decreases non-monotonically with $dxy_{q,q'}$.
- For a fixed θ_0^{AOA} , differences in δ between the URA and UCA come from the oscillatory nature of $J_0(2\pi dxy_{q,q'})$, which is a function of the x, y -plane inter-element spacings. Note that $dxy_{q,q'}^{\text{URA}} \geq dxy_{q,q'}^{\text{UCA}}$ with equality only if $q = q' \pm 1$, where the layout of the antenna topologies are described in Section 2.3.

- If $\theta_0^{\text{AOA}} = \vartheta^{\text{AOA}}$ as in [114], then

$$\delta = \frac{1}{Q(Q-1)} \sum_{q=1}^Q \sum_{\substack{q'=1 \\ q' \neq q}}^Q |J_0(2\pi d_x y_{q,q'} \sin(\vartheta^{\text{AOA}}))|, \quad (5.64)$$

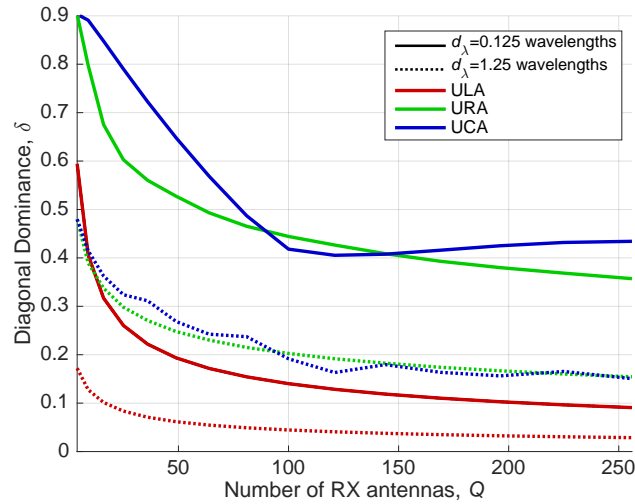


Figure 5.5: Diagonal dominance of a user’s channel, δ , for a narrow AOA PES, as a function of the number of receive antenna elements, Q , antenna topology and antenna inter-element spacing.

In Figure 5.5, we show the diagonal dominance of a user’s channel, δ , for a narrow AOA PES, where $\theta_0^{\text{AOA}} = \vartheta^{\text{AOA}}$, as in (5.64) [114]. As was the case in the wide AOA PES scenario, an increase in inter-element spacing from $d_\lambda = 0.125$ to 1.25 wavelengths results in a large decrease in δ . Since δ is independent of the z -axis inter-element spacing, the ULA now performs significantly better than the URA and UCA topologies. The slope of the UCA δ is not smooth, as seen for the ULA and URA topologies, and intersects the URA δ at different numbers of RX antenna elements, Q . For large antenna spacings, the diagonal dominance of the URA and UCA converge to similar spacings.

5.4.3 Von Mises AOA PES

In this subsection, the diagonal dominance expression in (5.53) is evaluated for a Von Mises AOA PES.

Corollary 5.3. *If $p_\Theta(\theta_{c,l}^{\text{AOA}}) \sim \frac{\exp(\bar{\kappa} \cos(\theta_{c,l}^{\text{AOA}} - \mu))}{2\pi I_0(\bar{\kappa})}$, then analogous to the steps in*

(5.34)-(5.42), δ can be approximated by

$$\delta \approx \frac{1}{Q(Q-1)} \left| \operatorname{sinc} \left(j \frac{\tilde{\kappa} \cos(\mu)}{\pi} \right) \right|^{-1} \times \sum_{q=1}^Q \sum_{\substack{q'=1 \\ q' \neq q}}^Q \left| \operatorname{sinc} \left(2 \sqrt{dxy_{q,q'}^2 + \left(dz_{q,q'} - j \frac{\tilde{\kappa} \cos(\mu)}{2\pi} \right)^2} \right) \right|. \quad (5.65)$$

From (5.65):

- Increasing the inter-element spacing on the either the x, y -plane or z -axis decreases δ non-monotonically.
- If $dxy_{q,q'} = 0$, δ is never zero apart from when $dz_{q,q'} = 0$, since $2dz_{q,q'} \neq \frac{j\tilde{\kappa} \cos(\mu)}{\pi} \forall dz_{q,q'}$.
- If $dz_{q,q'} = 0$, δ is zero when $dxy_{q,q'} = \sqrt{\frac{n}{4} + \left(\frac{\tilde{\kappa} \cos(\mu)}{2\pi} \right)^2}$ for $n \in \mathbb{Z}^+$.
- For $\mu = \frac{\pi}{2}$, δ becomes equal to the wide AOA PES diagonal dominance in (5.61).
- As μ approaches 0 or π , δ increases.
- As the concentration parameter $\tilde{\kappa} \rightarrow 0$, the distribution of $\theta_{c,l}^{\text{AOA}}$ becomes uniform over $[0, \pi) \forall c, l$ and δ becomes equal to the wide AOA PES δ in (5.61).
- As the concentration parameter $\tilde{\kappa} \rightarrow \infty$, the AOA PES becomes infinitesimally small and thus $\delta \rightarrow \infty$.

5.4.4 General PES Upper Bound

In this subsection, an upper bound on the diagonal dominance expression in (5.53) is derived for any AOA PES.

Corollary 5.4. *Analogous to the steps in (5.46)-(5.49), the diagonal dominance upper bound of the expectation in (5.53) can be expressed as*

$$\delta \leq \frac{1}{Q(Q-1)} \sum_{q=1}^Q \sum_{\substack{q'=1 \\ q' \neq q}}^Q \frac{1}{\pi CL \sqrt{dxy_{q,q'}}} \left\| \sum_{c=1}^C \sum_{l=1}^L \mathbb{E} \left[\frac{1}{\sqrt{\sin(\theta_{c,l}^{\text{AOA}})}} \right] \right\| \quad (5.66)$$

$$= \frac{1}{Q(Q-1)} \sum_{q=1}^Q \sum_{\substack{q'=1 \\ q' \neq q}}^Q \frac{1}{\pi CL \sqrt{dxy_{q,q'}}} \sum_{c=1}^C \sum_{l=1}^L \mathbb{E} \left[\frac{1}{\sqrt{\sin(\theta_{c,l}^{\text{AOA}})}} \right]. \quad (5.67)$$

For a single elevation AOA, θ^{AOA} ,

$$\delta \leq \frac{1}{Q(Q-1)} \sum_{q=1}^Q \sum_{\substack{q'=1 \\ q' \neq q}}^Q \frac{1}{\pi \sqrt{dxy_{q,q'} \sin(\theta^{\text{AOA}})}}. \quad (5.68)$$

Hence the value of δ decays proportional to $\frac{1}{\sqrt{dxy_{q,q'}}$ and with $\mathcal{O}\left(\frac{1}{\sqrt{\sin(\theta^{\text{AOA}})}}\right)$. The bound on δ is therefore minimized when $\theta^{\text{AOA}} = \frac{\pi}{2}$, i.e., when the elevation AOA is perpendicular to the z -axis of the antenna array.

5.5 Numerical Mutual Coupling Results

In this section, the effects of mutual coupling on different antenna array topologies is numerically examined, by analysing the resultant spatial correlation against inter-element spacing, eigenvalue structure and user rate of a mmWave system. In Sections 5.5.1 and 5.5.1, the effects of mutual coupling, on spatial correlation and eigenvalue structure, respectively, are investigated for the two opposing spatial correlation cases: wide and narrow AOD PES. Here, the expressions derived in Section 5.3 are used, given in (5.17) and (5.32) for the two respective cases. In Section 5.5.3, the user rate of a mmWave channel [114] is simulated for a carrier frequency of 28 GHz.

In all cases where mutual coupling is modelled, (2.51) is used with antenna impedance of $Z_A = 73 + j42.5 \Omega$ [171, 239].

5.5.1 Impact of Antenna Separation

All results in this subsection are applicable to either the TX or RX antenna array. Without loss of generality the effects of spatial correlation and mutual coupling are explored with multiple antennas employed at the TX, i.e., $\mathbf{Z}_{\text{RX}} = \mathbf{I}_Q$ in (2.53).

To draw insight into how different array topologies are affected by mutual coupling, its effects are numerically shown on three different dipole antenna pairs [171]:

1. *Side-by-side*: where $dxy_{m,m'} \neq 0$ and $dz_{m,m'} = 0$ for $m, m' \in 1, \dots, M$.
2. *Collinear*: where $dxy_{m,m'} = 0$ and $dz_{m,m'} \neq 0$ for $m, m' \in 1, \dots, M$.
3. *Parallel-in-echelon*: where $dxy_{m,m'} \neq 0$ and $dz_{m,m'} \neq 0$ for $m, m' \in 1, \dots, M$. For simplicity, the case where $dxy_{m,m'} = dz_{m,m'}$ is considered.

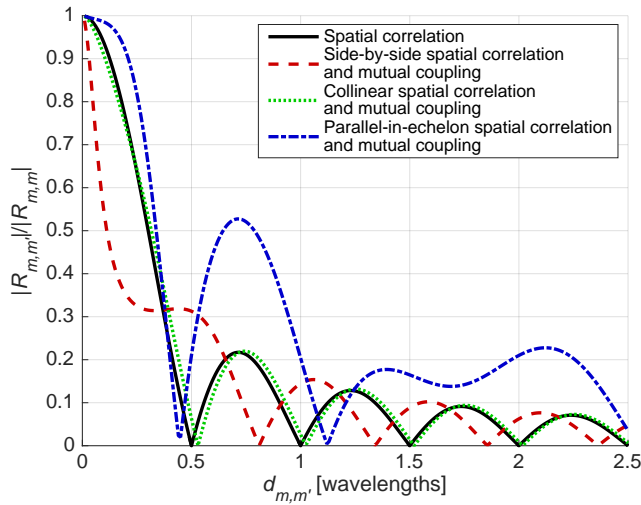
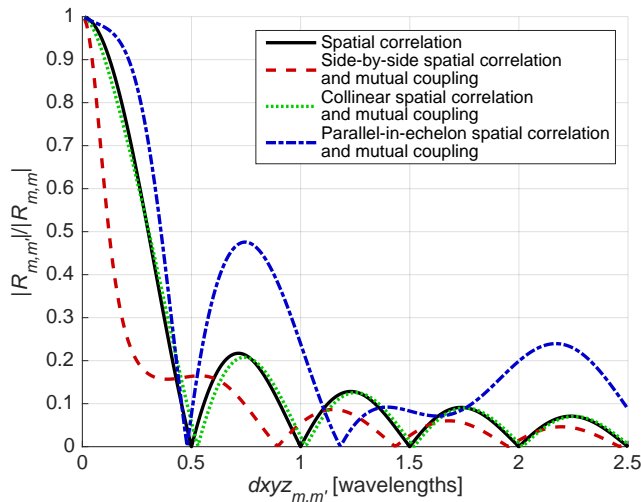
(a) Load (or termination) impedance of $Z_L = 50 \Omega$.(b) Load (or termination) impedance equal to the conjugate antenna impedance, Z_A^* , i.e., $Z_L = 73 - j42.5 \Omega$.

Figure 5.6: Normalized magnitude of a wide AOD PES spatial correlation, $|R_{m,m'}|/|R_{m,m}|$, with and without mutual coupling, between two TX antennas, $m, m' \in 1, \dots, M$, as a function of their inter-element spacing, $d_{m,m'}$, for three different antenna configurations.

Wide AOD PES

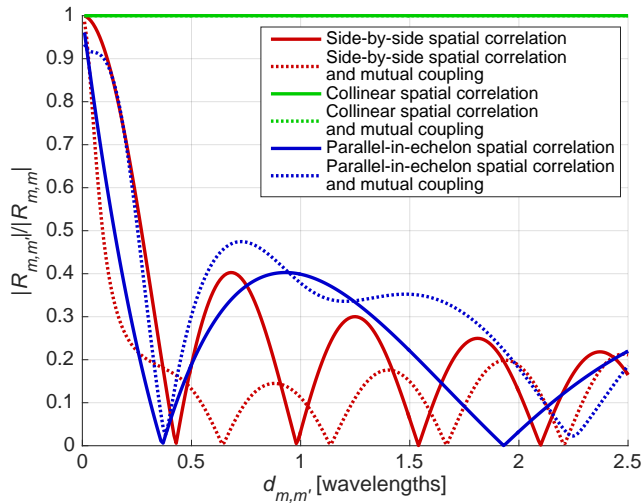
In Figure 5.6 the *normalized* magnitude of a wide AOD PES spatial correlation, $|R_{m,m'}|/|R_{m,m}|$, is shown with and without mutual coupling⁸, between two

⁸In the case where only spatial correlation is modelled, $R_{m,m'}$ is given as in derived in Section 5.3. When mutual coupling is added, $R_{m,m'} = \mathbb{E}[\bar{\mathbf{h}}_m^H \bar{\mathbf{h}}_{m'}] = Z_{\text{TX},m,m}^H \mathbb{E}[\mathbf{h}_m^H \mathbf{h}_{m'}] Z_{\text{TX},m',m'}$, where \mathbf{h}_m is the m th column of \mathbf{H} , since the elements of the mutual coupling matrix are a function of deterministic parameters [171].

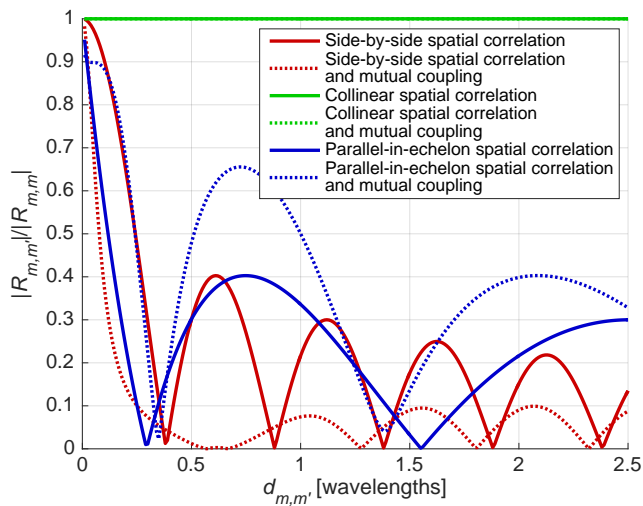
TX antennas, $m, m' \in 1, \dots, M$, as a function of their inter-element spacing, $d_{m,m'}$, for three different antenna configurations. For the side-by-side antenna configuration, the effects of mutual coupling are more obvious at smaller antenna separations. For example, it can be seen that mutual coupling reduces the magnitude of the normalized spatial correlation for inter-element spacings $d_{m,m'} < 0.37$ wavelengths and $d_{m,m'} < 0.43$ wavelengths for $Z_L = 50 \Omega$ and $Z_L = 73 - j42.5 \Omega$, respectively. There is a negligible impact on the spatial correlation when antennas are in the collinear configuration, because the ideal dipole radiation pattern has a singularity at its ends and therefore the impinging radiation on (collinear) adjacent antennas is minimal. On the other hand, when antennas are in the parallel-in-echelon configuration, the mutual coupling causes a strong increase in the normalized spatial correlation and its magnitude is yet to converge to the scenario with no mutual coupling, as the other configurations do, even for inter-element spacings of up to $d_{m,m'} = 2.5$ wavelengths. Comparing Figure 5.6a with Figure 5.6b, it is noted that the shape of the decay, before a half-wavelength spacing for the side-by-side configuration, is dependent on the load impedance, Z_L , chosen [24, 87, 89, 105, 239]. The magnitude of the normalized spatial correlation peaks for the side-by-side and parallel-in-echelon configurations are reduced when the load impedance, Z_L , is chosen to be the conjugate of the antenna impedance, Z_A . In all results following, a load impedance of $Z_L = 50 \Omega$ is used.

Narrow AOD PES

In Figure 5.7 the normalized magnitude of a narrow AOD PES spatial correlation, $|R_{m,m'}|/|R_{m,m}|$, is shown with and without mutual coupling, between two TX antennas, $m, m' \in 1, \dots, M$, as a function of their inter-element spacing, $d_{m,m'}$, for three different antenna configurations. Two user locations are considered: a minimum distance of 30m and a maximum distance of 200m away from the BS [114], shown in Figure 5.7a and Figure 5.7b, respectively. It can be seen that for the side-by-side antenna configuration, mutual coupling reduces the magnitude of the normalized spatial correlation for all inter-element spacings less than $d_{m,m'} = 2.5$ wavelengths. As was the case with the wide AOD PES spatial correlation (Figure 5.6), antennas in the collinear configuration have almost no difference when mutual coupling is modelled. For example, in both user locations the normalized spatial correlation magnitude with and without mutual coupling is unity. As discussed in Section 5.3.2, this is because the AOD between two antennas only has a phase variation, i.e., no changes in the magnitude. Comparing Figure 5.7a with Figure 5.7b, it is seen that as the central elevation AOD, θ_0^{AOD} , approaches 90° (i.e., the user gets further away from the BS), the spatial correlation nulls for side-by-side and parallel-in-echelon antenna configurations occur for smaller spacings. For the side-by-side antenna configu-



(a) Minimum TX to RX distance of $d = 30$ m, therefore $\theta_0^{\text{AOD}} = 116.6^\circ$.



(b) Maximum TX to RX distance of $d = 200$ m, therefore $\theta_0^{\text{AOD}} = 94.3^\circ$.

Figure 5.7: Normalized magnitude of a narrow AOD PES spatial correlation, $|R_{m,m'}|/|R_{m,m}|$, with and without mutual coupling, between two TX antennas, $m, m' \in 1, \dots, M$, as a function of their inter-element spacing, $d_{m,m'}$, for three different antenna configurations.

ration, this is because the modulus of the narrow AOD PES spatial correlation, given in (5.32), decreases as $\sin(\vartheta^{\text{AOD}})$ increases. For the parallel-in-echelon configuration case (where $dx_{m,m'} = dz_{m,m'}$), this suggests that the reduction in spatial correlation from the modulus decrease outweighs the increase in spatial correlation from a smaller phase shift (as $\cos(\vartheta^{\text{AOD}})$ is reduced). For the parallel-in-echelon configuration, however, a large increase in the spatial correlation with mutual coupling magnitude is seen as ϑ^{AOD} approaches 90° .

Compared with the wide AOD PES spatial correlation (Figure 5.6) the normalized spatial correlation magnitude shows an increase when the AOD PES is narrow (Figure 5.7) for all cases of antenna configurations with and without mutual coupling, over nearly all spacings. This is intuitive and results from a lack of spatial diversity when the AOD PES is narrow. In general, Figures 5.6 and 5.7 show that mutual coupling can increase or decrease the spatial correlation at a given inter-element spacing, which is consistent with [24, 85, 87, 105, 239]. If there are no physical space constraints on the antenna array, the ULA topology is preferred, as the side-by-side antennas are seen to have less spatial correlation with and without mutual coupling effects.

5.5.2 Eigenvalue Structure

In this subsection, the eigenvalue magnitude vs the eigenvalue index for spatially correlated TX antenna arrays is investigated with and without mutual coupling⁹. The number of significant eigenvalues provides a measure of the number of streams which can be used for efficient spatial multiplexing [233, 240, 241]. Each figure is truncated at an eigenvalue magnitude of -20 dB, as eigenvalues below this value are essentially in the noise floor and do not contribute to the antenna array's spatial multiplexing abilities. When mutual coupling is modelled, both the unnormalized eigenvalue magnitude (main figure) and the normalized mutual coupling¹⁰ case (subfigure) are shown as to determine the impact of mutual coupling on the power of the eigenvalues.

Wide AOD PES

In Figure 5.8a and Figure 5.8b the eigenvalue magnitude vs eigenvalue index is shown for wide AOD PES spatially correlated TX antenna topologies with and without mutual coupling, with $M = 100$ TX antenna elements, for inter-element spacings of $d_\lambda = 0.125$ and $d_\lambda = 1.25$ wavelengths, respectively. For small inter-element spacings, mutual coupling reduces the magnitude of the largest eigenvalues in all antenna topologies when mutual coupling is unnormalized, and only the ULA eigenvalues when mutual coupling is normalized. This indicates that the resultant spatial correlation, with mutual coupling, is having almost no effect on the eigenvalues of the URA and UCA for small inter-element spacings. However, mutual coupling is causing a power reduction in the magnitude of the largest eigenvalues.

⁹When only spatial correlation is modelled, the eigenvalues of $\mathbb{E}[\mathbf{H}^H\mathbf{H}]$ are considered, where \mathbf{H} is the Saleh-Valenzuela channel matrix given in (2.14). When mutual coupling is included, the eigenvalues of $\mathbb{E}[\overline{\mathbf{H}}^H\overline{\mathbf{H}}]$ are considered, where $\overline{\mathbf{H}}$ denotes the mutually coupled channel matrix given in (2.53).

¹⁰Normalized mutual coupling is calculated by forcing the diagonal elements of the composite matrix to unity.

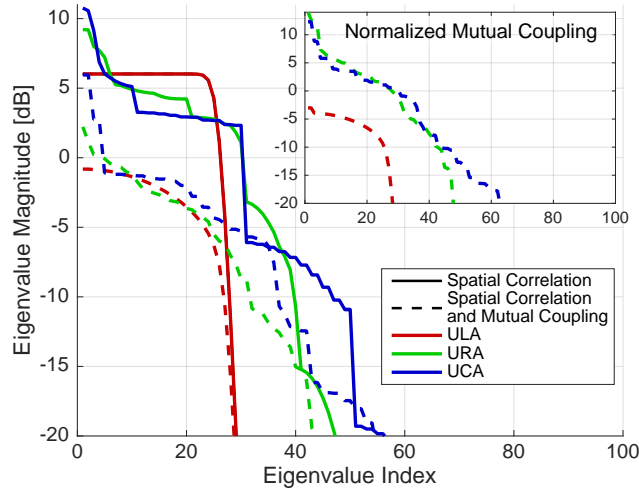
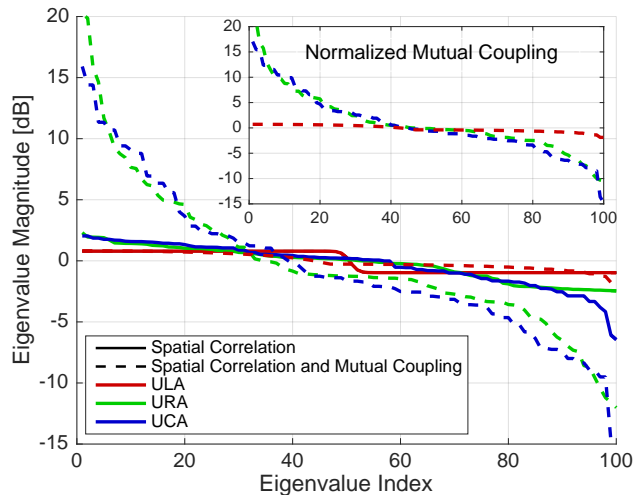
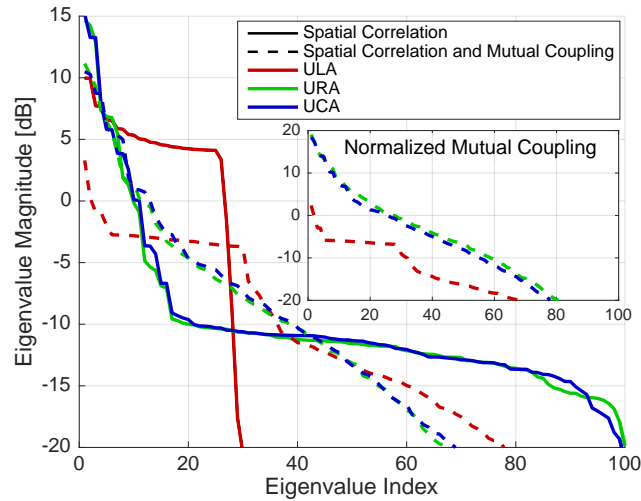
(a) $d_\lambda = 0.125$ wavelengths.(b) $d_\lambda = 1.25$ wavelengths.

Figure 5.8: Eigenvalue magnitude vs eigenvalue index for wide AOD PES spatially correlated antenna topologies with and without mutual coupling, for $M = 100$ TX antenna elements.

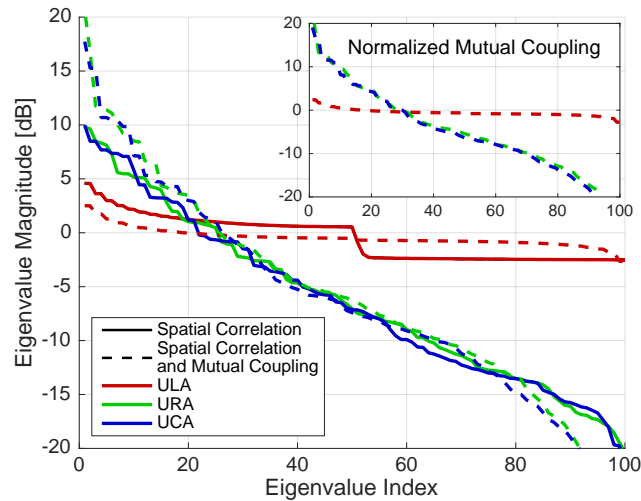
At small inter-element spacings, the UCA has the largest number of eigenvalues above a magnitude of -20 dB, and therefore best spatial multiplexing capabilities. On the other hand, the ULA has only a small number of eigenvalues which are not very small in magnitude. For large inter-element spacings, the eigenvalues for all topologies with only spatial correlation become more similar, as they are approaching an i.i.d. scenario. When mutual coupling is added for large inter-element spacings, the magnitude of the first eigenvalue is increased significantly for the URA and UCA, while the magnitude of the smaller eigenvalues is reduced for these topologies. This is because, even at larger inter-element spacings, there is still a significant increase in spatial correlation, when mu-

tual coupling is included, for antennas in the parallel-in-echelon configuration, specific to the URA and UCA. Also, at $d_\lambda = 1.25$, there is little difference in eigenvalue structure between normalized and unnormalized mutual coupling.

Narrow AOD PES



(a) $d_\lambda = 0.125$ wavelengths.



(b) $d_\lambda = 1.25$ wavelengths.

Figure 5.9: Eigenvalue magnitude vs eigenvalue index for narrow AOD PES spatially correlated antenna topologies with and without mutual coupling, for $M = 100$ TX antenna elements.

In Figure 5.9a and Figure 5.9b the eigenvalue magnitude vs eigenvalue index is shown for narrow AOD PES spatially correlated antenna topologies with and without mutual coupling, with $M = 100$ TX antenna elements, for inter-element spacings of $d_\lambda = 0.125$ and $d_\lambda = 1.25$ wavelengths, respectively. The

ULA is seen to have a large increase in spatial multiplexing performance when mutual coupling is modelled for small inter-element spacings. This is because mutual coupling greatly reduces the side-by-side normalized spatial correlation for small spacings, as shown in Figure 5.7. Mutual coupling is also shown to reduce the number of significant eigenvalues (above -20 dB) for the URA and UCA with small inter-element spacings. This can be explained, with the help of Figure 5.7, by the increase in normalized spatial correlation magnitude for the parallel-in-echelon antenna configuration. Increasing the inter-element antenna spacings from $d_\lambda = 0.125$ to 1.25 wavelengths improves the performance of all antenna topologies, particularly for the ULA with mutual coupling, which has nearly equal eigenvalues. Note here that although mutual coupling increases the parallel-in-echelon normalized spatial correlation greatly, for a wide range of inter-element spacings, there is almost no difference for an inter-element spacing of $d_\lambda = 1.25$ wavelengths (looking at both Figure 5.7a and Figure 5.7b). This is why mutual coupling does not drastically affect the eigenvalue structure seen in Figure 5.9b, as was the case for small inter-element spacings in Figure 5.9a. Mutual coupling causes a power reduction to the largest eigenvalues of the URA and UCA for small spacings, whereas there is a very little power difference for large inter-element spacings.

In general, when mutual coupling is modelled, the ULA has the best spatial multiplexing performance since the normalized spatial correlation is greatly reduced for the side-by-side antenna configuration. This is more obvious at large inter-element spacings, where there is still a significant amount of spatial correlation for the parallel-in-echelon antenna configuration specific to the URA and UCA. Also, the power scaling effects of mutual coupling are only noticeable at small inter-element spacings, where the URA and UCA see a reduction in eigenvalue magnitude.

5.5.3 User Rate

In this subsection, the impact of mutual coupling on user rate is explored as a function of antenna inter-element spacing, number of antennas and antenna array topology. In all results following, the 28 GHz mmWave channel [114] is simulated with mutual coupling at both the TX and RX. The user rate, R_k , with mutual coupling is then described by (2.31), with \mathbf{H} replaced with the mutually coupled channel matrix $\overline{\mathbf{H}}$, given in (2.53). In order not to mask the effects of spatial correlation and mutual coupling on the user rate by large variations in path loss, the received SNR, ρ , is assumed constant. Perfect CSI is assumed to be available at the RX for all user rate simulations.

Table 5.1: Simulation Parameters

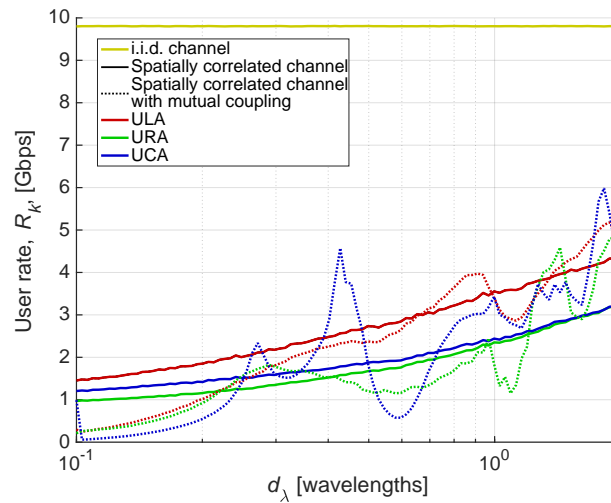
Parameter	Numerical Value
Carrier frequency, f	28 GHz
Bandwidth, B	100 MHz
Antenna length, ι	$\lambda/2$
Antenna impedance, Z_A	$73 + 42.5j \Omega$
Load impedance, Z_L	50Ω
Received SNR, ρ	10 dB
Number of clusters, C	$\sim \max[\text{Poisson}(1.8), 1]$
Number of rays per clusters, L	20
Azimuth AOA and AOD central cluster angles, $\phi_{0,c}^{\text{AOA}}, \phi_{0,c}^{\text{AOD}}$	$\sim \mathcal{U}[0, 2\pi) \forall c$
Elevation AOA and AOD central cluster angles, $\theta_{0,c}^{\text{AOA}}, \theta_{0,c}^{\text{AOD}}$	$\theta_{0,c}^{\text{AOA}} = \vartheta^{\text{AOA}} \forall c$ $\theta_{0,c}^{\text{AOD}} = \vartheta^{\text{AOD}} \forall c$
Azimuth AOA and AOD intra-cluster angular spreads	$\sigma_{\phi}^{\text{AOA}} \sim \text{Exp}(15.5)^\circ$ $\sigma_{\phi}^{\text{AOD}} \sim \text{Exp}(10.2)^\circ$
Elevation AOA and AOD intra-cluster angular spreads	$\sigma_{\theta}^{\text{AOA}} \sim \text{Exp}(6.0)^\circ$ $\sigma_{\theta}^{\text{AOD}} \sim \text{Exp}(3.9)^\circ$

Impact of Inter-Element Spacing

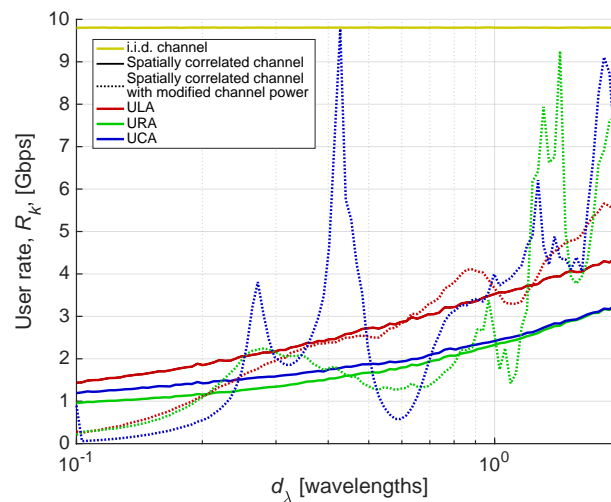
In Figure 5.10a, the single user rate vs inter-element antenna spacing with and without mutual coupling is shown for $M = 36$ TX antennas and $Q = 36$ RX antennas. Key simulation parameters are summarized in Table 5.1¹¹. Due to the very small number of clusters ($C = 1$ or 2 73% of the time [114]), all simulated channels have a poorer performance compared to the, ideal, i.i.d. channel rates [7]. When only spatial correlation is modelled, the rates of all antenna topologies increases as the inter-element antenna spacing is increased. The ULA performs the best here as it has fewer adjacent and surrounding antenna elements as compared to the URA and UCA. Also, as shown in Table 5.1, the small elevation RMS angular spreads, relative to the azimuth RMS angular spreads, limits the effectiveness of placing antenna elements with non-zero z -axis spacing. As a result, the URA and UCA performance is worse than the ULA, even for large inter-element antenna spacings, where the URA and UCA rates converge to similar values. When mutual coupling is modelled, the rates are reduced for inter-element spacings less than $d_\lambda \approx 0.65$ wavelengths for the ULA. This observation is interesting since the results presented in Section 5.5.1 show that the normalized spatial correlation is reduced for the ULA when mutual coupling is modelled. However, although the mutual coupling alters the spatial correlation structure, it also changes the effective gain of the antennas

¹¹Since [114] reports no measurable elevation AOD RMS angular spread, it is assumed that the ratio of mean azimuth to elevation RMS angular spreads is the same for AODs as AOA, i.e., $\sigma_{\theta}^{\text{AOD}} \sim \exp(6.0(10.2/15.5))^\circ = \exp(3.9)^\circ$.

[88], therefore varying the power in the resultant channel, $\overline{\mathbf{H}}$. This reduction in effective SNR was also seen in [89] for a ULA with small inter-element spacings. The oscillatory nature of the rates, against inter-element spacing, when mutual coupling is added [88] suggests that the effective gain of the antennas is strongly related to the antenna inter-element spacing. This is clearly seen by considering the UCA rate, which experiences the most channel power variation as the inter-element spacing is increased. For example, the user rate, with the UCA topology, at an inter-element spacing of $d_\lambda \approx 0.43$ wavelengths is more than eight times the rate seen at a *larger* inter-element spacing of $d_\lambda \approx 0.6$ wavelengths.



(a) Mutual coupling.



(b) Modified channel power.

Figure 5.10: User rate, R_k , vs inter-element antenna spacing, d_λ , with and without mutual coupling for $M = 36$ TX antennas, $Q = 36$ RX antennas. Key simulation parameters are detailed in Table 5.1.

To investigate the impacts of mutual coupling on the user rate by *only* variations

in the effective SNR, i.e., no spatial correlation changes, the user rate, R_k , is shown as a function of inter-element spacing, d_λ , with a modified channel power in Figure 5.10b. The variation in effective SNR, with mutual coupling, can be shown to be $v = \text{tr}(\overline{\mathbf{H}\mathbf{H}^H}) / \text{tr}(\mathbf{H}\mathbf{H}^H)$. Thus, the user rate in Figure 5.10b, is given by

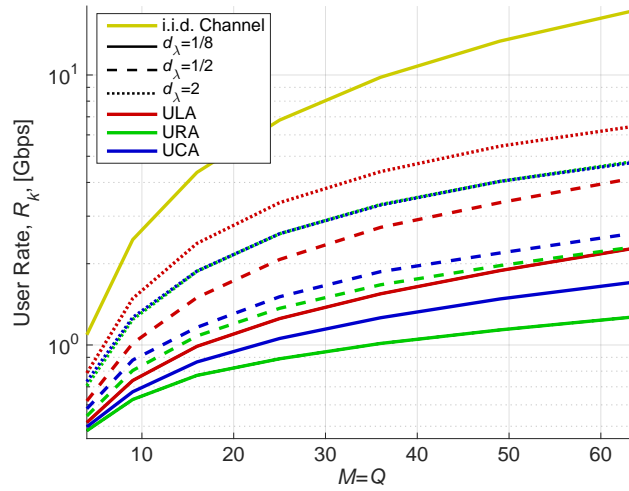
$$R_k = B \log_2 \left| \mathbf{I}_Q + \frac{\rho}{M} v \mathbf{H}\mathbf{H}^H \right|. \quad (5.69)$$

Comparing Figures 5.10a and 5.10b, reveals similar results for small inter-element spacings, where the power scaling effects are more noticeable, as discussed in Section 5.5.2. As d_λ is increased, the effects of spatial correlation become dominant and thus the two figures become dissimilar. The modified channel power user rate is more accurate for the ULA, where the spatial correlation is the lowest, than the other topologies and is emulates the effects of mutual coupling relatively well for inter-element spacings of up to $d_\lambda \approx 1$ wavelength.

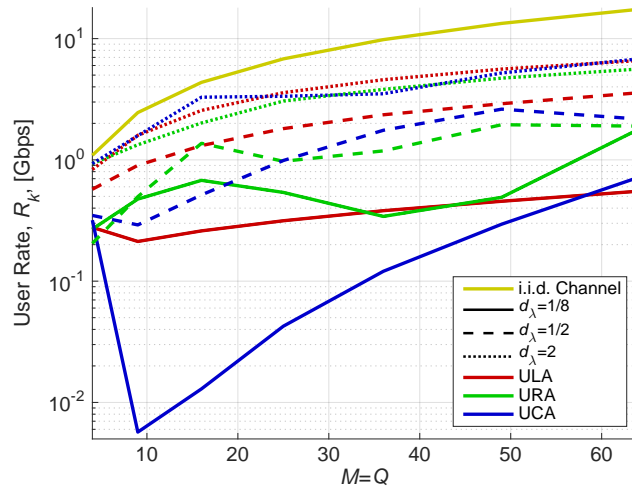
Impact of Antenna Numbers

In Figure 5.11 the impact of system size on user rate, R_k , is shown for various inter-element spacings and antenna topologies. When mutual coupling is not modelled, in Figure 5.11a, the UCA outperforms the URA for small inter-element spacings and becomes similar in performance as the inter-element spacing is increased. This trend was also seen in Figure 5.8 for the eigenvalue structure. The ULA has the largest rate for all inter-element spacings as it experiences less spatial correlation due to fewer adjacent antenna elements and larger azimuth diversity. When mutual coupling is modelled, in Figure 5.11b, the rates of the different antenna topologies are most affected at small inter-element spacings. For example, at $d_\lambda = 1/8$ and $M = Q = 9$, the UCA, relative to the URA, experiences a reduction in user rate of almost two orders of magnitude. This performance degradation of the UCA at small spacings was also seen in Figure 5.10a for $M = Q = 36$. For large inter-element spacings, the performance of the different antenna topologies become similar. There also becomes less of a difference between the performances of the relative antenna topologies at larger inter-element spacings with and without mutual coupling. This can be seen by comparing the rates of the various antenna topologies in Figures 5.11a and 5.11b, which indicates that the overall effects of mutual coupling on performance are more prominent at smaller inter-element spacings [87, 88].

When mutual coupling is not included, the ULA topology consistently has the largest user rate due to both the sparse nature of the PES and the inherently smaller number of adjacent antenna elements. The effects of mutual coupling on normalized spatial correlation do not translate into similar trends for user



(a) Spatially correlated channel.



(b) Spatially correlated channel with mutual coupling.

Figure 5.11: User rate, R_k , vs system size ($M = Q$) for various inter-element antenna spacings and antenna topologies. Key simulation parameters are detailed in Table 5.1.

rate due to the dominating effects of SNR variation. This effective antenna gain variation is strongly dependent on inter-element spacing and is seen to have more of an influence at smaller inter-element spacings.

5.6 Conclusion

In this chapter, closed-form expressions of the 3D spatial correlation have been derived for wide, narrow and Von Mises PES. An upper bound on the spatial correlation was also given for the general PES case. Diagonal dominance, a mea-

sure of massive MIMO convergence, was defined and derived for wide, narrow and Von Mises PES. The ULA was shown to have quicker diagonal dominance convergence than the URA and UCA topologies, due to the smaller numbers of adjacent antenna elements. Numerically, the effects of mutual coupling on normalized spatial correlation, eigenvalue structure and user rate was then shown. It was seen that mutual coupling impacts are more obvious at smaller inter-element spacings, agreeing with previous works [7, 24, 87, 89, 105]. At smaller inter-element spacings mutual coupling was shown to decrease the normalized spatial correlation for side-by-side antennas. However, the change to normalized spatial correlation do not translate into similar trends for user rate, as the effective gain of the antennas becomes a dominating effect [88] and its variation is shown to be highly dependent on the antenna inter-element spacings.

6

Channel Models for 5G Wireless Systems

While in previous chapters one-two channel models were considered, in this chapter channel models and measurements across a wide range of candidate bands for 5G wireless networks are considered. The chapter is motivated by the different propagation and spatial characteristics between both different bands and different channel models within the same band. Light is shed into key channel modelling and spatial parameter differences. In turn, the impact of these parameter differences for various antenna topologies is investigated in terms of system sum rate, channel eigenvalue structure, EDOF and massive MIMO convergence properties.

It is shown that because channels at mmWave bands are so sparse, any variation in spatial parameters can dramatically affect the sum rate. In microwave scenarios, where the probability of LOS propagation is low (due to larger cell radii), the structure of the eigenvalues is highly dependent on the richness of scattering. On the other hand, in mmWave bands, where the probability of LOS is high (due to smaller cell radii), the structure of the eigenvalues is largely dependent on the LOS channel model. The ULA is seen to have superior sum rate and eigenvalue structure due to the inherently larger inter-element spacings and the wider azimuth spectra (relative to elevation spectra), which makes it less effective for antennas to be placed vertically at the antenna array. These observations of the eigenvalue structure are seen to affect sum rate, EDOF and massive MIMO convergence performance.

Furthermore, an equivalent Rician channel model is developed to approximate the complex Saleh-Valenzuela channel model, proposed in [114], to model mmWave

systems. The simple equivalent model is shown to perform well for small numbers of receive antennas and is used to gain insight into mmWave channels.

6.1 Introduction

Microwave bands have a standardized 3D channel model, developed by 3GPP [129], for frequencies below 6 GHz. Here, a NLOS, i.e. scattered, channel path is modelled following the Saleh-Valenzuela [173] channel model, while LOS propagation is modelled via a Rician channel [165] extension of the NLOS component. 3GPP have also very recently published an extension of the standardized microwave 3D channel model, in [129], for frequencies above 6 GHz [130]. The additional modelling components in the new specification include: oxygen absorption (a function of the link distance), wideband transmission extensions, non-stationary user extensions, object blockages and multi-frequency simulation extensions. Therefore, the overall channel model structure remains the same as the standardized microwave channel model. This general structure of the channel model, or minor variations thereof, between different frequency bands have been supported by recent mmWave measurement campaigns. For example, the channel model presented by Akdeniz et al., in [114], for 28 and 73 GHz follows a path loss scaled Saleh-Valenzuela structure. This type of channel model is used widely in analysing beamforming techniques at mmWave frequencies, for example [133, 175]. Thus, frequency bands can not only be differentiated by slight variations in SCMs, but also by differences in key spatial parameters which form the basis of the complex channel impulse response. A detailed discussion of the differences in the channel models considered is left to Section 6.2.1. In this chapter, measurements at 6 GHz in China are reported, while both standardized SCMs [129] and recently published measurement campaigns [114, 117–119, 151, 235] are considered, all across a variety candidate frequency bands. Key channel model parameter differences between different frequency bands and different SCMs in the same frequency band are identified. In turn, the impact of these key parameters on sum rate, eigenvalue distributions and convergence to massive MIMO properties are investigated.

The second part of this chapter is motivated by the complexity of the Saleh-Valenzuela channel model, proposed by Akdeniz *et al.* [114], to model mmWave systems. The Saleh-Valenzuela channel model does not explicitly model LOS channels with a Rician K-factor as is done with the standardized models. Also, it is known that simplified statistical channel models can be used as good approximations to 3GPP microwave channels [47, 242], using Rician channels. The Rician channel model allows closed-form analysis and the exploration of signal processing techniques [165]. Therefore, the possibility of creating an *equivalent* Rician channel to approximate the Saleh-Valenzuela channel model in [114] is

investigated.

The contributions of this chapter are as follows:

1. The impact of intra-cluster angular spread and user numbers is examined for different antenna topologies on the cell edge, median and peak sum rates of different wireless channel models across microwave and mmWave bands.
2. The impacts of inter-element antenna spacings, receiver antenna numbers, propagation type and user numbers are investigated on the eigenvalue structure of various antenna topologies for different channel models across microwave and mmWave bands. Also, the rate of convergence to massive MIMO is explored by considering the eigenvalue ratio. It is shown that the rate of convergence is dependent on the environment, antenna topology and user separation.
3. A parameter is defined: EDOF, to measure the total number of data streams the system can support. The effects in terms of different antenna topologies, channel models, user numbers and numbers of receive antennas are then shown on the EDOF.
4. An equivalent Rician channel model is developed to approximate the mmWave channel and show agreement via spectral efficiency and ZF SNR. For single stream transmission, only the specular component is needed. For users with two antennas, the composition of a specular and an uncorrelated diffuse component shows good agreement. For more than two antennas per user, insights into the mmWave channel, provided by the Rician approximation, are drawn.

6.2 Channel Models

In this section the cellular environments considered are detailed, along with their respective channel model structure. A detailed discussion of the key modelling differences among the environments is also provided. The nine cellular environments considered are:

- *3GPP*: 2.6 GHz standardized channel model by 3GPP, detailed in [129].
- *BUPT*: 6 GHz measurements following the 3GPP channel model structure, carried out by Beijing University of Posts and Telecommunications (BUPT).
- *WPC*: 18 GHz measurements in a white paper collaboration (WPC), given in [151].

- *Hur*: 28 GHz measurements from a Samsung Electronics, University of Southern California, New York University, and Aalto University collaboration [119].
- *Akdeniz*: New York University 28 GHz and 73 GHz measurements given in [114].
- *Samimi*: New York University 28 GHz and 73 GHz measurements given in [235]. These measurements are for the channel model presented in [117], which extends a 2D ultra-wideband mmWave channel model given in [234]¹. The corresponding omnidirectional path loss measurements are given in [150].
- *Thomas*: 73 GHz measurements from a Nokia, Aalborg University, and New York University collaboration [118].

6.2.1 Channel Modelling Differences

All simulation environments use either variations of the Saleh-Valenzuela channel model [173] or the 3GPP channel model [129], given in (2.14) and (2.24), respectively, and described in Subsection 2.1.2.

3GPP, BUPT and WPC simulation environments follow the 3GPP channel model [129], with a different set of parameters used for users in LOS and NLOS propagation. In contrast, Samimi and Thomas environments use slight variations in the 3GPP channel model. In the case of the Samimi environment, a (different) Rician K-factor, κ , is defined for both LOS and NLOS users so that (2.24) is used to model LOS and NLOS propagation. Note that the 3GPP model only defines a K-factor for LOS channels. The 73 GHz Thomas simulation environment differs from 3GPP as it only defines a single set of spatial parameters for LOS and NLOS users. In this model LOS and NLOS users are solely differentiated by different path loss and shadow fading parameters.

On the other hand, the Akdeniz 28 GHz and 73 GHz measurements use the Saleh-Valenzuela channel model [173] described in Section 2.1.2. However, unlike the 3GPP channel model, the Saleh-Valenzuela channel model does not use a Rician channel to model LOS propagation. Instead the only difference between LOS and NLOS users is a different path loss from the BS to the user. The generation of the central cluster angles differs between the Akdeniz channel model and all other environments. In the case of the Akdeniz environment, the azimuth central cluster AOAs and AODs are generated as uniform random variables over the entire range of azimuth angles, $\phi \in [0, 2\pi)$. Also, the elevation central cluster AOAs and AODs are defined to be the LOS angle between the

¹Note: a narrowband channel model is considered and therefore the time and angular space correlation (lobe) extension, described in [234], is neglected.

BS and user. In contrast, in all environments which follow the basic 3GPP channel model structure, the azimuth and elevation central cluster angles are derived from a wrapped Gaussian and Laplacian distribution, respectively.

6.3 System Description

In this section key system and environmental specific parameters, the antenna topologies considered and channel model assumptions made are detailed.

6.3.1 Simulation Description

ULA, URA and UCA antenna topologies are considered, all described and depicted in Section 2.3. It is assumed that the cell is sectorized into 120° sectors, in which the BS serves users in this region [129]. Thus if the antenna array is broadside to an arbitrary azimuth angle, $\dot{\phi}$, then

$$[\phi_{\min}^{\text{AOD}}, \phi_{\max}^{\text{AOD}}] = [\dot{\phi} - 60^\circ, \dot{\phi} + 60^\circ]. \quad (6.1)$$

In all simulations the bandwidth is $B = 100$ MHz and cell edge received SNR is $\varrho = -5$ dB². Here, a noise figure of 8 dB, a fixed TX power of 15 dBm (independent of user numbers and carrier frequency) and a gain per TX antenna of 10 dBi are assumed. The path loss to each user is calculated via the close-in free space reference model in (2.3). Cell radii, r , for each environment are then derived from this based on 95% area coverage [4].

In Figure 6.1, the cell radius, r , is shown as a function of the carrier frequency, f , and the number of users, K , is shown for $M = 400$, $Q = 4$ and a cell edge SNR of $\varrho = -5$ dB with 95% area reliability. It can be seen that as both the carrier frequency and the number of users is increased, the cell radius is reduced. First, the TX power of 15 dBm is fixed and is thus divided over K users. Therefore, when K increases, the cell radius is seen to reduce exponentially to maintain the same average received SNR per user. Secondly, as detailed in Table 6.1, as the carrier frequency increases, the path loss offset constant, α , is increased due to higher signal attenuation [17]. Therefore, as with increasing user numbers, the cell size must be reduced.

The probability of LOS propagation, p_{LOS} , has been shown to increase with carrier frequency [17, 244], due to differences in diffraction, scattering, reflection and absorption of the wireless signal as the carrier frequency is varied. All p_{LOS} models, as a function of distance, encapsulate these effects for the various channel models. In Figure 6.2, the probability of LOS, p_{LOS} , as a function of BS to

²Although mmWave systems typically have higher bandwidth, low TX powers and strong blocking [243, 244] (resulting in a low received SNR), it is assumed that the bandwidth and received SNR is the same over all frequencies such that insights into the spatial and statistical differences of the various frequencies can be drawn.

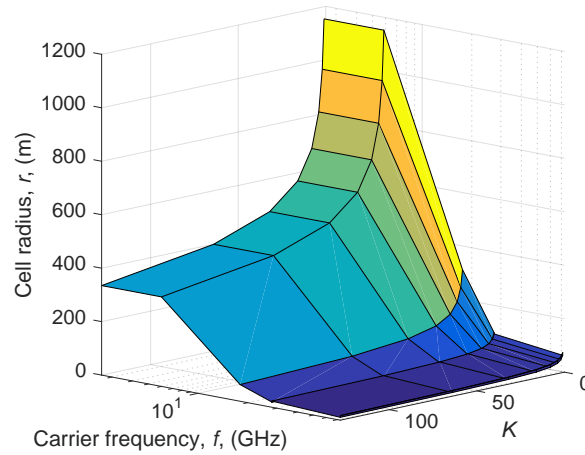


Figure 6.1: Cell radius, r , as a function of the number of users, K , and carrier frequency, f , for $M = 400$ and $Q = 4$.

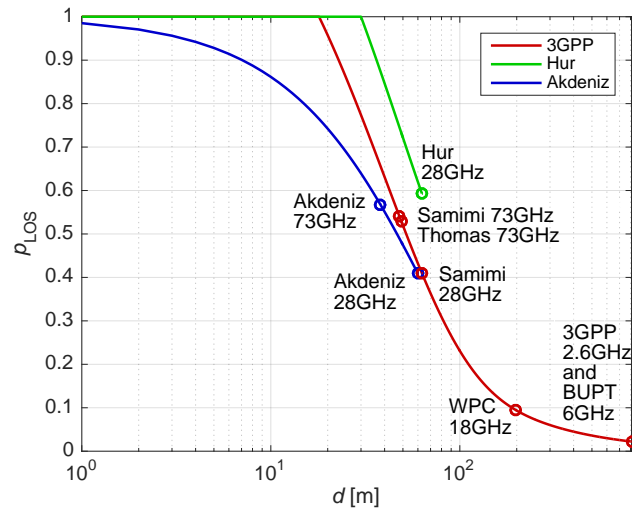


Figure 6.2: Probability of LOS propagation, p_{LOS} , as a function of BS to user distance, d , for different simulation environments.

user distance, d , is summarized for each environment. The circles represent the cell radius, where $M = 400$ and $K = 4$, based on the link budget parameters described above. Three different LOS probability models can be seen, where for a given distance, the Hur model gives the highest p_{LOS} . The mmWave environments are seen to have smaller cell radii and thus increased LOS probability for a typical user distance compared with the microwave environments.

Spatial correlation of intra-cluster spreads, Rician K-factors and shadow fading

standard deviations are modelled via [129, 245]

$$\rho(d_{k,k'}) = \exp\left(-\frac{d_{k,k'}}{d_{\text{SC}}}\right), \quad (6.2)$$

where $\rho(d_{k,k'})$ is the spatial correlation of a particular parameter between users $k, k' \in 1, \dots, K$, as a function of their separation distance $d_{k,k'}$. d_{SC} denotes the spatial correlation reference distance in the azimuth plane (different for every parameter). d_{SC} and all other key environmental statistical spatial parameters are detailed in Table 6.1. Here, ϕ_0 and θ_0 denote the central cluster angles of the azimuth and elevation domains, respectively, σ_ϕ and σ_θ denote the RMS angular spreads of the intra-cluster azimuth and elevation subpaths, respectively. Note that the per-cluster AOD elevation RMS spread, $\sigma_\theta^{\text{AOD}}$, is not specified for the mmWave measurements in [114]. We therefore assume $\sigma_\phi^{\text{AOD}}/\sigma_\theta^{\text{AOD}} = \sigma_\phi^{\text{AOA}}/\sigma_\theta^{\text{AOA}}$ for the two Akdeniz scenarios. A street width of 20m and building height of 20m are assumed for 3GPP 2.6 GHz, BUPT 6 GHz and WPC 18 GHz scenarios. We consider half-wavelength vertical dipole antenna elements with no polarization and assume that the TX and RX are static over the channel realization.

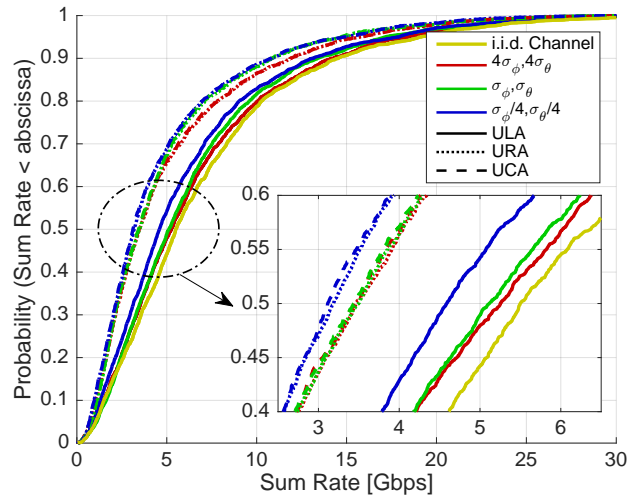
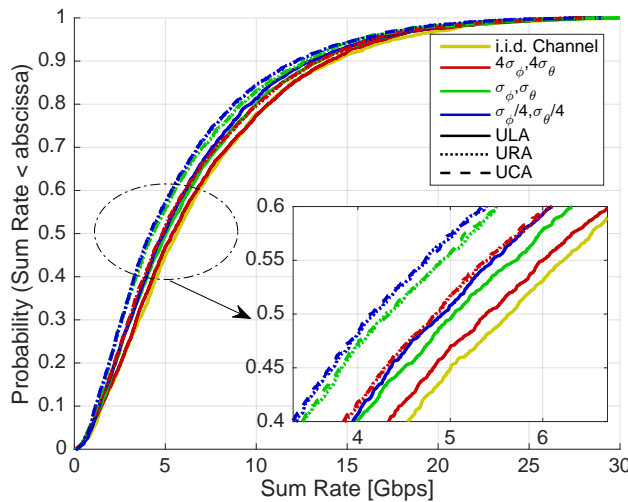
6.4 System Sum Rate

The effects of intra-cluster angular spreads, σ_ϕ and σ_θ , on the system sum rate, R , are considered for various simulation environments and bands. Also, the effects of channel modelling techniques are explored on the cell edge (0.05 CDF value), median (0.5 CDF value) and peak (0.95 CDF value) sum rates as well as the impacts of an increasing number of system users, whilst maintaining a fixed number of *total* RX antenna elements ($= KQ$). The sum rate, R , of a multi-user MIMO system can be described as given in (2.33) [28].

6.4.1 The Impact of Varying Intra-Cluster Angular Spread

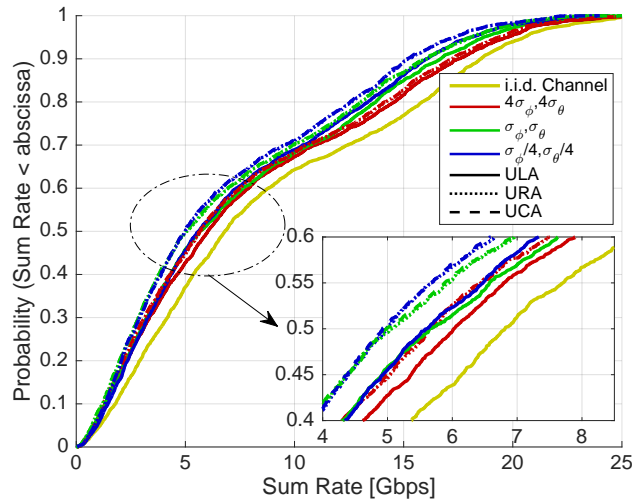
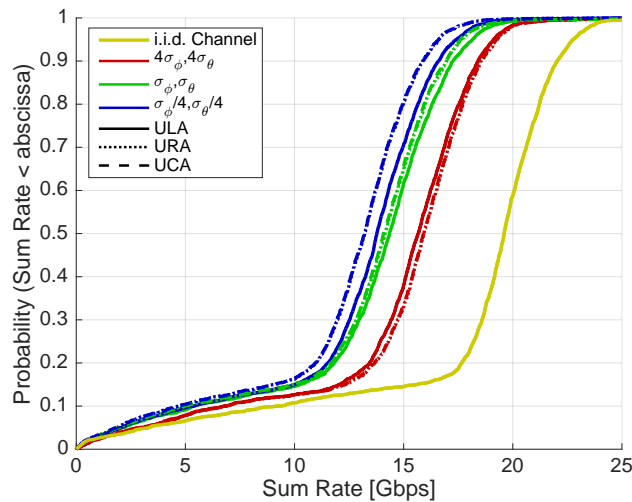
In Figures 6.3-6.11 the sum rate, R , CDFs are shown for each of the nine cellular environments, described in Section 6.2, for $M = 400$ and $K = Q = 4$, as a function of the antenna topology and intra-cluster azimuth and elevation RMS angular spreads, σ_ϕ and σ_θ , respectively³. Here both the AOA and AOD intra-cluster RMS spreads are varied from one-quarter of their tabulated values, $\sigma_\phi/4, \sigma_\theta/4$, to four times their tabulated values, $4\sigma_\phi, 4\sigma_\theta$. In each environment, cell edge users are receiving a SNR of -5 dB for all users and thus the i.i.d. channel CDFs should be similar, with marginal differences coming from differences

³Note that to find R per dimension, one should divide the sum rate by the number of streams [28].

Figure 6.3: Sum rate, R , CDF for 3GPP 2.6 GHz.Figure 6.4: Sum rate, R , CDF for BUPT 6 GHz.

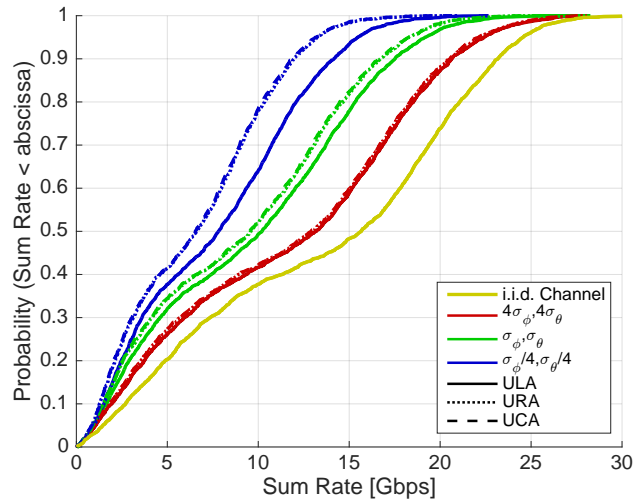
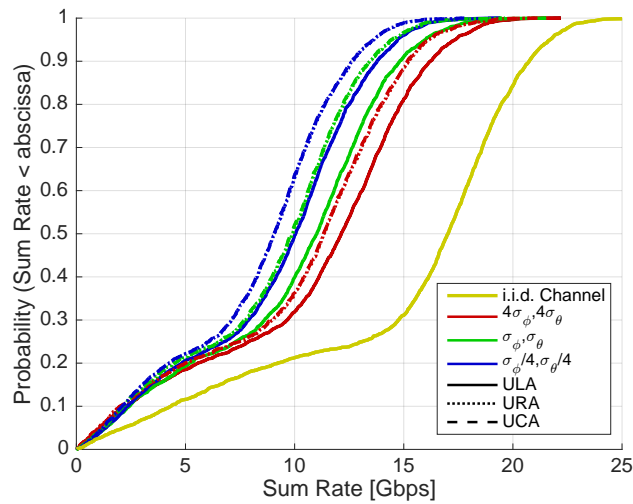
in the distribution of path loss between the models. For all environments, an increase in intra-cluster azimuth and elevation RMS angular spreads, σ_ϕ and σ_θ , produces a greater sum rate for each antenna topology resulting from more spatial diversity and, therefore, a reduction in spatial correlation.

In nearly all environments, the ULA antenna topology has the largest sum rate over all ranges of intra-cluster RMS angular spreads and CDF values. Although the ULA cannot resolve angular discrepancies in the elevation domain, it performs better because of the inherently larger inter-element spacings between antenna element combinations of the array, as well as the (nearly always) wider azimuth angular spectrum, compared with the (narrower) elevation angular spectrum. For scenarios with a very narrow intra-cluster elevation AOD RMS spread, such as the case in the Samimi 73 GHz environment, ($\sigma_\theta^{\text{AOD}} \sim \mathcal{N}(0.8, 1)$)

Figure 6.5: Sum rate, R , CDF for WPC 18 GHz.Figure 6.6: Sum rate, R , CDF for Hur 28 GHz.

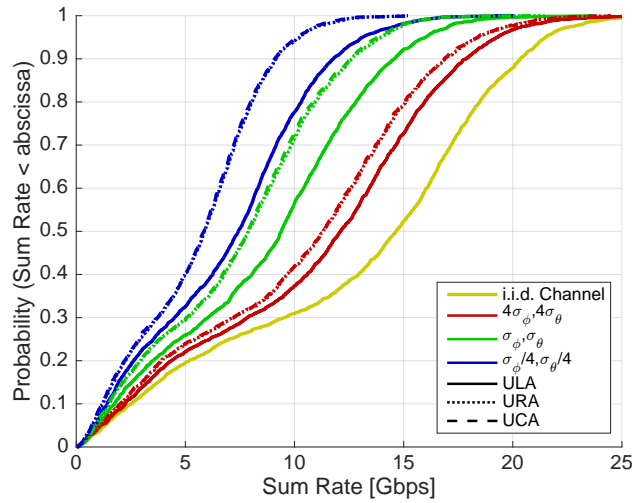
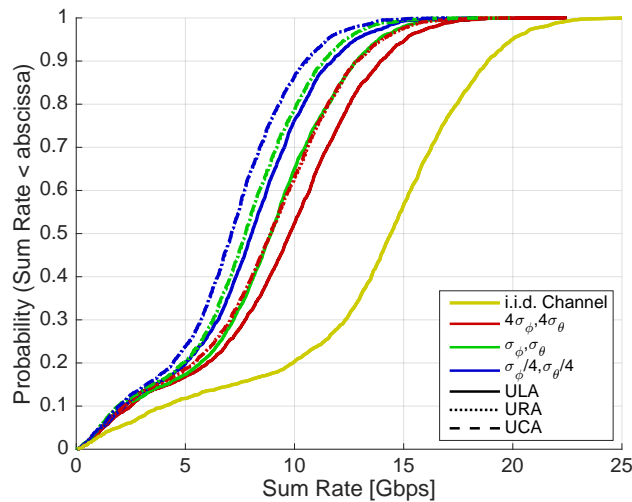
and $\sigma_{\theta}^{\text{AOD}} \sim \mathcal{N}(0.8, 1.3)$ degrees for LOS and NLOS, respectively), the URA and UCA essentially function as a smaller ULA with fewer TX antenna elements, since antenna elements stacked vertically provide a little additional gain. In the Thomas 73 GHz scenario, the URA and UCA outperform the ULA because the intra-cluster elevation RMS AOA spread is in fact larger than the corresponding azimuth angular spread. More specifically, the intra-cluster elevation RMS AOA spread (equal to $\log_{10}(\sigma_{\theta}^{\text{AOA}}) = \max[0, -0.002d + 0.83]$ degrees) is always greater than $\sigma_{\phi}^{\text{AOA}} = 5.3^{\circ}$ for every user location within the cell radius ($r = 49\text{m}$). Therefore, in the Thomas 73 GHz environment, the vertical spacing of antenna elements at the antenna array provides more benefit than horizontal spacing.

Most of the CDFs have a noticeable bimodal distribution which indicates two

Figure 6.7: Sum rate, R , CDF for Akdeniz 28 GHz.Figure 6.8: Sum rate, R , CDF for Samimi 28 GHz.

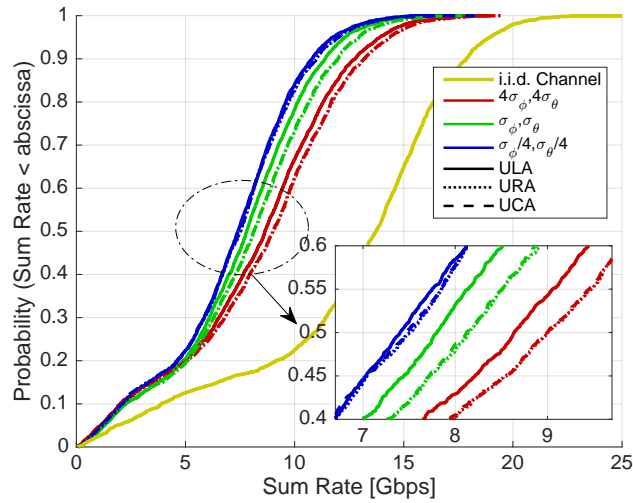
underlying PDFs, resulting from different path loss exponent, β , and shadow fading variances, ϵ^2 , for LOS and NLOS propagation. This is most obvious in the Hur 28 GHz scenario CDFs, which show a large kink just below a CDF value of 0.2. Here, the difference in the shadow fading variance between LOS and NLOS is significantly large ($\epsilon^2 = 3.4$ dB for LOS vs $\epsilon^2 = 31.8$ dB for NLOS). In the 3GPP 2.6 GHz and BUPT 6 GHz environments, the two PDFs are less obvious as both the path loss exponent and shadow fading variances are similar for LOS and NLOS (e.g., $\beta = 4$ and 3.92 73.2% of the time for 3GPP 2.6 GHz LOS and NLOS, respectively⁴). The y-axis value where the CDF changes from NLOS to LOS propagation is dependent on the LOS probability, p_{LOS} ,

⁴These values occur 73.2% of the time since the distance dependent value of β is 4 for 73.2% of the channel drops.

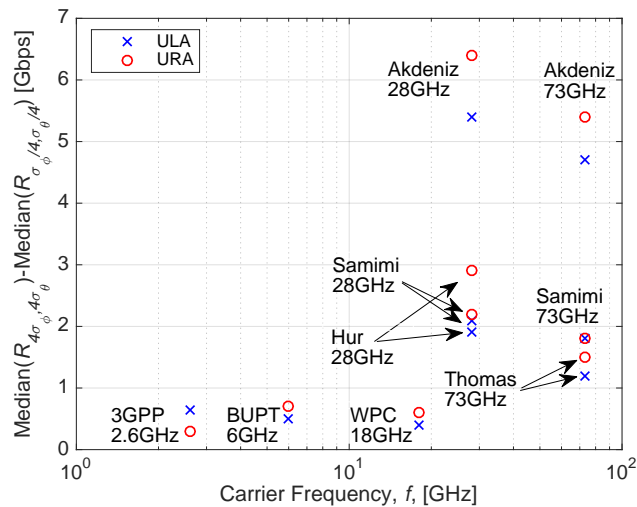
Figure 6.9: Sum rate, R , CDF for Akdeniz 73 GHz.Figure 6.10: Sum rate, R , CDF for Samimi 73 GHz.

which is a function of the BS to user distance, d , as shown in Figure 6.2 for all environments. The Hur 28 GHz scenario has the largest probability of LOS propagation over all user locations, and thus the kink occurs at a smaller CDF value than any other environment.

For environments in the microwave bands, there are typically a large number of clusters, e.g., $C = 20$ clusters for the 3GPP 2.6 GHz NLOS environment, and therefore the performance of all antenna topologies is relatively close to the (ideal) i.i.d. scenario. Here, the impact of intra-cluster RMS angular spreads on sum rate is minor as there is still richness in the scattering, even when the intra-cluster RMS angular spread is reduced to one-quarter of its measured value. On the other hand, for mmWave bands, there are large sum rate differences between the i.i.d. CDFs and the spatially correlated cases. In general, this can

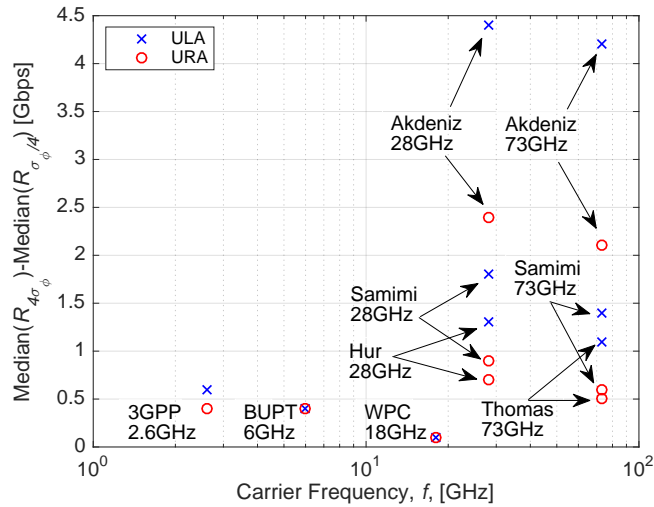
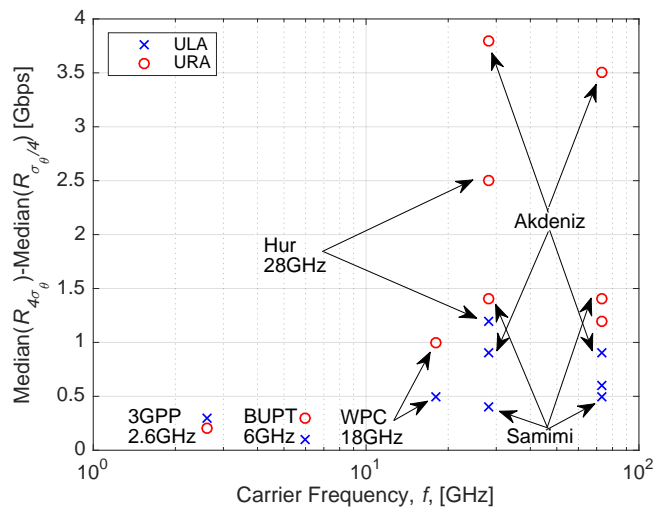
Figure 6.11: Sum rate, R , CDF for Thomas 73 GHz.

be explained by the smaller number of clusters and subpaths as well as narrower inter-cluster and intra-cluster angular spreads for the measurements at mmWave bands⁵. For example, the Akdeniz 28 GHz channel experiences just $C = 1$ or $C = 2$ clusters 73% of the time.

Figure 6.12: Azimuth and elevation RMS angular spread, σ_ϕ and σ_θ , variation.

In Figures 6.12-6.14 the difference in median sum rate, as a function of carrier frequency, f , is summarized as the intra-cluster RMS angular spread is varied between four times and one quarter the tabulated intra-cluster RMS angular spread (Table 6.1), for the ULA and URA antenna topologies with $M = 400$

⁵An exception to this statement is the inter-cluster angular spread for both 28 GHz and 73 GHz Akdeniz channels. Here, the azimuth cluster central angles are uniformly distributed over the entire range of possible azimuth angles. Whereas in all other environments, azimuth cluster central angles are normally distributed with a mean spread less than 90° .


 Figure 6.13: Azimuth RMS angular spread, σ_ϕ , variation.

 Figure 6.14: Elevation RMS angular spread, σ_θ , variation.

and $K = Q = 4$. Here it can be seen that as the intra-cluster RMS angular spreads are varied, there is a larger change in median sum rate for mmWave bands, compared with the microwave bands. When *both* azimuth and elevation intra-cluster RMS angular spreads are varied, the URA is seen to have a larger variation than the ULA in median sum rate for nearly all environments. This trend is also clearly seen in Figures 6.3-6.11 for the Akdeniz 73 GHz environment, where the relative gap between the ULA and URA median sum rate is reduced when the intra-cluster RMS angular spread is increased. When only the azimuth intra-cluster RMS angular spread, σ_ϕ , is varied, the ULA has the largest median sum rate difference as it has \sqrt{M} more antennas than the URA on the x, y -plane which are able to fully utilize the azimuth spread. On the other hand, when only the elevation intra-cluster RMS angular spread, σ_θ , varies, the

URA has a significantly larger difference in median sum rate. In this scenario, the ULA effectively only has a single antenna element with respect to the z -axis, whereas the URA has \sqrt{M} antenna elements which are able to resolve more independent subpaths.

The Akdeniz 28 and 73 GHz channels have a much larger variation than the other mmWave channels because the spread of the azimuth cluster central angles is significantly larger ($\phi_0 \sim \mathcal{U}[0, 2\pi)$). Due to the clusters having a more diverse location, any variation in the intra-cluster RMS angular spreads is likely to directly influence the sum rate. For all other simulation environments, clusters are grouped (Gaussian and Laplacian distributed for azimuth and elevation, respectively) and therefore any increase in the intra-cluster RMS angular spreads are likely to result in subpath angles from one cluster spatially overlapping with another cluster, therefore providing no additional spatial diversity. This is more evident in environments with a large number of clusters, such as 3GPP 2.6 GHz, BUPT 6 GHz and WPC 18 GHz.

6.4.2 Cell Wide Sum Rate

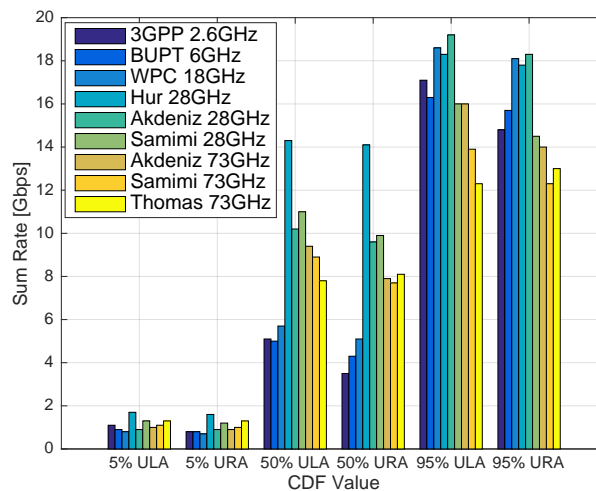


Figure 6.15: Bar chart of cell edge (5%), median (50%) and peak (95%) sum rates, R , CDF values. Different environments are shown for a ULA and URA at half-wavelength inter-element antenna spacing, where $M = 400$ and $K = Q = 4$.

In Figure 6.15, a bar chart of the cell edge (5%), median (50%) and peak (95%) sum rates is shown. Here, different environments are shown for a ULA and URA at half-wavelength inter-element antenna spacing. All environments are seen to have a similar cell edge sum rate as the corresponding SNR is fixed at -5 dB for all cases. Median rates for the mmWave bands are larger, whereas the peak sum rates are lower. This is due to the particular shape of the CDFs at different bands, seen in Figures 6.3-6.11, which are directly related to the probability of

LOS, p_{LOS} (shown in Figure 6.2). For mmWave channels the median is larger due to the LOS behaviour, evident in the rapid rise of the CDFs at higher sum rates. Whereas, in the case of 3GPP, BUPT and WPC environments, the CDF at the median is dominantly NLOS propagation. Therefore, higher median sum rates are seen in the mmWave bands due to the smaller (LOS) path loss as compared to the (NLOS) path loss of the microwave bands. As was seen in the sum rate CDFs, in Figures 6.3-6.11, the ULA performs better than the URA for most of the environments. This is most evident in the 3GPP 2.6 GHz scenario, where both the inter-cluster angular spreads and the intra-cluster RMS angular spreads are significantly larger in the azimuth domain.

6.4.3 Impact of User Numbers

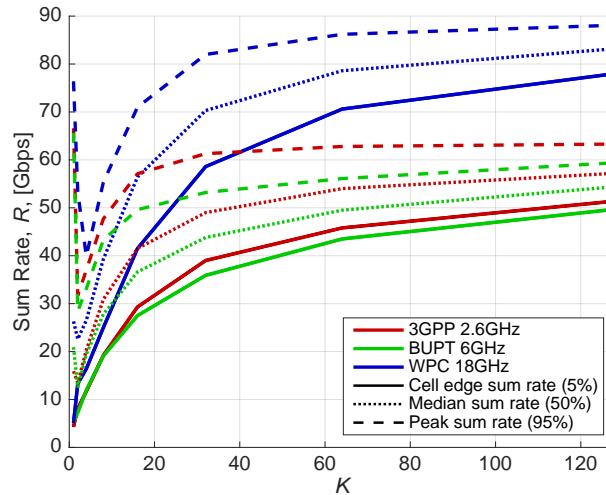


Figure 6.16: Cell edge (5%), median (50%) and peak (95%) sum rates, R , CDF values as a function of the number of users, K , where $KQ = 128$ is fixed and $M = 400$. All curves are for a ULA with a half-wavelength inter-element antenna spacing.

In Figure 6.16 the cell edge (5%), median (50%) and peak (95%) sum rates are shown as a function of the number of users, K , where the total number of receive antenna elements $KQ = 128$ is fixed⁶. All curves are for a ULA with a half-wavelength inter-element antenna spacing. As the number of users increases beyond $K = 4$ (and the number of receive antennas per user, Q , decreases), the sum rate increases. This is due to the reduced receive spatial correlation at each receiver and the resultant increase in spatial diversity by having widely

⁶Since the sum rate performance when users become more closely spaced is of interest, only 3GPP, BUPT and WPC environments are considered since they define spatial correlation reference distances between parameters, d_{SC} . In none of the other environments are any of these distances given.

separated users, and therefore antennas. However, as the number of users, K , is increased further, the cell radius shrinks due to the fixed transmit power of 15 dBm divided equally amongst the users (this is shown in Figure 6.1). As a result, users become more closely spaced and experience spatial correlation amongst their parameters. This is one factor in the saturation of the sum rate. The initial drop in peak rates as K increases is due to the fact that one user with excellent signal strength will make very good use of its antennas and achieve a very high peak rate. In contrast, it is less likely to find two users, both experiencing excellent signal strength.

The WPC 18 GHz environment is seen to significantly outperform the 3GPP 2.6 GHz and BUPT 6 GHz cellular environments in all CDF sum rate values shown. This can be explained by the much larger NLOS path loss offset constant, α , used to calculate the cell radius, r , resulting in a much smaller cell size for the WPC 18 GHz environment, as compared to the other two environments. For example, for $K = 128$ users, the cell radius of the WPC 18 GHz environment is $r = 62\text{m}$, whereas the 3GPP 2.6 GHz and BUPT 6 GHz cell radii are both $r = 334\text{m}$. For smaller cell sizes, users have a higher probability of LOS propagation and therefore less path loss on average, boosting the signal power and sum rate. For example, (as shown in Figure 6.2) for $K = 128$ users, WPC 18 GHz $p_{\text{LOS}} = 0.42$, whereas 3GPP 2.6 GHz and BUPT 6 GHz $p_{\text{LOS}} = 0.05$. The BUPT environment performs the worst since, on average, the Rician K-factor is the largest, therefore further reducing the channel rank [166] and sum rate.

6.5 Channel Eigenvalue Properties

In this section the effects of inter-element antenna spacing, receiver antenna numbers, Q , propagation type and user numbers, K , on the eigenvalue distributions and EDOF of the various antenna array topologies is investigated.

6.5.1 Impact of Inter-Element Antenna Spacings

Spatial multiplexing abilities of the antenna array topologies are evaluated by considering the normalized eigenvalue magnitudes [233]. The magnitude of the i th normalized eigenvalue, $\bar{\eta}_i^2$, is given as

$$\bar{\eta}_i^2 = \frac{\eta_i^2}{\sum_{i'=1}^{KQ} \eta_{i'}^2}, \quad (6.3)$$

where η_i denotes the i th singular value of $\mathbf{H}\mathbf{H}^H$. The normalized eigenvalue magnitude is useful in constructing a measure of the maximum number of eigenchannels for spatial multiplexing.

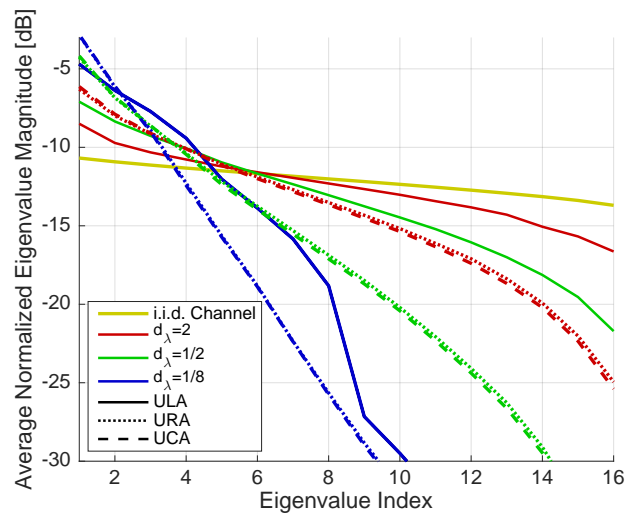


Figure 6.17: Average normalized eigenvalue magnitude vs eigenvalue index for 3GPP 2.6 GHz.

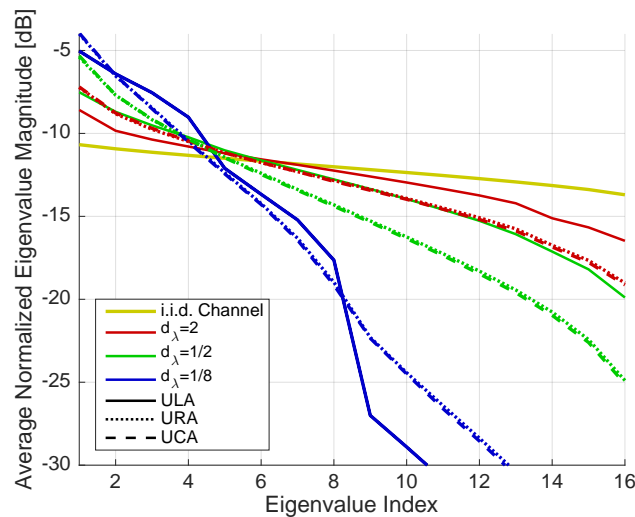


Figure 6.18: Average normalized eigenvalue magnitude vs eigenvalue index for BUPT 6 GHz.

In Figures 6.17-6.25 the average normalized eigenvalue magnitude vs eigenvalue index is shown as a function of antenna topology and antenna inter-element spacings for $M = 400$, $K = 1$ and $Q = 16$, where d_λ denotes the inter-element antenna spacing in wavelengths. In every scenario, the average normalized eigenvalue magnitude axis is truncated at -30 dB, as all eigenvalues below this value are extremely weak and do not contribute to the spatial multiplexing capabilities of the TX antenna array. Due to the large number of TX antennas ($M = 400$), it can be seen that the i.i.d. channel has almost equal eigenvalues. If the number of TX antennas, M , was to increase further, one would expect the eigenvalues would converge in magnitude (known as favourable propagation [43]). For

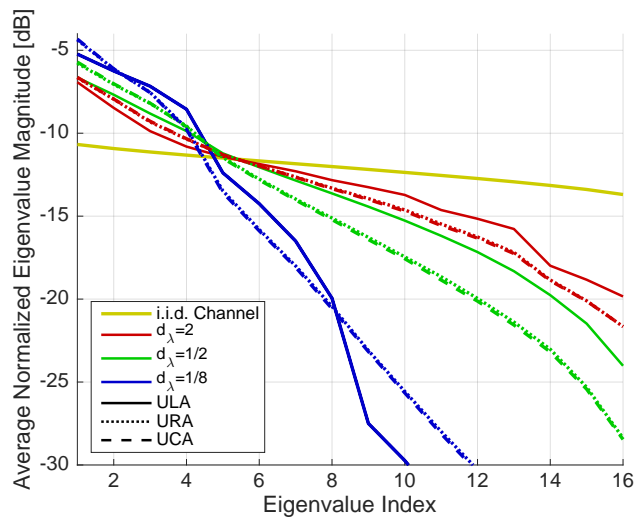


Figure 6.19: Average normalized eigenvalue magnitude vs eigenvalue index for WPC 18 GHz.

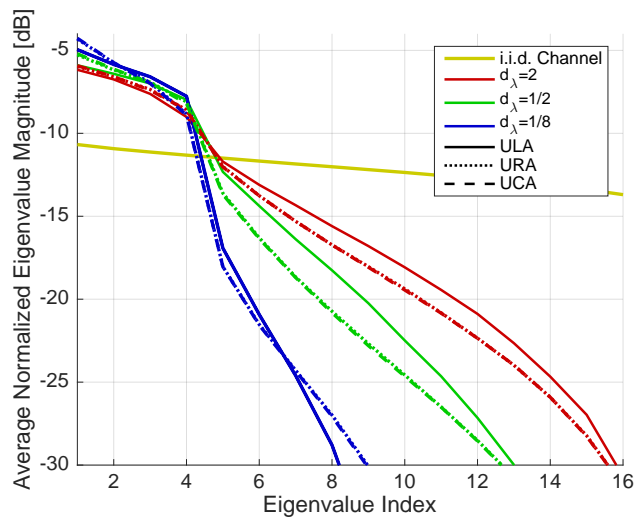


Figure 6.20: Average normalized eigenvalue magnitude vs eigenvalue index for Hur 28 GHz.

spatially correlated channels in every environment, the eigenvalue magnitudes become more equal [48] as the antenna inter-element spacing is increased from $d_\lambda = 1/8$ to $d_\lambda = 2$ wavelengths.

For the microwave bands, the magnitude of the eigenvalues with large antenna spacings are reasonably equal and approach the i.i.d. case. For example, in the BUPT 6 GHz environment, the smallest (16th) eigenvalue for a ULA with $d_\lambda = 2$ wavelengths is only about 3 dB less than the corresponding i.i.d. eigenvalue. Whereas, in the mmWave bands, the eigenvalue magnitudes are significantly reduced. For example, in the Thomas 73 GHz environment, the average normalized magnitude of the 16th eigenvalue is below -30 dB, even for large antenna

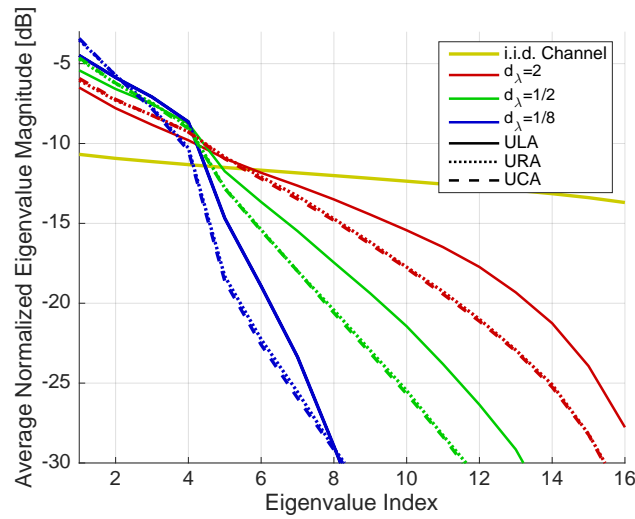


Figure 6.21: Average normalized eigenvalue magnitude vs eigenvalue index for Akdeniz 28 GHz.

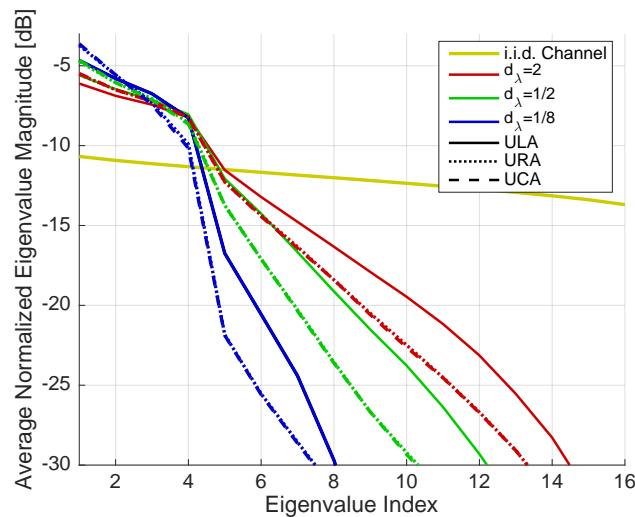


Figure 6.22: Average normalized eigenvalue magnitude vs eigenvalue index for Samimi 28 GHz.

inter-element spacings. This is a result of the small number of clusters seen at mmWave frequencies which effectively reduces the multipath richness of the channel. For more sparse channels, at mmWave bands, a greater inter-element spacing is required to get the same eigenvalue structure as the rich scattering microwave environments, e.g., the URA and UCA eigenvalue structure in the Akdeniz 73 GHz for $d_\lambda = 1/2$ is approximately the same as the 3GPP 2.6 GHz at $d_\lambda = 1/8$. This is intuitive since the spatial coherence distance is inversely proportional to the angular spread.

As was the case for the sum rate in Section 6.4, the ULA usually performs the best in terms of spatial multiplexing over all environments, due to the inher-

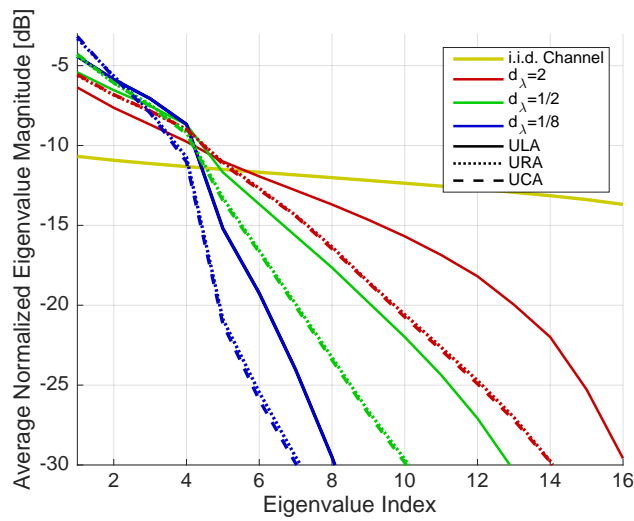


Figure 6.23: Average normalized eigenvalue magnitude vs eigenvalue index for Akdeniz 73 GHz.

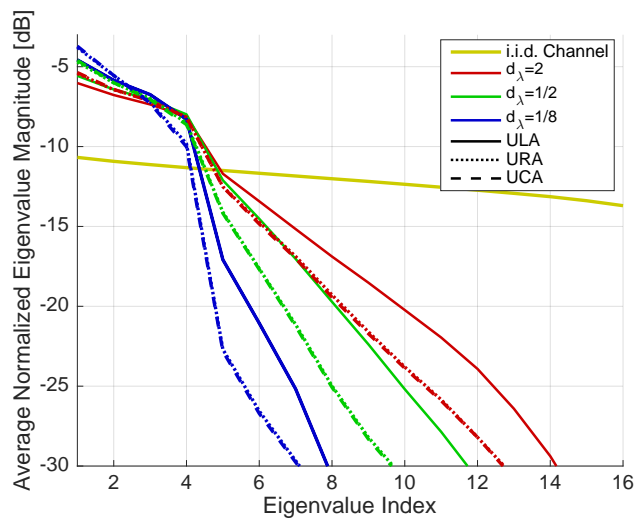


Figure 6.24: Average normalized eigenvalue magnitude vs eigenvalue index for Samimi 73 GHz.

ently larger antenna spacings. The wider azimuth spectrum, compared to the elevation spectrum, makes it more effective for antennas to be placed in the azimuth domain. In scenarios with sparse elevation scattering, such as BUPT 6 GHz, additional inter-element spacing is required for the URA and UCA to have the same eigenvalue structure as the ULA, e.g., the URA and UCA eigenvalue structure at $d_\lambda = 2$ is approximately the same as the ULA for just $d_\lambda = 1/2$.

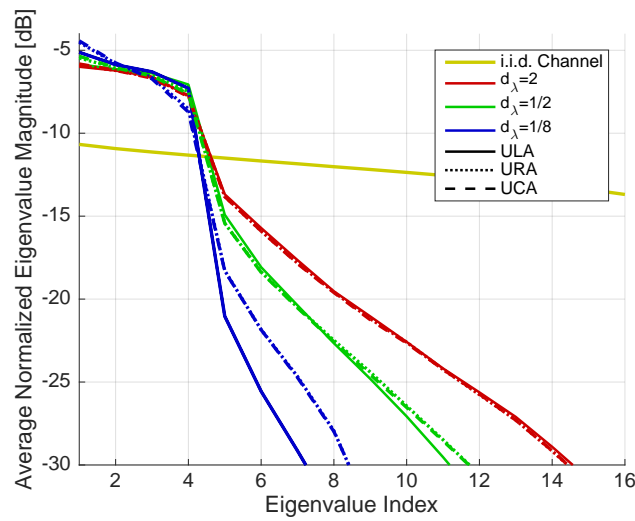


Figure 6.25: Average normalized eigenvalue magnitude vs eigenvalue index for Thomas 73 GHz.

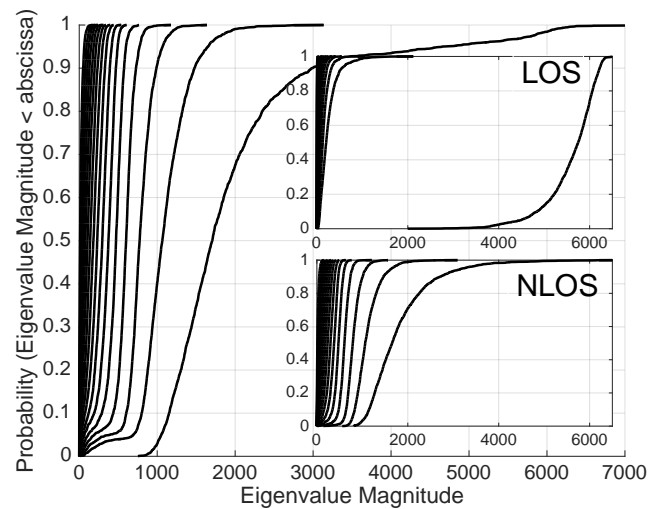


Figure 6.26: Single-user eigenvalue CDFs with a half-wavelength spacing ULA for 3GPP 2.6 GHz.

6.5.2 Impact of Propagation Type

In Figures 6.26-6.34 single-user eigenvalue CDFs are shown for a ULA with half-wavelength spacings, for $M = 400$ and $Q = 16$. For each environment, the combined channel eigenvalue CDFs as well as both the LOS and NLOS eigenvalue CDFs are shown. As the carrier frequency is increased from microwave to mmWave bands, the eigenvalue CDFs become more widely spread. For example, the Thomas 73 GHz environment only has a single eigenvalue which is much larger in magnitude than all the others. This is a result of both the lack of randomness in the channel, which is coming from smaller numbers of clusters

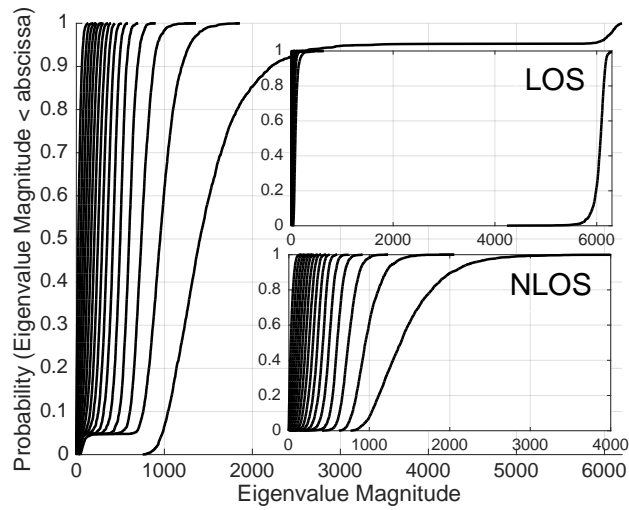


Figure 6.27: Single-user eigenvalue CDFs with a half-wavelength spacing ULA for BUPT 6 GHz.

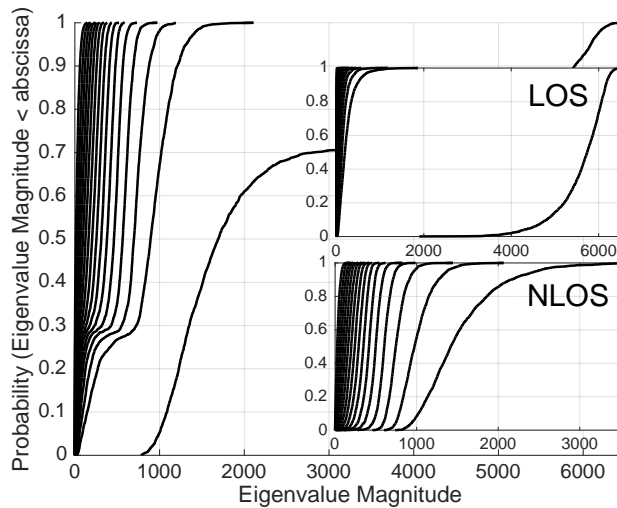


Figure 6.28: Single-user eigenvalue CDFs with a half-wavelength spacing ULA for WPC 18 GHz.

and subpaths, and the increased probability of LOS propagation, causing the combined eigenvalue CDFs to have more similarity to the LOS only case.

The distribution of the NLOS eigenvalue CDFs are completely dependent on the amount of scattering in the environments. In microwave environments, there are large numbers of clusters and subpaths, therefore the NLOS eigenvalue CDFs are more similar than the corresponding mmWave NLOS eigenvalues. On the other hand, the distribution of the LOS eigenvalue CDFs are dependent on how LOS propagation is modelled.

In the simulation environments which use a Rician channel to model LOS propagation exclusively (i.e., all environments except Akdeniz and Samimi), the

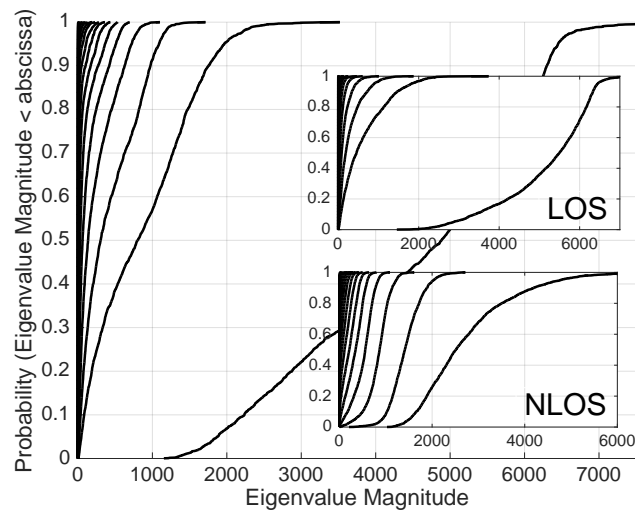


Figure 6.29: Single-user eigenvalue CDFs with a half-wavelength spacing ULA for Hur 28 GHz.

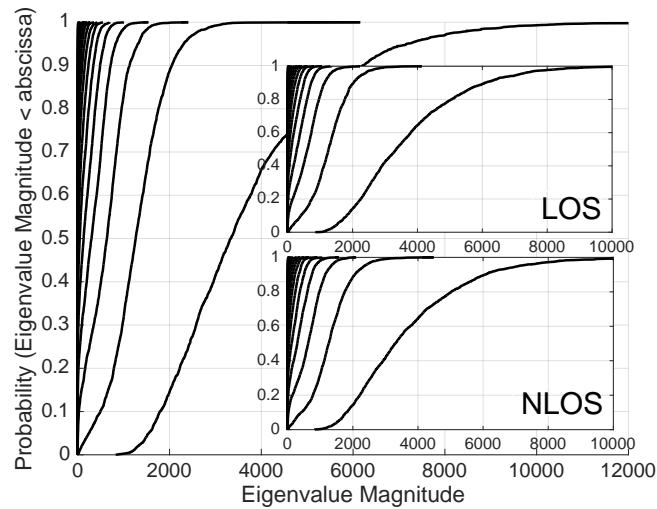


Figure 6.30: Single-user eigenvalue CDFs with a half-wavelength spacing ULA for Akdeniz 28 GHz.

distribution of LOS eigenvalues are seen to have just one dominant CDF. The Rician K-factor mean in these environments is large (e.g., 9 dB for 3GPP) and thus the one dominant eigenvalue represents the strong specular ray. The magnitude of this dominant eigenvalue, in LOS propagation, increases as the Rician K-factor increases. Furthermore, as the Rician K-factor increases, the variability of the dominant eigenvalue reduces. This is due to an increased proportion of the, deterministic, specular component in the combined channel. For example, the BUPT 6 GHz environment has a mean Rician K-factor of 12.4 dB (vs 9 dB for 3GPP) and the dominant LOS eigenvalue CDF is seen to be almost vertical at a magnitude of 6000 (vs a variability of almost 2000 for 3GPP). In

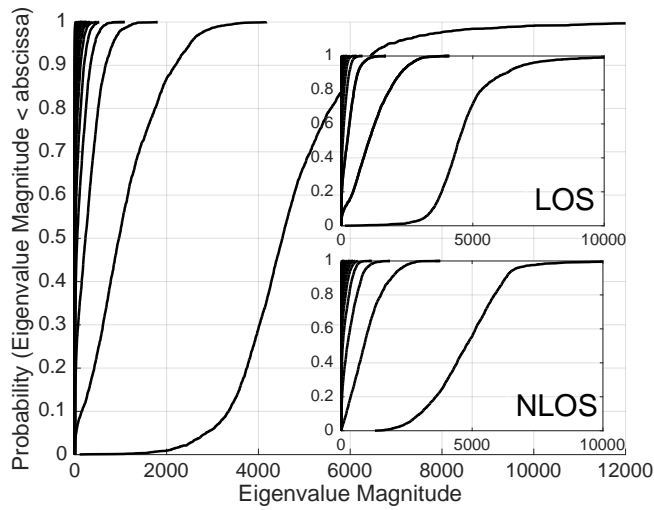


Figure 6.31: Single-user eigenvalue CDFs with a half-wavelength spacing ULA for Samimi 28 GHz.

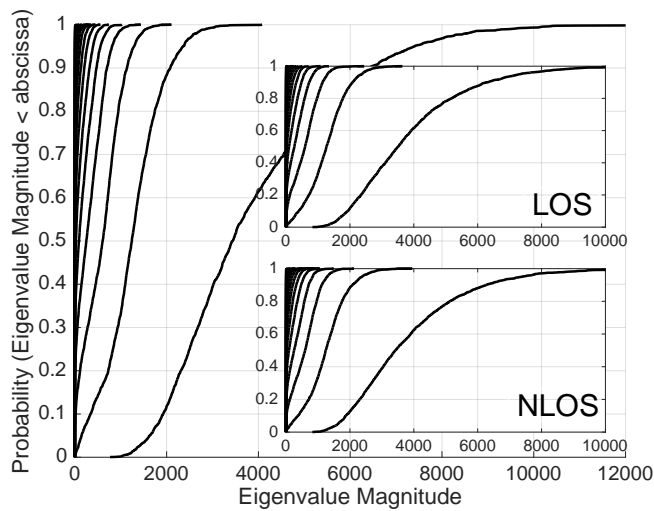


Figure 6.32: Single-user eigenvalue CDFs with a half-wavelength spacing ULA for Akdeniz 73 GHz.

the Samimi simulation environments, a Rician channel is used to model both LOS and NLOS propagation, therefore the eigenvalue CDFs are more similar than the environments which only use a Rician channel for LOS propagation. The small difference between LOS and NLOS eigenvalues for the Samimi environments is mostly coming from the difference in Rician K-factor mean and standard deviation of the two propagation types. However, in the Akdeniz environments, the eigenvalues for LOS and NLOS are exactly the same⁷, since the only difference in the channel modelling approach between LOS and NLOS come from different path loss parameters, which do not affect the eigenvalue

⁷This is only true for a single-user channel, as is shown in Figures 6.26-6.34.

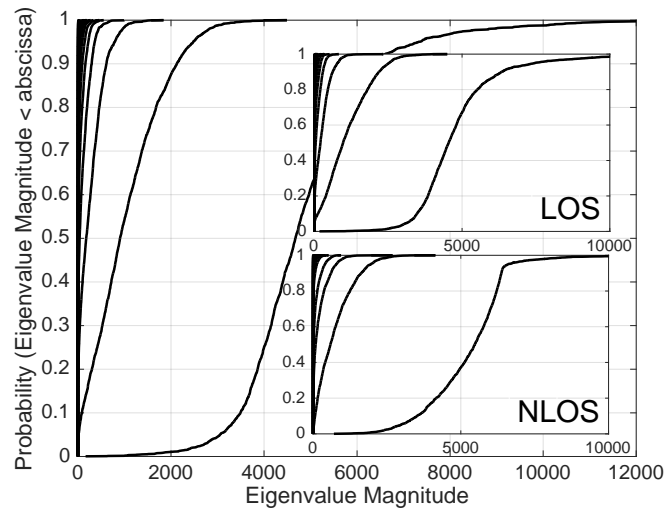


Figure 6.33: Single-user eigenvalue CDFs with a half-wavelength spacing ULA for Samimi 73 GHz.

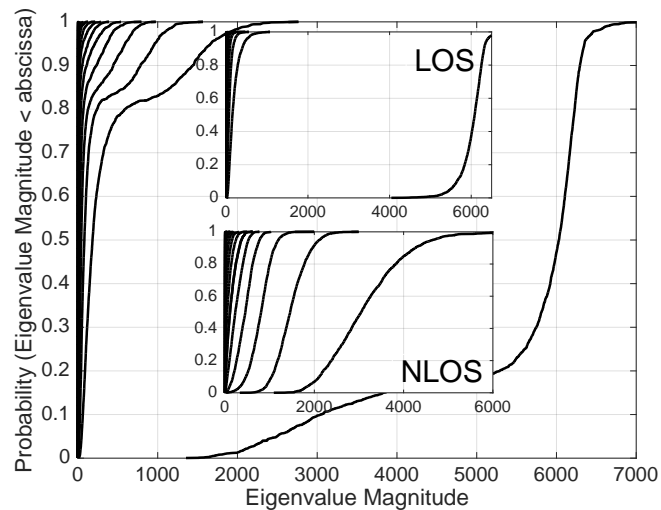


Figure 6.34: Single-user eigenvalue CDFs with a half-wavelength spacing ULA for Thomas 73 GHz.

structure.

In summary, the largest channel eigenvalue is dependent on how the LOS channel is modelled. For Rician channels, such as 3GPP, the dominant eigenvalue represents a strong specular, deterministic, path whereas for Akdeniz environments, the largest eigenvalue is coming from a lack of clusters and variation of the path loss parameters. However, this strong difference in eigenvalue structure between the different channel models is less obvious in the sum rate results, in Section 6.4, since LOS probability and variation in the path loss parameters dominate the shape of the CDFs.

6.6 Channel Effective Degrees of Freedom

EDOF is motivated by the fact that in typical (rank deficient) systems, many of the smallest eigenvalues contribute little to the system rate (seen in (2.32) and (2.33)). Therefore, the conventional DOF system measure $= \min(KQ, M)$ becomes misleading. A new metric EDOF is proposed to more accurately quantify the number of independent data streams in which the system can simultaneously support. Thus, EDOF is defined as the number of eigenchannels which contribute to greater than or equal to 1% of the sum rate. In this section, the impact of receiver antenna numbers and user numbers on both the EDOF and EDOF% is explored, where EDOF% is defined as

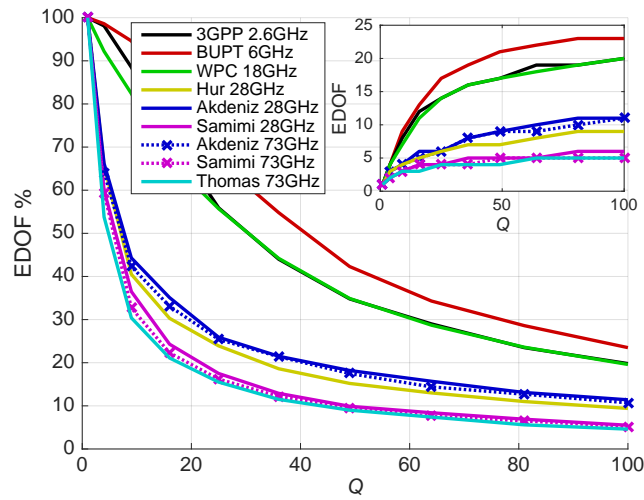
$$\text{EDOF\%} = 100 \frac{\text{EDOF}}{\min(M, KQ)}, \quad (6.4)$$

i.e., the EDOF of the system out of the total possible streams available.

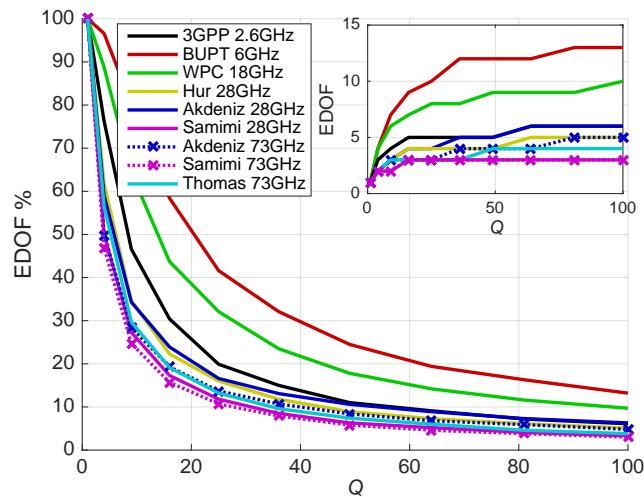
6.6.1 Impact of Receiver Antenna Numbers

In Figure 6.35, the EDOF and EDOF% are shown for the ULA and URA as a function of the number of receive antennas, Q , for a single-user, with $M = 400$. Both the ULA and URA antenna topologies have half-wavelength antenna spacings at both the TX and RX. As the number of receive antennas at the user increases from $Q = 1$ to $Q = 100$, the EDOF increases. Therefore it is better to have more users with less receive antennas. However, the increase in EDOF of all environments starts to saturate to a fixed value, as Q increases to 100. This suggests that adding more and more antennas at the user gives diminishing returns on the EDOF and therefore the EDOF% for all environments decreases as Q increases. Note that the ULA EDOF at $Q = 16$ can be compared to Figures 6.26-6.34. For example, the EDOF for the Samimi 73 GHz environment at $Q = 16$ is approximately three. Correspondingly in Figure Figures 6.26-6.34, the Samimi 73 GHz environment shows three significant eigenvalue CDFs.

In general, the EDOF decreases with frequency and there is little gain in adding more receive antennas at the mmWave bands as compared to microwave bands. This is because when the number of clusters is large, there is a reduced spatial correlation and thus more independent data streams can be supported. For example, at $Q = 40$ receive antennas, the ULA EDOF% for the Thomas 73 GHz scenario is 10%, whereas the corresponding EDOF% for the BUPT 6 GHz is 50%. Therefore, at 73 GHz the ULA is only sending 4 spatial streams vs 20 spatial streams at 6 GHz. In these environments, the intra-cluster azimuth AOA RMS spread, $\sigma_{\theta}^{\text{AOA}}$, is 5.5 and 4.5 times larger in the BUPT 6 GHz case, for LOS and NLOS propagation, respectively. At the mmWave scenarios, when the EDOF is reduced, the number of eigenvalues which contribute to sum rate



(a) ULA half-wavelength inter-element antenna spacing.



(b) URA half-wavelength inter-element antenna spacing.

Figure 6.35: Single-user ($K = 1$) EDOF% as a function of the number of receive antennas, Q , for $M = 400$.

is reduced and therefore the rate per dimension [28] is increased. This results in a higher order of modulation needed [246].

Even at the same frequency, there is still a large difference in EDOF% performance, e.g., the Akdeniz and Samimi 28 GHz environments have a constant difference in EDOF% as the number of receive antennas increases beyond about $Q = 20$. This is more evident in the case of the ULA topology. Even though the Samimi 28 GHz environment has larger cluster numbers, the Akdeniz 28 GHz environment has a greater azimuth angular diversity for both intra-cluster and inter-cluster spreads which result in the ULA supporting more spatial streams.

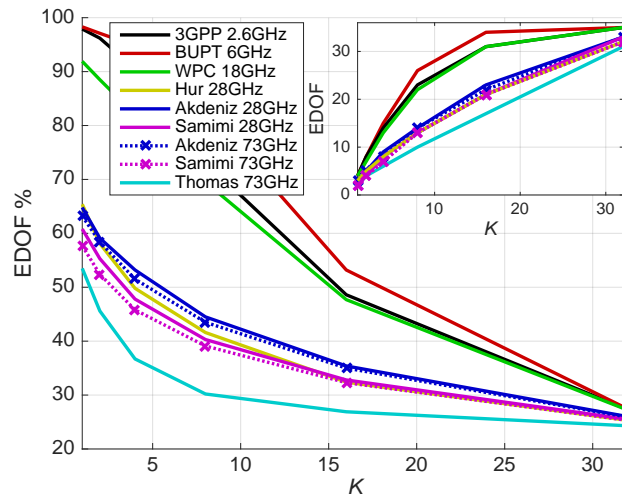
Comparing the EDOF% of the ULA and URA, in Figure 6.35, the URA has a significantly worse performance for all environments. As the number of receive antennas, Q , increases, the inter-cluster and intra-cluster AOA spreads have more of an effect on the EDOF. For example, at $Q = 100$ receive antennas at the user, the ULA provides 20 EDOF for the 3GPP 2.6 GHz environment, whereas the URA only provides 6 EDOF. The NLOS intra-cluster AOA RMS spreads here are $\sigma_{\phi}^{\text{AOA}} = 15^\circ$ and $\sigma_{\theta}^{\text{AOA}} = 3^\circ$, for azimuth and elevation domains, respectively. Compared with the azimuth AOA spreads, the narrow elevation AOA spreads are significantly reducing the EDOF when antennas are placed vertically at the BS.

6.6.2 Impact of Number of Users

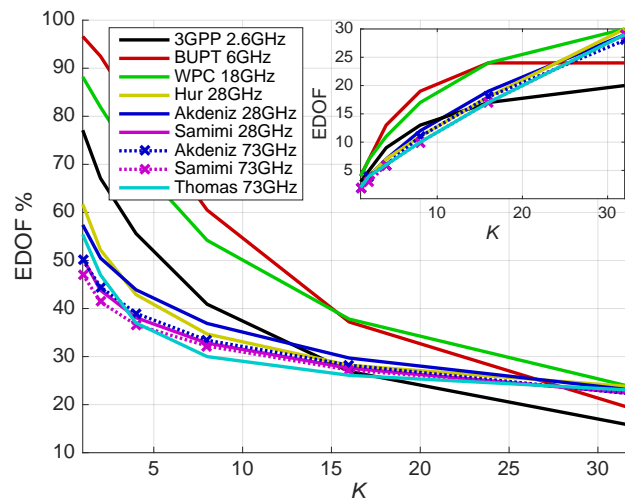
In Figure 6.36 the impact of user numbers on the EDOF% and EDOF is shown, where $M = 400$ and $Q = 4$. Both ULA and URA topologies are considered with a half-wavelength spacing at the TX and RX. As the number of users, K , increases, the EDOF for each environment also increases. However, the increase in EDOF is at a smaller rate than the number of users, K , and so the EDOF% decreases in every case. In general, the microwave bands have more EDOF than the mmWave bands, as was the case in Section 6.6.1, as a function of the number of receive antennas, Q , due to richer scattering. However, the increase in EDOF for the microwave environments starts to saturate for large numbers of users, whereas the mmWave bands increase almost linearly with K . This is because users start to experience similar channels, thus reducing the number of independent streams.

At mmWave frequencies there are very little difference between the EDOF and EDOF% performances of the ULA and URA, since the azimuth and elevation angular spectrums are more equal in width at higher frequencies. However, for the microwave bands, the ULA performs the best for all numbers of users due to the very narrow elevation spectrum. For example, as the number of users is increased to more than $K = 16$, the ULA in all mmWave bands outperform the URA in the 3GPP 2.6 GHz environment, since there is a narrow elevation spectrum in the 3GPP 2.6 GHz environment.

In summary, from Figures 6.35 and 6.36, it is more beneficial to add more users in a system instead of more antennas per user, since the increased spatial separation of users reduces the spatial correlation. This is more evident in environments which have narrow angular spectrums.



(a) ULA half-wavelength inter-element antenna spacing.



(b) URA half-wavelength inter-element antenna spacing.

Figure 6.36: EDOF% as a function of the number of users, K , for $M = 400$ and $Q = 4$.

6.7 Channel Convergence to Massive MIMO

To examine the convergence to the massive MIMO regime, the eigenvalue ratio of the composite channel matrix, \mathbf{H} , is considered and defined as given in (3.2). In Figures 6.37-6.39 the CDF of the eigenvalue ratio, with $M = 400$, $K = Q = 4$ and half-wavelength spacing is shown as a function of different user spatial separations [65, 69, 75] and antenna array topologies for 3GPP, BUPT and WPC environments, which define spatial correlation between parameters. For each environment two user location scenarios are considered: users randomly located

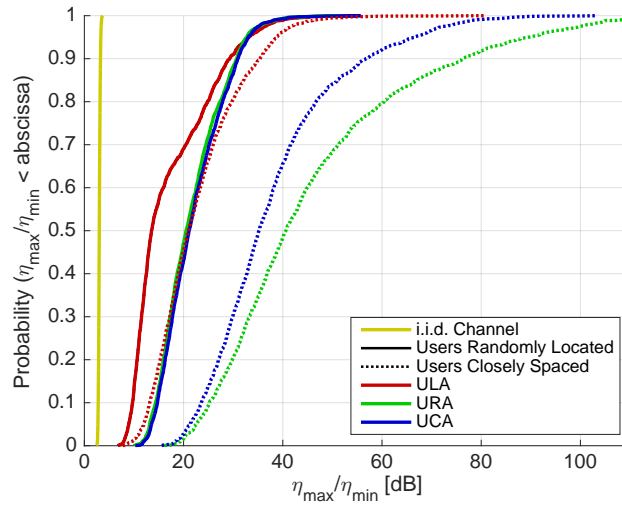


Figure 6.37: Eigenvalue Ratio CDF with randomly and closely spaced users for 3GPP 2.6 GHz.

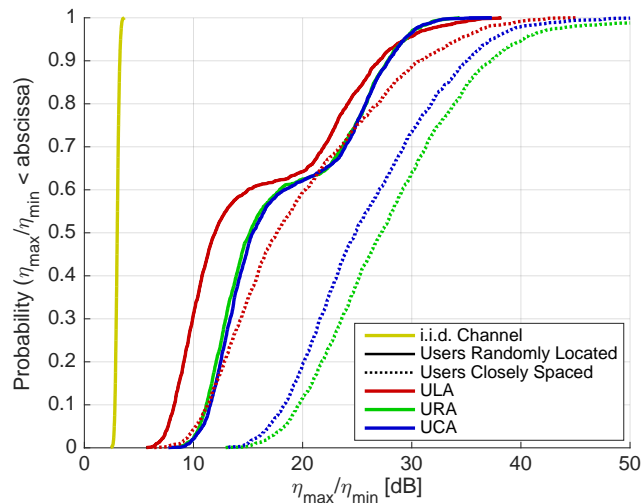


Figure 6.38: Eigenvalue Ratio CDF with randomly and closely spaced users for BUPT 6 GHz.

within the coverage region and users located within 2m of each other (closely spaced) on the *azimuth* plane. Closely spaced users experience correlated parameters, share the same clusters, but have independent subpaths. For all environments, users being randomly located is shown to reduce the eigenvalue ratio and approach the i.i.d. eigenvalue ratio, which is almost vertical due to the large number of transmit antennas, $M = 400$, therefore approaching favourable propagation [6, 7, 43, 247]. On the other hand when users are closely spaced, the highly correlated user channels are reducing the composite channel rank, and in turn, degrading the onset of favourable propagation.

Close user spacing is shown to have a significantly adverse impact on eigenvalue

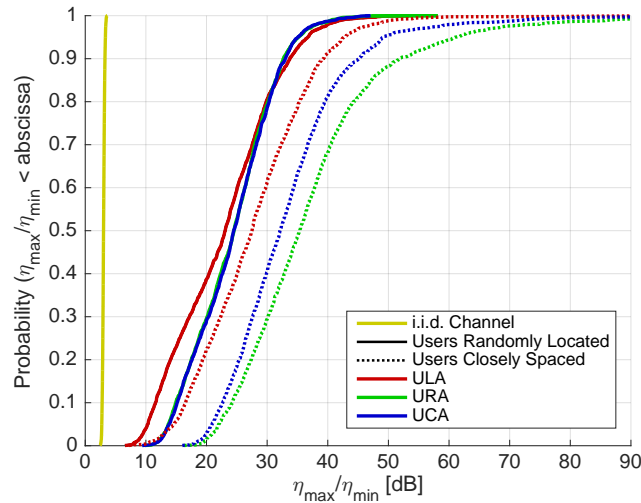


Figure 6.39: Eigenvalue Ratio CDF with randomly and closely spaced users for WPC 18 GHz.

ratio convergence for all environments, but less so in the WPC 18 GHz environment, which only has a reduction in the median eigenvalue ratio of 4 dB for the ULA topology. This is because the WPC has a wider azimuth power spectrum in comparison to the 3GPP and BUPT scenarios. The CDF knee in many of the CDFs indicates a bimodal distribution and is due to the large difference in parameters between LOS and NLOS propagation. This is most noticeable for the BUPT environment which has a Rician K-factor mean of 12.4 dB (vs. 9 dB for both 3GPP and WPC).

Comparing the relative convergence rates of the different antenna topologies in Figures 6.37-6.39, it can be seen that the ULA performance is superior in all cases where users are randomly located and closely spaced, agreeing with the results presented in [65]. This is a consequence of the large aperture of the ULA, which is able to resolve more spatial variation, thus reducing spatial correlation effects. Even for closely spaced users, the ULA still has the same performance as the URA and UCA for randomly located users. Therefore, the ULA is recommended as the antenna array approaches the onset of favourable propagation more quickly than the URA and UCA.

6.8 Equivalent Rician Fading Channel Model

The proposed Akdeniz mmWave channel model in [114], and (2.14), does not model LOS scenarios with an explicit specular component as in (2.24), but instead gives more variability to the size of the small-scale fading coefficients so that some paths tend to dominate leading to a similar effect.

In this section, a new model to approximate the, complex, Saleh-Valenzuela

channel model is proposed based on the classical statistical Rician fading channel model. If such a process is possible, then it opens up more opportunities for system analysis. A simple, spatially correlated *equivalent* Rician fading channel, $\ddot{\mathbf{H}}$, is defined as

$$\ddot{\mathbf{H}} = \sqrt{P} \left(\sqrt{\frac{1}{\ddot{\kappa} + 1}} \ddot{\mathbf{R}}_{\text{RX}}^{1/2} \mathbf{H}_{\text{iid}} \ddot{\mathbf{R}}_{\text{TX}}^{1/2} + \sqrt{\frac{\ddot{\kappa}}{\ddot{\kappa} + 1}} \ddot{\mathbf{H}}_{\text{LOS}} \right), \quad (6.5)$$

where P is the link gain, $\ddot{\kappa}$ is the Rician K-factor, \mathbf{H}_{iid} is the $Q \times M$ matrix of i.i.d. $\mathcal{CN}(0, 1)$ entries, $\ddot{\mathbf{R}}_{\text{TX}}$ and $\ddot{\mathbf{R}}_{\text{RX}}$ are the TX and RX spatial correlation matrices, respectively, and $\ddot{\mathbf{H}}_{\text{LOS}}$ is the $Q \times M$ specular channel matrix. Such a model allows a different link gain, P , and a different Rician K-factor, $\ddot{\kappa}$, for each user. However, it fixes the spatial correlation matrices $\ddot{\mathbf{R}}_{\text{TX}}$ and $\ddot{\mathbf{R}}_{\text{RX}}$, for simplicity. This is possibly the simplest classical model which might be expected to approximate the Saleh-Valenzuela behaviour. In order to parametrize the model in (6.5), P , $\ddot{\kappa}$, $\ddot{\mathbf{H}}_{\text{LOS}}$, $\ddot{\mathbf{R}}_{\text{TX}}$ and $\ddot{\mathbf{R}}_{\text{RX}}$ must be defined. The value of P is simply the link gain defined (2.14). However, the value of $\ddot{\kappa}$ is less easy to obtain. While one approach would be identify the strongest of the CL paths as the LOS component, this ignores the projections of the other paths onto this dominant path. The singular value decomposition (SVD) offers a method of obtaining the strength of the strongest possible rank one specular channel matrix. If $\mathbf{H} = \mathbf{T}\mathbf{\Lambda}\mathbf{U}^H$ is the SVD of \mathbf{H} , with $\mathbf{T} = [\mathbf{t}_1, \dots, \mathbf{t}_Q]$ and $\mathbf{U} = [\mathbf{u}_1, \dots, \mathbf{u}_M]$ being the $Q \times Q$ and $M \times M$ unitary matrices, respectively. $\mathbf{\Lambda} = [\text{diag}(\eta_1, \dots, \eta_Q) \mathbf{0}_{Q \times (M-Q)}]$ is the $Q \times M$ matrix with singular values on the diagonal. The LOS matrix $\mathbf{t}_1 \mathbf{u}_1^H$ could then be proposed with

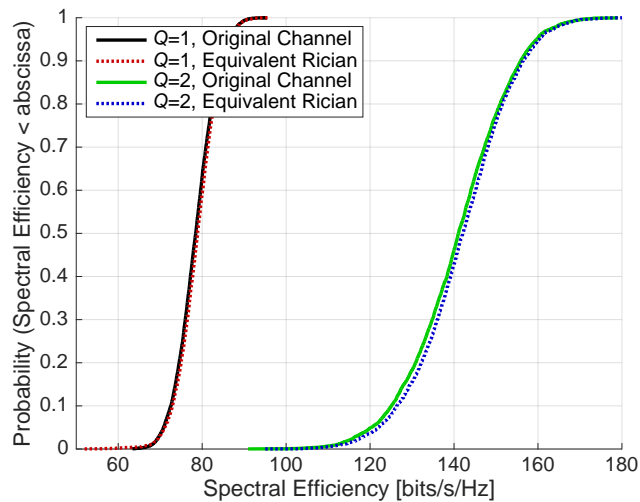
$$\ddot{\kappa} = \frac{\eta_1^2}{\sum_{i=2}^Q \eta_i^2}. \quad (6.6)$$

This is the approach taken here. Since the singular vectors are not of the correct form given in (2.15)-(2.16), they can be replaced by antenna array response vectors with fixed AOAs and AODs. Hence, for simplicity, a rank one specular matrix of the form

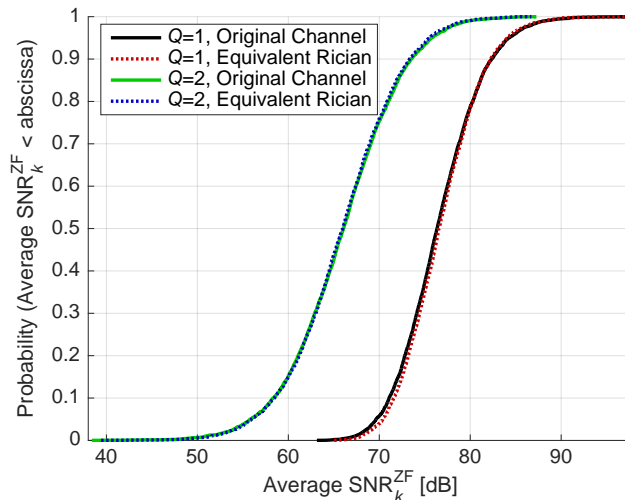
$$\ddot{\mathbf{H}}_{\text{LOS}} = \mathbf{a}_{\text{RX}}(\varphi^{\text{AOA}}, \vartheta^{\text{AOA}}) \mathbf{a}_{\text{TX}}^H(\varphi^{\text{AOD}}, \vartheta^{\text{AOD}}), \quad (6.7)$$

is assumed, as in (2.9), where φ and ϑ are the LOS azimuth and elevation angles between the BS and the user, respectively. The spatial correlation matrices, $\ddot{\mathbf{R}}_{\text{TX}}$ and $\ddot{\mathbf{R}}_{\text{RX}}$, are also complex to model. The Saleh-Valenzuela channel generates spatial correlations similar to the Bessel function, $J_0(\cdot)$, but every drop gives a spatial correlation structure with different zero crossings. Hence, if you compute the average spatial correlation from the Saleh-Valenzuela model, the individual

spatial correlations tend to cancel out and the average values are small. In contrast, if you average the absolute spatial correlations then the average decays in an exponential-like fashion at first and then reaches a constant. This motivates two very simple models: exponential spatial correlation [189] (described in Section 2.3.1) and equal spatial correlation. In summary, the simple spatially correlated Rician model in (6.5) with P provided in (2.14), is investigated with $\bar{\kappa}$ given in (6.6), $\ddot{\mathbf{H}}_{\text{LOS}}$ given in (6.7) and spatial correlation matrices modelled as an exponential decay or equal spatial correlation.



(a) Spectral efficiency.



(b) Average per-user instantaneous ZF SNR.

Figure 6.40: Akdeniz 28 GHz channel, given in [114], vs equivalent Rician channel for $M = 100$ TX antennas and $K = 4$ users.

To explore this model, a $M = 100$ element ULA is considered with $K = 4$ users in the Akdeniz 28 GHz channel [114] for all equivalent Rician results. Three cases are discussed: where $Q = 1$, $Q = 2$ and $Q \geq 3$. In order to evaluate

the Rician equivalence, two metrics are considered: spectral efficiency and the average per-user instantaneous ZF SNR. The CDFs of these two metrics are shown in Figure 6.40. Using two metrics is a more thorough approach to testing the equivalence.

6.8.1 Single Antenna Users, $Q = 1$

For the case where $Q = 1$, the tendency for large K-factors led us to investigate a pure LOS model, setting $\bar{\kappa} = \infty$ in (6.5). It can be seen that this equivalent Rician channel model gives almost the same performance as the Akdeniz 28 GHz channel for both spectral efficiency and average per-user instantaneous ZF SNR. Hence, a greatly simplified analysis becomes possible.

6.8.2 Double Antenna Users, $Q = 2$

For $Q = 2$, again an agreement in performance is seen between the original Akdeniz 28 GHz channel and the equivalent Rician. An excellent agreement is obtained even when we use (6.5) with no spatial correlation, i.e., $\mathbf{\ddot{R}}_{\text{TX}} = \mathbf{I}_M$, $\mathbf{\ddot{R}}_{\text{RX}} = \mathbf{I}_Q$. The equivalent Rician channel fits well with no spatial correlation because the Rician K-factor is so large and the diffuse component of the channel only has a slight effect.

6.8.3 Multiple Antenna Users, $Q \geq 3$

In the case where users have multiple antenna users ($Q \geq 3$), it is possible to tune the parameters in (6.5) to give a good agreement between Akdeniz 28 GHz and equivalent Rician models for spectral efficiency and average per-user instantaneous ZF SNR separately. However, a single model does not adequately reproduce both spectral efficiency and ZF SNR results. Hence, the Akdeniz 28 GHz model has subtleties which cannot be represented in such a simple Rician model. Nevertheless, some insights can be noted:

- The equivalent Rician K-factors obtained from the SVD, as in (6.6), are large. In decibels, the K-factors tend to look quite exponential and the distribution of the equivalent Rician K-factor can be approximated by $\bar{\kappa} \sim \text{Exp}(7.7)$.
- Spatial correlation decays smoothly to a fixed value and does not decay with antenna separation past this point.
- By either having a fixed spatial correlation value or using an exponential model [189], the equivalent Rician can give similar spectral efficiency or ZF SNR results to the original Akdeniz 28 GHz channel, but extremely high spatial correlations are required, of the order 0.95-1.

- The spectral efficiency CDFs for the equivalent Rician channel are typically steeper than those of the original model. Agreement between the two requires the use of a random exponential spatial correlation decay parameter or a random constant spatial correlation parameter. This increases the spectral efficiency at high SNR and vice-versa.

Overall, for $Q \geq 3$ RX antennas per user, a Rician model is insufficient to mimic the true channel. Nevertheless, the broad behaviour of the Akdeniz 28 GHz channel can be identified. This includes a very strong Rician K-factor and high spatial correlation, as would be expected. It is particularly interesting that spatially correlated Rician channels which yield similar performance rely on a random spatial correlation parameter. Hence, the variation in spatial correlation between drops appears to play an important role in performance.

6.9 Conclusion

The system sum rate, eigenvalue structure, EDOF and massive MIMO convergence have been shown to be significantly affected by the frequency band and antenna topology. The system performance is typically worse at mmWave bands, relative to microwave, where there is sparse scattering. However, because the channel is so sparse at mmWave bands, any change in the intra-cluster RMS angular spread drastically affects the sum rate. Furthermore, because the elevation spectrum is typically narrower than the azimuth, the URA topology experiences the largest variation in sum rate with angular spread. A larger number of system users, with a fixed number of streams, has been shown to both reduce the cell radius and increase the sum rate from an increase in angular diversity. However, due to the smaller cell radius, users become more closely spaced causing in the increase in diversity (and sum rate) to saturate.

In microwave scenarios, where the probability of LOS propagation is low, the structure of eigenvalues is highly dependent on the richness of scattering. On the other hand, in mmWave bands, where the probability of LOS is high, the structure of the eigenvalues is largely dependent on the LOS channel model. For Rician channels, the eigenvalue structure deteriorates with larger Rician K-factor. However, for a path loss scaled Saleh-Valenzuela LOS channel model, such as in Akdeniz et al. [114], the eigenvalues are the same as the NLOS case. The ULA is seen to have superior eigenvalue structure due to the inherently larger inter-element spacings and wider azimuth spectra (relative to elevation spectra), which makes it less effective for antennas to be placed vertically at the antenna array. These observations in eigenvalue are seen to affect sum rate performance. The EDOF has been explored for all environments and antenna topologies as a function of the number of users and receive antennas. A

larger gain in EDOF is seen when the user numbers are increased since this provides a greater angular diversity than adding more co-located antennas [248]. The ULA topology and microwave environments are shown to have the largest EDOF since the azimuth resolution is wider and cluster numbers are larger, respectively. This conclusion is also seen in terms of the eigenvalue ratio, where the ULA has the same performance for closely spaced users as the URA and UCA with randomly located users. Based on these observations, the ULA is able to support more users simultaneously and is recommended due to its superior massive MIMO convergence properties.

Furthermore, an equivalent Rician fading channel model has been proposed to replicate both spectral efficiency and ZF SNR performance of a Saleh-Valenzuela mmWave channel (Akdeniz 28 GHz), for scenarios with single and double antenna users. Here, it has been shown that the statistically complex Saleh-Valenzuela channel model can be represented by simple statistical channel models offering far greater analytical tractability.

Table 6.1: Environmental Statistical Spatial Parameters

Parameter	Microwave Bands		Intermediate Bands	mmWave Bands					
	3GPP [129]	BUPT	WPC [151]	Hur [119]	Akdeniz [114]	Samimi [117, 150]	Akdeniz [114]	Samimi [117, 150]	Thomas [118]
f (GHz)	2.6	6	18	28	28	28	73	73	73
r (m)	810	810	198	63	60	63	38	48	49
α (dB)	X_0 13.5	43.6 13.5	57.6	61.4	61.4 72.0	61.4	69.8 82.7	69.8	69.7
β (dB)	X_1 3.92	2.2 3.92	2 3	1.87 2.97	2 2.92	2.1 3.4	2 2.69	2.0 3.3	2.1 3.3
ϵ (dB)	4 6	4 6	4.1 6.8	1.7 15.9	5.8 8.7	3.6 9.7	5.8 7.7	5.2 7.6	4.9 7.6
C	12 20	15 16	12 20	6 6	X_2	X_3 X_4	X_5	X_3 X_7	5
L	20 20	7 7	20 20	10 10	20	X_8 X_9	20	X_8 X_{11}	10
κ (dB) \sim $\mathcal{N}(\mu, \sigma^2)$	$\mu = 9$ N/A $\sigma = 3.5$ N/A	$\mu = 12.4$ N/A $\sigma = 6.6$ N/A	$\mu = 9$ N/A $\sigma = 3.5$ N/A	$\mu = 7$ N/A $\sigma = 6.84$ N/A	N/A	$\mu = 2.4$ -0.4 $\sigma = 2.0$ 4.3	N/A	$\mu = 2.4$ 1.5 $\sigma = 2.0$ 6.8	$\mu = 12$ N/A $\sigma = 3$ N/A
Cluster ϕ_0^{AOA} spread ($^\circ$)	$\mathcal{N}(64.6, 2.5)$ $\mathcal{N}(74.1, 1.7)$	$\mathcal{N}(49.0, 2.0)$ $\mathcal{N}(67.6, 1.7)$	$\mathcal{N}(64.6, 2.5)$ $\mathcal{N}(55.1, 1.7)$	$\mathcal{N}(30.9, 5.8)$ $\mathcal{N}(32.4, 6.9)$	N/A	$\mathcal{N}(49.0, 3.5)$ $\mathcal{N}(24.5, 6.0)$	N/A	$\mathcal{N}(49.0, 3.5)$ $\mathcal{N}(31.6, 2.5)$	$\mathcal{N}(20.0, 5.2)$
Cluster ϕ_0^{AOD} spread ($^\circ$)	$\mathcal{N}(14.1, 3.6)$ $\mathcal{N}(25.7, 3.6)$	$\mathcal{N}(22.4, 2.8)$ $\mathcal{N}(19.5, 3.6)$	$\mathcal{N}(15.8, 3.6)$ $\mathcal{N}(22.7, 3.6)$	$\mathcal{N}(11.7, 12.0)$ $\mathcal{N}(16.2, 22.9)$	N/A	$\mathcal{N}(19.1, 10.0)$ $\mathcal{N}(24.0, 6.6)$	N/A	$\mathcal{N}(19.1, 10.0)$ $\mathcal{N}(21.9, 6.0)$	$\mathcal{N}(12.6, 6.9)$
Cluster θ_0^{AOA} spread ($^\circ$)	$\mathcal{N}(8.9, 2.1)$ $\mathcal{N}(18.2, 2.1)$	$\mathcal{N}(22.9, 1.7)$ $\mathcal{N}(23.4, 1.9)$	$\mathcal{N}(8.9, 2.1)$ $\mathcal{N}(12.8, 2.1)$	$\mathcal{N}(4.6, 5.2)$ $\mathcal{N}(3.4, 5.5)$	N/A	$\mathcal{N}(4.0, 1.5)$ $\mathcal{N}(5.2, 4.0)$	N/A	$\mathcal{N}(4.0, 1.5)$ $\mathcal{N}(3.5, 2.0)$	$\mathcal{N}(X_{12}, 3.3)$
Cluster θ_0^{AOD} spread ($^\circ$)	$\mathcal{N}(Y(0.75), 6.3)$ $\mathcal{N}(Y(0.9), 9.5)$	$\mathcal{N}(13.2, 2.6)$ $\mathcal{N}(17.4, 6.3)$	$\mathcal{N}(Y(0.75), 6.3)$ $\mathcal{N}(Y(0.9), 9.5)$	$\mathcal{N}(Y(0.75), 6.3)$ $\mathcal{N}(Y(0.9), 9.5)$	N/A	N/A	N/A	N/A	$\mathcal{N}(X_{13}, 4.4)$
ϕ_0 distribution	Gaussian	Gaussian	Gaussian	Gaussian	$\mathcal{U}[0, 2\pi)$	Gaussian	$\mathcal{U}[0, 2\pi)$	Gaussian	Gaussian
θ_0 distribution	Laplacian	Laplacian	Laplacian	Laplacian	LOS angle	Laplacian	LOS angle	Laplacian	Laplacian
σ_ϕ^{AOA} ($^\circ$)	11 15	24 29	11 15	2.7 6.8	Exp(15.5)	$\mathcal{N}(6.7, 259.2)$ $\mathcal{N}(9.6, 404.0)$	Exp(15.4)	$\mathcal{N}(6.7, 259.2)$ $\mathcal{N}(5.2, 146.4)$	5.3
σ_ϕ^{AOD} ($^\circ$)	5 2	9 11	5 2	1.9 4.8	Exp(10.2)	$\mathcal{N}(1.5, 4.8)$ $\mathcal{N}(3.0, 20.2)$	Exp(10.5)	$\mathcal{N}(1.5, 4.8)$ $\mathcal{N}(2.1, 47.6)$	6
$\sigma_\theta^{\text{AOA}}$ ($^\circ$)	3 3	3 3	3 3	3.4 6.4	Exp(6.0)	$\mathcal{N}(1.8, 4)$ $\mathcal{N}(1.6, 12.2)$	Exp(3.5)	$\mathcal{N}(1.8, 4)$ $\mathcal{N}(1.5, 3.6)$	X_{14}
$\sigma_\theta^{\text{AOD}}$ ($^\circ$)	$Y(0.75)$ $Y(0.9)$	$Y(0.75)$ $Y(0.9)$	$Y(0.75)$ $Y(0.9)$	1.0 2.2	N/A	$\mathcal{N}(0.8, 1)$ N/A	N/A	$\mathcal{N}(0.8, 1)$ $\mathcal{N}(0.8, 1.3)$	X_{15}
ϵd_{SC} (m)	37 50	37 50	37 50	N/A	N/A	N/A	N/A	N/A	N/A
κd_{SC} (m)	12 N/A	40 N/A	12 N/A	N/A	N/A	N/A	N/A	N/A	N/A
$\sigma_\phi^{\text{AOA}} d_{\text{SC}}$ (m)	15 50	44 8.3	15 50	N/A	N/A	N/A	N/A	N/A	N/A
$\sigma_\phi^{\text{AOD}} d_{\text{SC}}$ (m)	18 50	47 2	18 50	N/A	N/A	N/A	N/A	N/A	N/A
$\sigma_\theta^{\text{AOA}} d_{\text{SC}}$ (m)	15 50	15 50	15 50	N/A	N/A	N/A	N/A	N/A	N/A
$\sigma_\theta^{\text{AOD}} d_{\text{SC}}$ (m)	15 50	15 50	15 50	N/A	N/A	N/A	N/A	N/A	N/A

where $\log_{10}(Y(x)) = \max[-0.5, x - 2.1(d/1000)]$, $\{X_0, X_1\} = \{36.3, 2.2\}$ for $d < 417\text{m}$ and $\{X_0, X_1\} = \{-10.9, 4\}$ for $d \geq 417\text{m}$. $X_2 \sim \max[\text{Poisson}(1.8), 1]$, $X_3 \sim \mathcal{N}(5, 12.3)$, $X_4 \sim \mathcal{N}(5.3, 5.8)$, $X_5 \sim \max[\text{Poisson}(1.9), 1]$, $X_7 \sim \mathcal{N}(4.6, 10.9)$, $X_8 \sim \mathcal{N}(12.4, 219.0)$, $X_9 \sim \mathcal{N}(12.8, 458.0)$, $X_{11} \sim \mathcal{N}(13.2, 488.4)$, $\log_{10}(X_{12}) = \max[0.3, -0.0025d]$, $\log_{10}(X_{13}) = \max[0.4, -0.002d]$, $\log_{10}(X_{14}) = \max[0, -0.002d + 0.83]$ and $\log_{10}(X_{15}) = \max[0, -0.0023d + 0.81]$.

7

Conclusions and Future Work

This chapter includes a summary and conclusion for the research presented in this thesis. Several potential directions for future research are also provided.

7.1 Conclusions

In this thesis, a DL large-scale MU-MIMO system was considered. Chapter 3 demonstrated that for increasing numbers of antennas, a Rician fading channel (which is more deterministic than a Rayleigh fading channel) converged to the massive MIMO property of channel hardening quicker. It was also seen that effects of spatial correlation significantly reduced the performance of the MF SINR.

In order to mitigate the effects of spatial correlation, a distributed antenna system was considered for in Chapter 4 where the performance and convergence, to its limiting value, of the MF precoder was analytically and numerically shown. It was seen that the reduction in spatial correlation, and better cell-wide coverage, from distributing antennas into multiple clusters increased the MF SINR performance.

Although spatial correlation is reduced when distributing antennas into multiple clusters, the antenna arrays at each cluster are still large in size and thus the aggregate effects of small amounts of spatial correlation from all antennas is still prominent. Thus, in Chapter 5 spatial correlation is analysed for a (more realistic) Saleh-Valenzuela channel model. Including the effects of mutual coupling, it was seen that the performance of a large antenna array operating at mmWave bands is dominated by the change in antenna effective gain, and therefore SNR, of the coupling mechanisms between the antennas.

Channel models and measurements across a wide range of candidate bands for 5G wireless networks were considered in Chapter 6, motivated by the different propagation and spatial characteristics between both different bands and different channel models within the same band. Although mmWave channels have poor scattering characteristics, an increase in the EDOF can be seen by distributing the total number of RX antenna elements into single-antenna users (rather than one user with many antennas), since the large receive spatial correlation at mmWave bands becomes significantly reduced.

A detailed summary and conclusion of each chapter is now presented.

7.1.1 Convergence to Massive MIMO

In Chapter 3, the convergence properties of large scale MIMO systems were examined to determine the number of antennas required for a system to realize massive MIMO properties. Characteristics of both Rayleigh and Rician fading channel matrices were considered, and their asymptotic behaviour was studied. Limiting per-user ZF SNR and MF SINR were derived in a Rayleigh fading channel for scenarios of equal and unequal link gains, as the number of TX and RX antennas (with fixed ratio) increased without bound. Numerically, the effects of spatial correlation were then shown for both Rayleigh and Rician fading channels, as well as the impact of increasing LOS strength on the rate of convergence of the Rician fading channel.

For the Rayleigh fading channel, it was seen that the rate of convergence to favourable propagation and channel hardening was controlled by the rate of convergence of an i.i.d. channel to the identity matrix. Also the increased LOS strength, in a Rician fading channel, increased the rate of convergence to mean absolute deviation and diagonal dominance limiting values. However, the eigenvalue ratio convergence behaved differently since the eigenvalues are extremely sensitive to variations in the channel, which are increased for a larger Rician K-factor, since the LOS antenna array response vectors create a statistical structure in the channel affecting the eigenvectors.

The convergence properties of the per-user SNR/SINR for both ZF and MF precoders were less sensitive to the number of TX antennas. In particular, the rate of convergence of the per-user ZF SNR, to its limiting value, was quicker than that of the MF precoder due to its additional inter-user interference component. In a Rician fading channel, ZF SNR performance decreased with increased Rician K-factor, due to the reduced channel diversity. On the other hand, the MF SINR performance *increased* with increased Rician K-factor because the MF interference power reduced.

7.1.2 Distributed Antenna Systems

Chapter 4 analysed the performance and convergence, to its limiting value, of MF SINR for distributed antenna systems. Specifically, the instantaneous and limiting (in the number of TX antennas) performance of a MF precoder was investigated, whilst maintaining a fixed ratio of the number of TX antennas to single-antenna users, with the aim of determining and characterizing the impacts of distributing TX antennas into multiple clusters. The system model considered the effects of TX spatial correlation, unequal link gains and imperfect CSI. From the derived MF SINR expressions, a clear insight into the effect of link gains, spatial correlation and CSI imperfections were drawn.

Numerically, it was shown that distributing antennas into multiple clusters increased both the per-user instantaneous received SNR and average per-user instantaneous MF SINR, relative to a co-located antenna system. Significant increases in MF SINR were seen in a spatially correlated scenario since antenna inter-element antenna spacings increased and thus the spatial correlation effects reduced. In both spatially correlated and uncorrelated scenarios, CSI imperfections caused a considerable decrease in all instantaneous and limiting MF SINR results. Limiting MF SINR results further showed that the *rate* of convergence was not affected by spatial correlation or CSI imperfections, but the convergence of limiting link gain parameters, which was influenced by the link gain model considered.

7.1.3 Millimeter-Wave Wireless Communications

The Saleh-Valenzuela channel model was considered to model a large antenna array operating at mmWave frequencies. Based on the Saleh-Valenzuela channel model, closed-form expressions for the 3D spatial correlation between any two antenna elements was derived for wide, narrow and Von Mises PES as well as an upper bound for arbitrary PES. The effects of the PES on massive MIMO convergence properties was shown by defining and deriving a diagonal dominance metric. Numerically, the effects of mutually coupled antennas was then shown on the effective spatial correlation, eigenvalue structure and user rate for different antenna topologies.

The ULA was shown to have quicker diagonal dominance convergence than the URA and UCA topologies, due to the smaller numbers of adjacent antenna elements. Numerically, it was seen that the impacts of mutual coupling impacts were more obvious at smaller inter-element spacings, agreeing with previous works [7, 24, 87, 89, 105]. At these smaller inter-element spacings, mutual coupling was shown to decrease the normalized spatial correlation for side-by-side

antennas. However, the change to normalized spatial correlation did not translate into similar trends for user rate, as the effective gain of the antennas became a dominating effect and its variation was shown to be highly dependent on the antenna inter-element spacings. It is therefore concluded that although mutual coupling can significantly reduce spatial correlation for side-by-side dipole antennas, the change in antenna effective gain, and therefore SNR, from mutual coupling becomes a dominating effect and ultimately determines the antenna array performance of a mmWave system.

7.1.4 Channel Models for 5G Wireless Systems

Channel models and measurements across a wide range of candidate bands for 5G wireless networks were considered in Chapter 6, motivated by the different propagation and spatial characteristics between both different bands and different channel models within the same band. Key channel modelling and spatial parameter differences were identified and, in turn, their impact on various antenna topologies investigated, in terms of system sum rate, channel eigenvalue structure, EDOF and massive MIMO convergence properties. An equivalent Rician channel model was also developed to approximate the complex Saleh-Valenzuela channel model, proposed in [114], to model mmWave systems. The simple equivalent model was shown to perform well for small numbers of receive antennas and was used to gain insight into mmWave channels.

The system sum rate, eigenvalue structure, EDOF and massive MIMO convergence were shown to be significantly affected by the frequency band and antenna topology. The system performance was typically worse at mmWave bands, relative to microwave, since the scattering at higher frequencies is sparse. However, because the channel is so sparse at mmWave bands, any change in the intra-cluster RMS angular spread drastically affected the sum rate. Furthermore, because the elevation spectrum is typically narrower than the azimuth, the URA topology experienced the largest variation in sum rate with angular spread. A larger number of system users, with a fixed number of streams, was shown to reduce both the cell radius and increase the sum rate from an increase in angular diversity. However, due to the smaller cell radius, users become more closely spaced and the increase in diversity and therefore sum rate saturated

In microwave scenarios, where the probability of LOS propagation is low, the structure of eigenvalues is highly dependent on the richness of scattering. On the other hand, in mmWave bands, where the probability of LOS is high, the structure of the eigenvalues is largely dependent on the LOS channel model. For Rician channels, the eigenvalue structure deteriorates with larger Rician K-factor. However, for a path loss scaled Saleh-Valenzuela LOS channel model,

such as in Akdeniz et al. [114], the eigenvalues are the same as the NLOS case. The ULA is seen to have superior eigenvalue structure due to the inherently larger inter-element spacings and wider azimuth spectrums, which makes it less effective for antennas to be placed vertically at the antenna array. These observations in eigenvalue are seen to affect sum rate performance.

The EDOF was then explored for all environments and antenna topologies as a function of the user numbers and receive antennas. A larger gain in EDOF was seen when the user numbers were increased, since this provided a greater angular diversity than adding more co-located antennas at the same location. The ULA topology and microwave environments were shown to have the largest EDOF since the azimuth resolution is wider and cluster numbers are larger, respectively. This conclusion is also seen in terms of the eigenvalue ratio, where the ULA has the same performance for closely spaced users as the URA and UCA with randomly located users. Based on these observations, the ULA is able to support more users simultaneously and is recommended due to its superior massive MIMO convergence properties.

7.2 Future Work

Several potential directions for future work are provided.

7.2.1 Eigenvalue Sensitivity

It was shown in Chapter 3 that the convergence of the eigenvalue ratio to unity, as the number of transmit antennas increased, behaved differently in Rician fading channels the other convergence metrics. Specifically, the eigenvalue ratio converged at a slower rate for increased LOS propagation, whereas the mean absolute deviation and diagonal dominance was seen to converge at a faster rate. This phenomenon was explained by the extreme sensitivity of eigenvalues to variations in the channel. Whilst the entries of the NLOS, Rayleigh fading, component of the composite Rician fading channel are expected to converge to their statistical mean for large numbers of transmit antennas, the variation of the LOS component of the Rician fading channel is less influenced by the number of antennas. It is thus of interest to extend the above finding to explore, and characterize, the variations in the eigenvalue ratio (or individual eigenvalues as in [201]) to more realistic channel modelling techniques [249]. For example, exploring the eigenvalue sensitivity of the Saleh-Valenzuela channel, in terms of its underlying parameters, which forms the basis for standardized channel models (see [129, 130, 245, 250–252]), and is commonly used to model mmWave band channels.

7.2.2 Hybrid Beamforming with Sub-Arrays

Due to the larger signal attenuation in mmWave band channels, the TX must compensate to maintain coverage by providing an *additional* array gain proportional to the number of TX antenna elements [253]. Since digital beamforming requires a dedicated RF chain for each antenna, the hardware cost scales with the number of transmit antennas and conventional digital precoding techniques, such as MF, no longer become feasible. One way to mitigate the large hardware cost of this is to reduce the number of RF chains, such that each RF chain feeds digitally precoded data vector to a subset (*sub-array*) of antenna elements, before each antenna performs analog beamforming, altering the phase of the signal. This is referred to as hybrid (digital and analog) beamforming [113, 254–259]. Given a multi-user MIMO system with number of RF chains and antenna array constraints, the practical design of sub-arrays for different types of channels is of interest. For example, a sub-array of antennas sharing a single RF chain can be located as a tight group of adjacent antennas, or the antennas from multiple sub-arrays can be inter-leaved. Different designs will influence factors such as mutual coupling, spatial correlation, insertion loss and ultimately the system performance [98, 134, 260–263].

7.2.3 Massive MIMO for TDD or FDD?

All work in this thesis assumed TDD operation for massive MIMO to acquire CSI at the BS for DL transmission. However, it is still unknown whether massive MIMO will operate at TDD or frequency-division-duplexing (FDD) when deployed, since both have their advantages and disadvantages for acquiring CSI [53, 57, 264–267]. Namely, FDD operation, which current cellular systems use, requires each user to estimate and quantize its own channel, before sending codebook indices (common to the BS to the user) back to the BS. TDD on the other hand requires each user to send UL pilots to the BS, which then estimates the reciprocal (i.e., DL) channel before precoding. Since TDD UL pilots do not contain any payload, the overhead is greatly reduced, however the channel estimation at the BS relies on channel reciprocity and pilot contamination can occur (discussed in Section 2.5). It is noted that the performance of both duplexing protocols rely on accurate channel estimation.

In massive MIMO mmWave systems, the channel estimation techniques and approaches change to those more suited to sparse channels, e.g., compressive sensing [268, 269]. This motivates the exploration of the fundamental limits of various channel estimation techniques, as well as how they perform for both microwave and mmWave frequencies. This will provide a framework from which a duplexing protocol can be proposed for a given system.

Bibliography

- [1] DMC R&D Center, Samsung Electronics Co., Ltd., “5G Vision,” February 2015.
- [2] IWPC International Wireless Industry Consortium, “Evolutionary & disruptive visions towards ultra high capacity networks,” *White paper, Version 1.1*, April 2014.
- [3] International Telecommunications Union (ITU) World Radiocommunication Conference (WRC), “Provisional final acts,” November 2015.
- [4] J. G. Andrews, S. Buzzi, W. Choi, S. V. Hanly, A. Lozano, A. C. K. Soong, and J. C. Zhang, “What will 5G be?,” *IEEE J. Sel. Areas Commun.*, vol. 32, pp. 1065–1082, June 2014.
- [5] M. Agiwal, A. Roy, and N. Saxena, “Next generation 5G wireless networks: A comprehensive survey,” *IEEE Commun. Surveys. Tuts.*, vol. 18, pp. 1617–1655, February 2016.
- [6] T. L. Marzetta, “Noncooperative cellular wireless with unlimited numbers of base station antennas,” *IEEE Trans. Wireless Commun.*, vol. 9, pp. 3590–3600, November 2010.
- [7] F. Rusek, D. Persson, B. K. Lau, E. G. Larsson, T. L. Marzetta, O. Edfors, and F. Tufvesson, “Scaling up MIMO: Opportunities and challenges with very large arrays,” *IEEE Signal Process. Mag.*, vol. 30, pp. 40–60, January 2013.
- [8] E. G. Larsson, F. Tufvesson, O. Edfors, and T. L. Marzetta, “Massive MIMO for next generation wireless systems,” *IEEE Commun. Mag.*, vol. 52, pp. 186–195, February 2014.
- [9] D. López-Pérez, M. Ding, H. Claussen, and A. H. Jafari, “Towards 1Gbps/UE in cellular systems: Understanding ultra-dense small cell deployments,” *IEEE Commun. Surveys. Tuts.*, vol. 17, pp. 2078–2101, June 2015.

-
- [10] E. Björnson, M. Kountouris, and M. Debbah, “Massive MIMO and small cells: Improving energy efficiency by optimal soft-cell coordination,” *Intl. Conf. Telecommun.*, pp. 1–5, May 2013.
- [11] K. H. J. Hoydis, S. ten Brink, and M. Debbah, “Massive MIMO and small cells: How to densify heterogeneous networks,” *IEEE Intl. Conf. Commun.*, pp. 5442–5447, June 2013.
- [12] J. G. Andrews, H. Claussen, M. Dohler, S. Rangan, and M. C. Reed, “Femtocells: Past, present, and future,” *IEEE J. Sel. Areas Commun.*, vol. 30, pp. 497–508, April 2012.
- [13] D. Finn, H. Ahmadi, A. F. Cattoni, and L. A. DaSilva, “Improved spectral efficiency through multiuser MIMO across small cells,” *IEEE Trans. Veh. Technol.*, vol. 65, pp. 7764–7768, September 2016.
- [14] M. Kamel, W. Hamouda, and A. Youssef, “Ultra-dense networks: A survey,” *IEEE Commun. Surveys. Tuts.*, vol. 18, pp. 2522–2545, May 2016.
- [15] J. G. Andrews, “Seven ways that HetNets are a cellular paradigm shift,” *IEEE Commun. Mag.*, vol. 51, pp. 136–144, March 2013.
- [16] T. S. Rappaport, R. W. Heath Jr., R. C. Daniels, and J. Murdock, *Millimeter Wave Wireless Communications*. Prentice-Hall, September 2014.
- [17] T. S. Rappaport, S. Sun, R. Mayzus, H. Zhao, Y. Azar, K. Wang, G. N. Wong, J. K. Schulz, M. Samimi, and F. Gutierrez, “Millimeter wave mobile communications for 5G cellular: It will work!,” *IEEE Access*, vol. 1, pp. 335–349, May 2013.
- [18] Z. Pi and F. Khan, “An introduction to millimeter-wave mobile broadband systems,” *IEEE Commun. Mag.*, vol. 49, pp. 101–107, June 2011.
- [19] S. Rangan, T. S. Rappaport, and E. Erkip, “Millimeter-wave cellular wireless networks: Potentials and challenges,” *Proceedings of the IEEE*, vol. 102, pp. 366–385, February 2014.
- [20] T. S. Rappaport, J. N. Murdock, and F. Gutierrez, “State of the art in 60-GHz integrated circuits and systems for wireless communications,” *Proceedings of the IEEE*, vol. 99, pp. 1390–1436, August 2011.
- [21] W. Hong, K.-H. Baek, Y. Lee, and S.-T. Ko, “Study and prototyping of practically large-scale mmWave antenna systems for 5G cellular devices,” *IEEE Commun. Mag.*, vol. 52, pp. 63–69, September 2014.

- [22] A. K. Papazafeiropoulos, "Impact of general channel aging conditions on the downlink performance of massive MIMO," *IEEE Trans. Veh. Technol.*, vol. 66, pp. 1428–1442, February 2017.
- [23] D.-S. Shiu, G. J. Foschini, M. J. Gans, and J. M. Kahn, "Fading correlation and its effect on the capacity of multielement antenna systems," *IEEE Trans. Commun.*, vol. 48, pp. 502–513, March 2000.
- [24] T. Svantesson and A. Ranheim, "Mutual coupling effects on the capacity of multielement antenna systems," *IEEE Intl. Conf. Acoustics, Speech, and Signal Process.*, vol. 4, pp. 2485–2488, May 2001.
- [25] S. Wu, C.-X. Wang, E.-H. Aggoune, M. M. Alwakeel, and Y. He, "A non-stationary 3-D wideband twin-cluster model for 5G massive MIMO channels," *IEEE J. Sel. Areas Commun.*, vol. 32, pp. 1207–1218, June 2014.
- [26] A. Kammoun, H. Khanfir, Z. Altman, M. Debbah, and M. Kamoun, "Preliminary results on 3D channel modeling: From theory to standardization," *IEEE J. Sel. Areas Commun.*, vol. 32, pp. 1219–1229, June 2014.
- [27] F. Boccardi, R. W. Heath Jr., A. Lozano, T. L. Marzetta, and P. Popovski, "Five disruptive technology directions for 5G," *IEEE Commun. Mag.*, vol. 52, pp. 74–80, February 2014.
- [28] G. J. Foschini and M. J. Gans, "On limits of wireless communications in a fading environment when using multiple antennas," *Wireless Pers. Commun.*, vol. 6, pp. 311–335, March 1998.
- [29] E. Telatar, "Capacity of multi-antenna Gaussian channels," *European Trans. Telecommun.*, vol. 10, pp. 585–595, November 1999.
- [30] T. L. Marzetta and B. M. Hochwald, "Capacity of a mobile multiple-antenna communication link in Rayleigh flat fading," *IEEE Trans. Inf. Theory*, vol. 45, pp. 139–157, January 1999.
- [31] B. M. Hochwald and S. ten Brink, "Achieving near-capacity on a multiple-antenna channel," *IEEE Trans. Commun.*, vol. 51, pp. 389–399, March 2003.
- [32] S. Catreux, P. F. Driessen, and L. J. Greenstein, "Attainable throughput of an interference-limited multiple-input multiple-output (MIMO) cellular system," *IEEE Trans. Commun.*, vol. 49, pp. 1307–1311, August 2001.
- [33] A. F. Molisch, M. Z. Win, Y.-S. Choi, and J. H. Winters, "Capacity of MIMO systems with antenna selection," *IEEE Trans. Wireless Commun.*, vol. 4, pp. 1759–1772, July 2005.

- [34] A. F. Molisch, M. Steinbauer, M. Toeltsch, E. Bonek, and R. S. Thomä, “Capacity of MIMO systems based on measured wireless channels,” *IEEE J. Sel. Areas Commun.*, vol. 20, pp. 561–569, April 2002.
- [35] P. J. Smith, S. Roy, and M. Shafi, “Capacity of MIMO systems with semicorrelated flat fading,” *IEEE Trans. Inf. Theory*, vol. 49, pp. 2781–2788, October 2003.
- [36] L. Zheng and D. N. C. Tse, “Diversity and multiplexing: A fundamental tradeoff in multiple-antenna channels,” *IEEE Trans. Inf. Theory*, vol. 49, pp. 1073–1096, May 2003.
- [37] Q. H. Spencer, C. B. Peel, A. L. Swindlehurst, and M. Haardt, “An introduction to the multi-user MIMO downlink,” *IEEE Commun. Mag.*, vol. 42, pp. 60–67, October 2004.
- [38] A. Adhikary, A. Ashikhmin, and T. L. Marzetta, “Uplink interference reduction in large scale antenna systems,” *IEEE Trans. Commun.*, vol. PP, pp. 1–1, January 2017.
- [39] D. Gesbert, M. Kountouris, R. W. Heath Jr., C.-B. Chae, and T. Sälzer, “Shifting the MIMO paradigm,” *IEEE Signal Process. Mag.*, vol. 24, pp. 36–46, September 2007.
- [40] G. Caire and S. Shamai, “On the achievable throughput of a multiantenna Gaussian broadcast channel,” *IEEE Trans. Inf. Theory*, vol. 49, pp. 1691–1706, July 2003.
- [41] P. Viswanath and D. N. C. Tse, “Sum capacity of the vector Gaussian broadcast channel and uplink-downlink duality,” *IEEE Trans. Inf. Theory*, vol. 49, pp. 1912–1921, August 2003.
- [42] S. Vishwanath, N. Jindal, and A. Goldsmith, “Duality, achievable rates, and sum-rate capacity of Gaussian MIMO broadcast channels,” *IEEE Trans. Inf. Theory*, vol. 49, pp. 2658–2668, October 2003.
- [43] H. Q. Ngo, E. G. Larsson, and T. L. Marzetta, “Energy and spectral efficiency of very large multiuser MIMO systems,” *IEEE Trans. Commun.*, vol. 61, pp. 1436–1449, April 2013.
- [44] A. Pitarokoilis, S. K. Mohammed, and E. G. Larsson, “On the optimality of single-carrier transmission in large-scale antenna systems,” *IEEE Wireless Commun. Lett.*, vol. 1, pp. 276–279, August 2012.
- [45] J. Hoydis, S. ten Brink, and M. Debbah, “Massive MIMO in the UL/DL of cellular networks: How many antennas do we need?,” *IEEE J. Sel. Areas Commun.*, vol. 31, pp. 160–171, February 2013.

- [46] R. R. Muller, M. Vehkaperä, and L. Cottatellucci, “Blind pilot decontamination,” *Intl. ITG Workshop on Smart Antennas*, March 2013.
- [47] P. J. Smith, C. T. Neil, M. Shafi, and P. A. Dmochowski, “On the convergence of massive MIMO systems,” *IEEE Intl. Conf. Commun.*, pp. 5191–5196, June 2014.
- [48] C. T. Neil, M. Shafi, P. J. Smith, and P. A. Dmochowski, “On the impact of antenna topologies for massive MIMO systems,” *IEEE Intl. Conf. Commun.*, pp. 2030–2035, June 2015.
- [49] C. T. Neil, M. Shafi, P. J. Smith, and P. A. Dmochowski, “Deployment issues for massive MIMO systems,” *IEEE Intl. Conf. Commun. Workshop*, pp. 1298–1303, June 2015.
- [50] H. Huh, G. Caire, H. C. Papadopoulos, and S. A. Ramprasad, “Achieving “massive MIMO” spectral efficiency with a not-so-large number of antennas,” *IEEE Trans. Wireless Commun.*, vol. 11, pp. 3226–3239, September 2012.
- [51] H. Yang and T. L. Marzetta, “Performance of conjugate and zero-forcing beamforming in large-scale antenna systems,” *IEEE J. Sel. Areas Commun.*, vol. 31, pp. 172–179, February 2013.
- [52] A. Özgür, O. Lévêque, and D. Tse, “Spatial degrees of freedom of large distributed MIMO systems and wireless ad hoc networks,” *IEEE J. Sel. Areas Commun.*, vol. 31, pp. 202–214, February 2013.
- [53] J. Jose, A. Ashikhmin, T. L. Marzetta, and S. Vishwanath, “Pilot contamination and precoding in multi-cell TDD systems,” *IEEE Trans. Wireless Commun.*, vol. 10, pp. 2640–2651, August 2011.
- [54] K. T. Truong and R. W. Heath Jr., “Effects of channel aging in massive MIMO systems,” *J. Commun. Netw.*, vol. 15, pp. 338–351, August 2013.
- [55] F. Fernandes, A. Ashikhmin, and T. L. Marzetta, “Inter-cell interference in noncooperative TDD large scale antenna systems,” *IEEE J. Sel. Areas in Commun.*, vol. 31, pp. 192–201, February 2013.
- [56] X. Gao, O. Edfors, F. Rusek, and F. Tufvesson, “Linear pre-coding performance in measured very-large MIMO channels,” *IEEE Veh. Technol. Conf.*, pp. 1–5, September 2011.
- [57] E. Björnson, E. G. Larsson, and T. L. Marzetta, “Massive MIMO: Ten myths and one critical question,” *IEEE Commun. Mag.*, vol. 54, pp. 114–123, February 2016.

- [58] E. Björnson, E. G. Larsson, and M. Debbah, “Massive MIMO for maximal spectral efficiency: How many users and pilots should be allocated?,” *IEEE Trans. Wireless Commun.*, vol. 15, pp. 1293–1308, February 2016.
- [59] L. Lu, G. Y. Li, A. L. Swindlehurst, A. Ashikhmin, and R. Zhang, “An overview of massive MIMO: Benefits and challenges,” *IEEE J. Sel. Topics Signal Process.*, vol. 8, pp. 742–758, October 2014.
- [60] S. Yang and L. Hanzo, “Fifty years of MIMO detection: The road to large-scale MIMOs,” *IEEE Commun. Surveys. Tuts.*, vol. 17, pp. 1941–1988, September 2015.
- [61] C.-X. Wang, F. Haider, X. Gao, X.-H. You, Y. Yang, D. Yuan, H. M. Aggoune, H. Haas, S. Fletcher, and E. Hepsaydir, “Cellular architecture and key technologies for 5G wireless communication networks,” *IEEE Commun. Mag.*, vol. 52, pp. 122–130, February 2014.
- [62] D. A. Basnayaka, M. D. Renzo, and H. Haas, “Massive but few active MIMO,” *IEEE Trans. Veh. Technol.*, vol. 65, pp. 6861–6877, September 2016.
- [63] R. Couillet and M. Debbah, *Random Matrix Methods for Wireless Communications*. Cambridge University Press, 2011.
- [64] H. Cramer, *Random Variables and Probability Distributions*. Cambridge University Press, 1970.
- [65] X. Gao, O. Edfors, F. Rusek, and F. Tufvesson, “Massive MIMO performance evaluation based on measured propagation data,” *IEEE Trans. Wireless Commun.*, vol. 14, pp. 3899–3911, March 2015.
- [66] H. Q. Ngo, E. G. Larsson, and T. L. Marzetta, “Aspects of favorable propagation in massive MIMO,” *IEEE European Signal Process. Conf.*, pp. 76–80, September 2014.
- [67] H. Q. Ngo, E. G. Larsson, and T. L. Marzetta, “The multicell multiuser MIMO uplink with very large antenna arrays and a finite-dimensional channel,” *IEEE Trans. Commun.*, vol. 61, pp. 2350–2361, June 2013.
- [68] B. M. Hochwald, T. L. Marzetta, and V. Tarokh, “Multiple-antenna channel hardening and its implications for rate feedback and scheduling,” *IEEE Trans. Inf. Theory*, vol. 50, pp. 1893–1909, September 2004.
- [69] J. Flordelis, X. Gao, G. Dahman, F. Rusek, O. Edfors, and F. Tufvesson, “Spatial separation of closely-spaced users in measured massive multi-user MIMO channels,” *IEEE Intl. Conf. Commun.*, pp. 1441–1446, June 2015.

- [70] M. H. M. Costa, “Writing on dirty paper,” *IEEE Trans. Inf. Theory*, vol. 29, pp. 439–441, May 1983.
- [71] C. B. Peel, B. M. Hochwald, and A. L. Swindlehurst, “A vector-perturbation technique for near-capacity multiantenna multiuser communication—part I: Channel inversion and regularization,” *IEEE Trans. Commun.*, vol. 53, pp. 195–202, January 2005.
- [72] B. M. Hochwald, C. B. Peel, and A. L. Swindlehurst, “A vector-perturbation technique for near-capacity multiantenna multiuser communication—part II: Perturbation,” *IEEE Trans. Commun.*, vol. 53, pp. 537–544, March 2005.
- [73] M. Mazrouei-Sebdani, W. A. Krzymień, and J. Melzer, “Massive MIMO with nonlinear precoding: Large-system analysis,” *IEEE Trans. Veh. Technol.*, vol. 65, pp. 2815–2820, April 2016.
- [74] A. Firag, P. J. Smith, A. Papathanassiou, M. Shafi, D. Basnayaka, and P. Martin, “A comparison of linear transceiver techniques in multiuser MIMO broadcast systems,” *IEEE Australian Commun. Theory Workshop*, January 2012.
- [75] X. Gao, O. Edfors, F. Tufvesson, and E. G. Larsson, “Massive MIMO in real propagation environments: Do all antennas contribute equally?,” *IEEE Trans. Commun.*, vol. 63, pp. 3917–3928, July 2015.
- [76] X. Gao, F. Tufvesson, O. Edfors, and F. Rusek, “Measured propagation characteristics for very large MIMO at 2.6 GHz,” *Proc. 46th Annual Asilomar Conf. Signals, Systems, and Computers*, November 2012.
- [77] H. Q. Ngo and E. G. Larsson, “EVD-based channel estimation in multicell multiuser MIMO systems with very large antenna arrays,” *IEEE Intl. Conf. Acoustics, Speech, and Signal Process.*, pp. 3249–3252, March 2012.
- [78] A. Garcia-Rodriguez and C. Masouros, “Exploiting the tolerance of massive MIMO to incomplete CSI for low-complexity transmission,” *IEEE Global Commun. Conf.*, pp. 1–6, December 2015.
- [79] A. Garcia-Rodriguez and C. Masouros, “Exploiting the increasing correlation of space constrained massive MIMO for CSI relaxation,” *IEEE Trans. Commun.*, vol. 64, pp. 1572–1587, April 2016.
- [80] J. Zhang, X. Yuan, and L. Ping, “Hermitian precoding for distributed MIMO systems with individual channel state information,” *IEEE J. Sel. Areas Commun.*, vol. 31, pp. 241–250, February 2013.

- [81] M. Matthaiou, C. Zhong, M. R. McKay, and T. Ratnarajah, "Sum rate analysis of ZF receivers in distributed MIMO systems," *IEEE J. Sel. Areas Commun.*, vol. 31, pp. 180–191, February 2013.
- [82] H. Yin, D. Gesbert, and L. Cottatellucci, "Dealing with interference in distributed large-scale MIMO systems: A statistical approach," *IEEE J. Sel. Topics Signal Process.*, vol. 8, pp. 942–953, October 2014.
- [83] C. Masouros, M. Sellathurai, and T. Ratnarajah, "Large-scale MIMO transmitters in fixed physical spaces: The effect of transmit correlation and mutual coupling," *IEEE Trans. Commun.*, vol. 61, pp. 2794–2804, July 2013.
- [84] C. Masouros and M. Matthaiou, "Space-constrained massive MIMO: Hitting the wall of favourable propagation," *IEEE Commun. Lett.*, vol. 19, pp. 771–774, May 2015.
- [85] B. Clerckx, C. Craeye, D. Vanhoenacker-Janvier, and C. Oestges, "Impact of antenna coupling on 2x2 MIMO communications," *IEEE Trans. Veh. Technol.*, vol. 56, pp. 1009–1018, May 2007.
- [86] R. Zi, X. Ge, H. Wang, J. Zhang, and C.-X. Wang, "Multiuser massive MIMO uplink performance with mutual coupling effects," *IEEE Global Commun. Conf.*, pp. 3296–3301, December 2014.
- [87] J. W. Wallace and M. A. Jensen, "Mutual coupling in MIMO wireless systems: A rigorous network theory analysis," *IEEE Trans. Wireless Commun.*, vol. 3, pp. 1317–1325, July 2004.
- [88] M. K. Özdemir, E. Arvas, and H. Arslan, "Dynamics of spatial correlation and implications on MIMO systems," *IEEE Commun. Mag.*, vol. 42, pp. S14–S19, June 2004.
- [89] R. Janaswamy, "Effect of element mutual coupling on the capacity of fixed length linear arrays," *IEEE Antennas Wireless Propag. Lett.*, vol. 1, no. 1, pp. 157–160, 2002.
- [90] M.-T. Dao, V.-A. Nguyen, Y.-T. Im, S.-O. Park, and G. Yoon, "3D polarized channel modeling and performance comparison of MIMO antenna configurations with different polarizations," *IEEE Trans. Antennas and Propag.*, vol. 59, pp. 2672–2682, July 2011.
- [91] J. Salz and J. H. Winters, "Effect of fading correlation on adaptive arrays in digital mobile radio," *IEEE Trans. Veh. Technol.*, vol. 43, pp. 1049–1057, November 1994.

- [92] A. M. Sayeed, “Deconstructing multiantenna fading channels,” *IEEE Trans. Signal Process.*, vol. 50, pp. 2563–2579, October 2002.
- [93] A. M. Tulino, A. Lozano, and S. Verdú, “Impact of antenna correlation on the capacity of multiantenna channels,” *IEEE Trans. Inf. Theory*, vol. 51, pp. 2491–2509, July 2005.
- [94] E. Björnson, E. Jorswieck, and B. Ottersten, “Impact of spatial correlation and precoding design in OSTBC MIMO systems,” *IEEE Trans. Wireless Commun.*, vol. 11, pp. 3578–3589, November 2010.
- [95] J. P. Kermoal, L. Schumacher, K. I. Pedersen, P. E. Mogensen, and F. Frederiksen, “A stochastic MIMO radio channel model with experimental validation,” *IEEE J. Sel. Areas Commun.*, vol. 20, pp. 1211–1226, August 2002.
- [96] K. A. Alnajjar, P. J. Smith, P. Whiting, and G. K. Woodward, “Size and array shape for massive MIMO,” *IEEE Wireless Commun. Lett.*, vol. 4, pp. 653–656, December 2015.
- [97] S. K. Yong and J. S. Thompson, “Three-dimensional spatial fading correlation models for compact MIMO receivers,” *IEEE Trans. Wireless Commun.*, vol. 4, pp. 2856–2869, November 2005.
- [98] A. L. Swindlehurst, E. Ayanoglu, P. Heydari, and F. Capolino, “Millimeter-wave massive MIMO: The next wireless revolution?,” *IEEE Commun. Mag.*, vol. 52, pp. 56–62, September 2014.
- [99] M. Gauger, J. Hoydis, C. Hoek, H. Schlesinger, A. Pascht, and S. ten Brink, “Channel measurements with different antenna array geometries for massive MIMO systems,” *Intl. ITG Conf. Syst., Commun. and Coding*, pp. 1–6, February 2015.
- [100] W. Tan, S. Jin, J. Wang, and Y. Huang, “Achievable sum-rate analysis for massive MIMO systems with different array configurations,” *IEEE Wireless Commun. Netw. Conf.*, pp. 316–321, March 2015.
- [101] X. Ge, R. Zi, H. Wang, J. Zhang, and M. Jo, “Multi-user massive MIMO communication systems based on irregular antenna arrays,” *IEEE Trans. Wireless Commun.*, vol. 15, pp. 5287–5301, August 2016.
- [102] P. Wang, Y. Li, Y. Peng, S. C. Liew, and B. Vucetic, “Non-uniform linear antenna array design and optimization for millimeter wave communications,” *IEEE Trans. Wireless Commun.*, vol. 15, pp. 7343–7356, November 2016.

- [103] X. Artiga, B. Devillers, and J. Perruisseau-Carrier, "Mutual coupling effects in multi-user massive MIMO base stations," *IEEE Intl. Symp. Antennas and Propag.*, pp. 1–2, July 2012.
- [104] S. Biswas, C. Masouros, and T. Ratnarajah, "Performance analysis of large multiuser MIMO systems with space-constrained 2-D antenna arrays," *IEEE Trans. Wireless Commun.*, vol. 15, pp. 3492–3505, January 2016.
- [105] B. K. Lau, S. M. S. Ow, G. Kristensson, and A. F. Molisch, "Capacity analysis for compact MIMO systems," *IEEE Veh. Technol. Conf.*, vol. 1, pp. 165–170, May 2005.
- [106] P. N. Fletcher, M. Dean, and A. R. Nix, "Mutual coupling in multi-element array antennas and its influence on MIMO channel capacity," *IET Electron. Lett.*, vol. 39, pp. 342–344, February 2003.
- [107] T. E. Bogale and L. B. Le, "Massive MIMO and mmWave for 5G wireless HetNet: Potential benefits and challenges," *IEEE Veh. Technol. Mag.*, vol. 11, pp. 64–75, February 2016.
- [108] J. G. Andrews, X. Zhang, G. D. Durgin, and A. K. Gupta, "Are we approaching the fundamental limits of wireless network densification?," *IEEE Commun. Mag.*, vol. 54, pp. 184–190, October 2016.
- [109] H. Xu, T. S. Rappaport, R. J. Boyle, and J. H. Schaffner, "38 GHz wide-band point-to-multipoint radio wave propagation study for a campus environment," *IEEE Veh. Technol. Conf.*, pp. 1575–1579, August 1999.
- [110] A. V. Alejos, M. G. Sánchez, and I. C. nas, "Measurement and analysis of propagation mechanisms at 40 GHz: Viability of site shielding forced by obstacles," *IEEE Trans. Veh. Technol.*, vol. 57, pp. 3369–3380, November 2008.
- [111] S. Kutty and D. Sen, "Beamforming for millimeter wave communications: An inclusive survey," *IEEE Commun. Surveys. Tuts.*, vol. 18, no. 2, pp. 949–973, 2016.
- [112] A. F. Molisch, V. V. Ratnam, S. Han, Z. Li, S. L. H. Nguyen, L. Li, and K. Haneda, "Hybrid beamforming for massive MIMO - A survey," Available: *arXiv:1609.05078v1*, September 2016.
- [113] W. Roh, J.-Y. Seol, J. Park, B. Lee, Y. Kim, J. Cho, K. Cheun, and F. Aryanfar, "Millimeter-wave beamforming as an enabling technology for 5G cellular communications: Theoretical feasibility and prototype results," *IEEE Commun. Mag.*, vol. 52, pp. 106–113, February 2014.

- [114] M. R. Akdeniz, Y. Liu, M. K. Samimi, S. Sun, S. Rangan, T. S. Rappaport, and E. Erkip, "Millimeter wave channel modeling and cellular capacity evaluation," *IEEE J. Sel. Areas Commun.*, vol. 32, pp. 1164–1179, June 2014.
- [115] T. S. Rappaport, F. Gutierrez, E. Ben-Dor, J. N. Murdock, Y. Qiao, and J. I. Tamir, "Broadband millimeter-wave propagation measurements and models using adaptive-beam antennas for outdoor urban cellular communications," *IEEE Trans. Antennas and Propag.*, vol. 61, pp. 1850–1859, December 2012.
- [116] T. S. Rappaport, G. R. MacCartney, M. K. Samimi, and S. Sun, "Wideband millimeter-wave propagation measurements and channel models for future wireless communication system design," *IEEE Trans. Commun.*, vol. 63, pp. 3029–3056, May 2015.
- [117] M. K. Samimi and T. S. Rappaport, "3-D statistical channel model for millimeter-wave outdoor mobile broadband communications," *IEEE Intl. Conf. Commun.*, pp. 2430–2436, June 2015.
- [118] T. A. Thomas, H. C. Nguyen, G. R. MacCartney, and T. S. Rappaport, "3D mmWave channel model proposal," *IEEE Veh. Technol. Conf.*, pp. 1–6, September 2014.
- [119] S. Hur, S. Baek, B. Kim, Y. Chang, A. F. Molisch, T. S. Rappaport, K. Haneda, and J. Park, "Proposal on millimeter-wave channel modeling for 5G cellular system," *IEEE J. Sel. Topics Signal Process.*, vol. 10, pp. 454–469, April 2016.
- [120] M. K. Samimi and T. S. Rappaport, "3-D millimeter-wave statistical channel model for 5G wireless system design," *IEEE Trans. Microw. Theory Techn.*, vol. 64, pp. 2207–2225, July 2016.
- [121] M. K. Samimi, G. R. MacCartney Jr., S. Sun, and T. S. Rappaport, "28 GHz millimeter-wave ultrawideband small-scale fading models in wireless channels," *IEEE Veh. Technol. Conf.*, pp. 1–6, May 2016.
- [122] M. K. Samimi and T. S. Rappaport, "Statistical channel model with multi-frequency and arbitrary antenna beamwidth for millimeter-wave outdoor communications," *IEEE Global Commun. Conf.*, pp. 1–7, December 2015.
- [123] M. K. Samimi, K. Wang, Y. Azar, G. N. Wong, R. Mayzus, H. Zhao, J. K. Schulz, S. Sun, F. Gutierrez Jr., and T. S. Rappaport, "28 GHz angle of arrival and angle of departure analysis for outdoor cellular communications using steerable beam antennas in New York city," *IEEE Veh. Technol. Conf.*, pp. 1–6, June 2013.

- [124] N. A. Muhammad, P. Wang, Y. Li, and B. Vucetic, “Analytical model for outdoor millimeter wave channels using geometry-based stochastic approach,” *IEEE Trans. Veh. Technol.*, vol. 66, pp. 912–926, February 2017.
- [125] S. L. H. Nguyen, K. Haneda, J. Järveläinen, A. Karttunen, and J. Putkonen, “On the mutual orthogonality of millimeter-wave massive MIMO channels,” *IEEE Veh. Technol. Conf.*, pp. 11–14, May 2015.
- [126] M. Zhang, M. Polese, M. Mezzavilla, S. Rangan, and M. Zorzi, “ns-3 Implementation of the 3GPP MIMO channel model for frequency spectrum above 6 GHz,” Available: *arXiv:1702.04822v1*, February 2017.
- [127] H. Xu, V. Kukshya, and T. S. Rappaport, “Spatial and temporal characteristics of 60-GHz indoor channels,” *IEEE J. Sel. Areas Commun.*, vol. 20, pp. 620–630, April 2002.
- [128] S. Geng, J. Kivinen, X. Zhao, and P. Vainikainen, “Millimeter-wave propagation channel characterization for short-range wireless communications,” *IEEE Trans. Wireless Commun.*, vol. 15, pp. 5287–5301, August 2016.
- [129] “3GPP TR 36.873 V12.2.0 Technical Report: Study on 3D channel model for LTE (release 12),” June 2015, available: <http://www.3gpp.org/>.
- [130] “3GPP TR 38.900 V14.0.0 Technical Report: Study on channel model for frequency spectrum above 6 GHz (release 14),” June 2016, available: <http://www.3gpp.org/>.
- [131] A. Lozano, R. W. Heath Jr., and J. G. Andrews, “Fundamental limits of cooperation,” *IEEE Trans. Inf. Theory*, vol. 59, pp. 5213–5226, September 2013.
- [132] W. C. Jakes, *Microwave Mobile Communications*. New York: Wiley, 1974.
- [133] O. El Ayach, S. Rajagopal, S. Abu-Surra, Z. Pi, and R. W. Heath Jr., “Spatially sparse precoding in millimeter wave MIMO systems,” *IEEE Trans. Wireless Commun.*, vol. 13, pp. 1499–1513, January 2014.
- [134] J. Brady, N. Behdad, and A. M. Sayeed, “Beamspace MIMO for millimeter-wave communications: system architecture, modeling, analysis, and measurements,” *IEEE Trans. Antennas and Propag.*, vol. 61, pp. 3814–3827, March 2013.
- [135] Y. Kim, H. Ji, J. Lee, Y.-H. Nam, B. L. Ng, I. Tzanidis, Y. Li, and J. Zhang, “Full-dimension MIMO (FD-MIMO): The next evolution of MIMO in LTE systems,” *IEEE Wireless Commun.*, vol. 21, pp. 26–33, April 2014.

- [136] C. Lim, T. Yoo, B. Clerckx, B. Lee, and B. Shim, "Recent trend of multiuser MIMO in LTE-Advanced," *IEEE Commun. Mag.*, vol. 51, pp. 127–135, March 2013.
- [137] J. A. Zhang, X. Huang, V. Dyadyuk, and Y. J. Guo, "Massive hybrid antenna array for millimeter-wave cellular communications," *IEEE Wireless Commun.*, vol. 22, pp. 79–87, February 2015.
- [138] J. Zhang, X. Ge, Q. Li, M. Guizani, and Y. Zhang, "5G millimeter-wave antenna array: design and challenges," *IEEE Wireless Commun.*, vol. PP, pp. 2–8, October 2016.
- [139] H. Ji, Y. Kim, J. Lee, E. Onggosanusi, Y.-H. Nam, and J. Zhang, "Overview of full-dimension MIMO in LTE-Advanced Pro," *IEEE Commun. Mag.*, vol. 55, pp. 176–184, February 2017.
- [140] D. Solomitckii, Q. C. Li, T. Balercia, C. R. C. M. da Silva, S. Talwar, S. Andreev, and Y. Koucheryavy, "Characterizing the impact of diffuse scattering in urban millimeter-wave deployments," *IEEE Wireless Commun. Lett.*, vol. 5, pp. 432–435, August 2016.
- [141] M. Dohler, R. W. Heath Jr., A. Lozano, C. B. Papadias, and R. A. Valenzuela, "Is the PHY layer dead?," *IEEE Commun. Mag.*, vol. 49, pp. 159–165, April 2011.
- [142] A. Papoulis and S. U. Pillai, *Probability, Random Variables and Stochastic Processes*. McGraw-Hill Europe, 4 ed., 2002.
- [143] Q. Zhang, S. Jin, K.-K. Wong, H. Zhu, and M. Matthaiou, "Power scaling of uplink massive MIMO systems with arbitrary-rank channel means," *IEEE J. Sel. Topics Signal Process.*, vol. 8, pp. 966–981, October 2014.
- [144] J. Zhang, C. Pan, F. Pei, G. Liu, and X. Cheng, "Three-dimensional fading channel models: A survey of elevation angle research," *IEEE Commun. Mag.*, vol. 52, pp. 218–226, June 2014.
- [145] M. Shafi, M. Zhang, A. L. Moustakas, P. J. Smith, A. F. Molisch, F. Tufvesson, and S. H. Simon, "Polarized MIMO channels in 3-D: Models, measurements and mutual information," *IEEE J. Sel. Areas Commun.*, vol. 24, no. 3, pp. 514–527, 2006.
- [146] J. H. Winters, "On the capacity of radio communication systems with diversity in a Rayleigh fading environment," *IEEE J. Sel. Areas Commun.*, vol. 5, no. 5, 1987.

- [147] G. J. Foschini, “Layered space-time architecture for wireless communications in a fading environment when using multi-element antennas,” *Bell Labs Tech. J.*, vol. 1, no. 2, pp. 41–59, 1996.
- [148] T. M. Cover and J. A. Thomas, *Elements of Information Theory*. Jon Wiley & Sons, 2 ed., 2006.
- [149] E. Dahlman, S. Parkvall, J. Skold, and P. Beming, *3D Evolution: HSPA and LTE for Mobile Broadband*. Elsevier, 2 ed., 2008.
- [150] G. R. MacCartney Jr., M. K. Samimi, and T. S. Rappaport, “Omnidirectional path loss models in New York City at 28 GHz and 73 GHz,” *IEEE Intl. Symp. Pers. Indoor Mobile Radio Commun.*, pp. 227–231, September 2014.
- [151] Aalto University, AT&T, BUPT, CMCC, Ericsson, Huawei, INTEL, KT Corporation, Nokia, NTT DOCOMO, New York University, Qualcomm, Samsung, University of Bristol, and University of Southern California, “5G channel model for bands up to 100GHz, white paper, V2.0,” *IEEE Global Commun. Conf., 3rd Workshop on Mobile Commun. in Higher Frequency Bands*, December 2016.
- [152] S. Sun, T. S. Rappaport, T. A. Thomas, A. Ghosh, H. C. Hguyen, I. Z. Kovács, I. Rodriguez, O. Koymen, and A. Partyka, “Investigation of prediction accuracy, sensitivity, and parameter stability of large-scale propagation path loss models for 5G wireless communications,” *IEEE Trans. Veh. Technol.*, vol. 65, pp. 2843–2860, May 2016.
- [153] S. Sun, T. S. Rappaport, S. Rangan, T. A. Thomas, A. Ghosh, I. Z. Kovács, I. Rodriguez, O. Koymen, A. Partyka, and J. Järveläinen, “Propagation path loss models for 5G urban micro- and macro-cellular scenarios,” *IEEE Veh. Technol. Conf.*, pp. 1–6, May 2016.
- [154] T. A. Thomas, M. Rybakowski, S. Sun, T. S. Rappaport, H. Nguyen, I. Z. Kovács, and I. Rodriguez, “A predication study of path loss models from 2-73.5 GHz in an urban-macro environment,” *IEEE Veh. Technol. Conf.*, pp. 1–5, May 2016.
- [155] S. Sun, G. R. MacCartney Jr., and T. S. Rappaport, “Millimeter-wave distance-dependent large-scale propagation measurements and path loss models for outdoor and indoor 5G systems,” *IEEE European Conf. Antennas and Propag.*, pp. 1–5, April 2016.
- [156] G. R. MacCartney Jr., T. S. Rappaport, S. Sun, and S. Deng, “Indoor office wideband millimeter-wave propagation measurements and channel

- models at 28 and 73 GHz for ultra-dense 5G wireless networks,” *IEEE Access*, vol. 3, pp. 2388–2424, October 2015.
- [157] G. R. MacCartney Jr., T. S. Rappaport, M. K. Samimi, and S. Sun, “Millimeter-wave omnidirectional path loss data for small cell 5G channel modeling,” *IEEE Access*, vol. 3, pp. 1573–1580, August 2015.
- [158] V. Erceg, L. J. Greenstein, S. Y. Tjandra, S. R. Parkoff, A. Gupta, B. Kulic, A. A. Julius, and R. Bianchi, “An empirically based path loss model for wireless channels in suburban environments,” *IEEE J. Sel. Areas Commun.*, vol. 17, pp. 1205–1211, July 1999.
- [159] A. Goldsmith, *Wireless Communications*. Cambridge University Press, 2005.
- [160] A. Paulraj, R. Nabar, and D. Gore, *Introduction to Space-Time Wireless Communications*. Cambridge University Press, 2004.
- [161] D. Tse and P. Viswanath, *Fundamentals of Wireless Communication*. Cambridge University Press, 2005.
- [162] K. Yu, M. Bengtsson, B. Ottersten, D. McNamara, P. Karlsson, and M. Beach, “Modeling of wide-band MIMO radio channels based on NLoS indoor measurements,” *IEEE Trans. Veh. Technol.*, vol. 53, pp. 655–665, May 2004.
- [163] C.-N. Chuah, J. M. Kahn, and D. Tse, “Capacity of multi-antenna array systems in indoor wireless environment,” *IEEE Global Commun. Conf.*, vol. 4, pp. 1894–1899, November 1998.
- [164] S. O. Rice, “Mathematical analysis of random noise,” *Bell Syst. Tech. J.*, vol. 23, pp. 282–332, July 1944.
- [165] F. R. Farrokhi, G. J. Foschini, A. Lozano, and R. A. Valenzuela, “Link-optimal space-time processing with multiple transmit and receive antennas,” *IEEE Commun. Lett.*, vol. 5, pp. 85–87, March 2001.
- [166] H. Tataria, P. J. Smith, L. J. Greenstein, P. A. Dmochowski, and M. Shafi, “Performance and analysis of downlink multiuser MIMO systems with regularized zero-forcing precoding in Ricean fading channels,” *IEEE Intl. Conf. Commun.*, pp. 1185–1192, May 2016.
- [167] M. K. Samimi, S. Sun, and T. S. Rappaport, “MIMO channel modeling capacity analysis for 5G millimeter-wave wireless system,” *IEEE European Conf. Antennas and Propag.*, pp. 1–5, April 2016.

- [168] B. Clerckx and C. Oestges, *MIMO Wireless Networks*. Elsevier, 2 ed., 2007.
- [169] A. F. Molisch, *Wireless Communications*. Wiley, 2 ed., 2011.
- [170] M. N. Abdallah, T. K. Sarkar, M. Salazar-Palma, and V. Monebhurrun, “Where does the far field of an antenna start?,” *IEEE Antennas and Propag. Mag.*, vol. 58, pp. 115–124, October 2016.
- [171] C. A. Balanis, *Antenna Theory: Analysis and Design*. John Wiley and Sons, 3 ed., 2005.
- [172] C. Siriteanu, A. Takemura, S. Kuriki, D. St. P. Richards, and H. Shin, “Exact ZF analysis and computer-algebra-aided evaluation in rank-1 LoS Rician fading,” *IEEE Trans. Wireless Commun.*, vol. 15, pp. 5245–5259, August 2016.
- [173] A. A. M. Saleh and R. A. Valenzuela, “A statistical model for indoor multipath propagation,” *IEEE J. Sel. Areas Commun.*, vol. 5, pp. 128–137, February 1987.
- [174] A. Alkhateeb, O. El Ayach, G. Leus, and R. W. Heath Jr., “Channel estimation and hybrid precoding for millimeter wave cellular systems,” *IEEE J. Sel. Topics Signal Process.*, vol. 8, pp. 831–846, July 2014.
- [175] V. Raghavan and A. M. Sayeed, “Sublinear capacity scaling laws for sparse MIMO channels,” *IEEE Trans. Inf. Theory*, vol. 57, pp. 345–364, January 2011.
- [176] A. O. Martínez, P. Eggers, and E. De Carvalho, “Geometry-based stochastic channel models for 5G: Extending key features for massive MIMO,” *IEEE Intl. Symp. Pers. Indoor Mobile Radio Commun.*, September 2016.
- [177] A. Meijerink and A. F. Molisch, “On the physical interpretation of the Saleh-Valenzuela model and the definition of its power decay profiles,” *IEEE Trans. Antennas and Propag.*, vol. 62, pp. 4780–4793, September 2014.
- [178] T. Taga, “Analysis for mean effective gain of mobile antennas in land mobile radio environments,” *IEEE Trans. Veh. Technol.*, vol. 39, pp. 117–131, May 1990.
- [179] K. Kalliola, K. Sulonen, H. Laitinen, O. Kivekäs, J. Krogerus, and P. Vainikainen, “Angular power distribution and mean effective gain of mobile antenna in different propagation environments,” *IEEE Trans. Veh. Technol.*, vol. 51, pp. 823–838, September 2002.

- [180] Q.-U.-A. Nadeem, A. Kammoun, M. Debbah, and M.-S. Alouini, "A generalized spatial correlation model for 3D MIMO channels based on the Fourier coefficient of power spectrums," *IEEE Trans. Signal Process.*, vol. 63, pp. 3671–3686, July 2015.
- [181] B. Mondal, T. A. Thomas, E. Visotsky, F. W. Vook, A. Ghosh, Y.-H. Nam, Y. Li, J. C. Zhang, M. Zhang, Q. Luo, Y. Kakishima, and K. Kitao, "3D channel model in 3GPP," *IEEE Commun. Mag.*, vol. 53, pp. 16–23, March 2015.
- [182] J. Medbo, P. Kyösti, K. Kusume, L. Raschkowski, K. Haneda, T. Jamsa, V. Nurmela, A. Roivainen, and J. Meinilä, "Radio propagation modeling for 5G mobile and wireless communications," *IEEE Commun. Mag.*, vol. 54, pp. 144–151, June 2016.
- [183] C. E. Shannon, "A mathematical theory of communication," *Bell Syst. Tech. J.*, vol. 27, pp. 379–423, July 1948.
- [184] Q. H. Spencer, A. L. Swindlehurst, and M. Haardt, "Zero-forcing methods for downlink spatial multiplexing in multiuser MIMO channels," *IEEE Trans. Signal Process.*, vol. 52, pp. 461–471, February 2004.
- [185] T. Yoo and A. Goldsmith, "On the optimality of multiantenna broadcast scheduling using zero-forcing beamforming," *IEEE J. Sel. Areas Commun.*, vol. 24, pp. 528–541, March 2006.
- [186] M. Sadek, A. Tarighat, and A. H. Sayed, "A leakage-based precoding scheme for downlink multi-user MIMO channels," *IEEE Trans. Wireless Commun.*, vol. 6, pp. 1711–1721, May 2007.
- [187] H. Tataria, M. Shafi, P. J. Smith, and P. A. Dmochowski, "Coordinated two-tier heterogeneous cellular networks with leakage based beamforming," Available: *arXiv:1503.01566v1*, March 2015.
- [188] R. J. Muirhead, *Aspects of Multivariate Statistical Theory*. Wiley, 2 ed., 2005.
- [189] S. L. Loyka, "Channel capacity of MIMO architecture using the exponential correlation matrix," *IEEE Commun. Lett.*, vol. 5, pp. 369–371, September 2001.
- [190] J. Luo, J. R. Zeidler, and S. McLaughlin, "Performance analysis of compact antenna arrays with MRC in correlated Nakagami fading channels," *IEEE Trans. Veh. Technol.*, vol. 50, pp. 267–277, January 2001.

- [191] K. F. Warnick and M. A. Jensen, "Effects of mutual coupling on interference mitigation with a focal plane array," *IEEE Trans. Antennas and Propag.*, vol. 53, pp. 2490–2498, August 2005.
- [192] W. C. Y. Lee, "Effect of mutual coupling on a mobile-radio maximum ratio diversity combiner with a large number of branches," *IEEE Trans. Commun.*, vol. COMM-20, pp. 1188–1193, December 1972.
- [193] R. R. Ramirez and F. De Flaviis, "Mutual coupling study of linear polarized microstrip antennas for use in BLAST wireless communications architecture," *IEEE Antennas and Propag. Soc. Int. Symp. Dig.*, vol. 2, pp. 16–21, July 2000.
- [194] G. V. Tsoulos, "Experimental and theoretical capacity analysis of space-division multiple access (SDMA) with adaptive antennas," *IEEE Proceed. Commun.*, vol. 146, pp. 307–311, October 1999.
- [195] K. R. Dandekar, H. Ling, and G. Xu, "Effect of mutual coupling on direction finding in smart antenna applications," *IEEE Electron. Lett.*, vol. 36, pp. 1889–1891, October 2000.
- [196] A. M. Wyglinski and S. D. Blostein, "Mutual coupling and scattering effects on cellular CDMA systems using smart antennas," *IEEE Veh. Technol. Conf.*, vol. 4, pp. 1656–1662, September 2000.
- [197] E. Björnson, J. Hoydis, and L. Sanguinetti, "Pilot contamination is not a fundamental asymptotic limitation in massive MIMO," *Available: arXiv:1611.09152v1*, November 2016.
- [198] A. Ashikhmin and T. Marzetta, "Pilot contamination precoding in multi-cell large scale antenna systems," *IEEE Intl. Symp. on Inf. Theory*, pp. 1–6, July 2012.
- [199] M. Matthaiou, M. R. McKay, P. J. Smith, and J. A. Nossek, "On the condition number distribution of complex Wishart matrices," *IEEE Trans. Commun.*, vol. 58, pp. 1705–1717, June 2010.
- [200] N. L. Johnson, S. Kotz, and N. Balakrishnan, *Continuous Univariate Distributions, Volume 1*. John Wiley and Sons, 2 ed., 1994.
- [201] P. J. Smith, M. McKay, A. Giorgetti, and M. Chiani, "Random matrix processes: Quantifying rates of change in MIMO systems," *IEEE European Wireless Conf.*, April 2010.
- [202] B. Hochwald and S. Vishwanath, "Space-time multiple access: Linear growth in the sum rate," *Annual Allerton Conf. Commun., Control, and Comput.*, October 2002.

- [203] A. M. Tulino and S. Verdú, *Random Matrix Theory and Wireless Communications*. Now Publishers Inc., 2004.
- [204] L. Sanguinetti, A. Kammoun, and M. Debbah, “Asymptotic analysis of multicell massive MIMO over Rician fading channels,” *Available: arXiv:1605.02856v1*, May 2016.
- [205] H. Q. Ngo, A. Ashikhmin, H. Yang, E. G. Larsson, and T. L. Marzetta, “Cell-free massive MIMO: Uniformly great service for everyone,” *IEEE Intl. Workshop on Signal Process. Advances in Wireless Commun.*, pp. 201–205, June 2015.
- [206] D. Lee, H. Seo, B. Clerckx, E. Hardouin, D. Mazzaresse, S. Nagata, and K. Sayana, “Coordinated multipoint transmission and reception in LTE-Advanced: deployment scenarios and operational challenges,” *IEEE Commun. Mag.*, vol. 50, pp. 148–155, February 2012.
- [207] D. A. Basnayaka, P. J. Smith, and P. A. Martin, “Performance analysis of dual-user macrodiversity MIMO systems with linear receivers in flat Rayleigh fading,” *IEEE Trans. Wireless Commun.*, vol. 11, pp. 4394–4404, December 2012.
- [208] D. A. Basnayaka, P. J. Smith, and P. A. Martin, “Performance analysis of macrodiversity MIMO systems with MMSE and ZF receivers in flat Rayleigh fading,” *IEEE Trans. Wireless Commun.*, vol. 12, pp. 2240–2251, May 2013.
- [209] E. Björnson, M. Matthaiou, and M. Debbah, “Massive MIMO with non-ideal arbitrary arrays: Hardware scaling laws and circuit-aware design,” *IEEE Trans. Wireless Commun.*, vol. 14, pp. 4353–4368, August 2015.
- [210] R. W. Heath Jr., T. Wu, Y. H. Kwon, and A. C. K. Soong, “Multiuser MIMO in distributed antenna systems with out-of-cell interference,” *IEEE Trans. Signal Process.*, vol. 59, pp. 4885–4899, October 2011.
- [211] Z. Liu and L. Dai, “A comparative study of downlink MIMO cellular networks with co-located and distributed base-station antennas,” *IEEE Trans. Wireless Commun.*, vol. 13, pp. 6259–6274, November 2014.
- [212] D. Wang, J. Wang, X. You, Y. Wang, M. Chen, and X. Hou, “Spectral efficiency of distributed MIMO systems,” *IEEE J. Sel. Areas Commun.*, vol. 31, pp. 2112–2127, October 2013.
- [213] A. Yang, Y. Jing, C. Xing, Z. Fei, and J. Kuang, “Performance analysis and location optimization for massive MIMO systems with circularly

- distributed antennas,” *IEEE Trans. Wireless Commun.*, vol. 14, pp. 5659–5671, October 2015.
- [214] J. Choi, “Distributed beamforming for macro diversity and power control with large arrays in spatial correlated channels,” *IEEE Trans. Wireless Commun.*, vol. 14, pp. 1871–1881, April 2015.
- [215] K. T. Truong and R. W. Heath Jr., “The viability of distributed antennas for massive MIMO systems,” *Asilomar Conf. Signals, Systems and Computers*, pp. 1318–1323, November 2013.
- [216] J. Zuo, J. Zhang, C. Yuan, W. Jiang, and W. Luo, “Energy efficient downlink transmission for multi-cell massive DAS with pilot contamination,” *IEEE Trans. Veh. Technol.*, vol. 66, pp. 1209–1221, February 2017.
- [217] L. Sanguinetti, R. Couillet, and M. Debbah, “Large system analysis of base station cooperation for power minimization,” *IEEE Trans. Wireless Commun.*, vol. 15, pp. 5480–5496, August 2016.
- [218] K. Hosseini, W. Yu, and R. S. Adve, “Large-scale MIMO versus network MIMO for multicell interference mitigation,” *IEEE J. Sel. Topics Signal Process.*, vol. 8, pp. 930–941, October 2014.
- [219] E. Nayebi, A. Ashikhmin, T. L. Marzetta, and B. D. Rao, “Performance of cell-free massive MIMO systems with MMSE and LSFD receivers,” Available: *arXiv:1702.03231v1*, February 2017.
- [220] H. B. Almelah and K. A. Hamdi, “Spectral efficiency of distributed large-scale MIMO systems with ZF receivers,” *IEEE Trans. Veh. Technol.*, vol. PP, pp. 1–1, October 2016.
- [221] R. Senanayake, P. Smith, P. L. Yeoh, and J. Evans, “An SNR approximation for distributed massive MIMO with zero forcing,” *IEEE Commun. Lett.*, vol. 19, no. 11, pp. 1885–1888, 2015.
- [222] M. C. Filippou, P. de Kerret, D. Gesbert, T. Ratnarajah, A. Pastore, and G. A. Ropokis, “Coordinated shared spectrum precoding with distributed CSIT,” *IEEE Trans. Wireless Commun.*, vol. 15, pp. 5182–5192, August 2016.
- [223] M. K. Karakayali, G. J. Foschini, and R. A. Valenzuela, “Network coordination for spectrally efficient communications in cellular systems,” *IEEE Wireless Commun.*, vol. 13, pp. 56–61, August 2006.
- [224] M. J. Gans, “The effect of Gaussian error in maximal ratio combiners,” *IEEE Trans. Commun. Technol.*, vol. COM-19, no. 4, pp. 492–500, 1971.

- [225] H. A. Suraweera, P. J. Smith, and M. Shafi, "Capacity limits and performance analysis of cognitive radio with imperfect channel knowledge," *IEEE Trans. Veh. Technol.*, vol. 59, pp. 1811–1822, May 2010.
- [226] L. Yu, W. Liu, and R. Langley, "SINR analysis of the subtraction-based SMI beamformer," *IEEE Trans. Signal Process.*, vol. 58, pp. 5926–5932, November 2010.
- [227] O. Lieberman, "A Laplace approximation to the moments of a ratio of quadratic forms," *Biometrika*, vol. 81, pp. 681–690, December 1994.
- [228] H. Tataria, P. J. Smith, P. A. Dmochowski, and M. Shafi, "General analysis of multiuser MIMO systems with regularized zero-forcing precoding under spatially correlated Rayleigh fading channels," *IEEE Intl. Conf. Commun.*, pp. 2582–2588, May 2016.
- [229] C. Feng, Y. Jing, and S. Jin, "Interference and outage probability analysis for massive MIMO downlink with MF precoding," *IEEE Signal Process. Lett.*, vol. 23, pp. 366–370, March 2016.
- [230] T. Ratnarajah, R. Vaillancourt, and M. Alvo, "Complex Random Matrices and Rician Channel Capacity," *Problems of Information Transmission*, vol. 41, pp. 1–22, 2005.
- [231] D. A. Basnayaka, P. J. Smith, and P. A. Martin, "Ergodic sum capacity of macrodiversity MIMO systems in flat Rayleigh fading," *IEEE Trans. Inf. Theory*, vol. 59, pp. 5257–5270, September 2013.
- [232] Y. Yu, P. Wang, H. Chen, Y. Li, and B. Vucetic, "A low-complexity transceiver design in sparse multipath massive MIMO channels," *IEEE Signal Process. Lett.*, vol. 23, pp. 1301–1305, October 2016.
- [233] K. Haneda, A. Khatun, M. Dashti, T. A. Laitinen, V.-M. Komonen, J.-I. Takada, and P. Vainikainen, "Measurement-based analysis of spatial degrees of freedom in multipath propagation channels," *IEEE Trans. Antennas and Propag.*, vol. 61, pp. 890–900, February 2013.
- [234] M. K. Samimi and T. S. Rappaport, "Ultra-wideband statistical channel model for non line of sight millimeter-wave urban channels," *IEEE Global Commun. Conf.*, pp. 3483–3489, December 2014.
- [235] M. K. Samimi and T. S. Rappaport, "Local multipath model parameters for generating 5G millimeter-wave 3GPP-like channel impulse response," *IEEE European Conf. Antennas and Propag.*, April 2016.

- [236] A. Abdi, J. A. Barger, and M. Kaveh, "A parametric model for the distribution of the angle of arrival and the associated correlation function and power spectrum at the mobile station," *IEEE Trans. Veh. Technol.*, vol. 51, pp. 425–434, May 2002.
- [237] I. S. Gradshteyn and I. M. Ryzhik, *Table of Integrals, Series, and Products*. Elsevier Inc., 7 ed., 2007.
- [238] M. Abramowitz and I. A. Stegun, *Handbook of Mathematical Functions: with Formulas, Graphs, and Mathematical Tables*. Dover Publications, 1965.
- [239] Y. Wu, J. P. Linnartz, J. W. M. Bergmans, and S. Attallah, "Effects of antenna mutual coupling on the performance of MIMO systems," *Symp. Inf. Theory*, pp. 207–215, May 2008.
- [240] A. S. Y. Poon, R. W. Brodersen, and D. N. C. Tse, "Degrees of freedom in multiple-antenna channels: A signal space approach," *IEEE Trans. Inf. Theory*, vol. 51, pp. 523–536, February 2005.
- [241] S. Sun, T. S. Rappaport, R. W. Heath Jr., A. Nix, and S. Rangan, "MIMO for millimeter-wave wireless communications: Beamforming, spatial multiplexing, or both?," *IEEE Commun. Mag.*, vol. 52, pp. 110–121, December 2014.
- [242] Y. Zhang, J. Zhang, P. J. Smith, M. Shafi, and P. Zhang, "Reduced complexity channel models for IMT-advanced evaluation," *EURASIP J. Wireless Commun. and Networking*, April 2009.
- [243] T. Bai, A. Alkhateeb, and R. W. Heath Jr., "Coverage and capacity of millimeter-wave cellular networks," *IEEE Commun. Mag.*, vol. 52, pp. 70–77, September 2014.
- [244] J. G. Andrews, T. Bai, M. N. Kulkarni, A. Alkhateeb, A. K. Gupta, and R. W. Heath Jr., "Modeling and analyzing millimeter wave cellular systems," *IEEE Trans. Commun.*, vol. 65, pp. 403–430, January 2017.
- [245] P. Kyösti, J. Meinilä, L. Hentilä, X. Zhao, T. Jämsä, C. Schneider, M. Narandzić, M. Milojević, A. Hong, J. Ylitalo, V.-M. Holappa, M. Alatossava, R. Bultitude, Y. de Jong, and T. Rautiainen, "WINNER II channel models, D1.1.2 V1.2," September 2007, available: <http://www.ist-winner.org/deliverables/>.
- [246] B. M. Hochwald and T. L. Marzetta, "Unitary space-time modulation for multiple-antenna communications in Rayleigh flat fading," *IEEE Trans. Inf. Theory*, vol. 46, pp. 543–564, March 2000.

- [247] P. J. Smith and M. Shafi, "The impact of complexity in MIMO channel models," *IEEE Intl. Conf. Commun.*, vol. 5, pp. 2924–2928, June 2004.
- [248] S. Buzzi and C. D' Andrea, "Doubly massive mmWave MIMO systems: Using very large antenna arrays at both transmitter and receiver," *Available: arXiv:1607.07234v1*, July 2016.
- [249] J. Medbo, K. Börner, K. Haneda, V. Hovinen, T. Imai, J. Järveläinen, T. Jämsä, A. Karttunen, K. Kusume, J. Kyröläinen, P. Kyösti, J. Meinilä, V. Nurmela, L. Raschkowski, A. Roivainen, and J. Ylitalo, "Channel modelling for the Fifth Generation mobile communications," *8th European Conf. on Antennas and Propag.*, pp. 219–223, April 2014.
- [250] "3GPP TR 36.814 V9.0.0 Technical Report: Further advancements for E-UTRA physical layer aspects (release 9)," March 2010, available: <http://www.3gpp.org/>.
- [251] J. Meinilä, P. Kyösti, L. Hentilä, T. Jämsä, E. Suikkanen, E. Kunnari, and M. Narandžić, "WINNER+ final channel models, D5.3 V1.0," June 2010, available: <http://projects.celtic-initiative.org/winner+/WINNER+>.
- [252] V. Nurmela, A. Karttunen, A. Roivainen, L. Raschkowski, T. Imai, J. Järveläinen, J. Medbo, J. Vihriälä, J. Meinilä, K. Haneda, V. Hovinen, J. Ylitalo, N. Omaki, K. Kusume, P. Kyösti, T. Jämsä, A. Hekkala, R. Weiler, and M. Peter, "Mobile and wireless communications Enablers for the Twenty-twenty Information Society (METIS), D1.4 V1.0," February 2015, available: <https://www.metis2020.com/>.
- [253] A. Alkhateeb, G. Leus, and R. W. Heath Jr., "Limited feedback hybrid precoding for multi-user millimeter wave systems," *IEEE Trans. Wireless Commun.*, vol. 14, pp. 6481–6494, November 2015.
- [254] X. Song, N. Babu, W. Rave, S. Majhi, and G. Fettweis, "Two-level spatial multiplexing using hybrid beamforming antenna arrays for mmWave communications," *Available: arXiv:1607.08737v1*, July 2016.
- [255] S. Park, A. Alkhateeb, and R. W. Heath Jr., "Dynamic subarrays for hybrid precoding in wideband mmWave MIMO systems," *Available: arXiv:1606.08404v1*, June 2016.
- [256] X. Huang, Y. J. Gao, and J. D. Bunton, "A hybrid adaptive antenna array," *IEEE Trans. on Wireless Commun.*, vol. 9, pp. 1770–1779, May 2010.

- [257] R. W. Heath Jr., N. González-Prelcic, S. Rangan, W. Roh, and A. M. Sayeed, “An overview of signal processing techniques for millimeter wave MIMO systems,” *IEEE J. Sel. Topics in Signal Process.*, vol. 10, pp. 436–453, April 2016.
- [258] O. El Ayach, R. W. Heath Jr., S. Rajagopal, and Z. Pi, “Multimode precoding in millimeter wave MIMO transmitters with multiple antenna sub-arrays,” *IEEE Global Commun. Conf.*, pp. 3476–3480, December 2013.
- [259] A. Alkhateeb, J. Mo, N. González-Prelcic, and R. W. Heath Jr., “MIMO precoding and combining solutions for millimeter-wave systems,” *IEEE Commun. Mag.*, vol. 52, pp. 122–131, December 2014.
- [260] A. Sayeed and N. Behdad, “Continuous aperture phased MIMO: Basic theory and applications,” *IEEE Annual Allerton Conf. on Commun., Control, and Computing*, pp. 1196–1203, September 2010.
- [261] A. M. Sayeed and N. Behdad, “Continuous aperture phased MIMO: A new architecture for optimum line-of-sight links,” *IEEE Intl. Symp. Antennas and Propag.*, pp. 293–296, July 2011.
- [262] G. H. Song, J. Brady, and A. Sayeed, “Beamspace MIMO transceivers for low-complexity and near-optimal communications at mm-wave frequencies,” *IEEE Intl. Conf. on Acoustics, Speech and Signal Process.*, pp. 4394–4398, May 2013.
- [263] A. M. Sayeed and J. Brady, “Beamspace MIMO for high-dimensional multiuser communications at millimeter-wave frequencies,” *IEEE Global Commun. Conf.*, pp. 3679–3684, December 2013.
- [264] J. Choi, D. J. Love, and P. Bidigare, “Downlink training techniques for FDD massive MIMO systems: Open-loop and closed-loop training with memory,” *IEEE J. Sel. Topics Signal Process.*, vol. 8, pp. 802–814, October 2014.
- [265] E. Björnson and B. Ottersten, “A framework for training-based estimation in arbitrarily correlated Rician MIMO channels with Rician disturbance,” *IEEE Trans. Signal Process.*, vol. 58, pp. 1807–1820, March 2010.
- [266] H. Yin, D. Gesbert, M. Filippou, and Y. Liu, “A coordinated approach to channel estimation in large-scale multiple-antenna systems,” *IEEE J. Sel. Areas Commun.*, vol. 31, pp. 264–273, February 2013.
- [267] A. Adhikary, E. Al Safadi, M. K. Samimi, R. Wang, G. Caire, T. S. Rappaport, and A. F. Molisch, “Joint spatial division and multiplexing

- for mm-Wave channel,” *IEEE J. Sel. Areas Commun.*, vol. 32, pp. 1239–1255, June 2014.
- [268] X. Rao and V. K. N. Lau, “Distributed compressive CSIT estimation and feedback for FDD multi-user massive MIMO systems,” *IEEE Trans. Signal Process.*, vol. 62, pp. 3261–3271, June 2014.
- [269] Z. Zhang, Y. Xu, J. Yang, X. Li, and D. Zhang, “A survey of sparse representation: Algorithms and applications,” *IEEE Access*, vol. 3, pp. 490–530, May 2016.